Flow Physics Beyond the Betz Limit

Daniel Dehtyriov
Lady Margaret Hall
University of Oxford

A thesis submitted for the degree of
Doctor of Philosophy

Michaelmas 2023

Acknowledgements

This research has been supported by an EPSRC Centre for Doctoral Training in Wind and Marine Energy Systems and Structures scholarship and by resources provided by the Advanced Research Computing service within the University of Oxford.

I extend my warmest gratitude to my supervisors. Their expertise and passion for fluid mechanics & renewable energy has been as invaluable as their support, patience, guidance and advice.

To my colleagues and fellow lab-mates, for their openness to countless discussions on submission deadlines, life and everything in between.

To my friends, whose laughter was always a welcome hindrance to my work.

Finally, to my partner and family, to whom I am indebted by love.

Abstract

A pivotal theoretical result of the early 20^{th} century demonstrated that the limit of energy extraction for a wind or tidal stream turbine from an unconstrained flow is 16/27 of the upstream kinetic flux passing through the turbine area, known as the 'Betz Limit'. This result relies on several simplifying assumptions, including inviscid, unconstrained and steady flow. The aim of this thesis is to relax these assumptions for more realistic flow conditions, leading to increased energy extraction efficiencies. The thesis first considers relaxing the unconstrained flow assumption. It has previously been shown that tidal fences consisting of turbines placed side-by-side can make use of constructive interference to raise energy extraction efficiency. The current work shows that the asymptotic performance limit of a multi-layered array is a power coefficient of unity, a 27/16 increase on the Betz limit. Contrary to intuition, the minimisation of mixing losses is not the mechanism by which power extraction increases; instead, wake mixing is found to provide an additional source of static pressure recovery. Building on this physical understanding, a new theoretical model is developed that relaxes the inviscid assumption by considering wake mixing for a single turbine, demonstrating an increase in power coefficient under the same pressure recovery mechanism observed for turbine arrays. New algebraic estimates for the optimal power coefficient are proposed, with the maximum disc performance in an unbounded flow of between 0.71 and 0.81, depending on the mixing conditions. For turbine arrays partially spanning a channel, the leading order steady flow assumption is then relaxed to consider unsteady sinusoidal forcing on the coupling between the channel and array, where the mass flux through the turbine fence can respond dynamically and is governed by the channel head. The coupled framework enables optimisation of the number and spacing of turbines in a channel to maximise power per turbine area as a proxy for revenue per cost. The thesis also presents an analytical two-scale momentum-based method for correcting experimental turbine fence performance data. Unwanted global blockage effects due to domain constraints are separated from the intended constructive interference effects caused by local system blockage. The theoretical work highlights the importance of multi-scale energy extraction and mixing-induced wake pressure recovery by which turbine performance can be boosted. Exploiting the underlying physics may allow for increases in energy capture efficiency to pave the way for next-generation turbines, accelerating the shift to energy decarbonisation.

Contents

Chapter 1

Introduction

> "Begin at the beginning," the King said gravely, "and go on till you come to the end: then stop."
>
> — Lewis Carroll, Alice in Wonderland

This introduction provides a brief and broad overview of the literature on energy extraction from fluid flows. In particular, it outlines a framework by which to interpret the Lanchester-Betz-Joukowsky limit. Detailed introductions to the theoretical problems elaborated in the thesis outline may be found in chapters 2-5.

1.1 Motivation

Sustainable forms of energy production are anticipated to rapidly develop within the coming decades as nations move to reduce carbon emissions to mitigate the adverse effects of climate change. In particular, energy extraction from fluid flow is expected to be a key ingredient in the future energy mix, with scientific and industrial advance a necessity to reduce costs in a competitive energy market.

A detailed understanding of the fluid mechanics underlying this energy extraction process is hence of significant interest, but the complete picture is highly complex (see figure 1.1). Wind and tidal turbines, the focus of this work, operate in highly turbulent flows within topologically complex environments, and are typically comprised of rotating wings with multiple degrees of rotational freedom. As the energy density of this renewable power is comparatively low, many devices are routinely grid-integrated into a complete power station or "farm". The devices within each farm then interact with one another fluid dynamically, and the farm as a whole additionally interacts in a coupled manner with the incoming flow. This complexity motivates a vast body of

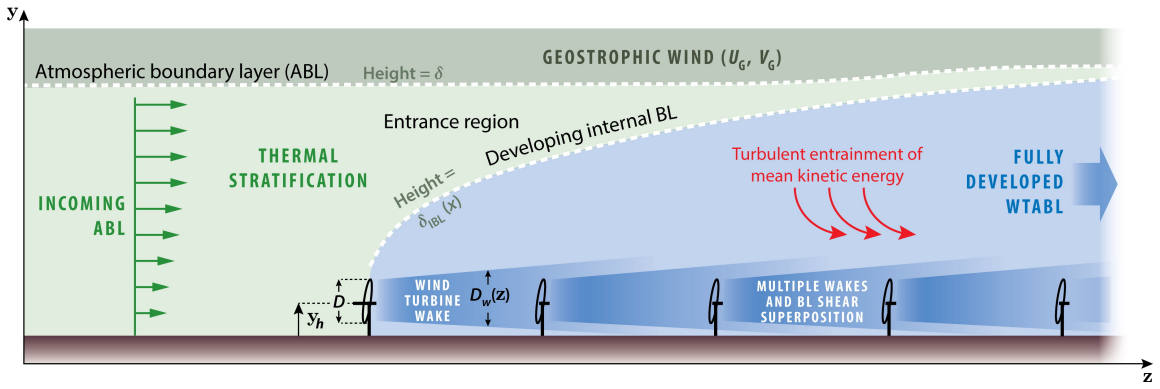

(a) Schematic illustrating the dominant wind farm physics

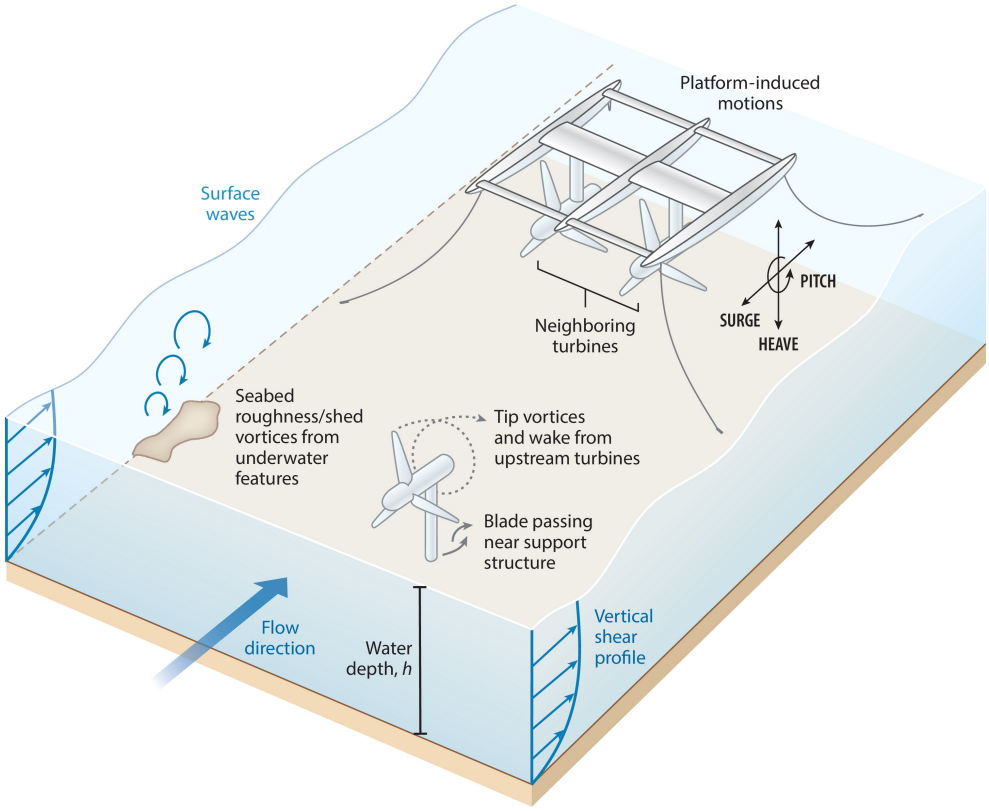

(b) Schematic illustrating the dominant tidal farm physics

Figure 1.1: Various fluid mechanics flow phenomena affecting wind and tidal turbine energy extractors including (a) wake interaction, atmospheric/internal boundary layer interaction and turbulence in the case of wind farms and (b) the addition of surface waves, seabed roughness, turbine motions and blockage effects for tidal turbines. Figures reproduced from [Stevens and Meneveau, 2017] and [Adcock et al., 2021].

scientific interest in the flow physics, with the aim to both predict and optimise the energy extraction from these devices.

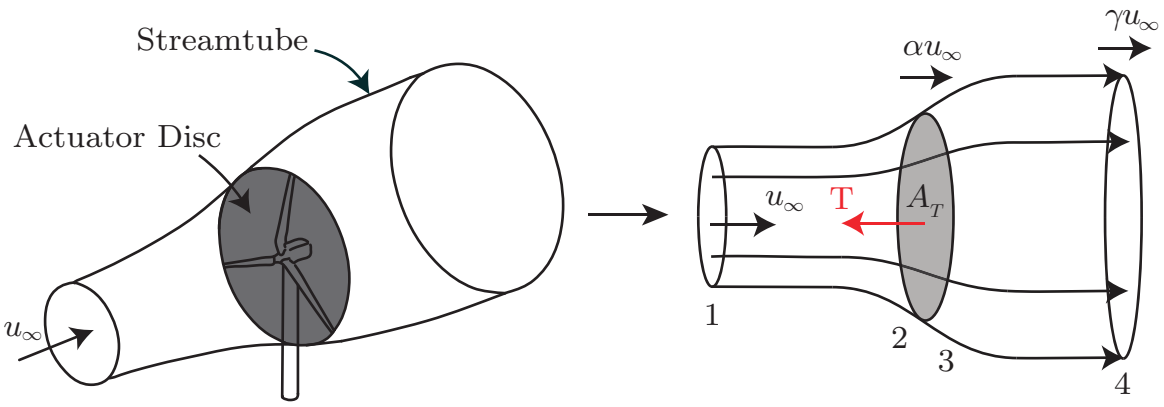

Figure 1.2: Schematic of the actuator disc representation of a turbine extracting energy from fluid flow. The disc is a thin region with area A_T representing the swept area of the blades, and is assumed to provide a uniform resistance T to the fluid. The flow then decelerates by factors α and γ at the disc plane and far-wake respectively.

1.2 Lanchester-Betz-Joukowsky theory

For turbomachines intended for energy extraction, these complexities render fully parametric studies intractable, necessitating numerous simplifications for turbine design. Instead of attempting to model all of the physical phenomena shown in figure 1.1, an alternative approach is to first develop a low-order model for analytic tractability, where much complexity is stripped from the system. Complexities may then be reintroduced as incremental variations to the model, and ultimately combined for an understanding of their nonlinear interaction. This approach offers the advantage of isolating and analysing the underlying physics from each element of complexity, allowing for a deeper understanding of the overall flow system, and ultimately for the improvement of turbine design and operation.

A widely-applied low-order model is that of the conceptual *actuator disc*, which simplifies a turbine by reducing it to a permeable disc which applies a constant resistance to the flow over the area swept by the blades of a wind or tidal turbine, see figure 1.2. By assuming constant, uniform, and inviscid flow upstream of the disc, the flow problem can be treated as quasi one-dimensional, and conservation of mass, energy and momentum can readily be applied across appropriate domains for a low-order understanding of the physics of energy extraction from fluid flow.

This flow problem is fully parameterised and solved for in terms of the uniform disc resistance T. Principally of interest is the power absorbed, $T\alpha u_\infty$, where u_∞ is the undisturbed upstream streamwise velocity, which provides a meaningful upper limit for the power generated by a rotating turbine (which would then be converted to

electrical power via a generator). Joukowsky [1920], Lanchester [1915] and Betz [1920] showed that for this system, the limit of power extraction is 16/27 of the upstream kinetic flux passing through the turbine area, widely known as the eponymous 'Betz limit' [1].

This can be intuitively understood by considering the limiting cases of varying the disc thrust, where $T \to 0$ (a fully permeable disc) and where $T \to \infty$ (a solid disc). In the first case, the streamtube shown in figure 1.2 does not deform, allowing the upstream kinetic energy flux bounded by the area of the turbine to pass entirely through the disc. Clearly however, no work is done on the flow, and the power absorbed is zero. In the latter case, the streamtube deforms such that the area of the streamtube cross-section containing the upstream kinetic energy flux (at station 1 in figure 1.2) approaches zero, and no fluid passes through the disc. Although T is large, $\alpha \to 0$, and no power is again absorbed.

These limiting cases suggest that there exists an optimal resistance T^* for peak power absorption. The flow physics through the disc can thus be reformulated as an optimisation problem. While this reformulation may seem superfluous for this comparatively simple flow problem, this approach is better generalisable to cases where complexity is reintroduced. The Betz theory can in fact be represented by constrained optimisation, with the constraints originating from the assumptions underlying the low-order theory. By normalisation on the upstream conditions, a thrust coefficient is defined

$$C_T = \frac{T}{\frac{1}{2}\rho u_\infty^2 A_T}, \tag{1.1}$$

where ρ is the fluid density and A_T the frontal disc area. The power extraction coefficient is defined as

$$C_P = \frac{P}{\frac{1}{2}\rho u_\infty^3 A_T} = \frac{T\alpha u_\infty}{\frac{1}{2}\rho u_\infty^3 A_T}. \tag{1.2}$$

Now consider a control volume which contains the actuator disc and streamtube shown in figure 1.2. Assuming steady, inviscid, incompressible and unbounded flow, the governing (Euler) equations in integral form can be written as constraints

$$\max_{C_T} \quad C_P, \tag{1.3}$$

$$\text{s.t.} \quad \oiint_{CS} \rho \mathbf{u} \cdot \hat{\mathbf{n}} \, dA = 0, \tag{1.4}$$

$$\oiint_{CS} (\hat{\mathbf{n}} \cdot \rho \mathbf{u}) \mathbf{u} \, dA = \oiint_{CS} -p\hat{\mathbf{n}} \, dA - qA_T \mathbf{C_T}, \tag{1.5}$$

$$\alpha \geq 0, \tag{1.6}$$

[1] This limit is known as the Joukowsky limit in Russian literature

where $\mathbf{u}$ is the velocity field, q is the dynamic head, a vectorised $\mathbf{C_T}$ allows for an arbitrary inflow angle, p is the static pressure field, and where equations 1.4-1.5 assume negligible body forces and represent mass and momentum conservation respectively.

This system can be simplified and solved to derive the widely known Joukowsky-Lanchester-Betz limit of $C_P^* = C_{P,\text{Betz}} = 16/27$, i.e. that the optimal energy extraction efficiency is ~60% of the undisturbed kinetic flux bounded by the rotor plane. The solution to this flow problem also provides the optimal rotor and flow conditions for peak power; $C_T^* = 8/9$, $\alpha^* = 2/3$ and $\gamma^* = 1/3$. Additionally, the pressure field can be solved for with the addition of Bernoulli's principle

$$p + \frac{1}{2}\rho|\mathbf{u}|^2 = \text{constant}, \tag{1.7}$$

which is derived from the momentum equation and is only valid along an energy conserving streamline. As energy is not conserved across the actuator disc, this needs to be applied separately on either side of the disc, showing that the pressure coefficient $c_p = (p - p_\infty)/(1/2\rho u_\infty^2)$, where p_∞ is the undisturbed upstream static pressure, on the upstream and downstream side of the disc at the optimal power point is $c_{p,u}^* = 5/9$ and $c_{p,d}^* = -3/9$ respectively, and where inviscid and axial flow has been assumed.

The Betz theory places a theoretical upper bound to the energy that a turbine may extract, with modern horizontal axis turbines approaching power coefficients of $C_P = 0.5$ [Gaertner et al., 2020]. Despite the simplicity of the linear momentum actuator disc theory (LMADT) approach, it serves as a valuable first-order predictor for the energy extraction efficiency of any device operating in a fluid and offers insights for design. This result has been widely applied to engineering practice, including an important extension by Glauert [1926], known as blade element momentum theory, which connects the momentum analysis to rotor thrust and torque via aerofoil lift and drag polar data, and is now widely employed for the development of real turbines [Burton et al., 2021].

Nevertheless, the classical theory rests upon several simplifying assumptions: that the energy extraction mechanism of rotating blades can be idealised by an infinitesimally thin disc imposing uniform resistance to the flow, that the intricate physics depicted in figure 1.1 can be disregarded for an approximation to the upper bound of power extraction, and that the quasi-one-dimensional inviscid streamtube analysis remains valid. Fundamentally, the theory assumes inviscid, steady, incompressible and unbounded flow.

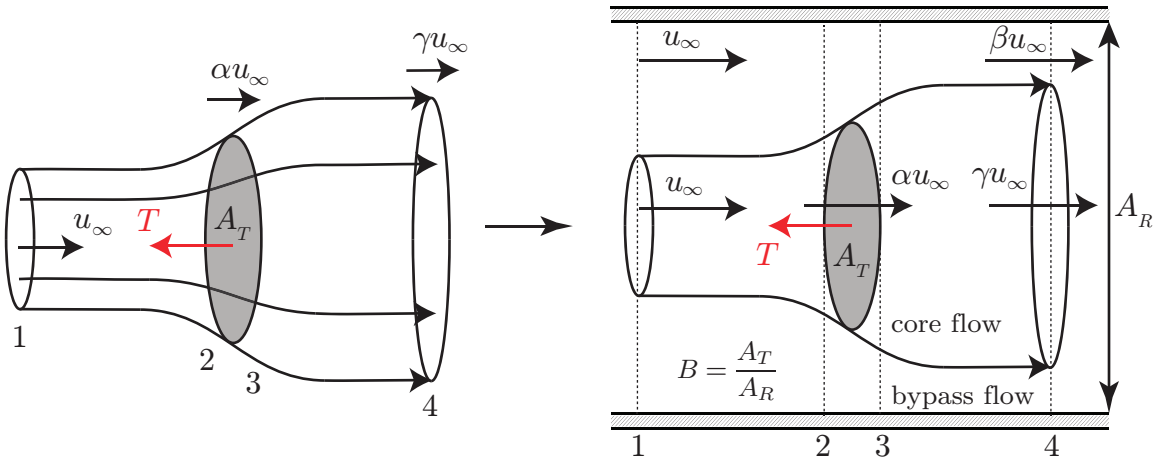

Figure 1.3: A schematic comparing an energy extracting actuator disc in an unbounded flow with one in a constrained, blocked channel [Garrett and Cummins, 2007] with representative area A_R. The non-dimensional velocity factors α, β, γ and the area based blockage ratio B characterise the flow problem.

Modifying these assumptions relaxes the constraints in equations 1.4-1.5 and can lead to power extraction efficiencies beyond the Betz limit, the focus of this thesis. Solutions to the optimisation problem can inform understanding of the underlying physics and inform design though the examination of optimal disc resistance and corresponding velocity and pressure fields.

1.3 Blockage effects

A widely studied example illustrating the importance of these constraints is the effect of blockage. Although the Betz theory provides the theoretical limit of power extraction in an unbounded flow, blockage can be used to constrain the flow to exceed this theoretical limit. This has been particularly relevant in tidal channels [Garrett and Cummins, 2007], where the sea-bed, the free surface of the sea and the channel's lateral walls constrain the expansion of the quasi-one-dimensional streamtube. Consider an extension of actuator disc theory for a constrained turbine, shown in figure 1.3, where the blockage ratio $B = A_T/A_R$, or ratio of turbine-swept to channel cross-sectional area, is finite. Here, the governing equations can be applied separately to the *core* and *bypass* regions of the flow, and the resultant equations can be solved for the optimal power, yielding a key result that

$$C_P = C_{P,\text{Betz}} \frac{1}{(1-B)^2}, \tag{1.8}$$

which is later derived analytically (the result has previously only been numerically demonstrated) through the constraint optimisation framework in chapter 2. The analysis assumes full pressure equalisation across the channel downstream of the turbine prior to turbulent mixing, with numerical investigations of actuator disc flows showing both that the theoretical model broadly agrees with numerical predictions, and that turbulent mixing prior to pressure equalisation can act to increase the limit further [Nishino and Willden, 2012b]. This result suggests that for even modest increases in the blockage ratio, the power coefficient can significantly exceed the Betz limit. Constraining the flow, therefore, provides a mechanism by which the power extraction efficiency of turbines can be significantly enhanced. Further extensions to this model have included the influence of free-surface deformation with a non-zero Froude number $\mathrm{Fr} = u/\sqrt{gh}$, where g is the gravitational acceleration and h is the channel depth [Vogel et al., 2016], and the development of an updated blade element momentum theory method for tidal turbines [Vogel et al., 2018]. Nonetheless, there are a number of limitations to exploiting this in practice, due to the necessity for other uses of channels including shipping lanes, complex bathymetry which precludes installation, and environmental considerations which set limits on the maximum permissible channel flow rate reduction.

1.3.1 Turbine fences

The ratio of swept rotor to channel cross-section area is typically small for commercial-scale tidal energy extraction [Coles and Walsh, 2019], and negligible for wind energy, such that achievable power uplift through global blockage effects is modest. However, the flow through an actuator disc may also be constrained by placing actuator discs adjacent to one another to form a turbine fence, schematically illustrated in figure 1.4.

In this case, there are two scales of blockage. Alongside the familiar global blockage, B_G (the ratio of total turbine swept to channel cross-section area), an additional local blockage ratio B_L (the ratio of frontal turbine swept to local flow passage area) may be defined, representing the spacing between each individual turbine in the fence. It has been shown theoretically that fences consisting of multiple turbines placed side-by-side can make use of this local blockage constructive interference effect to raise the energy extraction efficiency of the fence above that of the Betz limit applicable to unblocked flow problems. For the two-scale problem of a long array of turbines partially spanning the width of a much wider channel (vanishing global blockage) the efficiency of energy extraction, normalised by the undisturbed kinetic energy flux, rises from

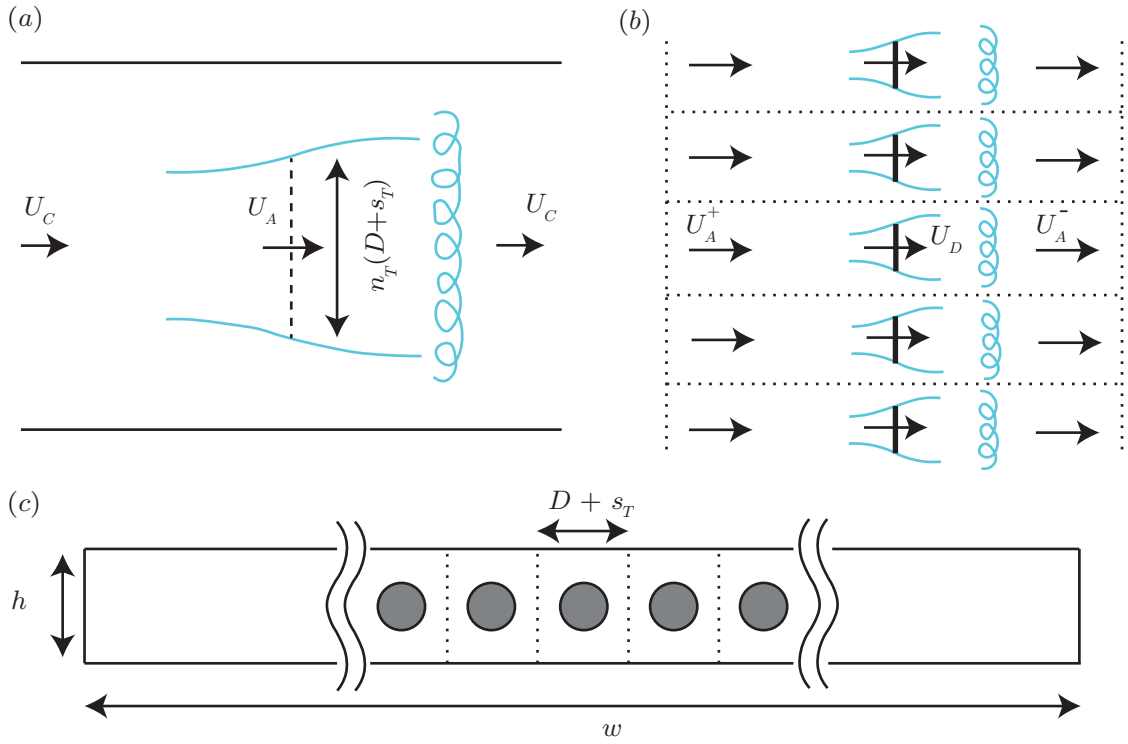

Figure 1.4: Schematic of a turbine fence model in a finite width channel. (a) Turbine fence scale illustrating array scale flow expansion and mixing; (b) individually arrayed turbines illustrating device scale flow expansion and mixing; and (c) the cross-sectional view of the fence in the channel. Figure reproduced from [Nishino and Willden, 2012a].

the Betz limit of 0.593 to the partial fence limit of 0.798 for a local blockage ratio of $B_L = 0.4$, representing a $\sim 35\%$ increase on the Betz limit [Nishino and Willden, 2012a].

Theoretical work by Cooke et al. [2016] extended the two-scale fence model to a three-scale model to show that if a third scale is introduced to the flow problem, i.e. sub-arrays within the partial fence, the performance limit can be further increased to a new limit of 0.865 whilst maintaining negligible global blockage. Meanwhile, staggered configurations of turbines have been studied theoretically and numerically [Draper and Nishino, 2014, Hunter et al., 2015], where it was shown that arraying turbines side-by-side produced more power than locally staggering the same number of turbines. Furthermore, it was found that multiple rows of turbines required larger turbine spacing within each row to optimise power. The single-turbine model has additionally been extended to shear flow [Draper et al., 2016], where the power extraction remains unaltered as compared to a turbine in uniform flow.

Cooke et al. [2015] conducted experiments using porous discs in a wide channel to assess the validity of partial fence theory in practice, finding closely spaced ar-

rays supported higher thrust and inferred power extraction. Arrays of rotors have been studied experimentally (Stallard et al. [2013]; Olczak et al. [2016]), showing the accelerating bypass flows between turbines, and wake effects for staggered arrays. These wake effects were further investigated experimentally by Noble et al. [2020], who found a power increase of upwards of 10.4% for downstream rotors in the bypass flow. Schluntz and Willden [2015] found that rotor redesign was necessary to fully reap the benefits of local blockage effects, but that a rotor designed for high blockage would operate sub-optimally for low local blockage. McNaughton et al. [2021] experimentally arrayed two blockage-designed turbines, confirming the important aspects of the underlying partial fence theory and demonstrating that some of the performance benefits offered by constructive interference effects can be achieved in practice. McNaughton et al. [2023] extended these twin turbine tests to a pseudo four-turbine fence by using a side-wall as a symmetry plane, observing a beneficial effect on overall fence performance with decreasing turbine spacing towards the theoretical optimum. Similar beneficial effects have been experimentally observed by Kolekar et al. [2019] on interference with free-surface proximity, who demonstrated an increase in power coefficient as the rotor approached the free-surface until a choking effect was observed analogous to the effect of inter-turbine spacing in the partial fence theory.

Finally, blocked disc models have been applied to assess tidal stream power resources for real sites and to suggest optimal configurations (see for example Adcock et al. [2013]; Martin-Short et al. [2015]; Grabbe et al. [2009]; Walters et al. [2013]).

There is clearly wide applicability to the flow constraining mechanism for energy extracting devices. Figure 1.5 summarises the effects of constraining turbines in various ways on the optimal power extraction efficiency, with aligned sub-arrays providing the highest efficiency in an unbounded channel. In chapter 2, the impact of local blockage on power extraction is formalised by the constrained optimisation framework developed in section 1.2. The solutions obtained establish a further upper limit on energy extraction from a fluid flow, and provide insight into the underlying physics of this energy extraction process.

1.4 Unsteady upstream flow

The inclusion of the blockage effects at large scales in both tidal channels [Vennell, 2010] and wind farms [Bleeg et al., 2018] have illustrated the importance of considering the impact of blockage on the classical theoretical assumption of constant upstream mass flux. Note that this coupling is only important for problems in which the global

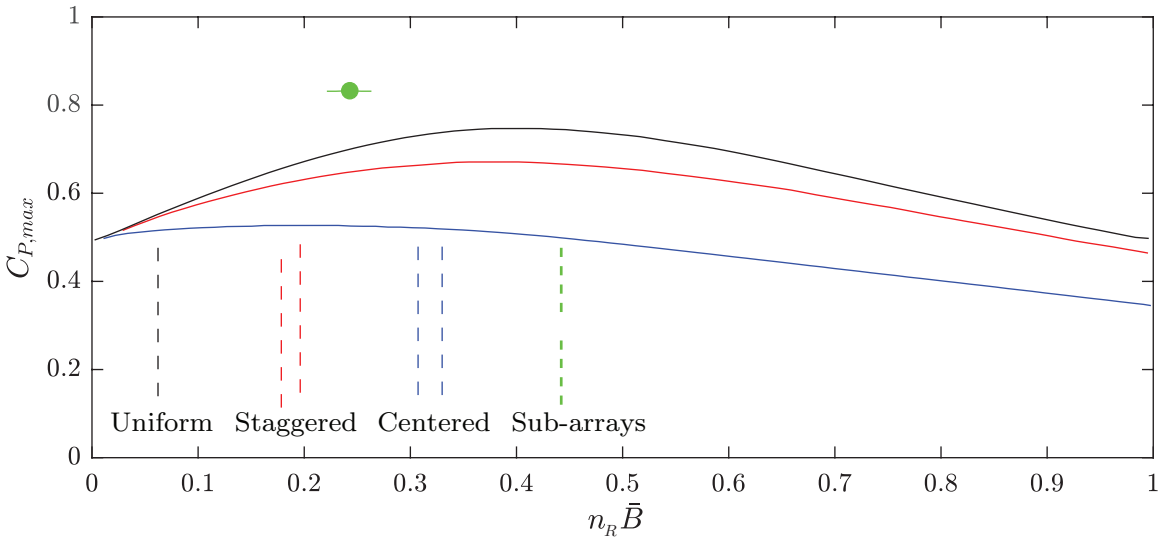

Figure 1.5: LMADT predictions of maximum power coefficient for various turbine arrangements against the number of rows n_R multiplied by the mean blockage per row $\bar{B}$. The various turbine arrangements are shown as dashed lines. Here the uniform array configuration (in black) represents the two-scale problem, and the sub-array (in green, for which only the optimal power point is shown) represents the three-scale problem. Staggered and centered configurations show reduced peak power compared to single row arrays. Figure reproduced from [Adcock et al., 2021].

blockage is non-zero, and so several of the theoretical models described earlier remain completely valid in this circumstance.

Figure 1.6 shows an example for tidal channels, where the upstream velocity is approximated by a time varying sinusoid representative of the tidal cycle, and the rows of turbines apply a time dependent resistance depending on both the magnitude and direction of the channel velocity. Vennell [2010] combined a one-dimensional mass-flux model with the blocked flow model of Garrett and Cummins [2007], finding that the interaction between a tidal turbine and the channel dynamics leads to a departure from both the Garrett and Cummins [2007] and Betz [1920] models, and that the efficiency of these arrays can be diminished by a global choking effect which reduces the mass flux through the devices. This analysis was extended by Vennell [2011] to consider multiple arrays of turbines by locating the updated power optima depending on the channel characteristics, and has been further applied to practical tidal turbine arrays to consider the broader possibility of exceeding the Betz limit [Vennell, 2013]. Gupta and Young [2017] proposed a quasi-steady theoretical model which combines the short fence extension to the two-scale theory [Nishino and Willden, 2013a] and includes both a free-surface deformation correction and the coupling of upstream flow rate with the turbine array resistance based on a simplified static channel model

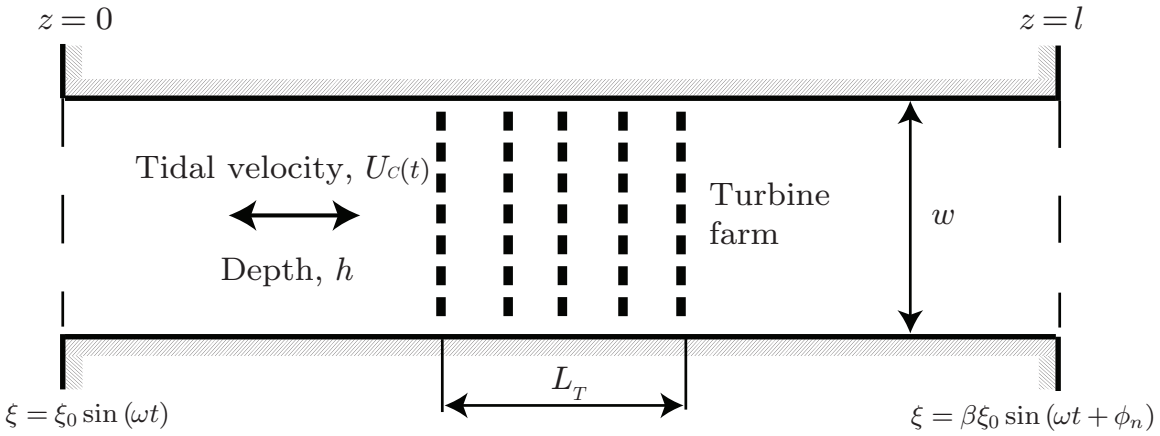

Figure 1.6: Schematic diagram of the interaction between a turbine farm and the sinusoidal mass flux of a tidal channel. Figure reproduced from [Vennell, 2010].

detailed in Bryden and Couch [2007].

The importance of this two-way coupling between the turbines and upstream mass flux is also important for wind farms, with Bleeg et al. [2018], Wu and Porté-Agel [2017] reporting large overestimates in wind-farm performance if the coupling is neglected. Recent studies have proposed empirical corrections to account for these coupling effects [Segalini and Dahlberg, 2020], but the detailed physics of the coupling remains poorly understood. A theoretical model for the impact of relaxing the steady assumption for an array of turbines in a tidal channel is developed in chapter 4.

1.5 Extensions of linear momentum actuator disc theory

Actuator disc theory has been extended in a number of different ways to account for various inherent simplifications implicit to the model. For instance, Glauert [1947] proposed a rotating wake model to account for the torque applied by the rotor to the fluid. The rotational motion represents an additional loss of energy from the axial flow, reducing the power available to the turbine below that of the classical actuator disc theory. Non-linear actuator disc theory has been developed as a further extension [Greenberg and Powers, 1970] to account for tip losses and non-uniform loading, with a full formalisation for complete stream-function solutions for heavily loaded discs derived by Conway [1998]. The Betz theory has additionally been extended to a number of flow problems, such as analysing the variation in the angle of attack seen by vertical axis wind turbine blades through a multiple stream-tube analysis [Berry and Yao, 2011]. Recently, Dabiri [2020] relaxed the steady assumption of the Betz

theory by allowing for time-dependent motion of the actuator disc in the streamwise direction, leading to time-averaged energy conversion efficiencies that exceed the Betz limit, modelling oscillating turbines as might occur on floating wind or tidal platforms.

Additional extensions may include the widely studied complexities introduced in figure 1.1. Drag, both from the blades and support structures, significantly impacts the extraction efficiency and wake characteristics. In general, blade element momentum theory is typically extended with various additions to cope with complex three-dimensional and unsteady flow physics [Sørensen, 2011]. The vertical shear profile depends on a large number of physical factors including atmospheric stability for wind turbines or the local bathymetry for tidal turbines. Waves generate significant loads and additional turbulence toward the free surface, and induce dynamic loading conditions on the rotor for floating tidal and wind converters [Adcock et al., 2021]. Additionally, the control of turbines in farms as they respond dynamically to the flow conditions, including yaw control to redirect wakes, must be integrated with a low-order model to enable closed-loop control for regulating or maximising power [Shapiro et al., 2022]. Finally, and particularly as farms grow in size, the two-way coupling between the atmospheric boundary layer and aerodynamic farm interaction becomes increasingly important for wind farms [Stevens and Meneveau, 2017].

1.6 Aim and Objectives

The foregoing studies indicate significant interest in relaxing the assumptions underpinning the Betz model, and further scientific inquiry is necessary to obtain a full understanding to exploit the physics for industrial application. The aim of this thesis is to relax some of the assumptions underpinning the Betz limit for more realistic flow conditions, exploring constraints related to boundedness, inviscid flow, and unsteadiness (see figure 1.7). This will be achieved as follows: For boundedness, the blockage theory is extended in a constrained optimisation framework to solve for the upper bound of energy extraction efficiency from a fluid flow. For the inviscid assumption, a model is developed that takes into account the effect of mixing between core and bypass flows in the turbine wake, as would occur in a real turbulent flow. For steadiness, the leading order effect of sinusoidal forcing for tidal arrays and the upstream mass-flux, turbine-thrust interaction is modelled. In all cases, new limits of power extraction are quantified theoretically, and the physical mechanisms governing flow physics beyond the Betz limit are explored. The theoretical results clearly demonstrate the potential for the development of high-efficiency energy extraction devices.

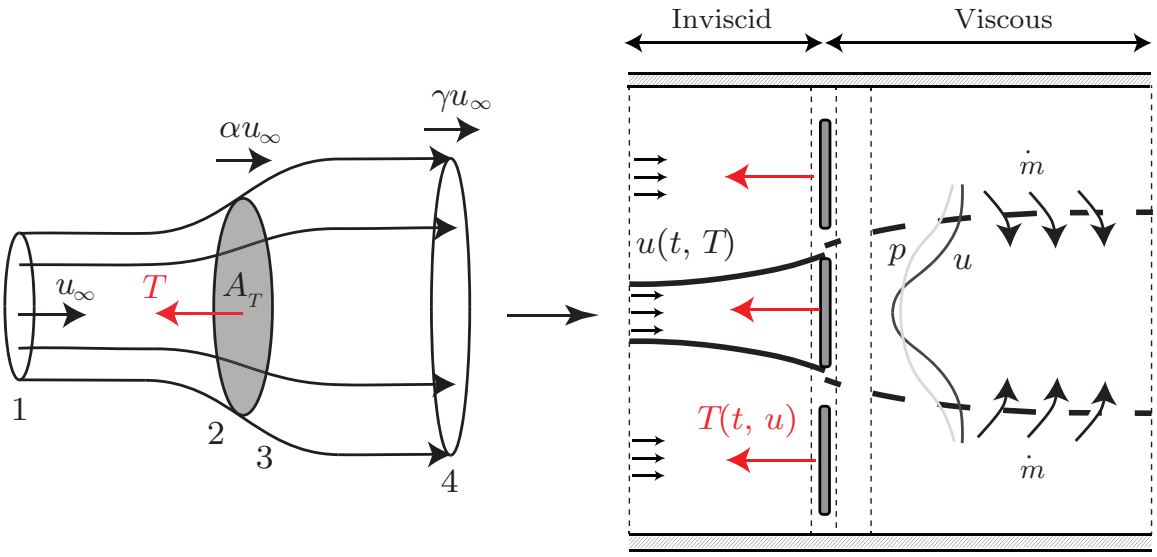

Figure 1.7: A schematic of the various constraint relaxations addressed in this thesis. The classical Betz model (left) is extended to consider performance limits for co-planar multi-turbine fences placed in channels (relaxing the unbounded assumption), head-driven unsteady forcing flows (relaxing the steady assumption) and turbulent wake-mixing (relaxing the inviscid assumption).

This work can hence contribute to the development of novel system designs and inform operating conditions for the increased energy extraction efficiency of next-generation renewable energy farms.

1.6.1 Thesis outline

Chapters 2-5 are each reproductions of submitted or published papers appended by a brief discussion linking each work. Conclusions are drawn in chapter 6. An overview of the contents of each chapter follows:

- Relaxation of the unbounded assumption: Theoretical derivation with the resulting solution providing insight into the underlying physics behind extracting power above the Betz limit using the local blockage (flow constraining) effect

  Chapter 2 determines the limits of energy extraction efficiency through placing turbines side-by-side and explores the underlying physics which allows for energy extraction above the Betz limit. The chapter shows that the limit in power coefficient of an energy extraction device in unbounded flow approaches unity, and that wake-mixing is a counter-intuitive source of improved kinetic efficiency. This work has been published in the *Journal of Fluid Mechanics* [Dehtyriov et al., 2021].

- Relaxation of the inviscid assumption: Theoretical derivation leading to improved understanding of the underlying physics of energy extraction in turbulent flow

  The Betz model assumes inviscid flow not representative of the highly turbulent environment typical of wind and tidal engineering. Chapter 3 develops a wake-mixing model for a single rotor to develop rotor performance theory that accounts for wake-mixing due to turbulence. The energy extraction efficiency is found to increase to between 0.71 and 0.81 from the Betz limit depending on where mixing occurs and whether the pressure recovery processes are sequential or concurrent, providing a new upper bound on the efficiency for a single turbine in an unbounded flow. Blocked flows are considered and the theoretical results are numerically validated. This work is in preparation for journal submission.

- Relaxation of the steady flow assumption: Development of a theoretical model allowing for interaction between a turbine fence and sinusoidally unsteady inflow

  Another constraint of the Betz model is the assumption of constant, steady upstream flow. This holds significant relevance for tidal channel flows, where the installation of numerous turbines within a channel can significantly influence the channel dynamics, especially the tidal velocity. Chapter 4 thus constructs an analytical model to capture the interplay between channel dynamics theory and turbine fence theory. This model is designed to optimise both the number and spacing of turbines within a channel, aiming to maximise power output per unit turbine area. This work has been published in the *Journal of Fluid Mechanics* [Dehtyriov et al., 2023a].

- A method for experimental correction for the flow constraining theory

  A key challenge in conducting experimental tests on turbine arrays is that the flow conditions within a wind or water tunnel differ from those in an actual flow system. This disparity arises primarily because the cross-section of the testing tunnel is limited in size. Chapter 5 develops an analytical blockage correction model for the experimental testing of turbine arrays, allowing for experimental quantification of the constructive interference effect by removing global blockage effects due to the tunnel constraint whilst preserving the intended local blockage effect. This work has been published in the 15^{th} *European Wave and Tidal Energy Conference, 2023* [Dehtyriov et al., 2023b].

Chapter 2

Fractal-like actuator disc theory for optimal energy extraction

> "There is a fine Jewish proverb: Man thinks, God laughs. (...) It pleases me to think that the art of the novel came into the world as the echo of God's laughter. But why does God laugh at the sight of man thinking? Because man thinks and the truth escapes him."
>
> — Milan Kundera

This chapter describes relaxation of the unbounded assumption of the Betz model by analysing turbines arrayed at multiple physical scales. The material within this chapter was published in the *Journal of Fluid Mechanics* on the 30$^{\text{th}}$ September, 2021 [Dehtyriov et al., 2021].

Expanding upon the research on flow passage constraints conducted by Garrett and Cummins [2007] for a single scale of blockage and Nishino and Willden [2012a] for two scales of blockage, our objective is to ascertain the extraction efficiency limits achieved through the constraint mechanism, specifically by deploying multiple turbines in a co-planar turbine fence or array. A theoretical understanding of the flow dynamics governing the raising of the limit of power extraction above the Betz limit for arbitrary multi-scale arrays is critical as a basis for a detailed understanding of the physics dictating optimal arrangements of turbines for power production. We find that the energy extraction efficiency approaches 100% as the number of scales approaches infinity and provide new upper limits of energy extraction in both unbounded and globally blocked flows. We then detail the physics underlying the increase in power extraction efficiency. Significantly, this chapter highlights that the enhancement of

power extraction with an increasing number of scales cannot be attributed to the minimisation of mixing losses. Instead, it reveals that wake mixing plays a pivotal role by contributing to a supplementary static pressure rise in the device wake.

2.1 Paper abstract

The limit of power extraction by a device which makes use of constructive interference, i.e. local blockage, is investigated theoretically. The device is modelled using actuator disc theory in which we allow the device to be split into arrays and these then into sub-arrays an arbitrary number of times so as to construct an $n-$level multi-scale device in which the original device undergoes $n-1$ sub-divisions. The alternative physical interpretation of the problem is a planar system of arrayed turbines in which groups of turbines are homogeneously arrayed at the smallest n^{th} scale, and then these groups are homogeneously spaced relative to each other at the next smallest $n-1^{\text{th}}$ scale, with this pattern repeating at all subsequent larger scales. The scale separation idea of Nishino & Willden (2012) is employed which assumes mixing within a sub-array occurs faster than mixing of the by-pass flow around that sub-array, so that in the $n-$scale device mixing occurs from the inner scale to the outer most scale in that order.

We investigate the behaviour of an arbitrary level multi-scale device, and determine the arrangement of actuator discs (n^{th} level devices) which maximise the power coefficient (ratio of power extracted to undisturbed kinetic energy flux through the net disc frontal area). We find that this optimal arrangement is close to fractal, and fractal arrangements give similar results. With the device placed in an infinitely wide channel, i.e. zero global blockage, we find that the optimum power coefficient tends to unity as the number of device scales tends to infinity, a 27/16 increase over the Lanchester-Betz limit of 0.593. For devices in finite width channels, i.e. non-zero global blockage, similar observations can be made with further uplift in the maximum power coefficient.

We discuss the fluid mechanics of this energy extraction process and examine the scale distribution of thrust and wake velocity coefficients. Numerical demonstration of performance uplift due to multi-scale dynamics is also provided. We demonstrate that bypass flow remixing and ensuing energy losses increase the device power coefficient above the limits for single devices, so that although the power coefficient can be made to increase this is at the expense of the overall efficiency of energy extraction which decreases as wake scale remixing losses necessarily rise. For multi-scale

devices in finite overall blockage two effects act to increase extractable power; an overall streamwise pressure gradient associated with finite blockage, and wake pressure recoveries associated with bypass scale remixing.

2.2 Introduction

Turbine energy extraction efficiency in fluid flow has been an area of significant scientific and industrial interest, with Lanchester [1915], Betz [1920] and Joukowsky [1920] first deriving an upper bound of energy extraction for a single unconstrained turbine based on actuator disc theory. The classic result, eponymously named the 'Betz' or 'Lanchester-Betz-Joukowsky' limit, shows that the proportion of the upstream kinetic energy flux that can be usefully extracted (the power coefficient, C_P) is 16/27 of the undisturbed upstream kinetic energy flux through an area equal to the turbine swept area. This is achieved when the flow velocity, normalised by the undisturbed upstream flow speed, reduces to a factor of 2/3 at the turbine plane and to 1/3 in the far wake once the static pressure has recovered to upstream levels. This result has been widely used in engineering practice, including an important extension by Glauert [1926], which connected an extended theoretical analysis of the quasi one-dimensional momentum balance with aerofoil lift and drag polar data, and is now widely employed to both analyse the flow field and predict the energy extraction efficiency of real turbines.

Although the Betz limit provides the theoretical limit of power extraction for a single device in an unconstrained flow, beneficial interactions between multiple devices and/or overall flow confinement can be used to constrain the flow to raise this theoretical limit. Garrett and Cummins [2007] extended the actuator disc theory for application to confined flows where the turbines occupy a finite area of the flow passage cross-section. Confinement of the flow may be provided by flow boundaries such as the ground plane, free surface (in the case of tidal stream turbines), the inversion layer (in the case of wind turbines) and/or adjacent turbines. The ratio of the turbine frontal (swept) area relative to the channel cross-sectional area is given by the blockage ratio, B. Garrett and Cummins [2007] showed that this confinement of the flow enabled the extraction of additional power. The maximum extractable power is increased relative to unconfined flow by $(1-B)^{-2}$. Performance uplift due to blockage may have significance for tidal stream turbines as they could potentially be arranged to occupy a significant portion of the channel cross-sectional area. It should be noted that blockage effects mean that it is theoretically possible to extract more

power than that available in the upstream kinetic flux as there is also a static pressure (or head) drop from far upstream to far downstream of the turbine. This analysis assumes full static pressure equalisation across the channel downstream of the turbine prior to turbulent remixing of the wake. Numerical investigations have shown that the theoretical model broadly agrees with numerical predictions. Turbulent mixing prior to static pressure equalisation can act to increase the limit further [Nishino and Willden, 2012b], implying that the analytical analysis slightly underestimates the power that can be extracted by actuator discs. Extensions of the Garrett & Cummins model have included the influence of free-surface deformation (non-zero Froude numbers) (Whelan et al., 2009, Vogel et al., 2016), and the development of an updated blade element momentum theory method for tidal turbines [Vogel et al., 2018]. Like the Betz limit, the maximum C_P for the Garrett and Cummins [2007] model occurs when the wake velocity coefficient is 1/3. This result was only shown numerically in the original paper. For completeness we confirm this result algebraically in Appendix 2.A.

A blockage effect can also be exploited by arrays of turbines, where the flow through a given turbine is further blocked on a local scale due to the proximity of adjacent turbines. By locally capitalising on the blockage effect the Betz limit can be surpassed. As large arrays of turbines are becoming more common in wind engineering and are needed in tidal to make a significant contribution, the optimal layout of these is clearly of interest. Nishino and Willden [2012a] explored this idea through an extension of the work of Garrett and Cummins [2007] to consider a two scale model. They assumed that an array of discs occupied part of the channel and that the local flow passing through and around the discs mixed on a length scale much shorter than the mixing between the flow through the array and the flow bypassing the array. Thus the analysis depends on two blockages: a global blockage (swept area of turbines divided by the cross-sectional area of the channel) and a local blockage (turbine swept area divided by the cross-sectional area of the turbine's local flow passage). This two scale model showed that for a given total turbine swept area (global blockage) there exists an optimum local blockage. An important limiting case was where the global blockage goes to zero. In this case, it was shown that local blockage effects can enhance the power coefficient to 0.798 of the upstream kinetic energy flux. The scale separation effect has been demonstrated experimentally using porous discs [Cooke et al., 2015] and is starting to be applied in the wind industry, whilst power uplift through constructive interference in short fences of turbines has been demonstrated in large laboratory experiments [McNaughton et al., 2021]. Cooke

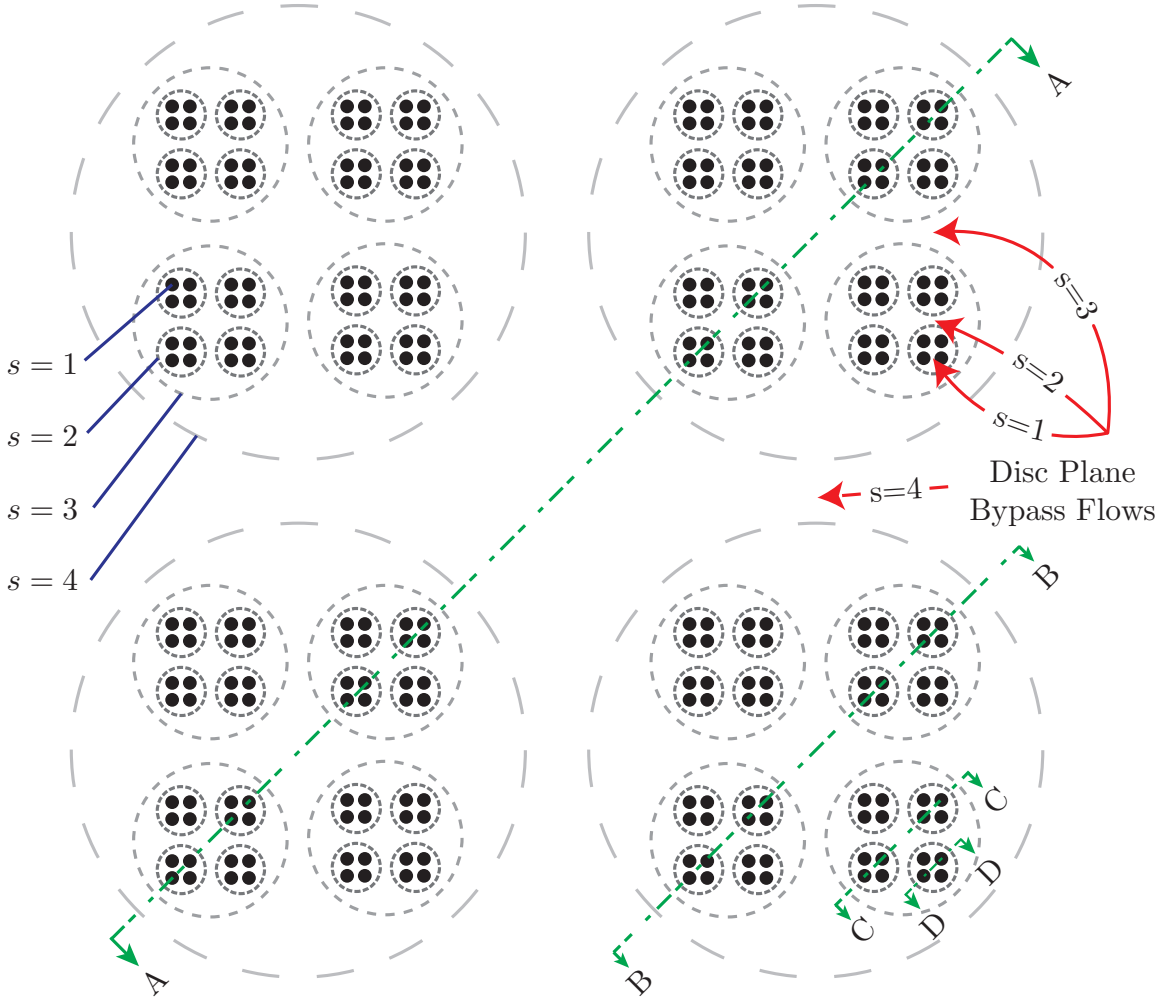

Figure 2.1: An illustration of the frontal view, with the flow going into the page, of an $n = 4$ scale model where each subsequent scale consists of sub-division into $d_s = 4$ discs. The resultant configuration of discs (the inner $s = 1$ scale) is drawn with black circles, and each larger dashed ring represents a new, larger, scale. The accelerated bypass flows at the disc plane at each scale are shown, and sections spanning the first 4 scales, over which the relevant flow equations are solved, are shown in detail in figure 2.2.

et al. [2016] further progressed the theoretical analysis by introducing an additional third scale; in this case the globally unblocked C_P increases to 0.865.

Accounting for the effects of arrangement on mass flux and general dynamic balance is also important. The inclusion of the blockage effects on large scales in both tidal channels [Vennell, 2010] and wind farms [Bleeg et al., 2018] have illustrated the importance of considering the impact of blockage on the mass flux of the upstream flow. The efficiency of arrays of energy extraction devices can be diminished by a global choking effect which reduces the mass flux through the channel and the de-

vices. Vennell [2010] combined a mass-flux model with the blocked flow model of Garrett and Cummins [2007], finding that the interaction between a tidal turbine and the channel dynamics leads to a departure from the Garrett and Cummins [2007] and Betz [1920] models, which predicted achieving maximum power by tuning the wake velocity to 1/3 of the free-stream flow. Optimal 'tunings' were instead found to increase monotonically with global blockage ratio, approaching unity for turbines which spanned close to the entire channel cross-section. This analysis was extended by Vennell [2011] to consider multiple arrays of turbines by locating the updated power optima depending on the channel characteristics, and has been further applied to practical tidal turbine arrays to consider the broader possibility of exceeding the Betz limit [Vennell, 2013]. For a review of other extensions of actuator disc theory for tidal flows see Adcock et al. [2021].

The aim of this paper is to derive a fundamental limit for power extraction and understand the underlying fluid mechanics. Early work has shown that a single side-by-side row outperforms staggered or multi-row arrays (Hunter et al., 2015, Draper and Nishino, 2014) so the focus here is on a large single row array. In this study we extend the theoretical analyses of Nishino and Willden [2012a] and Cooke et al. [2016] to consider n-scales with particular interest in the behaviour as $n \to \infty$. The use of multiple scales will be used to explore the array arrangement for optimal power extraction. Alternative interpretations of the present analysis are also possible. For example, self-similarity across scales could be interpreted as a single device with non-uniform resistance. The problem is formulated following the previous analyses and solving the equations numerically. Specifically, by making use of the constructive interference effects of local blockage over multiple scales, we attempt to characterise the optimal multi-scale energy extraction device through a detailed description of the optimal distributions of velocity tuning parameters and local blockage ratios, alongside discussion of the distribution of thrust and power coefficients across the scales. Similarly to the aforementioned studies, we assume that the mass flux through the channel is constant. We provide a physical explanation as to how multiple scales, and specifically wake remixing, leads to an increase in extractable power.

2.3 Array Model

The formulation of the model problem is conceptually the same as that in the previous study of Cooke et al. [2016] extended to an arbitrary number of scales. A frontal view of a $n = 4$-scale extractor is shown in figure 2.1, where the fractal nature of the

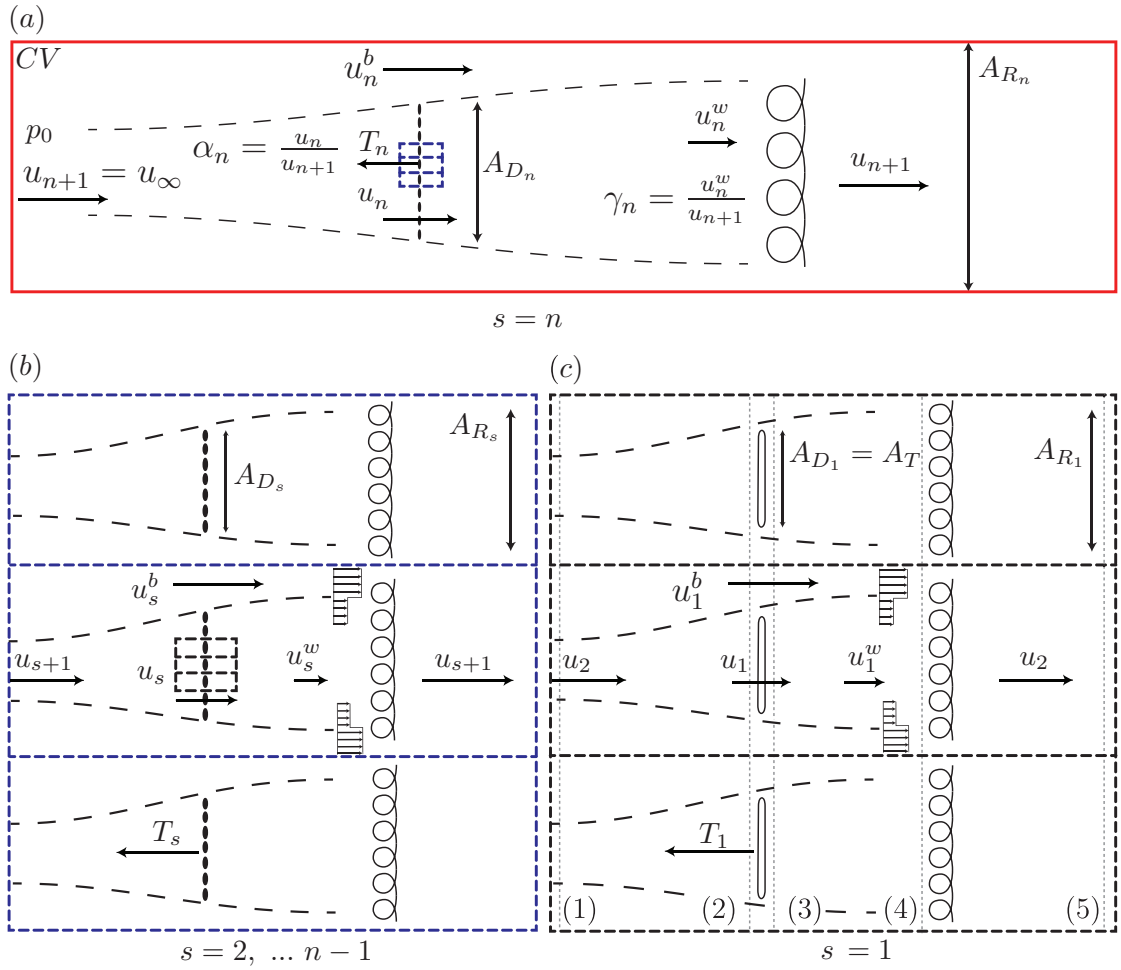

Figure 2.2: A plan-view realisation of a multi-scale array in a wide and shallow channel (as might occur for a tidal channel), with key parameters shown. The scales s are ordered from the smallest scale ($s = 1$) to the largest scale ($s = n$). The largest scale (a) consists of an array of devices (which is the plan-view realisation of section A-A in figure 2.1), with each device subsequently broken down into further arrays of devices until the smallest scale which extracts power through actuator discs (c) (plan-view realisation of section D-D in figure 2.1). Intermediate scales are shown in (b) (plan-view realisation of sections B-B or C-C in figure 2.1).

arraying is made clear, and from which an arbitrary-scale extractor may be visualised. An alternative interpretation of the configuration is a single row of discs in a channel sub-arrayed an arbitrary number of times.

Consider an n-scale flow problem schematically illustrated in figure 2.2, where the first ($s = 1$) scale denotes the smallest innermost (disc) scale and the $s = n\,$th scale denotes the largest outermost scale. Consider first a side-by-side row of equally spaced actuator discs as shown in figure 2.2c. Mass, linear momentum and inviscid

energy conservation relations may be written to relate the flow conditions, namely the static pressure and axial flow velocity (other flow components being neglected), at each of the stations 1-4 through both the core (flowing through the disc) and bypass regions as a function of the inter-disc spacing (local blockage). These relations, which account for finite blockage, here present due to the adjacent discs as well as sea bed and surface proximity, are an extension on the classic Betz actuator disc model (see appendix 2.A for details). The actuator exists between stations 2 and 3 across which the flow velocity is continuous but a discontinuous drop in pressure occurs. Downstream of the actuator the flow decelerates allowing pressure recovery in the core flow until the static pressure equilibrates with the accelerated bypass flow at station 4. Turbulent mixing is then assumed to occur between the bypass and core flows such that the static pressure and flow velocity fully equalise by station 5, with the flow velocity necessarily recovering to the inflow condition at station 1 (by mass conservation), and the pressure at 5 being less than at 1 due to the finite blockage effect.

We next consider the two scale problem [Nishino and Willden, 2012a] in which a large number of discs are arrayed in a side-by-side configuration in a single row in an infinitely wide (unblocked) channel; see figure 2.2a with $n = 2$. There are a large but finite number of discs in the row so that we may assume homogeneous behaviour across the array. The flow picture at this outer scale is analogous to the inner scale flow problem and we may write mass, momentum and energy conservation equations for this outer scale in a similar way to those for the inner scale. The inner and outer scales are kinematically and dynamically coupled so that the flow velocity decelerates from u_{n+1} upstream of the outer scale, to u_n at the extraction plane of that scale which is co-located with the upstream condition of the inner scale. Downstream of the inner scale actuators, recovery and mixing with the inner scale bypass flow enables the flow velocity to recover to u_n, which is compatible with the flow velocity downstream of the array of the outer scale in figure 2.2a. Dynamic coupling is achieved by requiring that the thrust force exerted by the actuator discs of the inner scale be equal to the force exerted at the extraction plane at the outer most scale. Mass, momentum and energy equations for the two scales may then be solved numerically.

Now assume that there are multiple disc rows, again all in a side-by-side configuration, of the type shown in figure 2.2a, and that these are further arrayed as in figure 2.2b, where each row of discs is now equally spaced apart. The model requires that there are a large, but finite, number of discs in each row, and a large, but finite, number of disc rows at the next scale, such that we may consider discs and disc rows

to be homogeneous across their scale of the model. At this larger scale, the flow problem looks similar to that of the disc ($s = 1$) scale. Analogous to the physics governing the disc scale therefore, conservation laws are used to dictate the relationship between inter-array spacing and flow velocities. This process can be repeated to construct larger and larger scales, each with a scale-specific spacing between the arrays at that scale. The resultant device, shown in figure 2.2a, is once again analysed through the same set of equations (see appendix 2.A). Rather than being confined by adjacent discs (as at the smallest scale) or adjacent arrays (as at all other scales), the largest $s = n$-scale device may be analysed both in an unbounded flow, as in the Betz actuator disc model, or in a bounded flow, as in the case of tidal turbines arrayed in a finite dimension channel. In either case the model assumes that the far upstream flow remains unaffected by the resistance presented by the disc array. This assumption is clearly only valid in the limit of vanishing resistance relative to flow inertia and will be explored later in the context of unbounded arrays.

The flow problems at each scale may be solved under the assumption that the static pressure and velocity (through turbulent mixing) fully equalises prior to mixing with the subsequent scale. For this assumption to hold the number of devices and sub-arrays at every scale needs to be sufficiently large [Nishino and Willden, 2013a]. In addition to the kinematic and dynamic coupling between scales, they are additionally coupled geometrically; the number and spacing of the discs in figure 2.2c dictates the size of each array in figure 2.2b. This allows for closure of the flow problem in terms of the thrust applied by each actuator disc at the smallest (figure 2.2c) scale, the spacing between the discs/arrays at each scale, and the global blockage. In particular, this paper focuses on maximising the power extraction

$$C_{P_1} = \frac{P_1}{\frac{1}{2}\rho u_2^3 A_T} = \frac{T_1 u_1}{\frac{1}{2}\rho u_2^3 A_T}, \tag{2.1}$$

as a function of the optimal arrangement of discs/arrays at each scale, with $P_1 = T_1 u_1$ the power generated by the inner scale actuator disc of area A_T.

Non-dimensional velocity induction factors are first defined for each scale such that

$$\alpha_s = \frac{u_s}{u_{s+1}}, \ \gamma_s = \frac{u_s^w}{u_{s+1}} \quad \text{for} \quad s = 1, 2, ..., n, \tag{2.2}$$

where the subscript s denotes the scale number, w denotes the wake flow, and $u_{n+1} = u_\infty$ is the assumed undisturbed velocity upstream of the multi-scale array (see figure 2.2). The assumption of a completely undisturbed velocity upstream is strictly only true in the case of vanishingly small disc resistance relative to flow inertia.

Blockage ratios at each scale are likewise defined as an area ratio

$$B_s = \frac{A_{D_s}}{A_{R_s}} = \frac{\text{Local frontal area of the } s \text{ scale device}}{\text{Local representative passage area}} \quad \text{for} \quad s = 1, 2, ..., n, \tag{2.3}$$

where the numerator represents the cross-sectional area of the device at any given scale (i.e. the turbine swept area at the smallest scale and the entire device area at the largest scale), and the local representative passage area represents the cross-sectional area of the flow passage around a single device at that scale (i.e. the flow passage encompassing an individual turbine's core and bypass flows at the smallest scale and the entire channel at the largest scale). Note that $B_n \to 0$ (i.e. B_s for $s = n$) in the case of an infinitely wide channel (implying globally unblocked flow).

The thrust coefficients at each individual scale may now be written out as a function of the velocity induction factor and blockage through the consideration of conservation of mass, momentum and energy in quasi one-dimensional form (see Nishino and Willden [2012a] for further details)

$$C_{T_s} = \frac{T_s}{\frac{1}{2}\rho u_{s+1}^2 A_{D_s}} = (1 - \gamma_s)\left[\frac{(1 + \gamma_s) - 2B_s\alpha_s}{(1 - \alpha_s B_s/\gamma_s)^2}\right], \tag{2.4}$$

where the wake induction factor γ_s is related to α_s through

$$\alpha_s = \frac{1 + \gamma_s}{1 + B_s + \sqrt{(1 - B_s)^2 + B_s(1 - 1/\gamma_s)^2}}. \tag{2.5}$$

Each scale can now be solved for simultaneously through kinematic coupling of the velocity and dynamic coupling through the balance of the net thrust force at all scales

$$C_{T_s} = \frac{d_{s-1}T_{s-1}}{\frac{1}{2}\rho u_{s+1}^2 A_{D_s}} = \alpha_s^2 B_{s-1} C_{T_{s-1}} \quad \text{for } s = 2, 3, ..., n, \tag{2.6}$$

where d_s is the number of devices at any given scale (and $d_n = 1$ always). The scales are hence coupled both geometrically by $d_s A_{R_s} = A_{D_{s+1}}$ and dynamically by $d_s T_s = T_{s+1}$.

In particular, following the same formulation as in appendix 2.A, for n-scales, the flow problem can hence be re-cast as the following non-linear optimisation problem

$$\max C_{P_G}(\gamma_1, \gamma_2, ..., \gamma_n, B_1, B_2, ..., B_{n-1}, B_G) = \alpha_1 C_{T_1} \prod_{s=2}^{n} \alpha_s^3, \tag{2.7}$$

where the expression for the global power coefficient C_{P_G} follows from equation (2.1), with C_{P_G} normalised by the upstream flow velocity u_{n+1} and the disc area A_T. As

a consequence of the dynamic coupling in equation (2.6), the objective function is subject to the following $n-1$ constraints

$$C_{T_j} = C_{T_1} \prod_{s=2}^{j} \alpha_s^2 B_{s-1} \quad \text{for } j = 2, 3, ..., n, \tag{2.8}$$

where C_{T_s} is given by equation (2.4) and α_s by (2.5) for $s = 1, 2, ..., n$.

Finally, the solution domain is physically constrained by $0 \leq \gamma_s \leq 1, 0 \leq B_s \leq 1$. Note that for an infinitely wide channel ($B_n \to 0$), the constraints on α_n and C_{T_n} reduce to $\alpha_n = (1+\gamma_n)/2$ and $C_{T_n} = (1-\gamma_n)(1+\gamma_n)$ respectively.

As in appendix 2.A, the Lagrangian for the multi-scale problem is now written as

$$\mathcal{L} = \alpha_1 C_{T_1} \prod_{s=2}^{n} \alpha_s^3 - \sum_{k=1}^{n-1} \lambda_k \left(C_{T_{k+1}} - C_{T_1} \prod_{j=1}^{k} \alpha_{j+1}^2 B_j \right), \tag{2.9}$$

where solutions to $\nabla \mathcal{L} = 0$ can be solved numerically for any given n.

For a given n and $B_G = \prod_{s=1}^{n} B_s$, the multi-scale problem therefore consists of $3n-2$ variables to optimise, namely γ_s for $s = 1...n$, and B_s and λ_s for $s = 1...n-1$. These can be substituted into the objective function 2.7 to locate the optimal global power coefficient. The thrust coefficient and the velocity induction factor at each scale can be calculated with equations 2.4 and 2.5 respectively. Finally, scale (local) power coefficients can be found by evaluating

$$C_{P_s} = \alpha_s C_{T_s}, \tag{2.10}$$

with additional global variables of interest including the global velocity induction

$$\alpha_G(n) = \frac{u_1}{u_{n+1}} = \prod_{s=1}^{n} \alpha_s, \tag{2.11}$$

the device blockage ratio

$$B_D(n) = \prod_{s=1}^{n-1} B_s, \tag{2.12}$$

the global velocity tuning factor

$$\gamma_G(n) = \prod_{s=1}^{n} \gamma_s, \tag{2.13}$$

and the global thrust coefficient

$$C_{T_G} = C_{T_1} \prod_{s=2}^{n} \alpha_s^2. \tag{2.14}$$

The turning points of equation (2.9) were solved for numerically for $n \leq 100$, with the results of these computations discussed in section 2.4. The optima were solved for using an interior point algorithm for non-linear programming of non-convex functions described in Byrd et al. [1999], where quasi-Newtonian approximations of the objective function are numerically determined for the first and second derivatives. To ensure convergence to a non-local optimum, a global optimisation search described in Ugray et al. [2007], where the solution space is seeded with trial points, is used in conjunction with the interior point algorithm. The algorithm can be validated by testing against the $n = 2$ [Nishino and Willden, 2012a] and $n = 3$ [Cooke et al., 2016] cases, and returns the same solutions cited in the literature. We have also compared this algorithm against alternative formulations of the problem and obtained consistent results.

2.4 Numerical results

2.4.1 Performance of a multi-scale device in an infinitely wide channel

We start by presenting results for the case of an infinitely wide channel ($B_n \to 0$), which is slightly simpler than the finite global blockage case. The optimal global power coefficient for an n-scale energy extraction device is plotted in figure 2.3. An analytic curve fit approximation to the optima, with the relative percentage error shown in figure 2.3b, is suggested to be

$$C_{P_G,\max}(n) = \frac{C_{P,\text{Betz}} - 1}{n} + 1, \tag{2.15}$$

where $C_{P,\text{Betz}}$ is the Betz limit of 16/27. Note that the function is concave for all $n > 1$, is always a lower bound on the numerical optima, and that

$$\lim_{n\to\infty} C_{P_G,\max}(n) = 1, \tag{2.16}$$

showing that the optimal efficiency of a multi-scale energy extraction device which makes use of constructive interference (local blockage) in an unbounded fluid is 100% of the undisturbed kinetic energy flux through the device area.

Of particular interest is why the maximum power extraction asymptotes to a C_{P_G} of unity, whether this is the maximum for any energy extraction device, and how the properties of the multi-scale energy extraction device are distributed across the scales. The following discussion addresses these questions.

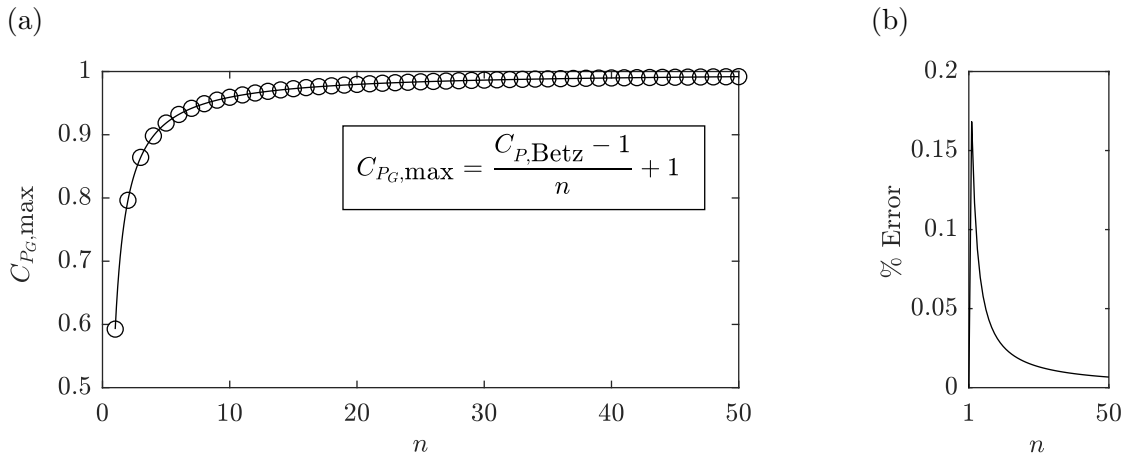

Figure 2.3: The maximum power coefficient for a multi-scale device in an infinitely wide channel, here shown for all scales to $n \leq 50$. (a) The circles indicate the numerical solutions, and the solid line gives an analytical approximation to the optimal C_P. (b) The relative percentage error between the approximation and numerical solution.

2.4.2 Properties of optimal unbounded multi-scale devices

For the case of an infinitely wide channel ($B_n \to 0$), the theoretical upper bound of energy extraction is limited by $C^*_{P_G} = 1$ as the static pressure upstream and downstream of the device must be the same. The only energy that can therefore be extracted must be derived from the upstream kinetic flux, which is analogous to the single scale unblocked energy extractor considered by Betz. In the limit, the multi-scale device clearly approaches this limit of energy extraction in an unbounded steady fluid. This section clarifies the physics of the convergence to this optimal condition for large n.

For the single scale Betz-like device, increasing the static pressure drop across the device by increasing the resistance to the flow comes at the cost of modifying the upstream stream-tube area. Additional scales allow for a decoupling of these two phenomena, and as the total number of scales becomes large, these conditions, namely the optimal static pressure drop across the device and no outer stream-tube modification can be simultaneously realised. At large n, the smallest scales are able to achieve blocked flow conditions, and can remove power with essentially no local flow divergence (hence large kinetic efficiency). At the same time, the entire array is becoming infinitely large, such that B_D tends to zero and so the discs at the smallest scale cannot cause large scale flow diversion. Numerical evidence is presented to illustrate the convergence to these two optimal conditions.

Figure 2.4a illustrates the convergence of α_G to 1/2 for large n, allowing for

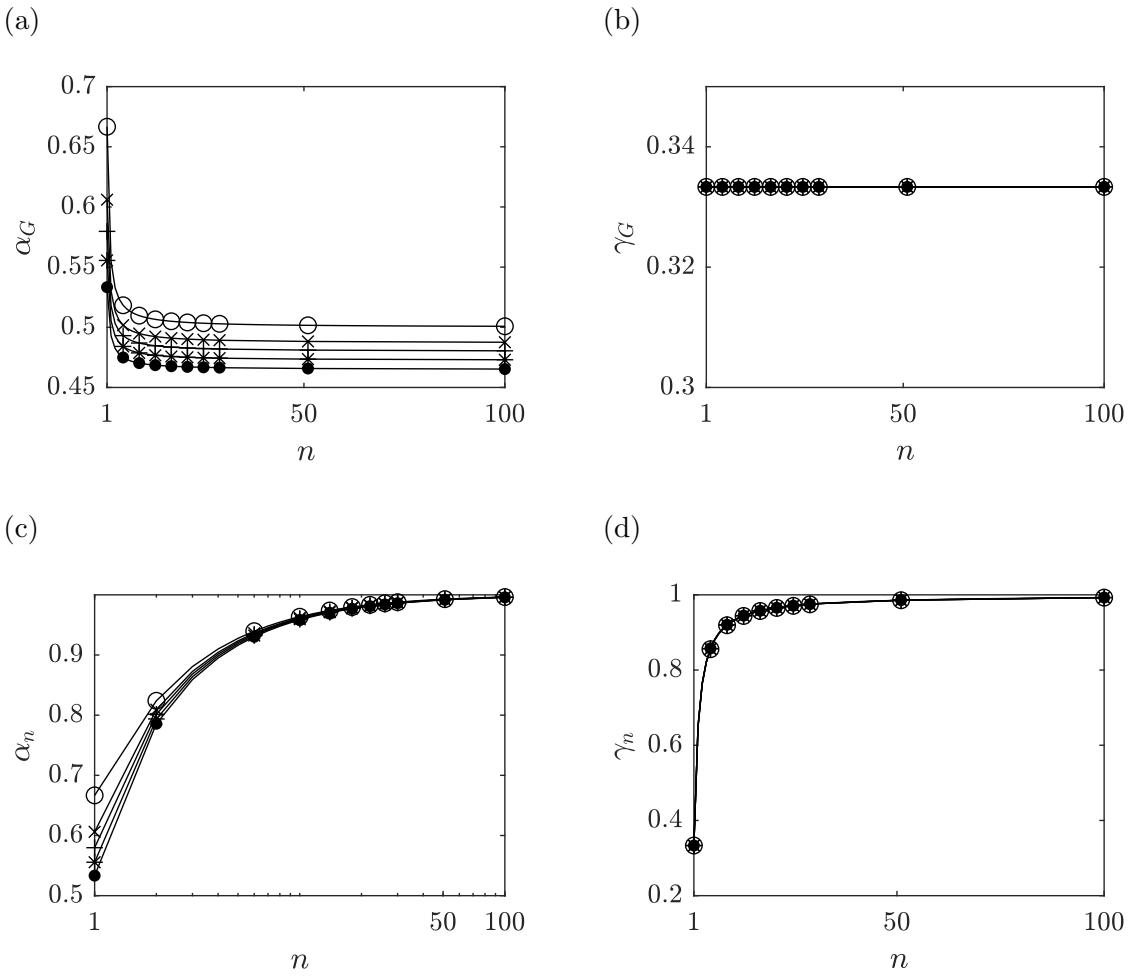

Figure 2.4: Global parameters exhibiting convergent behaviour for large n (markers indicating numerical solutions with circles for $B_G = 0$, crosses for $B_G = 0.1$, pluses for $B_G = 0.15$, stars for $B_G = 0.2$ and filled circles for $B_G = 0.25$; every 4^{th} simulated data point plotted). (a) The global velocity induction factor α_G, (b) the wake tuning velocity factor γ_G, the velocity factors at the largest scale (c) α_n (logarithmic scale for x-axis) and (d) γ_n.

an optimal pressure drop, normalised by the upstream dynamic pressure $\rho u_\infty^2/2$, of $\Delta c_p^* = 2$ across the smallest scale of the device. Figure 2.4c likewise illustrates the convergence of $\alpha_n \to 1$, implying that the stream-tube area remains unmodified at the largest scale without violation of the velocity constraint, namely that the velocity reduction factor in the far wake, $(1 - \gamma_n)$, is twice the disc plane's reduction factor, $(1 - \alpha_n)$.

In the limit as $n \to \infty$, the multi-scale energy extraction device therefore approaches the theoretical upper bound of energy extraction from an unbounded fluid,

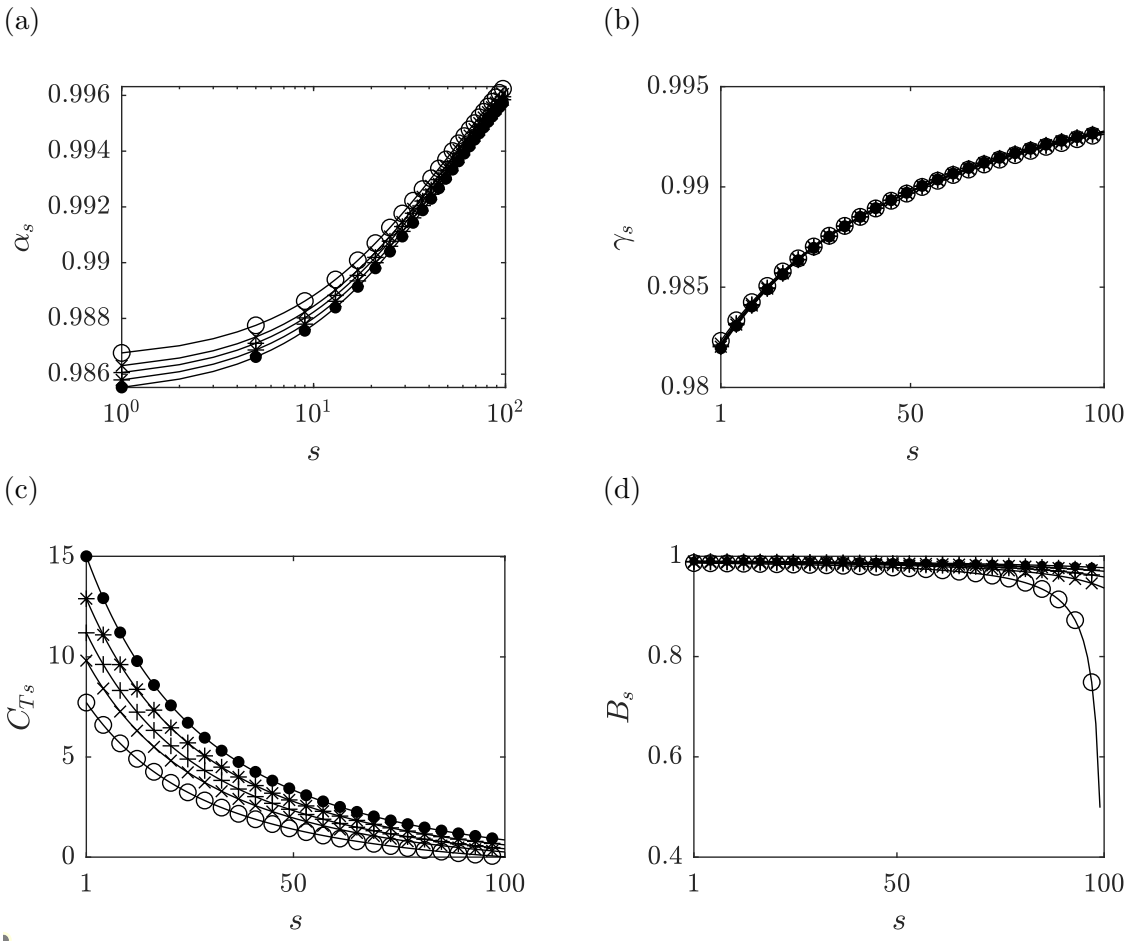

Figure 2.5: The solution for an $n = 100$ multi-scale energy extraction device illustrating the approximate limiting behaviour of an infinite-scale device (markers indicating numerical solutions with circles for $B_G = 0$, crosses for $B_G = 0.1$, pluses for $B_G = 0.15$, stars for $B_G = 0.2$ and filled circles for $B_G = 0.25$; every 4^{th} simulated data point plotted). The velocity induction factors (a) α_s (logarithmic scale for x-axis) and (b) γ_s, (c) the scale thrust coefficients C_{T_s}, (d) the local blockage ratios B_s, are shown for all scales $1 \leq s \leq 100$.

by simultaneously maximising the pressure drop across the discs at the smallest scale, and leaving the stream-tube unmodified at the largest scale. The distributions of the parameters that maximise the power extraction for an $n = 100$ multi-scale device are shown in figure 2.5, as a close approximation for the limiting behaviour of an optimal (infinite-scale) device. Figures 2.5a-2.5b demonstrate the gradual deceleration of the flow across each scale, with all γ_s and α_s nearing unity, and with the locally normalised static pressure drop gradually (and optimally) building up to the smallest scale (figure 2.5c). The distribution of the local blockage ratios, shown in figure 2.5d, satisfies the optimal constraints on velocity and static pressure drop, with the

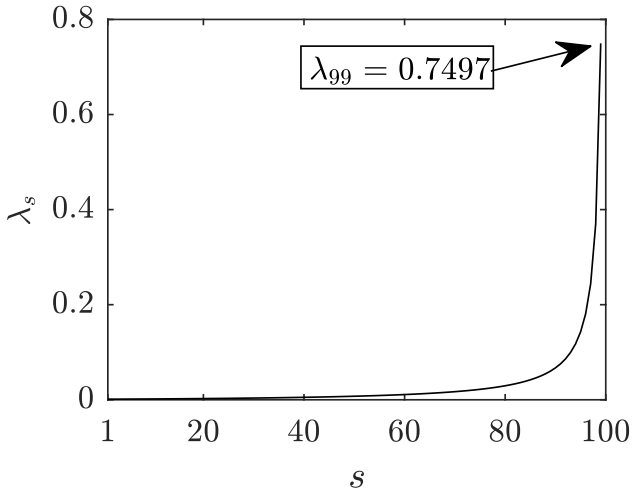

Figure 2.6: Lagrangian multiplier, λ_s, distribution across scales, $1 \leq s \leq n-1$, for an $n = 100$ unbounded multi-scale device.

blockage approaching near unity at the smallest scale. Figure 2.6 likewise shows the distribution of Lagrangian multipliers across scales, giving indication of the relative importance of a given thrust constraint between consecutive scales. This illustrates the relative decoupling of the critical thrust constraint at the largest (stream-tube) scale and the constraints between the smallest (pressure-drop) scales. In the limit, the thrust constraint on the smallest scale becomes negligible ($\lambda_1 \to 0$), and the smallest scale therefore decouples. All of the intermediate scales allow the flow to achieve both outer and inner scale optima subject to the physical constraints of the system. Variations in the constraint at the largest scale dictate the energy capture of the entire device; changes in outer scale blockage will therefore have a significant impact on the energy extraction efficiency.

Additional observations on the limiting parameters can be made with the aid of the governing equations, constraints and numerics. Consider a substitution of the constraints 2.8 into the objective function 2.7.

$$C_{P_G} = \frac{\alpha_1 C_{T_j} \prod_{s=2}^{n} \alpha_s^3}{\prod_{s=2}^{j} \alpha_s^2 B_{s-1}}, \tag{2.17}$$

which is true for all $j \geq 2$. By considering the large scale constraint $j = n$, we can write

$$C_{P_G} = \frac{(1-\gamma_n)(1+\gamma_n)}{\prod_{i=1}^{n-1} B_i} \prod_{i=1}^{n} \alpha_i. \tag{2.18}$$

As the number of scales becomes large ($n \to \infty$), the optimal induction factor at the outermost scale becomes $(1-\alpha_n) \to 0$. This condition is logical for optimal extraction

as in the limit it implies that, by mass conservation, no flow is diverted around the device. Additionally, by considering the constraint on velocity at the largest scale, this implies that $(1-\gamma_n) \to 0$. Substituting these optimal conditions into equation 2.18 allows for a consideration of the individual terms of the power coefficient

$$C^*_{P_G} = \lim_{\gamma_n \to 1} \frac{(1-\gamma_n)(1+\gamma_n)}{\prod_{i=1}^{n-1} B_i} \prod_{i=1}^{n} \alpha_i, \tag{2.19}$$

where for large n we observe numerically that the optimal α_G for energy extraction is (see figure 2.4a)

$$\lim_{n\to\infty} \prod_{i=1}^{n} \alpha_i = \alpha_G = \frac{1}{2}. \tag{2.20}$$

For the maximum C_{P_G} to be equal to the upper bound of 1, we must therefore have

$$(1-\gamma_n) \sim \prod_{i=1}^{n-1} B_i = B_D, \tag{2.21}$$

and

$$\lim_{n\to\infty} \prod_{i=1}^{n-1} B_i = 0, \tag{2.22}$$

which is confirmed by the numerical results. Considering the final constraint, we can also show that

$$(1-\gamma_n)(1+\gamma_n) = C_{T_1} \prod_{i=2}^{n} \alpha_i^2 B_{i-1}, \tag{2.23}$$

so that for large n

$$\lim_{n\to\infty} C_{T_1} = \lim_{n\to\infty} \left(\frac{(1-\gamma_n)}{\prod_{i=1}^{n-1} B_i} \frac{\alpha_1^2(1+\gamma_n)}{\prod_{i=1}^{n} \alpha_i^2} \right) = \frac{2\alpha_1^2}{\left(\frac{1}{2}\right)^2} = 8\alpha_1^2, \tag{2.24}$$

from which it is clear that to maximise the objective function (2.7), the product $\alpha_1 C_{T_1}$ is maximised (and $C_{P_G} \to 1$) when α_1 tends to 1 as $n \to \infty$. This shows that $\lim_{n\to\infty} C_{T_1} = 8$, which can clearly be observed in figure 2.5c. The constituent components for optimal energy extraction are therefore

$$C^*_{P_G} = \alpha_1^* C^*_{T_1} \prod_{i=2}^{n} (\alpha_i^*)^3 = 1 \cdot 8 \cdot \left(\frac{1}{2}\right)^3 = 1, \tag{2.25}$$

where $\alpha_1^* = 1$ physically represents (through mass conservation) the lack of inner stream-tube modification (note that $B_1 \to 1$ also), $C^*_{T_1} = 8$ (normalised by $1/2\rho u_2^2$) represents the optimal thrust (or alternatively the pressure drop $\Delta c_p^* = 2$ normalised by $1/2\rho u_\infty^2$) upon extraction, and $\alpha_G^* = 1/2$ the optimal deceleration of the potential

flow upstream of the extraction plane. The convergence to all of these conditions is observed in the numerical results. In the limiting case, therefore, a multi-scale energy extraction device approaches this upper bound of energy extraction without violation of conservation laws, providing a new theoretical limit of energy extraction from a steady unbounded fluid.

The condition that $(1 - \gamma_n) = 0$ as $n \to \infty$ also implies that

$$\lim_{n\to\infty} C_{T_n} = 0, \tag{2.26}$$

i.e. the thrust coefficient when referenced to the area of the n^{th}-scale device tends to zero, whilst the global thrust coefficient C_{T_G}, which is referenced to actuator disc area, must of course remain non-zero. That $C_{T_n} \to 0$ is of particular interest to the mass-flux and blockage coupling considerations in both tidal and wind engineering flows. In a head driven system, resistance to the flow will reduce the mass flux through the system (see Vennell 2010), with that reduction being a function of both the large scale blockage and thrust. The limiting behaviour of the multi-scale device, namely that $C_{T_n} \to 0$ and that $B_D \to 0$ removes the impact on the flux through the system. In the limit, therefore, the assumption that the mass fluxes far upstream and downstream of the energy extracting device are equal is implicit to the model for the case of an infinitely wide channel.

2.4.3 Fractal approximation to unbounded multi-scale devices

We stress here that although the multi-scale device approaches the optimal conditions for energy extraction, it is not necessarily the only method of optimal extraction. Other device configurations which satisfy the unmodified stream-tube at largest scale, optimal pressure drop at smallest scale and conservation law constraints remains an open question, and further investigations into satisfying these constraints could uncover both novel and practical methods for extracting power above the Betz limit.

A simple example of this which helps aid in the visualisation of a multi-scale device, is a fully fractal arrangement where the local blockage remains the same across all scales, i.e. $B_L = B_s$ for $1 \leq s \leq n - 1$. Figure 2.7 demonstrates that such an array does not significantly under-perform the optimal arrangement, with the large and small scale constraints also decoupling in the limit.

Figure 2.8 further illustrates the relationship between the local blockage ratio (which once again remains the same across scales for the fractal device) and the

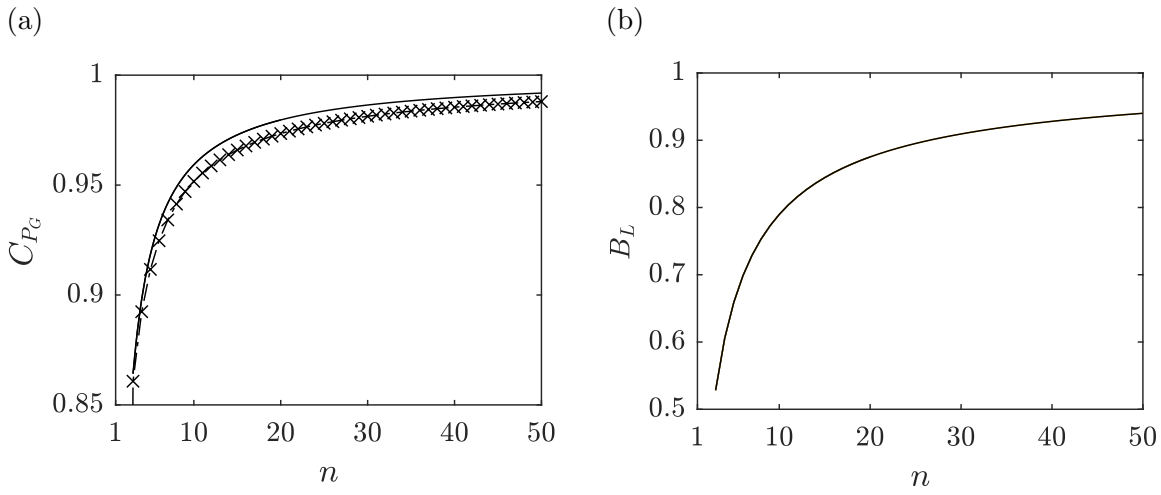

Figure 2.7: Properties of a fractal multi-scale energy extracting device where the local blockage is held constant for all scales. (a) A comparison of the optimal (solid line) and fractal device energy (crosses) extraction efficiency and (b) the local blockage ratio required for optimal extraction for an n-level fractal device.

resultant power coefficient. Given the small under-performance when compared to the optimal configuration, figure 2.8 condenses the complex multi-dimensional data of the optimal configuration and figuratively describes many of its conclusions. The maximum power extraction efficiency is seen to asymptote to 1 with increasing number of scales. This makes clear the diminishing returns of additional scales, as well as the increasing local blockage ratio required to realise optimal extraction as the layers of the fractal increase. Note that for equally sized discs, the maximum local blockage achievable at the inner most scale is $\pi/4 = 0.785$ for circular discs arrayed in a rectangular grid, and $\pi/2\sqrt{3} = 0.907$ for circular discs arrayed in rows staggered above and below each other. This provides useful upper physical bounds to the problem indicating that in practical terms no further power coefficient increase can be achieved beyond about 10 and 20 fractal layers for rectangular and staggered grid arrangements of equally sized circular actuators.

An approximation to the physical arrangement of the discs for the $n = 3$ fractal case is shown in figure 2.9, which illustrates both the conceptually fractal-like construction of such a device, and the final device with a $C_{P_G} \sim 87\%$ extraction efficiency (see optimum locus with $n = 3$ in figure 2.8). We note that the number of arrays and sub-arrays d_s each subsequent fractal iteration splits into would need to be greater than the four shown in the figure to fully realise the extraction limit (see Nishino and Willden [2013a] for details on the influence of the number of actuators required for a

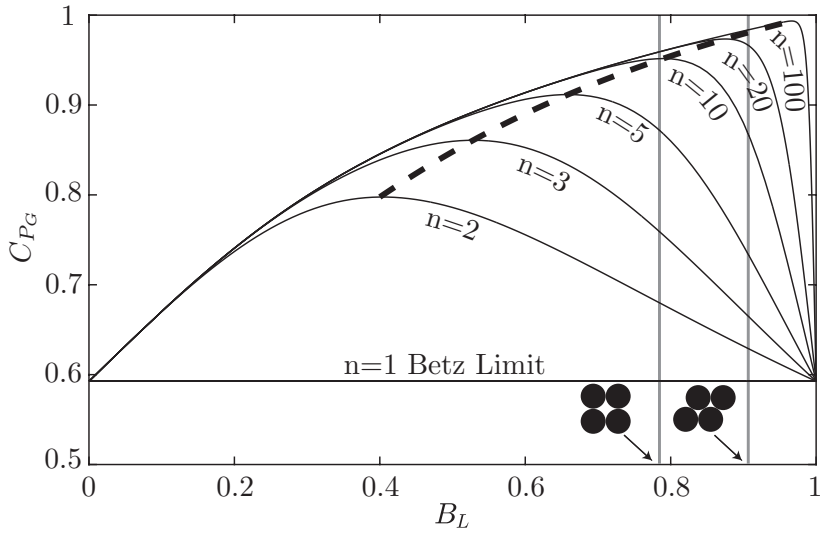

Figure 2.8: The relationship between local blockage and power extraction for multi-scale fractal devices in an unbounded flow ($B_n = 0$). The dashed line provides the locus connecting the optimal power coefficients for fractal devices up to $n = 100$ scales. Maximum achievable local blockage ratios are shown for both rectangular ($B_L = 0.785$) and staggered ($B_L = 0.907$) arrays of equally sized circular discs.

two scale device).

2.4.4 Properties of optimal unbounded finite-scale devices

Although an optimal pressure coefficient is only realised for an infinite number of scales, the maximum power coefficient (see figure 2.3) rapidly asymptotes to the optimal condition for relatively small n. Furthermore, in practice, it appears likely that the maximum number of scales will be limited to small n. This section therefore considers comparisons of parameter distributions for finite n, to highlight the differences in these distributions prior to convergence.

Figure 2.10a-2.10b illustrate the velocity factor distributions across scales for various n. For increasing numbers of device scales, the velocity factors always increase at any given normalised scale, with α_s and γ_s both nearing unity across all scales for $n = 100$. It is clear that as the number of scales increases, the flow across scales decelerates through each subsequent scale more gradually. The reduction in the differential between core and bypass flow velocities at any given scale minimises mixing losses at that scale, whilst keeping α_G as close to 1/2 as possible. For a very small number of scales the flow must be rapidly decelerated to ensure a large enough static pressure drop can occur across the energy extraction device, resulting in substantially larger stream-tube deformation.

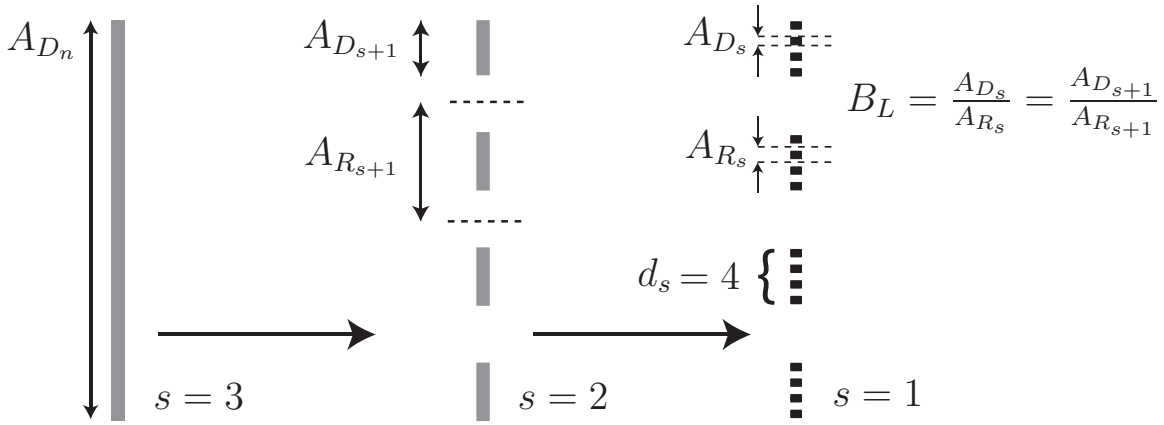

Figure 2.9: A schematic of a fractal arrangement of discs, which may be visually interpreted by considering the recurrent division of discs into d_s new sub-discs per disc with identical spacing between the sub-discs. Here the array is split $n - 1 = 2$ times into $d_s = 4$ discs each time, with a constant local blockage ratio of $B_L \sim 0.55$, which is near optimal for the fractal arrangement with $n = 3$. The final arrangement is shown in black.

Likewise, the thrust coefficient gradually builds up across scales to the smallest (disc) scale (figure 2.10c) for all numbers of device scales considered. Further, the thrust coefficient distribution appears relatively universal for different numbers of device scales, and approaches the limiting case ($n \to \infty$) from above as the number of problem scales is increased (i.e. at all normalized scales the thrust coefficient is slightly higher for a lower number of device scales). The physical interpretation of the shape of the C_{T_s} curve is analogous to the intuition of the optimum power extraction of the Betz actuator disc model. As a larger thrust is applied to the flow to attempt to increase power extraction, more fluid is 'diverted' around the disc. Likewise, with too little thrust, more flow passes through the disc but the power is poorly extracted from the fluid. In the multi-scale device, as n becomes larger, the device better decouples these scales such that at the largest scale little resistance is applied to the flow, and at the smallest scale the largest possible resistance is applied to the flow. The near universality of the curve with respect to s/n supports the observed higher optimal power coefficient as n increases; if the thrust distribution is bound to a universal curve then a greater range of scales from $1/n \leq s/n \leq 1$ is required to achieve greater pressure drop at the smallest scale, and least stream-tube deformation (lowest thrust)

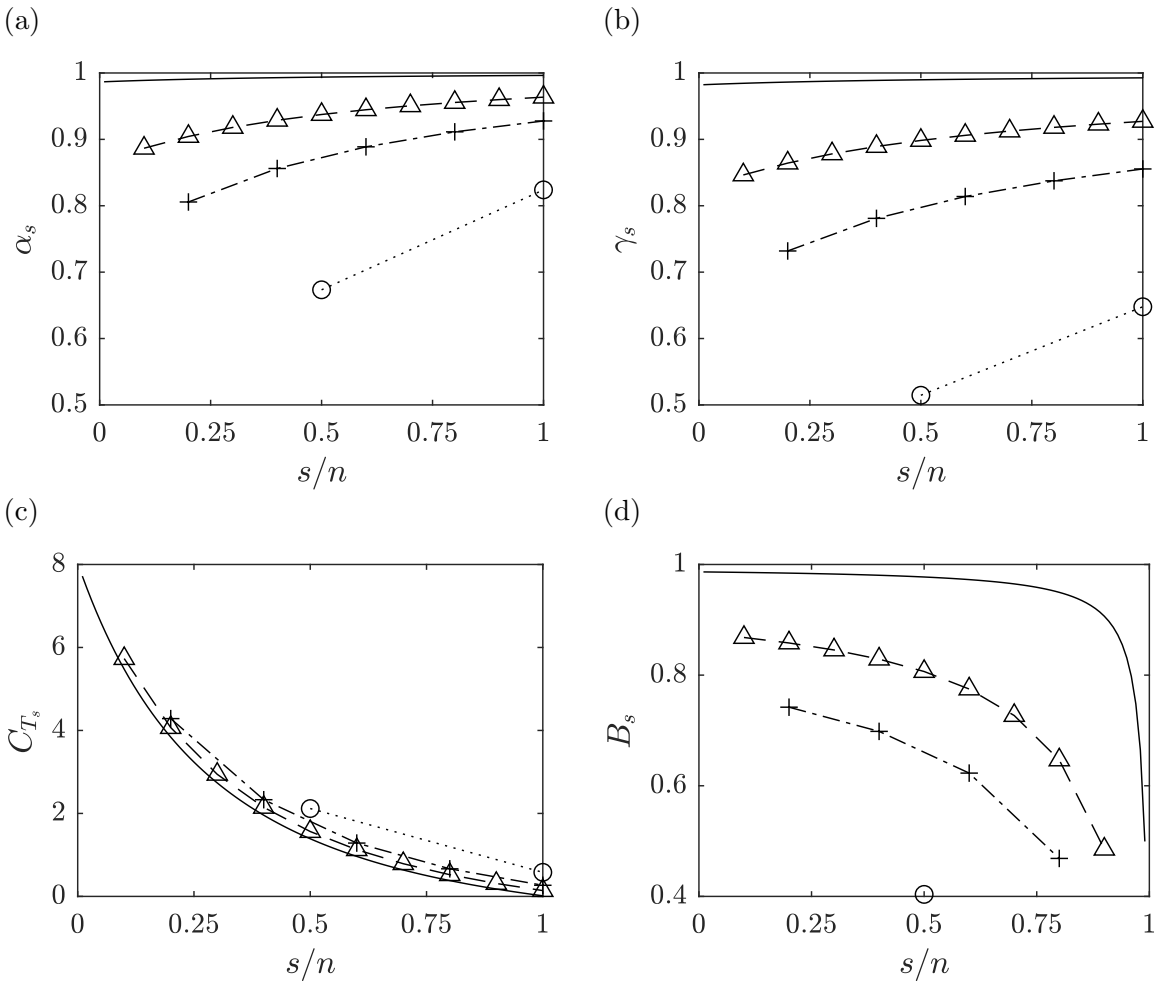

Figure 2.10: Distributions of (a) α_s, (b) γ_s, (c) C_{T_s} and (d) B_s for an $n = 2$ (circles connected by dotted line), $n = 5$ (pluses connected with a dash-dot line), $n = 10$ (triangles connected with a dashed line) and $n = 100$ (continuous line) multi-scale device for optimal power in an infinitely wide channel $B_n = 0$. For clarity, the scale in each device has been normalised by the total number of scales for that device.

at the largest scale. This is achieved as increasing n provides greater scale separation along the universal curve, leading to higher optimal power.

C_{T_n}, i.e. C_{T_s} at $s/n = 1$, is observed to decrease as n increases (less impact on outer most scale), and so, despite the power extraction efficiency increasing, the impact on global mass flux reduction is reduced. Interestingly, although the blockage ratios increase at all scales with increasing n (figure 2.10d), the device blockage ratio actually decreases (see figure 2.11). So that for optimal power extraction in globally unblocked flow, as the number of scales increases, the devices occupy a vanishingly small proportion of the spatial extent covered by the devices.

This is particularly relevant to both tidal [Vennell, 2013] and wind [Bleeg et al.,

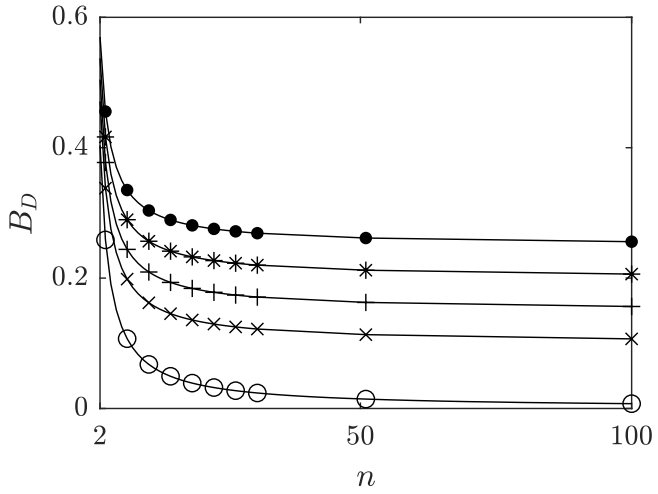

Figure 2.11: The device blockage ratio B_D for optimal power as a function of the number of scales of a multi-scale device (markers indicate numerical solutions with circles for $B_G = 0$, crosses for $B_G = 0.1$, pluses for $B_G = 0.15$, stars for $B_G = 0.2$ and filled circles for $B_G = 0.25$; every 4^{th} simulated data point plotted).

2018] energy extraction devices, where the coupling of mass flux and device blockage was observed to play an important role in limiting power extraction. In short, multi-scale devices operating at their optimal energy extraction efficiency, decrease the impact of this detrimental effect. For a fixed channel width, this does however come at the expense of reduced power generation, as the discs occupy a smaller fraction of the device area with increasing number of scales. Finally, note that the global thrust coefficient for an $n = 50$ scale device is near 2.5 fold larger than the $n = 1$ scale device (figure 2.12), showing that discs need to sustain higher thrust levels for devices with power extraction exceeding the Betz limit.

The distributions of blockage ratios shown in figure 2.10d further relate the configuration of the device to the physics. Note that presently the largest scale is not included, as the blockage for the largest n^{th}-scale is zero by definition. Across the entire $s - n$ parameter space, the blockage is bounded by $B_s \geq 0.4$, with the blockage at the largest interior $(n - 1^{th})$-scale converging to 1/2 and at the smallest scale to 1. Similar to the velocity factors, the blockage ratio for a given normalised scale monotonically increases with increasing n. As in the Garrett and Cummins [2007] model (see appendix 2.A), blockage at each scale is the physical mechanism by which the velocity factors are modified to optimise the power coefficient of the device. This is clear by consideration of the constraint equation (2.6), whereby the blockage ratio is used to constrain the thrust coefficient rise across scales.

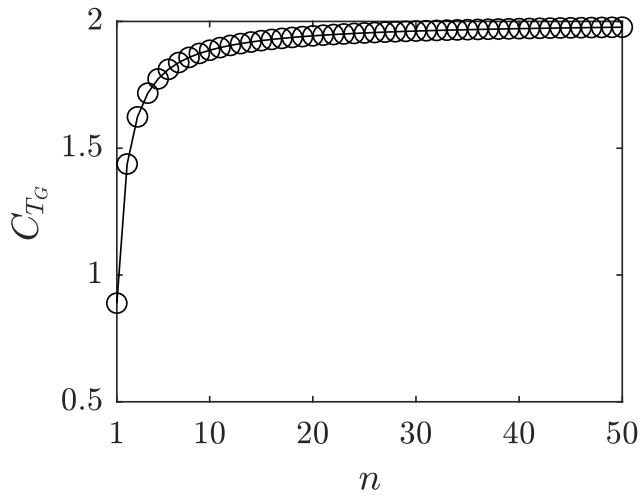

Figure 2.12: The relationship between global thrust coefficient C_{T_G} and the number of scales for $n \leq 50$ for optimal power in globally unblocked flow $B_G = 0$. The circles indicate the numerical solutions.

2.4.5 Finite blockage multi-scale devices

We next consider finite global blockage ratios. For practical purposes we limit our investigation to global blockages less than 0.25. It is not clear that, unless a free surface is introduced into the problem, any new physics emerges for blockages greater than our chosen value.

Figure 2.13a presents the optimal C_{P_G} for different blockage ratios at different problem scales. Numerical results (indicated by the markers) are compared with an empirical fit given by

$$C_{P_{G,\max}} \approx \frac{1}{n}(1 - B_G)^{-2}\Big[C_{P,\text{Betz}} + (n-1)(1 - B_G)^{4/9}\Big], \tag{2.27}$$

where we note that the leading term $C_{P,\text{Betz}}(1 - B_G)^{-2}$ is the limit determined by Garrett and Cummins [2007] for a (single scale) array of discs homogeneously arrayed across a channel so as to present blockage B_G. Analogous to the unbounded case, as $n \to \infty$, $C_{P_{G,\max}}$ converges to the limit $(1 - B_G)^{-14/9}$, which increases with global blockage as observed in figure 2.13a for $n = 100$. Even a modest global blockage of 20% is seen to increase the maximum power coefficient to 1.41 as $n \to \infty$. Consequently greater power than the upstream kinetic flux passing through an area equal to the net actuator frontal area may be extracted for $B_G > 0$. The relative percentage error between the numerical solution and the empirical fit is shown in figure 2.13b and is below 0.5% over the range of global blockage ratios and number of scales considered. We conclude therefore that the power coefficient limit for an

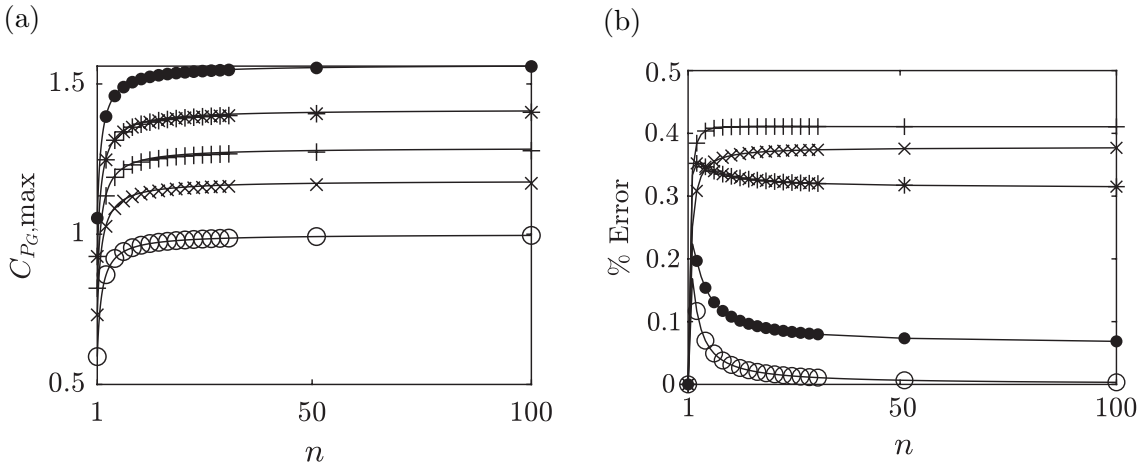

Figure 2.13: The maximum power coefficient for a multi-scale device with different global blockage ratios (circles for $B_G = 0$, crosses for $B_G = 0.1$, pluses for $B_G = 0.15$, stars for $B_G = 0.2$ and filled circles for $B_G = 0.25$; every other simulated data point plotted), here shown for all scales to $n \leq 100$. (a) The markers indicate the numerical solutions, and the solid line gives the empirical fit to the optimal C_{P_G} (equation 2.27). (b) The relative percentage error between the numerical solution and the empirical fit.

infinite-scale problem in arbitrary global blockage is then $C_{P_{G,\max}} = (1 - B_G)^{-14/9}$, over the range of global blockage considered herein ($0 \leq B_G \leq 0.25$).

Figure 2.14 illustrates how different effects contribute to enabling a higher optimal power coefficient. Adding more problem scales can be visualized as a vertical traverse in the direction of the blue arrow, whilst increasing global blockage can be visualized as a horizontal traverse in the direction of the red arrow. Starting at the Betz limit ($B_G = 0$ on the thin continuous line representing a single scale device), both multi-scale mixing (vertical traverse) or streamwise pressure gradients resulting from finite global blockage (horizontal traverse) may be used to increase the optimal power coefficient. Although it is tempting to think that very high power coefficients in excess of unity may be achievable, in all practical terms global blockages are likely not to exceed $B_G \sim 0.1$ aside from at exceptional locations, and it is difficult to see how more than 2 or 3 device scales may be realised. Thus the range of practical importance is confined to the lower left quadrant of Figure 2.14. Nevertheless, this figure provides a useful guide to the interplay between the two effects that serve to increase the optimal energy extraction efficiency.

The aforementioned decoupling of the inner scale pressure drop and the outer most scale stream tube modification is also evident for finite global blockage cases.

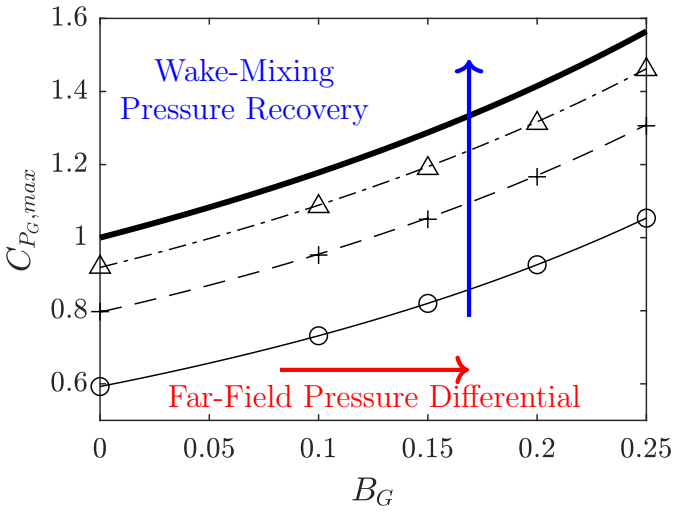

Figure 2.14: The maximum power coefficient as a function of global blockage (lines indicate the empirical fit (equation 2.27) whilst markers indicate the numerical data points) for an $n = 1$ (continuous line with circles), $n = 2$ (dashed line with pluses), $n = 10$ (dash-dot line with triangles) and $n = \infty$ (thick continuous line) multi-scale device. Arrows indicate the effects that contribute to an increase in $C_{P_G,\max}$.

Figure 2.4a shows that, in these cases, the limit for α_G for large n decreases with increasing B_G – leading to a higher static pressure drop across the smallest scale – while the stream-tube area remains unmodified ($\alpha_n \to 1$ for large n, figure 2.4c).

Figure 2.5 also presents the relevant parameters for an $n = 100$ multi-scale device with finite global blockages. Compared to the unbounded case the flow is further decelerated across all scales for finite global blockages (figure 2.5a), which leads to a steeper increase in static pressure towards the smallest scale (figure 2.5c). The optimal distribution of local blockage ratios on the other hand flattens with increasing global blockage, with even the local blockage at the larger scales approaching near unity. This, together with $\alpha_n \to 1$ for $n = 100$ (figure 2.4c), infers that even relatively low finite outer scale blockage is a very effective mechanism to constrain the outer stream-tube and prevent its significant expansion; by contrast, when the flow is globally unblocked, only modest levels of blockage can be imposed across the largest scales so as to limit outer stream-tube expansion (figure 2.5d). This observation is also captured through examination of the device blockage B_D (figure 2.11); for globally unblocked flows very low device blockage is permissible for optimal power efficiency, and $B_D \to 0$ as $n \to \infty$, whilst for even small but non-zero outer scale blockage, significant levels of local blockage $B_D \geq 0.1$ are permissible at even large n for optimal power efficiency. This infers that the optimal energy extractor is far more compact

in flows that are constrained at the outer most scale, i.e. for $B_n > 0$, as compared to globally unblocked ($B_n = B_G = 0$) flows.

Finally, we present the parameter distributions and trends across scales for devices of different numbers of scales for $B_G = 0.1$ (figure 2.15). Generally the results follow those of the unbounded case (figure 2.10), with slightly reduced velocity factors α_s due to the greater upstream deceleration permissible with a finite outer scale blockage constraint. As already discussed, finite outer scale blockage permits greater local blockage across the scales; compare figure 2.15c with figure 2.10c. As in the unbounded case, the local thrust coefficient variation approximately collapses to a single curve with peak C_{T_s} at the inner-most scale of the device with the largest number of scales. This device local thrust coefficient is then significantly in excess of the limiting value, $C_{T_s} = 8.0$, for unbounded flows.

2.4.6 Non-deforming free surface assumption

We can now consider the implicit assumption that the cross-sectional area of the flow remains approximately uniform, i.e. that the head loss is significantly smaller than the channel depth. The disc configuration shown in figure 2.2, namely a wide row of discs in a shallow channel where the channel height is smallest, represents the critical case for head loss considerations. Other configurations, such as that shown in figure 2.1, will be necessarily less restrictive. Although at first it may appear that the bypass flow velocity at the inner scale becomes infinitely large in the limit due to $B_1 \to 1$, we note that actually β_1 remains finite and asymptotic as evidenced by C_{T_1} remaining finitely bounded (this can only occur if $\alpha_s, \gamma_s \to 1$). At any given scale it can readily be shown by conservation that $C_{T_s} = \beta_s^2 - \gamma_s^2$. As $\gamma_s \to 1$ in the limit of $n \to \infty$, this implies that β_1 asymptotes to $\beta_1 = \sqrt{C_{T_1} + 1}$, with figure 2.16 demonstrating this from the numerical results. As C_{T_s} always decreases with increasing s (see for instance figure 2.10), it follows that β_1 will always be the largest bypass flow induction factor, and that the region of flow by-passing the inner disc scale therefore represents the critical span-wise location for maximum head loss in the critical case of the wide and shallow channel realisation of the multi-scale problem. Applying Bernoulli's principle along the bypass, the pressure drop $\Delta p_{\infty,1}$ between the far upstream pressure and the bypass of the innermost scale is therefore

$$\Delta p_{\infty,1} = \frac{1}{2}\rho u_\infty^2 \left(\beta_1^2 \left(\prod_{i=2}^{n} \alpha_i^2 \right) - 1 \right) = \frac{1}{2}\rho u_\infty^2 \left((C_{T_1} + 1) \left(\prod_{i=2}^{n} \alpha_i^2 \right) - 1 \right), \quad (2.28)$$

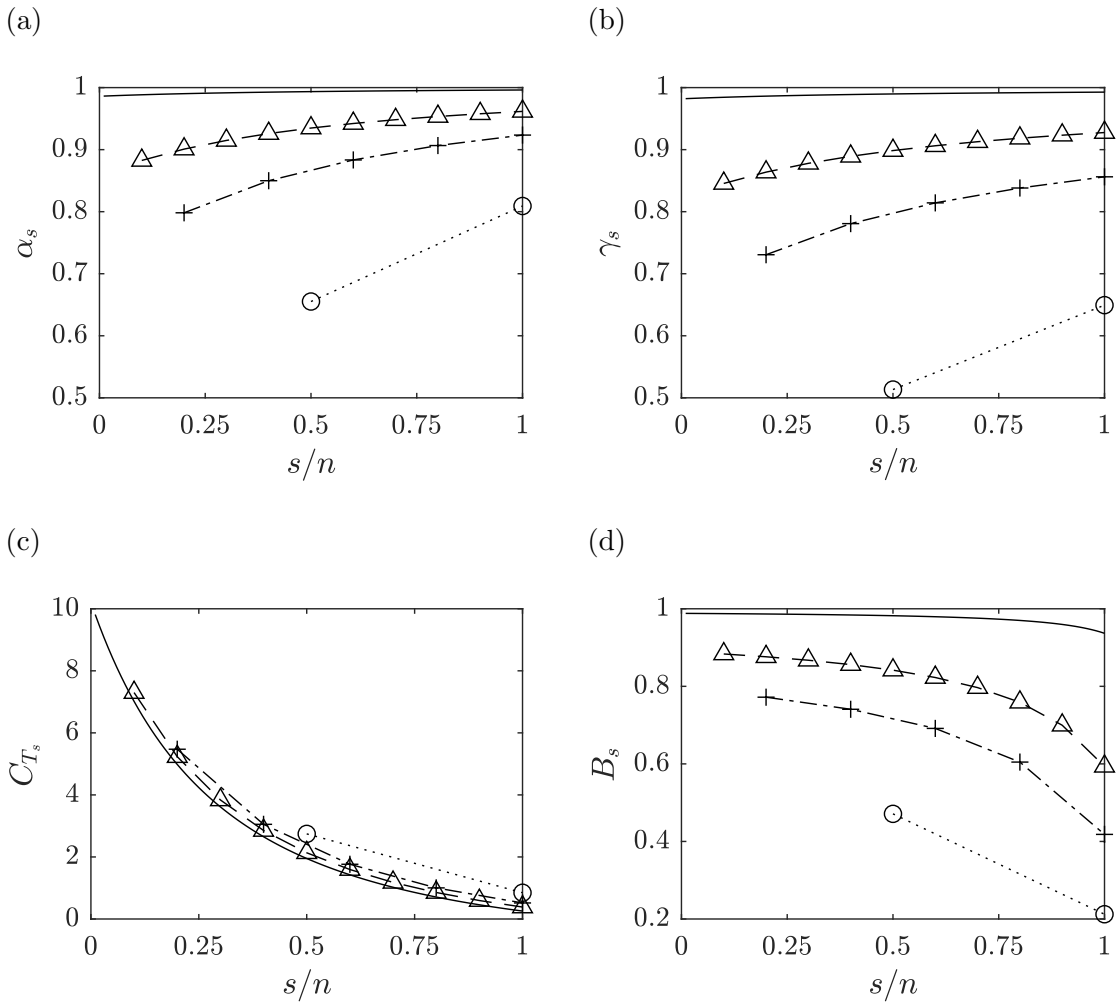

Figure 2.15: Distributions of (a) α_s, (b) γ_s, (c) C_{T_s} and (d) B_s for an $n = 2$ (circles connected by dotted line), $n = 5$ (pluses connected with a dash-dot line), $n = 10$ (triangles connected with a dashed line) and $n = 100$ (continuous line) multi-scale device for optimal power for a global blockage ratio $B_G = 0.1$. For clarity, the scale in each device has been normalized by the total number of scales for that device.

and the head loss is given by $\Delta H_{\infty,1} = \Delta p_{\infty,1}/(\rho g)$. Following Garrett and Cummins [2007], the assumption that the channel cross-sectional area remains unchanged requires that the head loss is significantly smaller than the channel height h, and so a

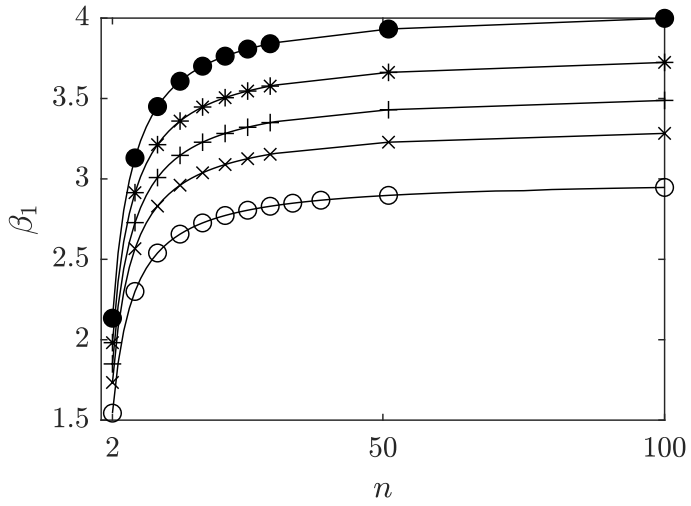

Figure 2.16: The inner scale bypass flow velocity β_1 for optimal power as a function of the number of scales of a multi-scale device (markers indicate numerical solutions with circles for $B_G = 0$, crosses for $B_G = 0.1$, pluses for $B_G = 0.15$, stars for $B_G = 0.2$ and filled circles for $B_G = 0.25$; every 4^{th} simulated data point plotted.

condition on the Froude number may be formulated as follows

$$h \gg \frac{u_\infty^2}{2g}\left((C_{T_1}+1)\left(\prod_{i=2}^{n}\alpha_i^2\right)-1\right), \tag{2.29}$$

$$\frac{u_\infty^2}{gh} \ll \frac{2}{(C_{T_1}+1)\left(\prod_{i=2}^{n}\alpha_i^2\right)-1}, \tag{2.30}$$

$$Fr \ll 2^{1/2}\left[(C_{T_1}+1)\left(\prod_{i=2}^{n}\alpha_i^2\right)-1\right]^{-1/2}. \tag{2.31}$$

This condition is well satisfied for tidal flows which typically have Froude numbers in the range of $0.05 \leq Fr \leq 0.25$, and almost always satisfied for wind farm flows. For instance, for the unbounded case where $\prod_{i=2}^{n}\alpha_i \to 1/2$ and $C_{T_1} \to 8$, the condition reduces to $Fr \ll 1.26$. For a large global blockage case of $B_G = 0.25$, where $\prod_{i=2}^{n}\alpha_i \to 0.47$ (see figure 4) and $C_{T_1} \to 15$ (see figure 5), the condition reduces to $Fr \ll 0.93$. It is clear therefore that the multi-scale model broadly satisfies the non-deforming free surface assumption for modest global blockage ratios. Analogous to the single-scale model of Garrett and Cummins [2007], the validity of this assumption for the multi-scale model is primarily dependant on the global blockage ratio, and is increasingly restrictive as the global blockage increases.

2.4.7 Numerical demonstration of multi-scale performance uplift

We now present three-dimensional RANS computations of the $n = 2$ and $n = 3$ optimal configurations, with the focus on demonstrating both the uplift in power coefficient and scale separation arguments. We simulate the configuration shown in figure 2.2, namely a wide row of discs in a shallow channel, where we compare the theoretical results to a set of four configurations (table 2.1), all with the same global blockage ratio. The methodology closely follows that of Nishino and Willden [2013a], where the governing RANS equations are solved assuming steady and incompressible flow, and turbulence closure is provided using the $k-\epsilon$ model [Launder and Spalding, 1974]. The height of the channel is set to $1.2D$, where D is the actuator disc diameter, and the width of the channel is set such that the global blockage ratio is $B_G = 0.0785$. The Reynolds number (based on the turbine diameter) is set to be large enough (Re $= 1.5 \times 10^6$) such that viscous forces are negligible, and the inlet turbulence model quantities are set to be very low ($k = 1.5 \times 10^{-6}$ m^{2}s^{-2} and $\epsilon = 1.5 \times 10^{-10}$ m^{2}s^{-3}, where the inlet velocity is set to unity). The actuator discs are likewise modelled following Nishino and Willden [2013a], where a change in momentum flux equal to $S_U = K(\frac{1}{2}U_D^2)$, where U_D is the local stream-wise velocity, is added to the momentum equation at the location of the discs to the momentum equation, and K, the disc momentum loss factor, is assumed to be uniform across the surface of all discs. The resultant disc averaged global thrust and power coefficients are then calculated by $\langle C_{TG} \rangle = K\langle U_D^2 \rangle / u_\infty^2$ and $\langle C_{PG} \rangle = K\langle U_D^3 \rangle / u_\infty^3$, noting that the reference flow speed is unity and where the angle brackets represent face averaging over all discs. See Nishino and Willden [2013a] for further details and numerical model validation.

As demonstrated by Nishino and Willden [2013a], the performance uplift for this specific configuration of discs is primarily limited by the mixing rate, which can be controlled by variations in the turbulence model coefficient $C_{\epsilon 1}$ and the number of discs. Here we leave $C_{\epsilon 1}$ at its widely used value of 1.44, although we note that lower values would promote mixing, and choose to vary the number of discs to better isolate the multi-scale effect.

The blockage ratios presented in table 2.1 are the theoretically optimal blockage ratios for the given global blockage ratio. The $n = 2$ scale studies can be readily compared to those of Nishino and Willden [2013a]. The 6-group $n = 3$ study can be readily compared against the 6 disc $n = 2$ study, and the 240 disc $n = 3$ study can be compared against the 3-scale theoretical optima.

n	Number of discs	B_1	B_2	B_3	B_G
2	6	0.4568	0.1719	-	0.0785
2	48	0.4568	0.1719	-	0.0785
3	6 groups of 8 discs (48 in total)	0.6216	0.5163	0.2447	0.0785
3	16 groups of 15 discs (240 in total)	0.6216	0.5163	0.2447	0.0785

Table 2.1: Summary of flow configurations studied in the numerical framework.

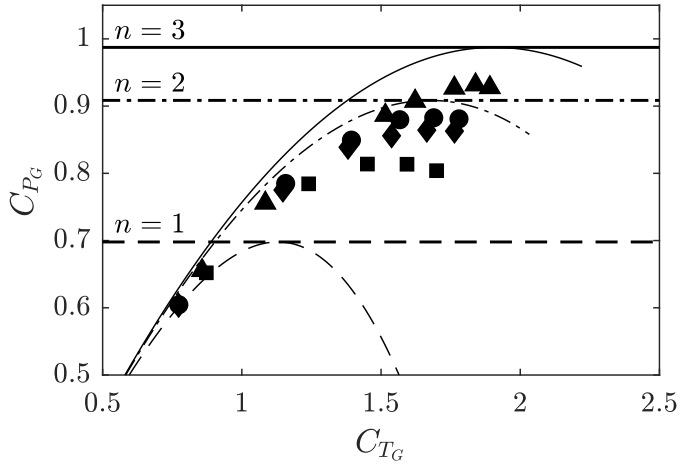

Figure 2.17: Power curves for the numerical configurations detailed in table 2.1, illustrating power uplift under multi-scale effects for a global blockage ratio $B_G = 0.0785$. The dashed line shows the single scale Garrett and Cummins [2007] limit, and the dash-dot and solid lines show both the $n = 2$ and $n = 3$ scale limits respectively, alongside their corresponding power versus thrust variations. Symbols indicate numerical results; squares, 6 disc, $n = 2$ configuration; diamonds, 48 disc, $n = 2$ configuration; circles, 48 disc, $n = 3$ configuration; triangles, 240 disc, $n = 3$ simulations.

The summary plot in figure 2.17 clearly demonstrates the uplift in performance and provides numerical validation for the theoretical model. The $n = 2$ device optima fall between the single scale Garrett and Cummins [2007] limit and the theoretical 2-scale limit. As anticipated, the fence underperforms the theoretical limit due to finite fence length effects, with the 48 disc fence significantly outperforming the 6 disc fence. For 48 discs, the 3-scale optimal configuration very slightly outperforms the 2-scale 48 disc configuration; this is the result of the balance between deleterious finite fence effects with only 8 discs at the inner scale and 6 discs at the outer scale, and performance uplift due to the additional scale. Finally, for a large number of discs, it is clear that the 3-scale array outperforms the 2-scale arrays, and the efficiency instead approaches the 3-scale theoretical limit.

The assumption underpinning the theoretical analysis is that of scale separation

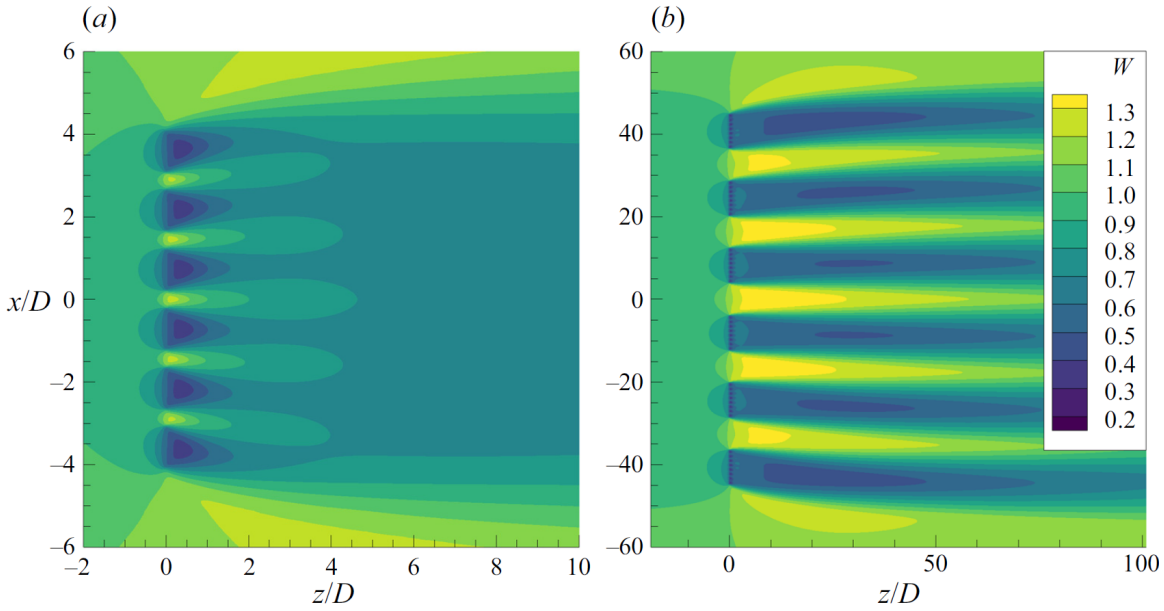

Figure 2.18: Normalised streamwise velocity field contours at hub-height qualitatively illustrating scale separation for the 6 disc $n = 2$ scale (left) and 6 group of 8 discs $n = 3$ (right) configurations. The flow is moving left to right, with bypass and core flow regions clearly visible. Note the differences in geometric scale between the two simulations.

between each sequential scale. Figure 2.18 shows how the mixing process across each scale occurs sequentially, and that the far wake mixing of a given scale takes place much faster than the horizontal expansion of the flow around the next scale. For this reason, the near-wake (from say $z/D \sim 5$) of the $n = 2$ scale simulation resembles a single scale wake, and the near-wake (from $z/D \sim 5$) of the $n = 3$ scale device resembles that of an $n = 2$ scale 6 disc array (which further mixes to resemble a single scale wake far downstream). With the aid of figure 2.17, one can inductively picture how with each additional scale the scale-separation assumption is satisfied. For instance, the near-wake of an $n = 4$ scale device will resemble an array of $n = 3$ scale devices (with the accelerated bypass between each array) and so forth.

We note that although the multi-scale shallow water array numerically approaches the theoretical optima, other configurations that encourage wake-mixing may also be useful for extracting power above the Betz limit. The theoretical optimum provides an upper bound on the energy extraction efficiency (which will always hold), and sets a benchmark against which the multi-faceted effects of finite mixing lengths, real array inefficiencies, number of devices, turbulence effects, and other flow physics can be evaluated.

2.5 Discussion

We now use the model to hypothesise the physical processes that enable multiple scale disc arrangements to extract more power than single extractors placed in unbounded flow. It is attractive to think, at first, that a higher device energy extraction efficiency from the flow, C_{P_G}, must result from a reduction in losses in the multi-stage process. Within the confines of this model the only energy losses that occur are in the wake remixing processes, and thus one might hypothesise that greater device energy extraction efficiency is a result of reduced mixing losses. In fact, the reverse turns out to be the case.

Consider a multi-scale energy extractor with arbitrary number of scales, for which the global velocity induction factor is α_G. The extractor is placed in a flow of finite dimension so that it presents a non-zero global blockage. We consider the changes between the far upstream and the far downstream location following all necessary flow remixing. As the flow area does not change from far upstream to far downstream there can be no change in momentum or kinetic energy flux. Hence, linear momentum gives that the global thrust on the array, T_G, is entirely due to the pressure difference from far upstream to far downstream:

$$T_G = \Delta p_\infty A_c, \tag{2.32}$$

with Δp_∞ the change in static pressure along the stream, and A_c the channel cross-section area. We consider the change in total pressure from far upstream to far downstream and hence the total change in energy flux due to both useful energy extraction and remixing:

$$\Delta \dot{E}_{05} = \Delta p_\infty A_c u_\infty. \tag{2.33}$$

Substituting with the expression from linear momentum enables the change in energy flux to be written in terms of the useful power generated $P_G = T_G u_\infty \alpha_G$

$$\Delta \dot{E}_{05} = \frac{P_G}{\alpha_G}. \tag{2.34}$$

Alternatively we may express this in the form of a basin efficiency, η, defined as the ratio of useful energy removed to the total energy removed from the flow

$$\eta = \frac{P_G}{\Delta \dot{E}_{05}} = \alpha_G. \tag{2.35}$$

We must be cautious here to distinguish between the actual efficiency of energy extraction from the flow, η, and the perceived efficiency of the device, C_{P_G}, which gives an indication of the density of power extraction at the disc plane.

The expression 2.35 yields the well known result that for a single unbounded disc operating at the optimal Betz limit, the overall efficiency of energy extraction is $\eta_{Betz} = 2/3$. For a single scale of disc (homogeneous array) operating in a blocked flow Garrett and Cummins [2007] showed that optimum C_{P_G} is accompanied by a reduction in α_G as blockage increases (see also appendix 2.A), and hence, by the above, the efficiency of energy extraction must also reduce. For multi-scale energy extraction in a vanishing outer scale blockage, it has been demonstrated that for maximum power coefficient $\alpha_G \to 1/2$ as the number of scales $n \to \infty$, and to even lower values of α_G for non-zero global blockage. Hence, we conclude that to extract higher levels of energy from the flow, the efficiency of energy extraction, η, must be reduced and a greater proportion of the overall energy removed expended on flow remixing. For the specific case of an infinite scale energy extractor operating in a vanishingly small global blockage it follows that at most 1/2 of the total energy removed from the flow will be usefully extracted when the device energy extraction efficiency, C_{P_G}, is maximised.

We next seek a physical explanation of how scale remixing enables an increase in pressure jump and hence power extraction across the disc plane. Consider the process of mixing two streams of the same incompressible fluid moving at different velocities but with the same initial pressure. It can be readily shown through conservation of mass and linear momentum that the static pressure of the fully mixed fluid will increase by $\Delta p_{mix} \propto \Delta u_{ab}^2$ where Δu_{ab} is the velocity difference between the two streams a and b. Static pressure increase is therefore an inevitable consequence of incompressible flow mixing processes.

Consider the variation of the static pressure from far upstream to far downstream of a disc or disc array, as illustratively depicted in figure 2.19. All processes upstream of the disc are inviscid and hence flow deceleration to the disc plane is energy conserving regardless of the number of scales so that the pressure coefficient upstream of disc plane $c_{pu} = 1 - \alpha_G^2$ always. The pressure coefficient on the downstream side of the disc plane is more complex due to viscous remixing processes and the streamwise pressure gradient associated with outer scale blockage. In the case of a single scale unbounded energy extractor the pressure coefficient downstream of the disc plane is given by $c_{pd} = \gamma_G^2 - \alpha_G^2$. The power extracted by the disc or disc array may be expressed in terms of the change in pressure coefficient through:

$$C_{P_G} = \alpha_G(c_{pu} - c_{pd}). \tag{2.36}$$

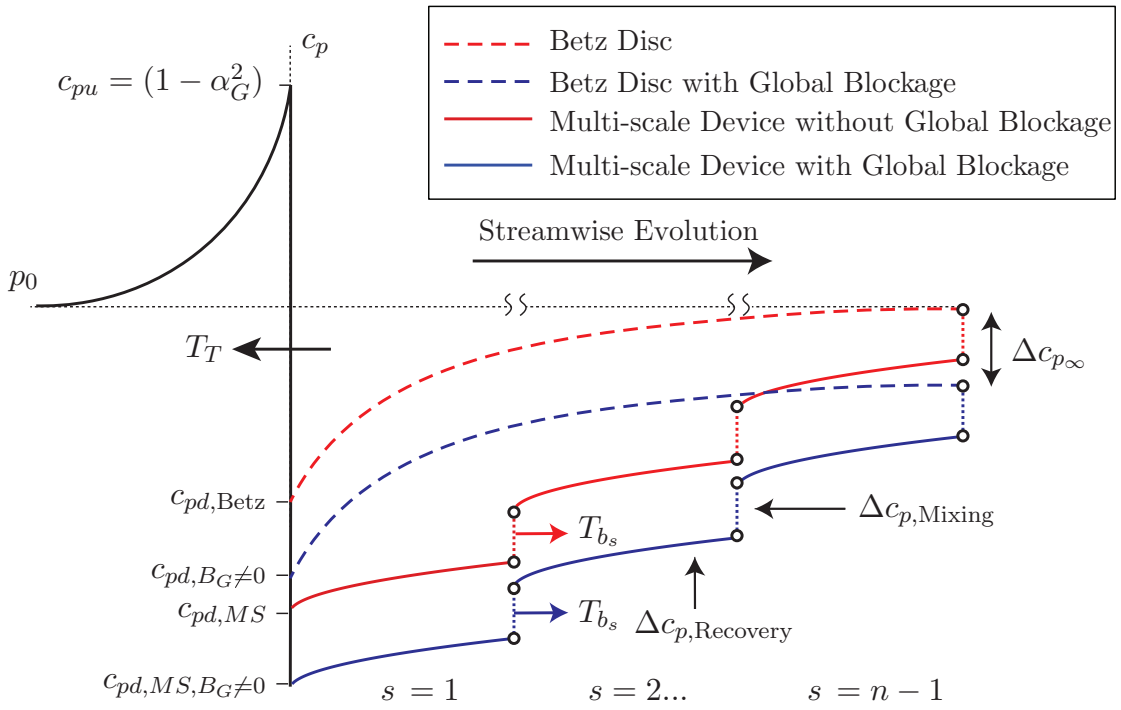

Figure 2.19: A schematic illustrating the impact of mixing in the wake of each scale of the multi-scale extractor. The curves represent the pressure of a given fluid particle as it travels through the scales from the undisturbed upstream conditions through the different models to the far wake. The mixing corresponds to pressure increases at each scale in the wake allowing for greater energy extraction across the disc plane. Global blockage allows for additional pressure extraction through a change in the pressure boundary condition in the far wake.

Hence, for the optimally operated single unbounded disc the pressure coefficient rises to 5/9 ahead of the disc and falls to $-1/3$ immediately after. For the case of the unbounded ($B_n \to 0$) infinite-scale extractor $\alpha_G \to 1/2$ for optimum extraction and so $c_{pu} - c_{pd} \to 2$. The rise in upstream pressure is limited by the change in α_G to $c_{pu} \to 3/4$, and so a downstream pressure coefficient $c_{pd} \to -5/4$ is needed to achieve the pressure balance required for $C_{P_G\max} \to 1$.

This low level of downstream pressure cannot be sustained if the flow is to recover inviscidly to free stream conditions, and additional mechanisms are required to increase the flow pressure through recovery. This is the role of bypass flow mixing which acts to increase the static pressure in the recovery enabling a lower pressure to be maintained immediately downstream of the discs. As depicted in figure 2.19 we may visualise each remixing processes that the flow undergoes in the wake as being a bypass propeller that imposes a streamwise thrust on the flow, T_{b_s}, that injects

additional momentum into the core flow through mixing with the bypass flow at scale s. The thrust exerted on an unbounded n-scale device is then given by

$$T_G = \dot{m}_t u_\infty (1 - \gamma_n) + \sum_{s=1}^{n-1} T_{b_s}, \tag{2.37}$$

where $T_{b_s} = \dot{m}_{b_s} u_\infty (1 - \gamma_n)$, and $\dot{m}_t$ and $\dot{m}_{b_s}$ are the mass fluxes through the disc core flows and the bypass of scale s. Conceptually every additional bypass mixing process that is added provides a pressure rise in the wake which may be visualized as an additional propeller thrust T_{b_s}. Each propeller thrust enables an additional equal and opposite thrust increment to be developed at the disc plane. Hence, any process that forces wake flow remixing is able to develop an increased pressure drop across the disc plane and exceed the single scale energy extraction limit. As more scales of mixing are added the pressure recovery that may be supported through the wake increases, leading to increased energy extraction.

Nishino and Willden [2012b] observed from numerical simulation that the performance of single actuator discs in blocked flows could be enhanced through turbulent wake mixing processes. This is consistent with the above argument, so that increasing the rate of mixing through turbulence leads to additional wake pressure recovery through the disc wake, and thus greater pressure drop across the actuator itself.

The above remixing argument applies equally to unbounded as well as finite outer scale blockage flows. In the case of the latter an additional streamwise pressure change occurs from far upstream to far downstream of the flow. This pressure change, Δc_{p_∞}, is readily understood and is the pressure change that results from any resistive force applied to a constrained flow. In terms of the pressure development through the flow the effect of finite outer scale blockage on single scale energy extraction can be visualised as the ability to reduce the pressure on the downstream side of the extractor so that $c_{pd,B_G \neq 0} < c_{pd,\text{Betz}}$, as well as to increase the pressure coefficient achievable on the upstream side of the extractor. Multi-scale energy extraction and the necessary flow remixing processes provide additional recovery in the wake flow so that an even lower pressure can be achieved immediately downstream of the discs $c_{pd,MS,B_G \neq 0} < c_{pd,B_G \neq 0}$ for optimum extraction.

The two processes of finite outer scale blockage leading to changes in far field pressure conditions, and flow scale remixing leading to additional wake pressure recovery, are of course interlinked, at the very least through the upstream flow deceleration which both mechanisms affect. It is, however, instructive to decompose a general multi-scale finite blockage problem into these mechanisms and visualise the potential effects of each mechanism on maximum extractable power as illustrated in figure 2.14.

2.6 Conclusions

This paper extends the two scale partial fence model of Nishino and Willden [2012a] to an n-scale energy extraction model. The extended model uses actuator disc theory to model the energy extractors, assumes scale separation between each subsequent sub-scale, and solves n quasi-inviscid problems with kinematic and dynamic coupling between each scale interface. The n-scale problem is solved by applying a Lagrange multiplier constraint based method to solve blockage constrained flows. The validity of the method is demonstrated through an analytical solution of Garrett and Cummins [2007] single scale constrained actuator disc problem. Both actuator disc theory and assumptions of scale separation are approximations to the real fluid mechanics but have been shown to be useful in understanding energy conversion from a flow. The presented analysis adds more "scales" than previous studies, but purely in terms of the fluid mechanics, makes no additional assumptions.

A simple approximate analytical expression for the maximum power coefficient as a function of the number of scales of the device is presented, $C_{P_G,\max} = 1 + (C_{P,\text{Betz}} - 1)/n$, and it is shown that the theoretical limit to power extraction for any energy extracting device in an unbounded fluid is bounded by $C_{P_G} = 1.0$, a $27/16 \sim 70\%$ increase on the Betz limit. The n-scale device is shown to approach this new true upper bound for unblocked flow energy extraction with increasing n, recalling that the upstream flow is assumed unperturbed by the device. This is physically achieved through using the intermediate scales to help to decouple the outermost device (largest) scale physics, where the area of the stream-tube is left unmodified, and the innermost disc/energy extraction (smallest) scale physics, where the static pressure drop across the disc is optimal. Taken another way, the results suggest that a single device should not have uniform resistance across its area – instead, it should introduce a near fractal distribution of resistance across its surface in order to achieve maximum power generation per area of active extractor.

Distributions of the local blockage ratios and velocity tuning factors across scales for a near optimal energy extraction device are presented, with a key result illustrating the gradual deceleration of the flow across each subsequent scale, alongside the gradual build-up of the static pressure. For optimal extraction, the flow decelerates by a factor of near 1/2 of the upstream velocity at the disc extraction plane, depending on the number of device scales. Further, for globally unblocked flow, as the number of device scales increase, the device blockage (ratio of total disc area to the flow passage area of the outermost device scale) decreases, tending to 0 as $n \to \infty$;

that is, although disc efficiency may increase with increasing n, the discs themselves must become vanishingly small (or the channel infinitely large) to achieve this. Additionally, as device blockage tends to 0 for optimal extraction at large number of device scales, there is no detrimental reduction of the mass flux through the system which could potentially reduce the extractable power. We further show that the optimal distribution of blockage to achieve optimum power extraction in unblocked flow is well approximated by a fractal multi-scale device; that is a device in which local blockage at all consecutive scales is equal.

As in the Garrett and Cummins [2007] single scale model, the addition of finite global (outer scale) blockage is shown to further increase the optimal power coefficient of a multi-scale device above 1. We provide an empirical fit to the computed optimal global power coefficient, $C_{P_{G,\max}} \approx (1/n)(1-B_G)^{-2}[C_{P,\mathrm{Betz}} + (n-1)(1-B_G)^{4/9}]$, that accounts for both the number of device scales as well as the overall global blockage, B_G. This expression is shown to be accurate for the range of practical global blockage ratios (including unblocked flow) considered herein.

Contrary to what one might intuitively think, we show that the minimisation of mixing losses is not the mechanism by which the power extraction increases with number of scales. In fact, wake mixing provides an additional source of static pressure rise in the device wake that enables additional reduction in static pressure on the downstream side of the extractor, and consequently an increase in the static pressure drop across the device, leading to increased power extraction. For the specific case of globally unblocked flow we show that at most 1/2 of the total energy removed from the flow can be usefully extracted when the device power coefficient is maximised, with the remaining 1/2 energy removed lost in wake remixing. This contrasts to the 1/3 energy that is lost in wake remixing by a single disc operating at the Betz limit in unblocked flow. We draw distinction between device efficiency, i.e. power coefficient, and overall energy extraction efficiency, i.e. basin efficiency, and observe that as the former increases the latter necessarily decreases.

For devices placed in a finite width channel, the streamwise pressure drop that must occur to balance device thrust enables a reduction in the pressure on the downstream side of the extractor, again providing the basis for increased power extraction. The two mechanisms to decrease the pressure on the downstream side of the extractor are shown to be additive so that multi-scale devices placed in bound flows can experience even higher levels of power extraction through wake remixing pressure recoveries and overall streamwise pressure drops between far-field conditions.

Both multi-scale interactions and global blockage further decelerate the flow upstream of the disc, raising the upstream static pressure and consequently increasing the extractable power. The optimal arrangement of discs changes with global blockage to account for the additional deceleration that global blockage causes, with the blockage ratios at the largest scales increasing significantly from those of the unbounded extractor.

We have demonstrated numerically, using large actuator disc simulations in a RANS framework, that by increasing the number of scales from two to three that the power delivered by the array can be increased beyond that that can be achieved for the same finite number of discs at two scales with global blockage preserved.

Realistically for wind or tidal power applications, separating the flow into more than a few scales does not appear feasible, and achieving very high levels of global blockage, perhaps maximum $B_G \sim 0.1$, unachievable without serious environmental impact. The physical space of realistic exploitation is thus confined to the bottom left quadrant of figure 2.14, but if properly designed for and managed, some plausible, yet significant, increases in power coefficient through blockage and use of scale remixing are possible.

This article provides the first theoretical construction of an arbitrary multi-scale optimal energy extraction device in a steady flow, and presents a theoretical upper bound on its energy extraction. One of the primary conclusions of the paper is that wake-mixing is responsible for sustaining low pressure on the downstream side of the actuator disc. Whilst the multi-scale array demonstrates that this may be achieved through recursive scale-to-scale wake mixing events, other configurations that encourage wake-mixing may also be useful for extracting power above the Betz limit. Innovative devices that exploit the same physical processes without the use of multi-scale mechanisms may prove a fruitful avenue for future exploration. Our limiting cases use an infinite number of scales which can never be possible in a finite universe. Whilst this is a theoretical model, we hope this work may provide the scientific basis for others to innovate.

2.7 Acknowledgements

The authors would like to acknowledge the support of funding bodies as follows; DD is funded by an EPSRC studentship, grant number EP/S023801/1, RHJW is supported by an EPSRC Advanced Fellowship EP/R007322/1 and by the EPSRC Supergen ORE Hub, grant number EP/S000747/1.

2.8 Declaration of interests

The authors report no conflict of interest.

2.A Blocked flow past a homogeneous turbine array

Although Garrett and Cummins [2007] numerically demonstrated that the Betz limit is increased by a factor $(1-B)^{-2}$ for a single or homogeneous array of turbines that present a blockage B within a confined channel, there has yet to be an analytical verification of this key result in the literature. This section provides a re-framing of the flow problem as a non-linear constrained optimisation problem, that allows both an analytical verification of the key result, and sets the context in which the multi-scale flow problem is solved.

Consider the control volume shown in figure 2.20, where the bulk flow is split by the streamtube into the fluid flowing through the turbine (or homogeneous turbine array) and the fluid bypassing the turbine. By separately applying conservation of mass, momentum and energy to the two flow regions, the following relationship between the bypass and core flows can be derived [Garrett and Cummins, 2007]

$$\gamma^2 B + 2\gamma(\beta-1) + (\beta-1)^2 - B\beta^2 = 0, \tag{2.38}$$

where the turbine power coefficient $C_P = P/(1/2\rho u_1^3 A_T)$, with P, A_T and u_1 the turbine power, swept area and undisturbed upstream velocity respectively, can be shown to be

$$C_P = (\beta+\gamma)(\beta-1)\frac{\gamma}{B}. \tag{2.39}$$

Spurious solutions are identified by considering the physical constraints:

$$0 < \gamma \leq 1, \tag{2.40}$$

$$1 \leq \beta < \infty, \tag{2.41}$$

$$0 \leq B \leq 1. \tag{2.42}$$

To analytically determine the maximum C_P, these equations are re-cast in constrained optimisation form, where we are interested in maximising equation 2.39 subject to the constraint equation 2.38. Consider, therefore, the Lagrangian

$$\mathcal{L} = (\beta+\gamma)(\beta-1)\frac{\gamma}{B} + \lambda\left[\gamma^2 B + 2\gamma(\beta-1) + (\beta-1)^2 - B\beta^2\right], \tag{2.43}$$

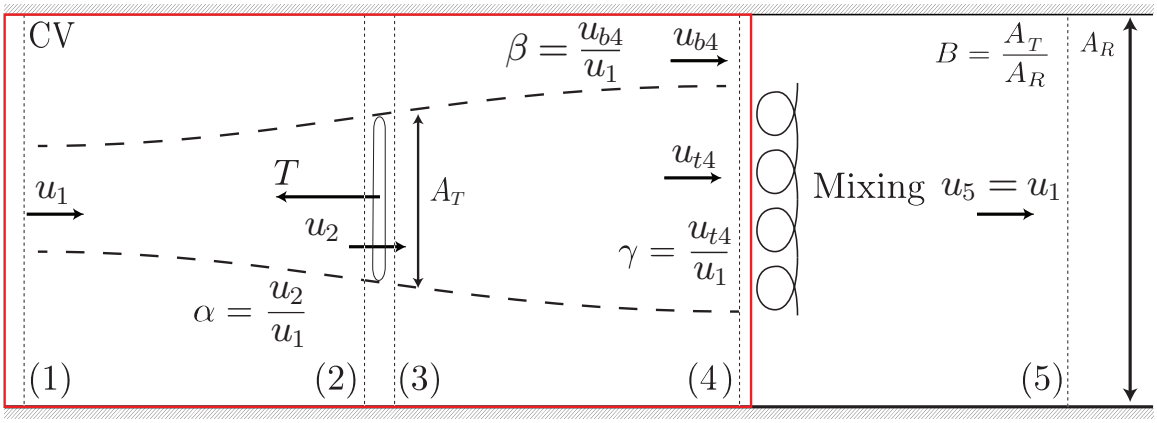

Figure 2.20: A schematic of an energy extracting actuator disc in a constrained channel Garrett and Cummins [2007]. The schematic shows the control volume taken for the quasi-one dimensional analysis, with the non-dimensional velocity factors α, β, γ, and the blockage ratio B characterising the flow problem.

for which the stationary points are identified by

$$\nabla_{\beta,\gamma,\lambda}\mathcal{L} = 0. \tag{2.44}$$

The following system of equations can then be solved for β, γ and λ as a function of the blockage B for the optimum, where the physical constraints 2.40-2.42 once again identify spurious solutions.

$$\frac{\gamma(\beta-1)+\gamma(\gamma+\beta)}{B} + \lambda(2\gamma+2\beta-2B\beta-2) = 0, \tag{2.45}$$

$$\frac{\gamma(\beta-1)+(\beta-1)(\gamma+\beta)}{B} + \lambda(2\beta+2B\gamma-2) = 0, \tag{2.46}$$

$$(\beta-1)^2 + B\gamma^2 - B\beta^2 + 2\gamma(\beta-1) = 0. \tag{2.47}$$

A trivial solution may first be found by setting λ to 0, giving $\gamma = -1$ and $\beta = 1$. The non-trivial solutions involve considerable algebraic complexity with solutions in the form of roots of quartic equations. If one considers the physical constraints (equations 2.40-2.42), however, there is only one solution to the stationary points of $\mathcal{L}$.

Re-arranging equation 2.46 for λ and substituting into equation 2.45 gives

$$\frac{\gamma(\beta-1)+\gamma(\beta+\gamma)}{B} - \frac{(2\gamma+2\beta-2B\beta-2)(\gamma(\beta-1)+(\beta-1)(\beta+\gamma))}{B(2\beta+2B\gamma-2)} = 0. \tag{2.48}$$

Multiplying through by B, multiplying out the fraction and collecting in terms of β yields

$$\beta^3(B-1)+\beta^2(2B\gamma+2-B-\gamma)+\beta(2B\gamma^2+2\gamma-2B\gamma-\gamma^2-1)+ B\gamma^3-B\gamma^2+\gamma^2-\gamma = 0, \tag{2.49}$$

which factors into a product of two terms

$$(B\gamma + \beta(B-1) + 1)(\beta^2 + \beta(\gamma - 1) + \gamma^2 - \gamma) = 0, \tag{2.50}$$

with the three roots therefore being

$$\beta_{1,2,3} = \frac{B\gamma + 1}{1 - B} \vee \frac{1-\gamma}{2} \pm \sqrt{\frac{(\gamma-1)^2}{4} + \gamma - \gamma^2}. \tag{2.51}$$

For the physically possible range of the wake induction factor, $0 < \gamma \leq 1$, the quadratic solutions for β are $0 \leq \beta_2 < 1$ and $\beta_3 \leq 0$ which can not satisfy the physical constraints of mass conservation $\beta \geq 1$. Hence, only the first non-quadratic solution for β is physical. Substituting this root into equation 2.47 simplifies to

$$\begin{aligned} &B\gamma^2 - \frac{B(-B\gamma - 1)^2}{(B-1)^2} + 2\gamma\left(\frac{-B(\gamma+1)}{B-1}\right) + \left(\frac{-B(\gamma+1)}{B-1}\right)^2 = 0, \\ &(B^2 - B)(3\gamma^2 + 2\gamma - 1) = 0, \end{aligned} \tag{2.52}$$

which trivially reduces to $\gamma = 1/3$ or -1, for which the only physical solution is $\gamma^* = 1/3$. Further substituting this into equation 2.51 for the first root, followed by substitution into equation 2.45 for λ returns the optimal solutions namely,

$$\gamma^* = \frac{1}{3},\ \beta^* = -\frac{B+3}{3(B-1)},\ \lambda^* = -\frac{2}{3B - 3B^2}, \tag{2.53}$$

which can readily be verified by back-substitution into the system of equations 2.45-2.47.

Evaluating the objective function (equation 2.39) at this point gives analytical verification that the numerical result of Garrett and Cummins [2007] is exact,

$$C_{P_{\max}} = (\beta^* + \gamma^*)(\beta^* - 1)\gamma^*/B = \frac{16}{27(B-1)^2} = C_{P_{\text{Betz}}}\frac{1}{(B-1)^2}, \tag{2.54}$$

and that a further key result, namely that $\gamma^* = 1/3$ irrespective of the blockage ratio, is likewise true.

We draw attention to the relevance of the optimal Lagrangian multiplier

$$\lambda^* = \frac{dC_P^*}{dc}, \tag{2.55}$$

where c is the constraint equation 2.38, which can be physically interpreted as the change of the optimal power coefficient with a relaxation of the constraint. For example, in the case for $B = 0$, the bypass flow ratio must be exactly $\beta = 1$ to satisfy the constraint, else the power coefficient will be infinite. The Lagrangian multiplier hence gives indication to the relative importance of the given constraint on the optimal power coefficient, which is relevant to the comparison of the optimal multipliers for the multi-scale device.

2.B Statement of authorship

The preceding chapter has been reformatted from an article published in the *Journal of Fluid Mechanics*. The inclusion of co-authors reflects the fact that the work came from active collaboration between researchers and acknowledges input into team-based research.

Publication details	
Title of paper	Fractal-like actuator disc theory for optimal energy extraction
Publication status	Published
Publication reference	D. Dehtyriov, A.M. Schnabl, C.R. Vogel, S. Draper, T.A.A. Adcock, and R.H.J. Willden. Fractal-like actuator disc theory for optimal energy extraction. *Journal of Fluid Mechanics*, 927:A40, 2021. doi: 10.1017/jfm.2021.766

Student Confirmation	
Student Name	Daniel Dehtyriov
Contribution to the paper	The model and text was primarily developed and written by DD. Sections 1 (Introduction) and 2 (Array model) were developed and written by DD with the input of co-authors. The numerical results derived from the solution to the model (Section 3) can be broadly split into the globally unblocked ($B_G = 0$) and blocked ($B_G > 0$) flow problems. Sections 3.1-3.4, detailing the globally unblocked flow problem was written by DD and the results for section 3.5 written by AMS both with the input of co-authors. Sections 4 (Discussion) and 5 (Conclusions) was a collaborative effort between all co-authors, with the writing split 80-10-10 between DD, RHJW, and TAAA. Appendix A (Analytic derivation of Garrett and Cummins [2007]) was developed and written by DD.

Student signature — 20th December 2023 (Date)

Supervisor Confirmation	
Supervisor name and title	Prof. Richard Willden
Supervisor comments	I confirm that Daniel has made a substantial contribution to the publication, and that the description above in the Statement of Authorship is accurate.

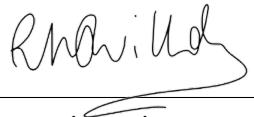

Supervisor signature — 20th December 2023 (Date)

Chapter 3

Turbulent wake mixing for power extraction above the Betz limit

> "A rock pile ceases to be a rock pile
> the moment a single man
> contemplates it, bearing within him
> the image of a cathedral."
>
> — Antoine de Saint-Exupery, The Little Prince

This chapter relaxes the inviscid assumption of the Betz model by considering the impact of turbulent mixing on the performance of a turbine. The contents of this chapter is in preparation for journal submission.

A key conclusion of the theoretical work of the preceding chapter has been to show that wake-mixing is a physical mechanism responsible for the increase in extraction efficiency. The Betz model assumes fully inviscid flow such that the velocity does not recover in the far-wake of the rotor. Even in modestly turbulent environments, typical of wind and tidal engineering flows, wake-mixing does however influence velocity recovery. We hence build on the theoretical understanding that flow mixing is the fundamental physical mechanism that allows for arrays of turbines to extract power above the Betz limit. By theoretically extending the results to a single turbine, we find that the energy extraction efficiency increases to between 0.71 and 0.81 from the Betz limit depending on the mixing boundary condition, providing a new upper bound on the efficiency for a single turbine in an unbounded flow. We then consider blocked flows and validate the new theoretical results numerically.

3.1 Paper abstract

The influence of turbulent wake mixing on the performance of a turbine for power generation is investigated theoretically and validated numerically. The turbine is modelled as an actuator disc and the wake mixing rate is controlled analytically by a mixing boundary condition and an entrainment area ratio, or numerically by the upstream turbulence intensity. Increases in the mixing rate result in an increase in extractable power at the expense of a lower overall energy extraction efficiency and higher thrust. Static pressure recovery in the turbine's core-wake results from two mechanisms: an inviscid mechanism associated with wake flow deceleration and a viscous mechanism associated with remixing of the turbine core-wake and bypass flows which necessitates a pressure rise. As compared to the classical inviscid Betz model, the viscous theoretical model better predicts two key features of turbine fluid mechanics, namely velocity recovery to the far-upstream conditions and the increased thrust coefficient for large axial induction factors in the turbulent wake state. Two limiting conditions are considered where the wake-bypass mixing commences either directly behind the disc or sequentially in the far wake after completion of the inviscid process, and analytic solutions of the disc performance for the two conditions are presented. It is found that the limit in power coefficient strongly depends on the conditions at the mixing interface, and increases from the Betz limit of 0.593 to between 0.71 and 0.81 for far and near wake mixing respectively, with the theoretical trends confirmed by Reynolds-Averaged Navier-Stokes actuator disc simulations at varying upstream turbulence intensity levels. The analytic model is extended to blocked flows in channels with an additional mechanism that increases thrust and is associated with the developed far-field streamwise pressure gradient. The physics underlying the theoretical and numerical models for actuator discs and their assumptions are discussed and contrasted to models for porous discs.

3.2 Introduction

For unconstrained flows, actuator disc momentum theory shows that the limit of energy extraction is 16/27 of the undisturbed kinetic energy flux through an energy conversion device [Betz, 1920, Lanchester, 1915, Joukowsky, 1920]. This result, widely known as the Betz limit, assumes steady, inviscid flow through an actuator disc in an unbounded domain. By relating the disc momentum theory to blade element theory, Glauert [1926] extended this theoretical analysis for an idealised energy converter

to allow for predictions of both flow field data and performance of real turbines. Relaxations in the assumptions underpinning the simplified theoretical model can provide better estimates to the limits of energy extraction and better inform the design of high efficiency turbine blades.

Dabiri [2020] demonstrated that relaxing the assumption of steady flow and streamwise actuator disc stationarity allowed for an increase in the energy conversion efficiency to a time-averaged value of 0.764 under streamwise disc motions.

Flow confinement has likewise been shown to increase the theoretical limit by relaxing the assumption that the actuator disc exists in an infinitely large domain. For a tidal turbine in a channel confined by the sea-bed and sea-surface, Garrett and Cummins [2007] showed that the power coefficient is increased by a factor of $(1-B)^{-2}$, where the global blockage ratio B is the ratio between actuator disc frontal area and the channel cross-sectional area. Nishino and Willden [2012b] further demonstrated that the beneficial effects of flow confinement may be realised by a large fence of discs, where the flow through a given disc is constrained by adjacent discs, even when the discs occupy a negligible fraction of the channel cross-section, for which the optimum power coefficient increases to 0.798. The analysis split the flow into two scales: a local scale, defined by a momentum balance across the flow passing through a single disc; and a global fence scale, defined by a momentum balance across the flow passing through the fence. Cooke et al. [2016] extended this theoretical analysis to consider further arraying these fences to include a third-scale and thereby increased the limiting value to 0.865, and Dehtyriov et al. [2021] found that the limit to the power coefficient in an unbounded flow approaches unity as the number of scales grows.

A key result of the disc array theory was to show that the physical mechanisms underlying the increase in power coefficient between a locally constrained (for example, by adjacent turbines) and globally bounded (for example, by channel boundaries) flow are fundamentally different [Dehtyriov et al., 2021]. Globally blocking the flow generates a pressure differential between far-upstream and far-downstream of the disc or fence, and additional energy is extractable from the potential energy or driving head of the fluid. This allows for power coefficients (normalised only by upstream kinetic energy flux) greater than 1. In the case of local constraints however, additional pressure-recovery due to wake-mixing on the inner scales of the extraction device allows for a lower static pressure to be maintained on the downstream side of the actuator disc, resulting in power coefficients above the Betz limit. In an unbounded

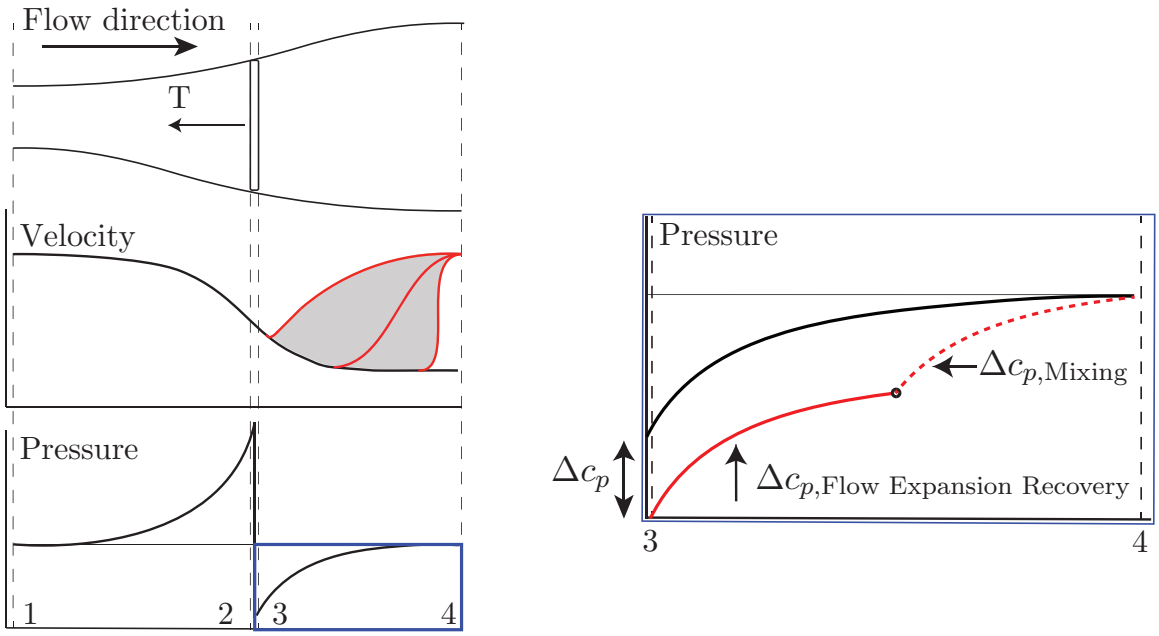

Figure 3.1: Simple schematic of flow through a rotor in an unbounded fluid, idealised as an actuator disc resisting the flow with uniform thrust T, located between stations 2 and 3. Qualitative centre-line profiles of the velocity and static pressure from far upstream (station 1) to far downstream (station 4) for an inviscid Betz model are shown in black. The red curves show schematic examples of the velocity recovery in the wake including turbulent mixing, where the location of the initial onset of the recovery in velocity depends on the turbulence conditions. Additional static pressure recovery due to mixing allows for a lower static pressure coefficient c_p on the downstream side of the extractor.

flow, the far-field streamwise pressure differential remains zero, and the power coefficient with wake-mixing enhanced pressure recovery is bounded by 1, based on kinetic flux. This is contrasted with the decrease in basin efficiency, or energy extraction efficiency, a measure of the ratio of power extracted by the turbines to the total power removed from the flow including mixing loses, due to greater wake-remixing as the power coefficient increases. Numerical studies have corroborated the theoretical performance uplift of turbine arrays at low inlet turbulence intensity levels, with only sufficient turbulence necessary to trigger the re-mixing for an increased efficiency [Nishino and Willden, 2013a].

For a single actuator disc in an infinite domain, the inviscid flow assumption underpinning the Betz limit implies no turbulent remixing between core and bypass flows. The wake pressure recovery to upstream (usually atmospheric) pressure is assumed to be entirely inviscid and governed by the deceleration of the fluid to 1/3 of the upstream speed in the far-wake. For even low turbulence intensity flows however,

mixing between the core wake and bypass fluid allows for the recovery of the velocity to upstream levels. Nishino and Willden [2013b] outlined a model for device near-wake mixing with empirical closure terms depending on the energy transfer between core and bypass flows, with numerical demonstration of the impact of near-wake mixing on performance. This wake-remixing is expected to increase the theoretical peak power coefficient of a single turbine through the same physical mechanism as postulated for turbine arrays in Dehtyriov et al. [2021], see figure 3.1.

The aforementioned actuator-disc based analyses originate with the work of Rankine [1865] and Froude [1889], which treats the disc as uniformly loaded with uniform axial inflow and implies the existence of a vortex sheet at the streamtube boundary shed from the rim of the disc [Johnson et al., 2013]. Conway [1998] extended this linearised actuator disc theory and provided an exact solution to the flow around the disc by considering the flow induced by a distribution of ring vortices, a technique first introduced by Wu [1962]. For straight lifting lines which lie in a plane, representative of the bound circulation of the blades of a turbine, the time-averaged velocity field induced by the turbine is correctly described by the actuator disc model (see Conway [1998] for details).

An alternate formulation of the problem originates with the work of Taylor [1944], which represented a porous plate by a uniform distribution of sources with source strength determined though application of Lagally's theorem. The resultant analysis predicts the same screen resistance as the Rankine-Froude theory applied by Betz [1920], however continuity through the screen is not satisfied based on the source formulation. Koo and James [1973] extended the formulation to ensure that mass and momentum were conserved across the screen and additionally modelled the rotational flow in the wake. Satisfying continuity was found to require a discontinuous variation in the radial velocity across the screen.

For the solid plate limit as the porosity of the screens approaches zero, the models under-predict the plate resistance, with the Taylor [1944] model in particular predicting zero drag in the limit. To account for this, Roshko [1955] first considered modification of drag predictions for bluff bodies through the inclusion of a base suction pressure term, which arises from the mixing between the wake and bypass flows. The analysis was extended to porous plates by Cumberbatch [1981], with both models parametrised in terms of the base pressure.

Steiros and Hultmark [2018] extended the formulation of Koo and James [1973] to explicitly determine the base suction pressure, and found agreement with experimental results for flows through screens with low porosity. The analysis first assumes a

mean radial velocity induced by a uniform distribution of sources [O'Neill, 2006], and then following Koo and James [1973], satisfies continuity across the screen through a discontinuous change in radial velocity. The base suction term, and resultant drag prediction, is then estimated through the consideration of a momentum and energy balance across the entire control volume.

The majority of porous plate literature is naturally focused on predicting drag, and the majority of actuator disc performance literature focused only on inviscid flow. A limited number of numerical studies have considered turbine performance sensitivity to inflow turbulence intensity as an analogue to the wake mixing rate, with the literature however predominantly concentrated on wake recovery and tip-vortex breakdown (see for example Ahmadi [2019], Afgan et al. [2013]). Juniper and Nishino [2023] developed a low order inviscid-viscous model for rapid predictions of turbine array performance in sheared flow, with a simplified mixing model to account for velocity recovery downstream of the turbine. Nishino and Willden [2012b] considered the effect of turbulent wake mixing on the limit of power extraction using a Reynolds-Averaged Navier-Stokes (RANS) model and found relatively large increases in actuator disc performance for both blocked and unblocked flows with increasing turbulence generated at the disc plane. Nishino and Willden [2013b] additionally varied the wake kinematic viscosity to show that near-wake mixing has an appreciable impact on extractable power.

This study is hence aimed at deriving a limit of power extraction for an actuator disc representing bound circulation of the blades of a turbine by applying linearised actuator disc theory to consider the momentum exchange between core and bypass flows in the wake and thereby coupling the viscous pressure-rise with the inviscid momentum balance by assuming streamwise separation of recovery mechanisms. Unlike the previous studies applying the actuator disc formulation, the present study is focused on the wake-remixing for power production at the largest scale which is ignored in both the inviscid and fence analyses. Numerical validation complements the theoretical model and some limitations of the one-dimensional theory are outlined. We show that elevated turbulence intensity levels can result in a large increase in extractable power across an actuator disc due to the pressure rise resulting from the wake-remixing process. Understanding this in the context of flow separation, tip-vortices and larger-scale atmospheric phenomena could help inform the design of efficient turbine blades for operation in turbulent flows.

3.3 Theoretical mixing model

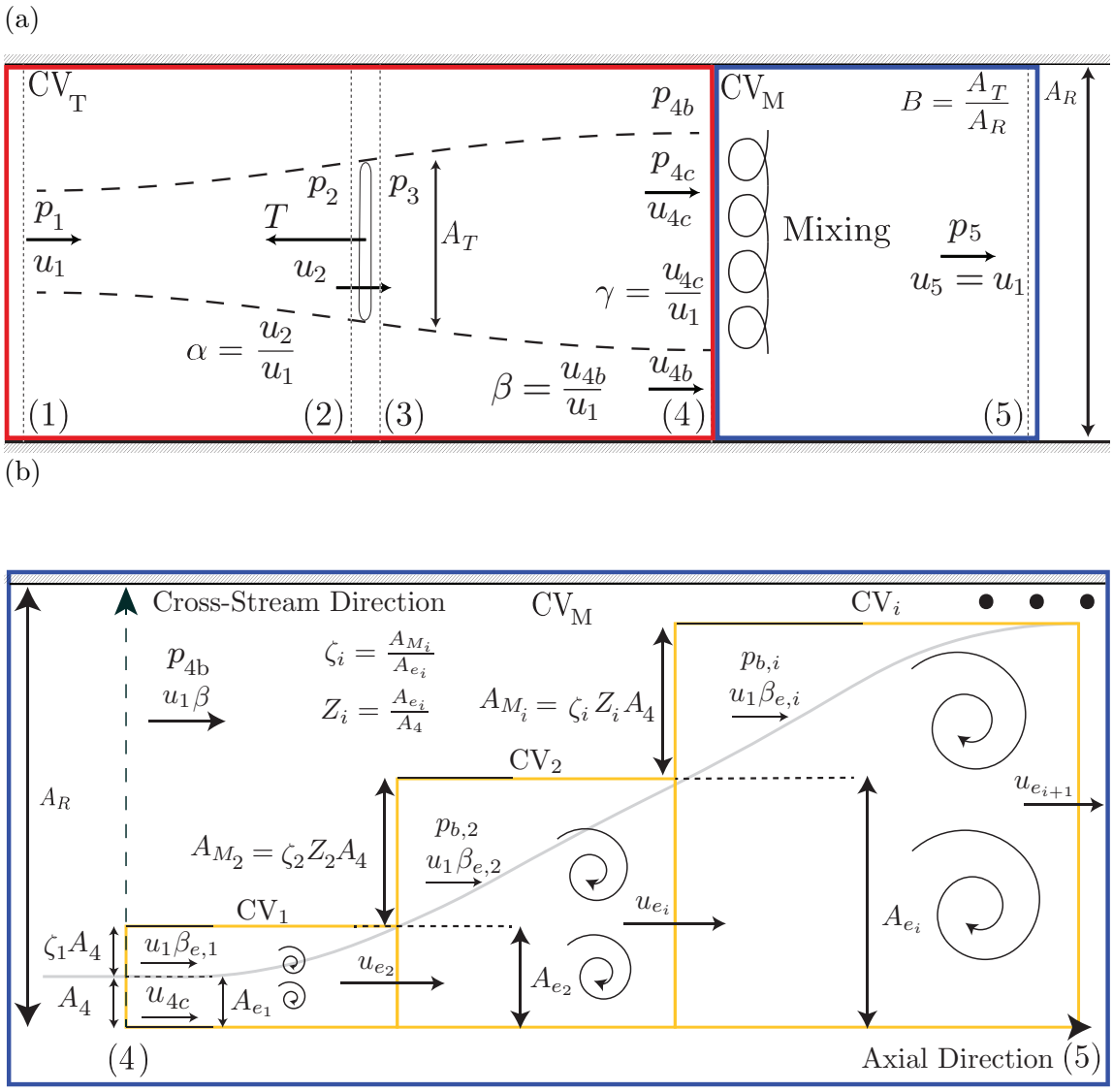

Figure 3.2: (a) Schematic of an energy extracting actuator disc in a constrained channel. The schematic shows the control volume taken for the quasi one-dimensional analysis, with the non-dimensional velocity factors α, β, γ, and the blockage ratio B characterising the flow problem. (b) Schematic of the control volumes for a simplified model of the wake mixing velocity recovery. The coordinate in the axial direction corresponds with the centerline of the core flow through the center of the actuator disc. Here, the flow is mixed sequentially over a finite axial distance instead of instantaneously, such that the exit velocity approaches the free-stream velocity as the number of mixing stages increases. The grey outline shows an illustrative wake boundary, across which local bypass flow is sequentially mixed into the core flow.

We first consider including the role of wake mixing on the extractable power across an

actuator disc by the application of linear momentum actuator disc theory (LMADT) to a constrained channel flow; see the problem schematic in figure 3.2. The disc exists between stations 2 and 3 across which the flow velocity is continuous but a discontinuous drop in pressure occurs. Far upstream of the actuator at station 1 the flow velocity and pressure are assumed constant and uniform, and downstream of the actuator the flow decelerates allowing pressure recovery at station 4 in the core flow. Turbulent mixing is then assumed to occur between the bypass and core flows such that the flow is homogeneous by station 5. We first define a number of dimensionless velocity factors: $\alpha = u_2/u_1$, representing the normalised velocity through the disc; $\gamma = u_{4c}/u_1$, representing the normalised wake-velocity (at station 4); and $\beta = u_{4b}/u_1$ representing the bulk bypass (accelerated) flow velocity (at station 4).

The model therefore aims to first provide an analytic estimate to the static pressure rise in the wake (stations 4 to 5 in figure 3.2), and then couple this to the inviscid section (stations 1 to 4 in figure 3.2) of the flow problem, to provide solutions to the disc performance limits inclusive of the wake-mixing physics.

3.3.1 Wake-mixing physics

We assume, as shown through prior application of LMADT by Dehtyriov et al. [2021], and observed in the context of porous discs by Roshko [1955] and Steiros and Hultmark [2018], that a lower static pressure on the downstream side of the disc can be sustained by a combination of wake-mixing pressure recovery and far-field axial pressure differential. We distinguish between two conditions: one where the mixing occurs in the near-wake, and one where the mixing occurs in the far-wake. For a multi-scale device in an unbounded flow ($B = 0$), where there is no far-field pressure differential, it has been shown that wake-mixing can increase the disc power coefficient, or the ratio of power removed to the upstream kinetic flux bounded by the disc area, from $C^*_{P,Betz} = 16/27$ to $C^*_P = 1$ [Dehtyriov et al., 2021]. In contrast, as wake mixing necessarily entails energy loss, the extraction efficiency $\eta = C_P/C_T$ (typically referred to as the basin efficiency in tidal flow literature), the ratio of power extracted by the actuator disc to the total power removed from the flow, decreases from 2/3 to 1/2 at the optimum C_P. The theoretical model proposed herein considers wake mixing downstream of a single disc, which is ignored in traditional actuator disc analyses, and only considered as a wake mixing pressure rise in two-scale partial fence models. Although the resulting power uplift is expected to be different, the underlying physical mechanisms, and therefore the general theoretical trends and conclusions, are expected to be similar.

The schematic in figure 3.1 shows how the viscous mixing mechanism influences the performance of the extractor. For an optimally operated unbounded disc in inviscid flow the static pressure coefficient rises to 5/9 ahead of the disc and falls to $-1/3$ immediately afterwards, with the pressure then assumed to recover to the upstream condition as the flow decelerates. A lower level of pressure downstream of the disc can however be sustained through the role of bypass flow mixing. It can be readily shown through conservation of mass and linear momentum that a static pressure rise must occur as a direct consequence of mixing two streams of incompressible fluid moving at different velocities. The wake pressure recovery mechanism is hence enhanced through velocity recovery due to mixing, which allows a lower pressure to be sustained on the downstream side of the extractor, given that the flow must ultimately recover to the upstream pressure condition for this unbounded problem. Increasing the rate of mixing, through turbulence for example, can be expected to lead to additional wake pressure recovery and thus a greater pressure drop across the actuator itself.

3.3.2 Mixing Zone

Consider first an analysis of the mixing zone represented by the set of control volumes in figure 3.2b. We represent the wake-mixing as a sequential process, where at every "stage" of the mixing process, the core flow mixes with some additional bypass flow area $\zeta_i A_{e_i}$, representing transport of mass and energy across the wake-boundary. This process continues until the final exit velocity gradually approaches the free-stream velocity u_1, fully satisfying the assumptions at the outlet boundary. Extending on the studies of Nishino and Willden [2013b] (for near-wake mixing) and Steiros and Hultmark [2018] (for far-wake mixing), we analyse this mixing zone in detail, and demonstrate how our mixing model in the far-wake limit is similar to the Steiros and Hultmark [2018] model, validated experimentally on porous discs.

Consider the first stage in the mixing process, or CV_1 in figure 3.2b, shown in detail in figure 3.3. The bypass flow is at pressure p_{4b} and velocity $u_1\beta$ ($p_{4b} = p_1$ and $\beta = 1$ in the case of an unblocked flow). The core wake-flow has reduced pressure p_{4c} and velocity u_{4c} due to the presence of the upstream actuator disc. Some flow mass of the bypass flow, bounded by $\zeta_1 A_4$, then mixes with the core flow in a viscous mixing event. It is expected that the flow drawn in from the bypass might accelerate as it is entrained resulting in a small reduction in its static pressure towards that of the core flow. If the pressure of this bypass mixing flow p_{4m} changes from the bypass flow pressure p_{4b} prior to the viscous mixing event, then the velocity of the bypass mixing stream, $u_1\beta_{e,1}$, must also change. Note that $p_{4c} \leq p_{4m} \leq p_{4b}$ such that $\beta_{e,1} \geq \beta$. The

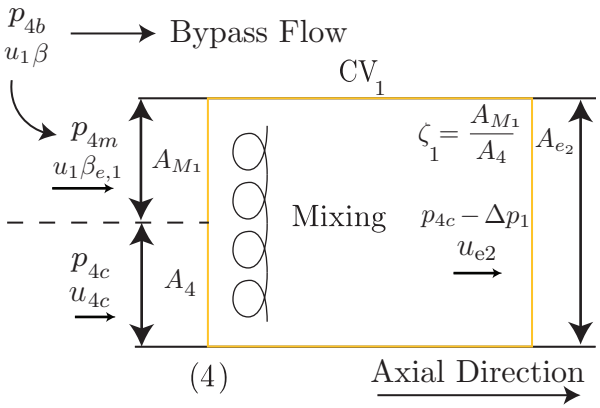

Figure 3.3: A detailed view of the first mixing control volume used to determine the axial wake pressure rise due to mixing of dissimilar velocities from core and bypass flows.

viscous mixing event then homogenises the velocity of the fluid streams to u_{e_2} with a new core wake area A_{e_2}. As will be shown, this process necessitates a rise in core pressure by $-\Delta p_1$. The exit flow conditions from this first stage then become the new core wake conditions, and undergo sequential viscous mixing events as shown in figure 3.2b. Here, ζ_i parametrises each stage by the ratio of mixing A_{M_i} to core A_{e_i} areas, and Z_i represents the cumulative volume by a ratio of core flow area to the initial wake area prior to the onset of mixing A_4. The entry conditions for the first stage are defined by the irrotational section of the flow problem $A_{e_1} = A_4$, so that $Z_1 = 1$. As the core wake velocity rises, the velocity differential between core and bypass flows decreases, and the incremental change in pressure across each stage $-\Delta p_i$ asymptotes to zero as the exit velocity $u_{e,i}$ asymptotes to u_5.

For the first stage shown in figure 3.3, by conservation of mass, the exit velocity due to viscous mixing is given by

$$\zeta_1 A_4 \beta_{e,1} u_1 + A_4 \gamma u_1 = u_{e,2} A_4 (\zeta_1 + 1), \tag{3.1}$$

$$u_{e,2} = \frac{u_1(\zeta_1 \beta_{e,1} + \gamma)}{\zeta_1 + 1}, \tag{3.2}$$

where $\zeta_1 = A_{M_1}/A_4$ is defined as the area ratio between the mixing bypass and core flows and $\beta_{e,1}$ represents the velocity of the bypass flow bounded by the mixing area A_{M_1} just prior to the onset of viscous mixing. Applying conservation of linear momentum in the axial direction to the flow through the control volume then allows for an expression for the static pressure drop

$$A_4 p_{4c} + \zeta_1 A_4 p_{4m} - A_4(\zeta_1 + 1)(p_{4c} - \Delta p_1) \\ = A_4(\zeta_1 + 1)\rho u_{e,2}^2 - \left(\rho A_4 \gamma^2 u_1^2 + \rho \zeta_1 A_4 \beta_{e,1}^2 u_1^2\right),$$

$$p_{4c} + \zeta_1 p_{4m} - (\zeta_1 + 1)(p_{4c} - \Delta p_1) = \frac{\rho u_1^2(\zeta_1 \beta_{e,1} + \gamma)^2}{\zeta_1 + 1} - \rho u_1^2(\gamma^2 + \zeta_1 \beta_{e,1}^2), \qquad (3.3)$$

where we have assumed that the boundaries of the control volume are shear-stress free. Equation 3.3 couples the pressure change in the mixing zone to the flow physics in the upstream core flow model through the wake velocity γ. We now consider two limiting mixing conditions on the bypass mixing pressure p_{4m}, physically representative of near-wake and far-wake mixing. The near-wake mixing limit assumes strong mixing just downstream of the actuator disc, where the bypass flow mixes with pressure $p_{4m} = p_{4b}$, and the far-wake mixing limit assumes mixing after pressure equalisation between core and bypass flows, where the bypass flow mixes with pressure $p_{4m} = p_{4c}$. As will be demonstrated, the far-wake mixing condition, is bounded by the Betz [1920] or Garrett and Cummins [2007] limits as the lower bound, and the mixing assumptions of the Steiros and Hultmark [2018] model as the upper bound. The near-wake mixing physics, on the other hand, is bounded from below by the mixing assumptions of the Steiros and Hultmark [2018] model, and the upper limit is comparable to theoretical limits for turbine arrays [Nishino and Willden, 2012b, 2013b], where the mixing occurs at the inner scale, and the upper bound is therefore expected to be similar to that of two-scale fence limits.

3.3.2.1 Near-wake mixing

First, we consider a near-wake mixing condition where the mixing process occurs directly behind the actuator disc, for which in the limiting case the static pressure in the bypass flow has not equilibrated with the core flow pressure $p_{4m} = p_{4b} \neq p_{4c}$ prior to the viscous mixing event. It can be shown that in general, the bypass pressure is given by

$$p_{4b} = (p_5 + TB/A_T) + \frac{1}{2}\rho u_1^2(1 - \beta^2), \qquad (3.4)$$

where the first term on the right side is derived from a static force balance from stations 1 to 5, $(p_1 - p_5) = TB/A_T$, and the second term by assuming the total pressure is constant in the bypass prior to the mixing event $(p_{4b} - p_1) = 1/2\rho u_1^2(1-\beta^2)$.

For an unbounded flow, equation 3.4 reduces to $p_{4b} = p_5 = p_1$. Combining equations 3.3 and 3.4 solves for the pressure rise across the first viscous mixing stage

$$(\Delta p_1)_{\mathrm{NW}} = \frac{\rho u_1^2(\zeta_1\beta_{e,1} + \gamma)^2}{\zeta_1 + 1} - \rho u_1^2\left(\gamma^2 + \zeta_1\beta_{e,1}^2\right) - \zeta_1\left(\frac{TB}{A_T} + \frac{1}{2}\rho u_1^2(1-\beta^2)\right), \quad (3.5)$$

where we have assumed that $(p_{4c} - p_5) = \sum_i \Delta p_i \approx \Delta p_1$ as a first estimate. This estimate is exact for $\zeta_1 \to \infty$, but otherwise needs to be iteratively refined for a complete solution, see section 3.3.2.3 for details. Note that $\beta_{e,1} = \beta = 1$ and $B = 0$ for an unbounded flow, for which the pressure rise in the mixing zone is fully parametrised by the velocity factors α, β, γ and the mixing area ratio ζ_1. The impact of near-wake mixing for a single actuator disc was first discussed in Nishino and Willden [2013b] in the context of turbine arrays.

3.3.2.2 Far-wake mixing

Next, we consider a far-wake mixing limit, where the mixing process occurs far downstream of the actuator disc for which the core and bypass pressures are equalised at the mixing interface ($p_{4m} = p_{4c}$; this is the normal LMADT assumption, illustrated in figure 3.2a). It is important here to recognise the limitations of the quasi one-dimensional assumption of LMADT. Algebraically, mixing in the far-wake necessitates a variation in static pressure across the mixing zone (equation 3.3). Outside of the mixing zone and in the freestream however (the area not bounded by A_M, in the cross-stream direction), there is no mixing and consequently no change in the static pressure. The pressure equality condition $p_{4m} = p_{4c}$ therefore holds for the region of fluid subject to mixing, with the bypass pressure outside of this zone equal to the bulk bypass flow pressure p_{4b}. As we will show, the limiting condition on the disc power coefficient for far-wake mixing occurs for $\zeta_i \to 0$, representing thin regions of bypass flow that are sequentially mixed into the wake. In these cases, for the static pressure in this bypass mixing flow region to equalise with the lower than freestream core wake pressure, there must necessarily be an increase in local flow velocity (in the region bounded by A_M) to conserve energy

$$\beta_{e,1}^2 = \frac{(p_{4b} - p_{4c})}{\frac{1}{2}\rho u_1^2} + \beta^2, \quad (3.6)$$

where $\beta_{e,1} \geq \beta$. In the case of far-wake mixing, this localised region of fluid therefore accelerates from the bypass freestream to match the core wake pressure prior to the viscous mixing event. We note that changes to the disc performance are still observed under the simplification that $\beta_{e,i} = \beta$, reducing to the Steiros and Hultmark [2018]

model (see section 3.5). Nonetheless, we include the effect of local bypass acceleration for completeness, and we note that it is observed in the numerical results (see section 3.6).

For far-wake mixing therefore ($p_{4m} = p_{4c}$), equation 3.3 reduces to equation 3.7

$$(\Delta p_1)_{\mathrm{FW}} = \frac{\rho u_1^2 \left(\zeta_1 \beta_{e,1} + \gamma\right)^2}{(\zeta_1 + 1)^2} - \frac{\rho u_1^2 \left(\gamma^2 + \zeta_1 \beta_{e,1}^2\right)}{\zeta_1 + 1}, \tag{3.7}$$

where, equation 3.6 can be solved alongside equation 3.7 to show that for the first mixing stage

$$\beta_{e,1} = \frac{(\zeta_1 + 1)\sqrt{2\gamma^2\zeta_1 + \zeta_1^2\beta^2 + \beta^2} - 2\gamma\zeta_1}{\zeta_1^2 + 1}, \tag{3.8}$$

that is that both the static pressure recovery and local bypass acceleration $\beta_{e,1}$, are fully parametrised by the mixing area ratio ζ_1, and axial velocity factors γ and β.

So far, we have only considered the first mixing event, where by conservation of mass (equation 3.2) the flow velocity recovers to $u_{e,2} < u_1$ due to viscous mixing for finite ζ_1. Noting that the exit conditions of the first mixing stage correspond to the core flow entry conditions of the second stage (figure 3.2b), we can recursively apply conservation of mass and momentum to show that the static pressure drop $p_4 - p_5$ can be determined by the recursive relationships:

$$Z_{i+1} = Z_i(1 + \zeta_i), \tag{3.9}$$

$$u_{e,i+1} = \frac{Z_i}{Z_{i+1}} \left(u_{e,i} + u_1 \beta_{e,i} \zeta_i\right), \tag{3.10}$$

$$\text{Far wake mixing: } \Delta p_i = \rho u_{e,i+1}^2 - \frac{\rho}{1 + \zeta_i} \left(u_{e,i}^2 + u_1^2 \beta_{e,i}^2 \zeta_i\right), \tag{3.11}$$

$$\text{Near wake mixing: } \Delta p_i = (1 + \zeta_i) \left[\rho u_{e,i+1}^2 - \frac{\rho}{1 + \zeta_i} \left(u_{e,i}^2 + u_1^2 \beta_{e,i}^2 \zeta_i\right)\right], \tag{3.12}$$

where $u_{e,1} = \gamma u_1$ and Z_i represents the cumulative mixing volume with $Z_1 = A_{e1}/A_4 = 1$ and where we have again assumed that the boundaries of the control volume are shear-stress free. Following from equation 3.8, for the total pressure to remain constant in the local bypass flow

$$\beta_{e,i}^2 = \frac{p_{4b} - p_{b,i}}{\frac{1}{2}\rho u_1^2} + \beta^2, \tag{3.13}$$

where $p_{b,i}$ is the bypass static pressure of the thin layer of fluid to be mixed with the core flow across the i^{th} mixing stage, and $p_{b,1} = p_{4c}$ across the first mixing stage.

We again highlight the difference between the bulk flow bypass velocity factor β and the local bypass mixing flow acceleration $\beta_{e,i}$ in the context of figures 3.2 and 3.3. At each sequential mixing stage, a small region (bounded by ζ_i) of the bulk bypass flow with velocity β, accelerates slightly to match the core wake pressure (in the case of far-wake mixing only) prior to the mixing event. As an example, the condition $\zeta_i \to 0$ therefore represents the continuous mixing of thin layers of fluid, resulting in the core static pressure continuously rising until the far-wake boundary condition $u_5 = u_1$ and $p_{4c} = p_5$ is satisfied.

3.3.2.3 Sequential mixing control-volume solutions

If we assume that viscous mixing is responsible for all of the velocity recovery in the wake, equations 3.9-3.12 can be iterated until $u_{e,i+1} \sim u_1$, and the mixing base suction pressure $(p_4 - p_5)$ is then simply the sum of all of the partial static pressure drops in each stage i.e. $(p_4 - p_5) = \sum_i \Delta p_i$, with the model parametrised in terms of the mixing area ratio at each stage ζ_i and the bypass static pressure at each stage $p_{b,i}$. The recursive expressions require an initial guess for the mixing base suction pressure term which can then be iteratively updated until convergence.

We note that the cumulative mixing area ratio Z in finite width channel flow is limited by the geometry of the problem such that (in two dimensions) $A_{e,i} \leq A_R$ or that $Z_{\max} = \gamma/(B\alpha)$ and hence for any $Z_i > Z_{\max}$ the problem is ill defined and no longer conserves mass.

These solutions to the static pressure change in the wake depend on the bulk bypass flow velocity β, and the core wake velocity γ, representing the velocity differential prior to mixing. Coupling the physics of the mixing zone to that of the actuator disc, which determine β and γ, therefore closes the flow problem and is the subject of the following section.

3.3.3 Unblocked flow model

We now turn our attention to the irrotational section of the flow problem, spanning from far upstream to the start of the remixing process, and represented by the control volume in figure 3.2a. We first consider the case of zero global blockage ($B = 0$), for which the optimal disc power coefficient for the traditional Betz [1920] analysis is $C_P^* = 16/27$. By conservation of linear momentum

$$T = p_1 A_R - (p_1(A_R - A_4) + p_4 A_4) + \rho A_1 u_1^2 - \rho A_4 u_4^2, \tag{3.14}$$

$$T = (p_1 - p_4)\frac{\alpha}{\gamma} A_T + \rho u_1^2 A_T \alpha(1 - \gamma), \tag{3.15}$$

and by conservation of energy through application of Bernoulli's equation between stations 1-2 and 3-4

$$T = A_T(p_2 - p_3) = A_T(p_1 - p_4) - \frac{1}{2}\rho u_1^2 A_T(\gamma^2 - 1), \tag{3.16}$$

$$T = A_T(p_5 - p_4) - \frac{1}{2}\rho u_1^2 A_T(\gamma^2 - 1), \tag{3.17}$$

where we have used that $p_1 = p_5$ for unblocked flow and assumed that the radial velocity is continuous across the disc plane (see section 3.5 for details). The mixing base suction term $(p_5 - p_4)$, not considered in the traditional actuator disc analyses, is now assumed to be non-zero due to the viscous wake mixing. We first define the performance of the actuator disc in terms of thrust and power coefficients

$$C_T = \frac{T}{\frac{1}{2}\rho u_1^2 A_T}, \tag{3.18}$$

$$C_P = \frac{T u_1 \alpha}{\frac{1}{2}\rho u_1^3 A_T}. \tag{3.19}$$

Equating thrust given by equations 3.15 & 3.17 for the relationship between α and γ, followed by substitution into equations 3.18 & 3.19, solves for the disc performance in terms of γ and Δp. For the first mixing stage only, and substituting Δp for the two mixing conditions governed by equations 3.5 and 3.7, these then reduce to

$$\text{Near-wake mixing: } C_T = (\gamma - 1)(\gamma - 3) - \frac{2(\gamma - 1)^2}{\zeta + 1}, \tag{3.20}$$

$$C_P = \frac{\gamma(1 - \gamma)(\gamma + 3\zeta - \gamma\zeta + 1)^2}{2(\gamma + \zeta)(\zeta + 1)}, \tag{3.21}$$

$$\text{Far-wake mixing: } C_T = \beta_{e,1}^2 - \gamma^2, \tag{3.22}$$

$$C_P = \frac{\gamma\left(\gamma^2 - \beta_{e,1}^2\right)^2}{\beta_{e,1}^2 - 2\gamma^2 + 2\gamma - 1}, \tag{3.23}$$

where $\beta_{e,1}$ is given by equation 3.8 and that for $\zeta = 0$ (no mixing, and equivalent to $\beta_{e,1} = 1$), the model returns to the lower bound of Betz [1920]. We again stress here that the bypass flow acceleration from β to $\beta_{e,1}$ is not the mechanism by which the disc performance coefficients are modified. Even under a lower bound approximation of $\beta = \beta_{e,1}$, wake mixing still induces a static pressure rise as a necessary consequence of mixing two streams of fluid with different velocities (see section 3.5 for details).

In the case of near-wake mixing, it can readily be shown that C_P is maximised for a single mixing event, see $\zeta_1 \to \infty$, for which $u_{e,2} \to u_1$. The limiting case for far-wake mixing is however realised for recursive mixing where $\zeta_i \to 0$, representative of continuous mixing of thin regions of fluid across sequentially updated pressures

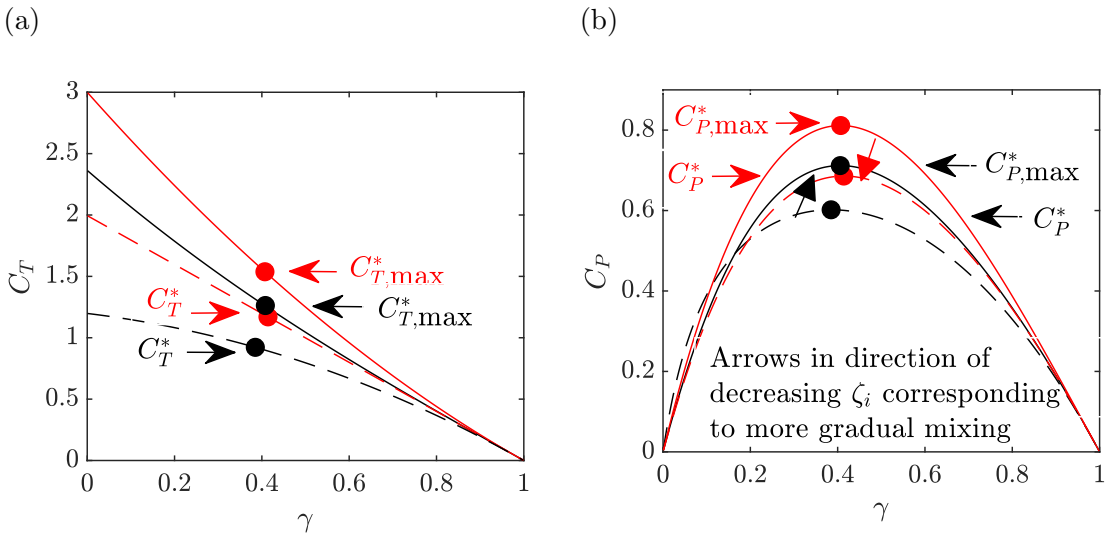

Figure 3.4: Example solutions to the recursive mixing model. The red curves are for near-wake and black curves for far-wake mixing conditions. The solid lines represent the performance limits for near and far-wake mixing, realised for $\zeta_i \to \infty$ and $\zeta_i \to 0$ respectively. Dashed lines show near lower-bound solutions at $\zeta_i Z_i = 0.01$ for near-wake mixing, and $\zeta_i Z_i = 10$ for far-wake mixing. The marked circles indicate C^*_P and C^*_T, i.e. the operating condition for peak power for a given ζ_i, with $C^*_{P,\max}$ and $C^*_{T,\max}$ representing the upper bounds for the near and far wake mixing models.

until $u_5 \to u_1$. We validate this case against the solution of Steiros and Hultmark [2018] (see sections 3.4-3.5). For these limiting mixing conditions, the limits of disc performance reduce to

$$\text{Near-wake mixing: } C_{T,\max} = (\gamma - 1)(\gamma - 3), \tag{3.24}$$

$$C_{P,\max} = \frac{\gamma}{2}(\gamma - 3)^2(1 - \gamma), \tag{3.25}$$

for which $C^*_{P,max} \approx 0.81$ for $\gamma \approx 0.41$ at which $C^*_{T,max} \approx 1.54$, and by curve fit to

$$\text{Far-wake mixing: } C_{T,\max} = \frac{9.06(1 - \gamma)}{\gamma + 3.84}, \tag{3.26}$$

$$C_{P,\max} = \frac{3.83\gamma(1 - \gamma)}{0.899 + \gamma}, \tag{3.27}$$

for which $C^*_{P,max} \approx 0.71$ for $\gamma = 0.41$ at which $C^*_{T,max} \approx 1.26$, where as illustrated in figure 3.4, the * superscript refers to the peak power condition for a fixed ζ_i and "max" subscript refers to the performance curves for which ζ_i achieves optimal power. The near-wake mixing model and upper limit can alternatively be written in terms of α where it can readily be shown that $\alpha = \gamma(3 - \gamma)/2$.

3.3.4 Blocked channel flow model

Next, consider conservation of mass for the control volume in figure 3.2 with finite blockage, where we can show that [Garrett and Cummins, 2007]

$$\alpha = \frac{\gamma}{B(\beta - \gamma)}(\beta - 1), \tag{3.28}$$

and from conservation of momentum that

$$T = A_R(p_1 - p_{4b}) + A_T\frac{\alpha}{\gamma}(p_{4b} - p_{4c}) - \rho A_R u_1^2 B\alpha(\gamma - 1) - \rho A_R u_1^2(1 - B\alpha)(\beta - 1). \tag{3.29}$$

The static pressure difference $(p_{4b} - p_{4c})$ is given by

$$(p_{4b} - p_{4c}) = (p_1 - p_5) - (p_1 - p_{4b}) + (p_5 - p_{4c}), \tag{3.30}$$

where by statics, the first static pressure difference term on the right hand side is $(p_1 - p_5) = TB/A_T$. By applying Bernoulli's theorem the second static pressure term in terms of velocity factors is $(p_1 - p_{4b}) = \frac{1}{2}\rho u_1^2(\beta^2 - 1)$. The final mixing base suction term $(p_5 - p_{4c})$, which is typically not considered in the inviscid analysis, can be estimated for the first mixing stage by equations 3.5 and 3.7 for the near and far-wake mixing cases respectively. Note that both $(p_1 - p_5)$ and $(p_5 - p_{4c})$ are functions of the disc thrust T, which can then be factored out in equation 3.29 for an explicit expression for T.

By conservation of energy we can likewise show that

$$T = A_T(p_2 - p_3) = A_T\left((p_2 - p_1) + (p_{4c} - p_3) + (p_5 - p_{4c}) + (p_1 - p_5)\right), \tag{3.31}$$

where $(p_2 - p_1) + (p_{4c} - p_3) = 1/2\rho u_1^2(1 - \gamma^2)$ by total pressure conservation upstream and downstream of the disc as before.

We present example algebraic solutions for the first mixing event of a blocked flow to demonstrate that the solutions are entirely parametrised by the blockage ratio B, representing the geometric constraint, a single velocity factor (α or γ), representing variations in the disc thrust, and the mixing area ratio ζ_1, representing the mixing physics. The example thrust and power coefficient solutions for the two mixing cases as a function of blockage ratio B and first stage area mixing ratio ζ_1 give

$$\text{Near-wake mixing: } C_T = \frac{(\beta^2 + 1)\zeta_1^2 - (\beta^2 - 4\beta\gamma + \gamma^2 + 2)\zeta + \gamma^2 - 1}{(\zeta_1 + 1)(B\zeta + B - 1)}, \tag{3.32}$$

$$C_P = \frac{\gamma(\beta - 1)}{B(\beta - \gamma)}C_T, \tag{3.33}$$

subject to the constraint

$$\beta^2(B\zeta_1+1)+2\beta B(\gamma+\zeta_1+1)+\gamma(B\gamma\zeta_1+2)+\zeta_1+1 \\ =\beta^2(B+\zeta_1)+2\beta(B\gamma\zeta_1+\gamma+1)+B\gamma(\gamma+2\zeta_1+2), \quad (3.34)$$

and

$$\text{Far-wake mixing: } C_T=\frac{2\beta_{e,1}^2\zeta_1-4\beta_{e,1}\gamma\zeta_1-\gamma^2\zeta_1^2-\gamma^2+\zeta_1^2+2\zeta_1+1}{(1-B)(\zeta_1+1)^2} \quad (3.35)$$

$$C_P=\frac{\gamma(\beta-1)}{B(\beta-\gamma)}C_T, \quad (3.36)$$

subject to the constraint

$$B(\gamma-1)(2\beta_{e,1}^2\zeta_1-4\beta_{e,1}\gamma\zeta_1-\gamma^2\zeta_1^2-\gamma^2+\zeta_1^2+2\zeta_1+1) \\ =(B-1)(\beta-1)(2\beta_{e,1}^2\zeta_1+\beta\gamma\zeta_1^2+2\beta\gamma\zeta_1-4\beta_{e,1}\gamma\zeta_1+\beta\gamma-\beta\zeta_1^2 \\ -2\beta\zeta_1-\beta-2\gamma^2\zeta_1^2-2\gamma^2\zeta_1-2\gamma^2+\gamma\zeta_1^2+2\gamma\zeta_1+\gamma+\zeta_1^2+2\zeta_1+1). \quad (3.37)$$

The constraints are derived from energy and momentum thrust equivalence (equations 3.29 & 3.31), where we note that every term (including the pressure terms) include a factor of $\rho u_1^2 A_T$ which then cancels. The same factor cancels with the denominator of both the thrust and power coefficients. Finally, mass conservation (equation 3.28) can be used to write α in terms of γ, β and B, deriving equations 3.32 - 3.37. We reiterate the key features of the far-wake mixing condition, in particular the distinction between $\beta_{e,1}$ and β for a blocked flow. The bulk flow in the bypass must accelerate by the factor β in the case of a non-zero blockage (see figure 3.2). The static pressure in the far wake and bypass must consequently be less than the upstream static pressure. We have shown that a static pressure rise is a necessary consequence of mixing, however this pressure rise only occurs in the wake mixing zone (here defined by the area bounded by ζ_i), where we have assumed (for the far-wake mixing case) that the pressure has equilibriated between core and local bypass flows prior to mixing. Some local fluid in the bulk bypass flow must hence accelerate to $\beta_{e,1}$ to match the core pressure just prior to the mixing event (see figure 3.3). With each sequential mixing stage, the core pressure and core flow velocity rise as a consequence of the mixing, and the layer of fluid which locally accelerates to mix in from the bulk bypass flow into the core flow gradually accelerates less such that $\beta_{e,1} \geq \beta_{e,i} \geq \beta_{e,i+1}$, until the wake boundary condition at station 5 is matched i.e. $u_5 = u_1$, for which $\beta_{e,\infty} = \beta$.

The expressions 3.34-3.35 can then be solved numerically for a given B and ζ_1 for estimates to the thrust and power coefficients for the first mixing stage only, where

we note that the expressions approach the derived zero global blockage curves for small B.

Solutions to the complete sequential flow problem requires iterating the recursive equations 3.9-3.12 for the mixing base suction as described in section 3.3.2.3. Analogous to the unblocked solution, and for near-wake mixing, the performance of the disc increases monotonically with the mixing ratio ζ_i (see section 3.4). The peak power condition is therefore realised for $Z_{\max} = \gamma/(B\alpha) - 1$. An iterative scheme can hence be applied to solve the flow problem, where ζ is first guessed and updated until convergence to $Z_{\max}$ as the solution for the flow velocity factors is improved.

For full recovery to the upstream flow conditions for the far-wake mixing condition, the case of infinitesimal incremental mixing, $\zeta_i \to 0$ similarly represents the peak performance for continuous mixing to achieve pressure equilibrium and $u_5 = u_1$. An iterative scheme is again required to solve the flow problem. First, for a given blockage ratio B, and for each $0 < \gamma < 1$, a guess for the mixing base suction term $(p_5 - p_{4c})$ is made based on equations 3.5 & 3.7. Then, the momentum and energy equivalence constraint (equations 3.29-3.31) can be solved for the bulk bypass flow speed β. The resultant thrust (equation 3.31) can be substituted into equation 3.30 for the difference in static pressure between core and bypass flows, and this then substituted into equation 3.13 for the local flow acceleration $\beta_{e,1}$. The recursive mixing model (equations 3.9-3.13) can then be used to update the pressure drop until β and $(p_5 - p_{4c})$ converge. The converged values may then be substituted into equations 3.28 & 3.31 for the axial velocity factor α and disc thrust T, followed by substitution into equations 3.18-3.19 for the peak performance coefficients C_T^* , C_P^*.

The solutions to the algebraic mixing model for the two limiting mixing cases are the subject of the following section.

3.4 Analytic Results

3.4.1 Performance in an infinitely wide channel

We first turn our attention to the role of the mixing ratio ζ on actuator disc performance. The resultant power, thrust and extraction (basin) efficiency parametrised in terms of the mixing ratio $\zeta_i Z_i = A_{M_i}/A_4$, which we here take to be constant across all mixing stages, are presented in figure 3.5. Note that the same conclusions can be drawn for constant ζ_i, however this grows the cumulative mixing volume exponentially (see equation 3.9). For $\zeta = 0$ (no viscous mixing and no velocity recovery), and regardless of the static pressure condition, the models return to Betz [1920]. With

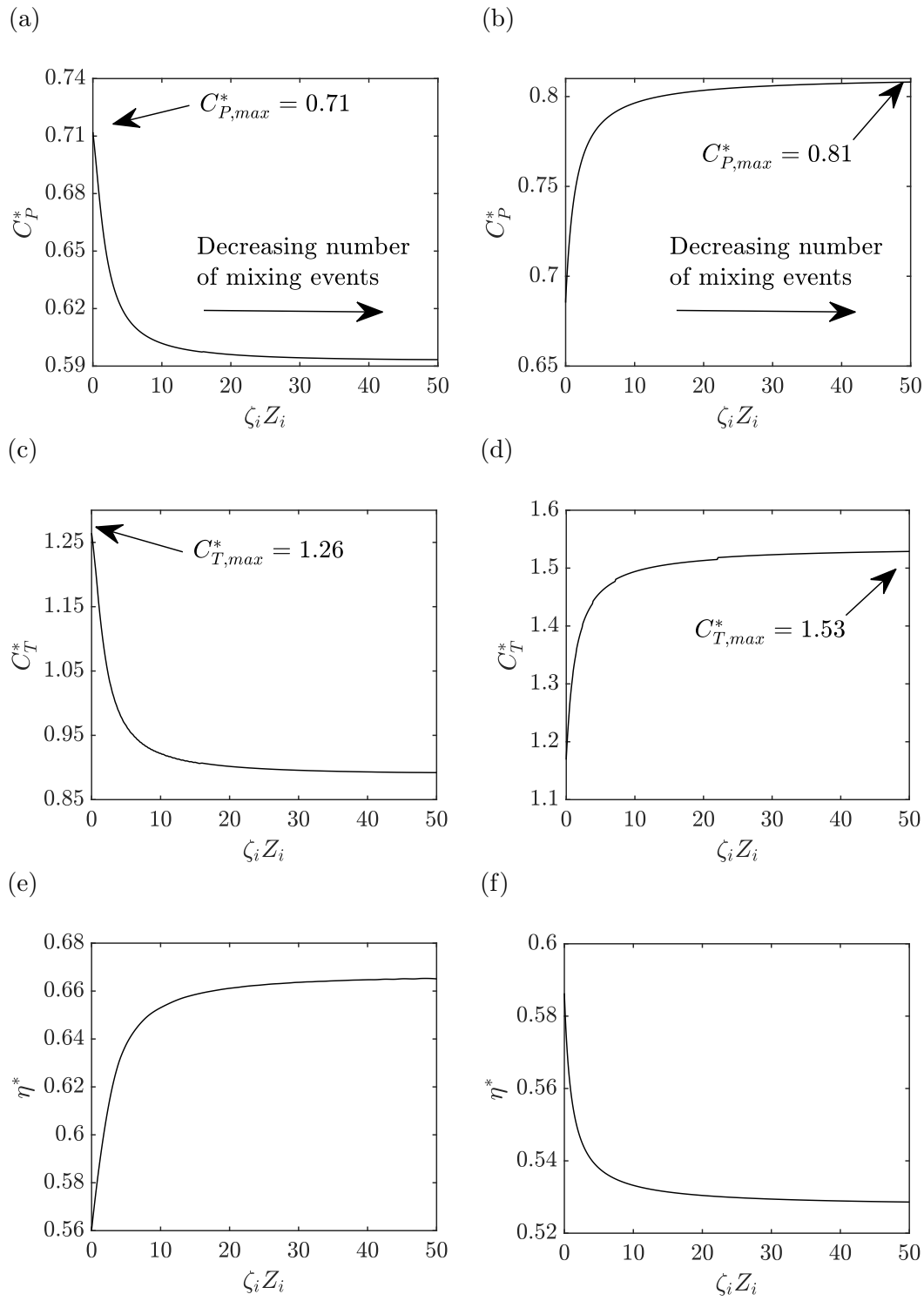

Figure 3.5: Peak power (top), and corresponding thrust (middle) and extraction (basin) efficiency (bottom) curves as a function of the mixing area ratio $\zeta_i Z_i = A_{m_i}/A_4$, taken to be constant across all mixing stages, for the far (left) and near (right) wake mixing models. Increasing $\zeta_i Z_i$ corresponds to a decreasing number of mixing events (or control volumes) to obtain a fully mixed wake condition.

increasing $\zeta_i Z_i$, the rate at which the wake velocity asymptotes to the exit boundary condition falls, in terms of the number of mixing events required in the model to achieve a fully mixed wake (see figure 3.2b).

In the case of the far-wake mixing condition, and for $\zeta_i \to \infty$, representing a single instantaneous mixing event, the performance coefficients again return to Betz [1920], and are consistent with the assumptions of the Garrett and Cummins [2007] model. As $\zeta_i Z_i$ falls, both power and thrust coefficient rise, with a maximum in the limit as $\zeta_i \to 0$ (but is not equal to zero), representing sequential mixing of infinitesimally thin layers of fluid into the wake so that the exit velocity is equal to the upstream flow speed. The sequential mixing events always occur across a constant pressure boundary, which is updated at every mixing stage. In this case, the performance is approximated by equations 3.26-3.27, with peak power coefficient $C^*_{P,\max} = 0.71$.

By contrast, for the near-wake mixing condition, thrust and power coefficients continue to rise as $\zeta_i \to \infty$, which represents rapid mixing in the near-wake, and with peak power comparable to that of two-scale arrays [Nishino and Willden, 2012b]. In this limit, the disc performance is given by equations 3.24-3.25, with peak power coefficient $C^*_{P,\max} = 0.81$. The limiting condition $\zeta_i \to 0$ converges to $C^*_P = 0.68$, which is also the far-wake upper bound under the assumption that for the far-wake model the bypass flow does not accelerate prior to the mixing events i.e. $\beta_{e,i} = \beta$. The near and far-wake models hence converge for gradual mixing, with the small difference attributable to the additional bypass acceleration required for mixing which begins in the far-wake. This can be understood for an unblocked flow by considering a single mixing stage (figure 3.3), for which the first order term of the Maclaurin series expansion of mixing base suction equations 3.5 & 3.7 about ζ_1 are identical ($\Delta p = -\rho u_1^2(\gamma - 1)^2\zeta_1 + O(\zeta_1^2)$) when setting $\beta_{e,1} = \beta = 1$. Therefore, for mixing events with very small ζ, the mixing base suction depends only on the velocity difference between core and bypass streams, and not the pressure boundary condition. This result is discussed with comparison to the literature in section 3.5.

Analogous to turbine-fence physics, any increase in power coefficient at the peak power point (again denoted by the * superscript) leads to a decrease in extraction (basin) efficiency as more energy is lost to the mixing process. With the underlying physics the same, the minimum extraction efficiency is here comparable to the optimal two-scale fence model [Nishino and Willden, 2012b].

Solutions to the theoretical model are plotted and compared to the Betz [1920] model in figure 3.6. We compare the non-zero ζ lower bound of the mixing model (far-wake mixing with $\zeta_i Z_i \to \infty$) to the recursively mixed near and far-wake upper

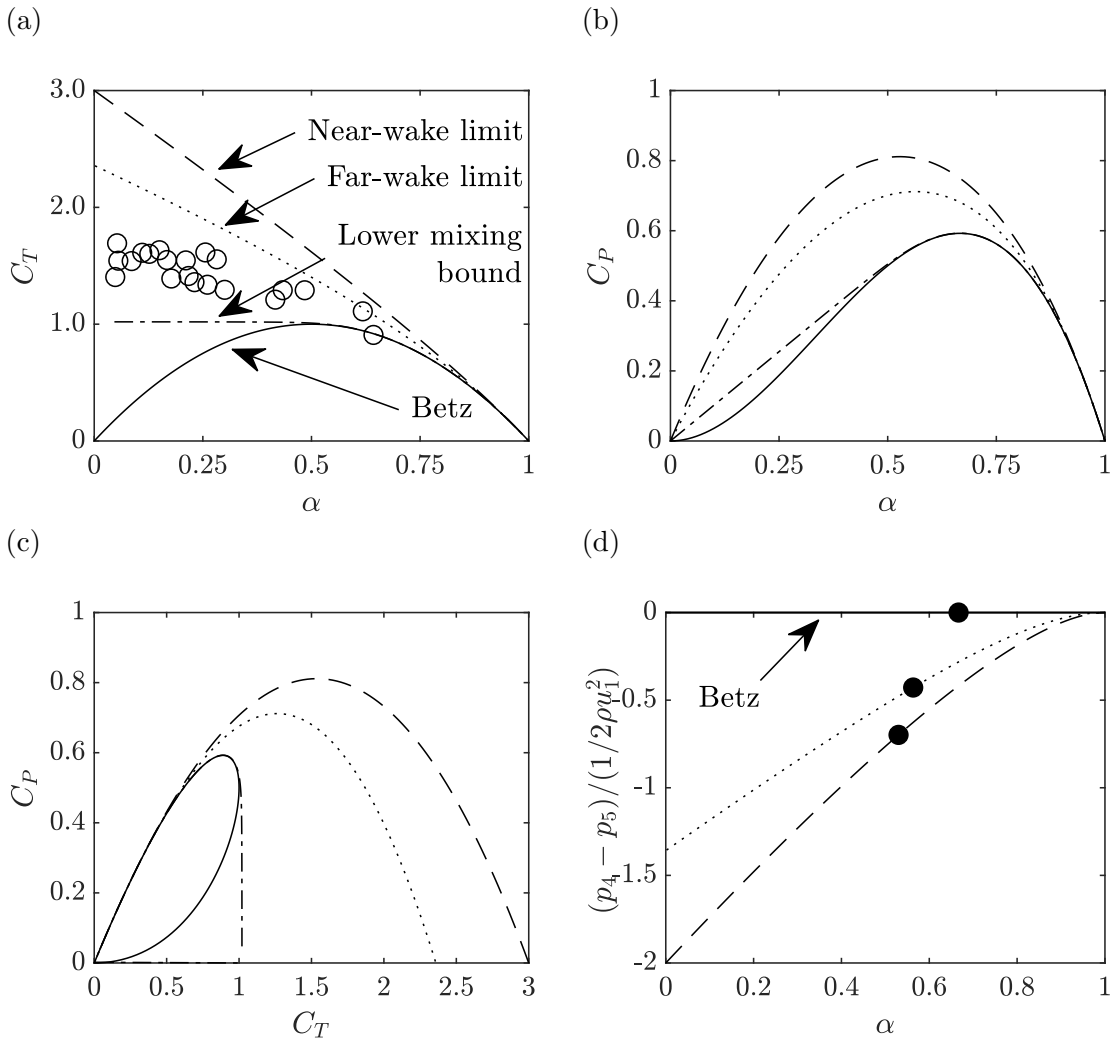

Figure 3.6: Thrust (a) and power (b) coefficients against the axial velocity factor at the disc plane α for an actuator disc in turbulent flow, with (c) then plotting the thrust and power coefficients against each other for comparison. (d) The wake mixing pressure coefficient against the axial velocity factor, with the solid circles indicating the peak power points. The solid line shows the classical Betz limit model, the dash-dot line shows the lower bound of the viscous mixing model corresponding to single stage far-wake mixing, the dotted line the far-wake mixing limit and the dashed line shows the near-wake mixing limit. Hollow circles indicate measurements for the thrust of operating turbines at large axial induction factors presented in Lock et al. [1926].

limits. A clear feature of the thrust curves is that the model predicts finite thrust at low axial velocity factors α, and that C_T may exceed unity, which is not observed in the inviscid analysis. As α approaches unity the curves are all well approximated by the Betz [1920] model.

With the wake mixing always generating additional base suction downstream of

the actuator disc [Roshko, 1955], the thrust and power coefficient predictions of the analytical model are always bounded from below by the Betz [1920] model. Changes in the mixing rate, or a mixing boundary condition which promotes lower mixing base suction (moving from the far to near-wake limit curves), therefore increases peak power, and the corresponding axial velocity factor to achieve peak power decreases (figure 3.6d). The lower mixing bound, which still allows for complete wake velocity recovery, begins to diverge from the Betz curves at low axial velocity factors, where the disc thrust cannot fall with further reductions in α due to the balance between thrust and base suction. Note that although the mixing base suction effect is maximised for low axial velocity factors, the coupling with the irrotational region of the flow nonetheless restricts the peak performance to $\alpha^* > 0.5$. The decrease of the optimal axial velocity factor with increased mixing leads to a higher optimal operating thrust coefficient, both from the change in mixing condition (moving between curves) and, with the exception of the Betz [1920] model, as the thrust monotonically increases with decreasing axial velocity.

Finally, we compare against experimental propeller data [Lock et al., 1926], which does not match the classical momentum theory for low axial velocity factors, with Buhl [2005] proposing a curve fit to match the data for $\alpha \leq 0.6$. It is clear that these experimental results are better bounded by the far-wake mixing limit of the analytic model, where we assume that mixing begins after pressure equalisation, notwithstanding the differences in physics between actuator discs and real turbines (e.g. tip-vortex losses). For real turbines where blade-tip vortices are expected to suppress turbulent mixing in the near-wake and mixing rates peak downstream of the tip-vortex breakdown [Lignarolo et al., 2014], we therefore recommend the gradual far-wake mixing equations 3.26-3.27 over the inviscid Betz [1920] model as an updated estimate to the upper bound turbine performance in turbulent flows. The assumptions underlying these equations have been validated experimentally in the context of porous discs by Steiros and Hultmark [2018], see section 3.5 for far-wake recursive mixing details.

3.4.2 Performance in a blocked channel

We extend the predictions of Garrett and Cummins [2007] to consider the pressure rise in the mixing process, with comparable conclusions to the unblocked case. The solutions to the blocked channel flow model are presented in figure 3.7. The presented analytical solution to the channel flow problem with no mixing base suction (i.e. Garrett and Cummins [2007]) is derived in Dehtyriov et al. [2021], and a blockage correction based on the Steiros and Hultmark [2018] porous disc model for far-wake

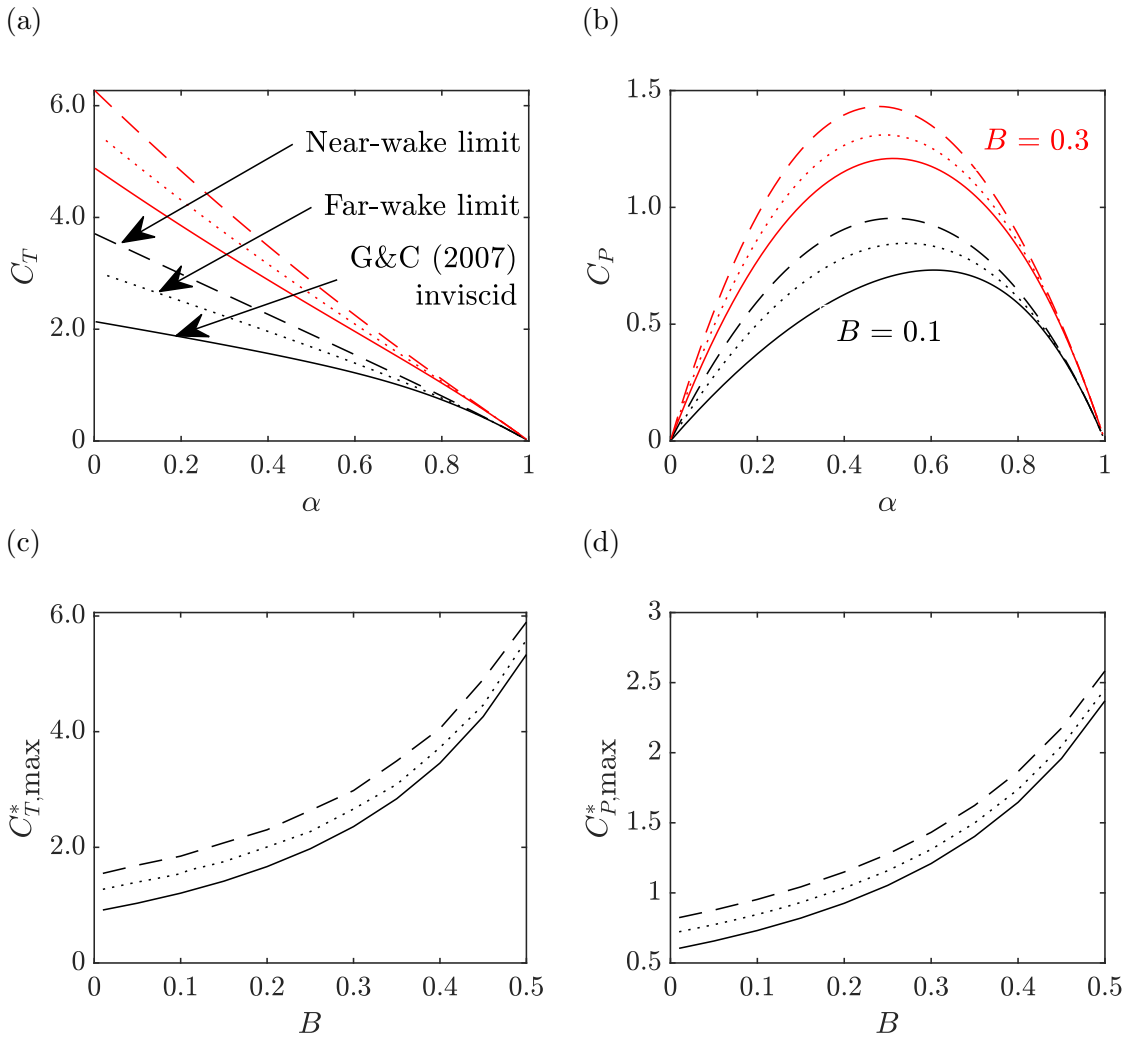

Figure 3.7: Figures (a)-(b) show thrust and power curves plotted against the disc plane axial velocity factor for discs in a channel with blockage $B = 0.1$ in black and $B = 0.3$ in red. Figures (c)-(d) show the thrust and power coefficients against blockage ratio for the peak power condition. The solid lines indicate the Garrett and Cummins [2007] inviscid limit, the dotted lines the far-wake mixing limit ($\zeta_i \to 0$), and the dashed-lines the near-wake mixing limit ($Z_i = Z_{\max}$). In all cases the cumulative mixing volume Z is bounded by mass conservation.

mixing is derived in Steiros et al. [2022]. In the limit as $B \to 0$, we converge to the unbounded solutions in section 3.4.1. However as the channel blockage is increased, we observe significant changes in the operating power and thrust across all velocity factors.

Increases in the blockage ratio broadly shift both the near and far-wake mixing limit solutions by factors comparable to Garrett and Cummins [2007] blockage uplift on the Betz limit (i.e. by a factor of $1/(1-B)^2$). With increasing blockage, there

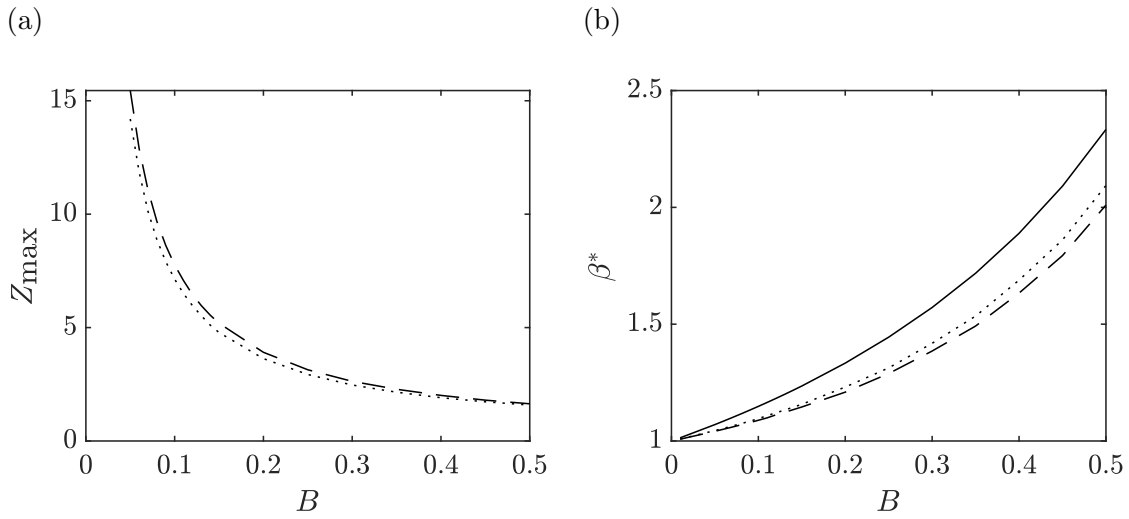

Figure 3.8: The variation in (a) the maximum permissible mixing ratio $Z_{\max} = \gamma/(B\alpha)$ in a channel flow with finite blockage and (b) the bypass flow speed β^* with blockage ratio B. The solid line represents the Garrett and Cummins [2007] solution, the dashed line represents the near-wake mixing limit, and the dotted line the far-wake mixing limit.

are three competing effects which constrain the impact of mixing on the flow problem leading to closer alignment of inviscid and mixing solutions at higher B. First, the maximum cumulative mixing area ratio $Z_{\max}$ falls (figure 3.8a), limiting the impact of the wake mixing pressure mechanism; second, the bypass flow speed β increases (figure 3.8b) leading to a larger variation in the mixing boundary adding to the wake mixing pressure rise; and finally, the blocked flow far-downstream boundary condition ($p_5 = p_1 - TB/A_T$) alters the pressure recovery available to the mixing process.

In the limit as $B \to 1$, the mixing ratio $Z_{\max} \to 1$, and hence the two model solutions converge to the Garrett and Cummins [2007] unmixed model. As B is increased from $B = 0$, the streamtube expansion and far-field pressure differential mechanisms become increasingly dominant over the mixing mechanism as the drivers of variation in disc performance. However, for modest blockage ratios ($B \leq 0.2$), likely to be observed in practice, the wake mixing effect remains significant. The far-wake mixing model increase in C_P at zero blockage is comparable to the performance increase in the inviscid model due to blockage of $B = 10\%$.

3.5 Discussion

3.5.1 Actuator and porous disc representations of momentum sinks

A comparison between the predictions of various models in the literature (which assume either no or far-wake mixing) against the proposed LMADT far-wake mixing case is presented in figure 3.9.

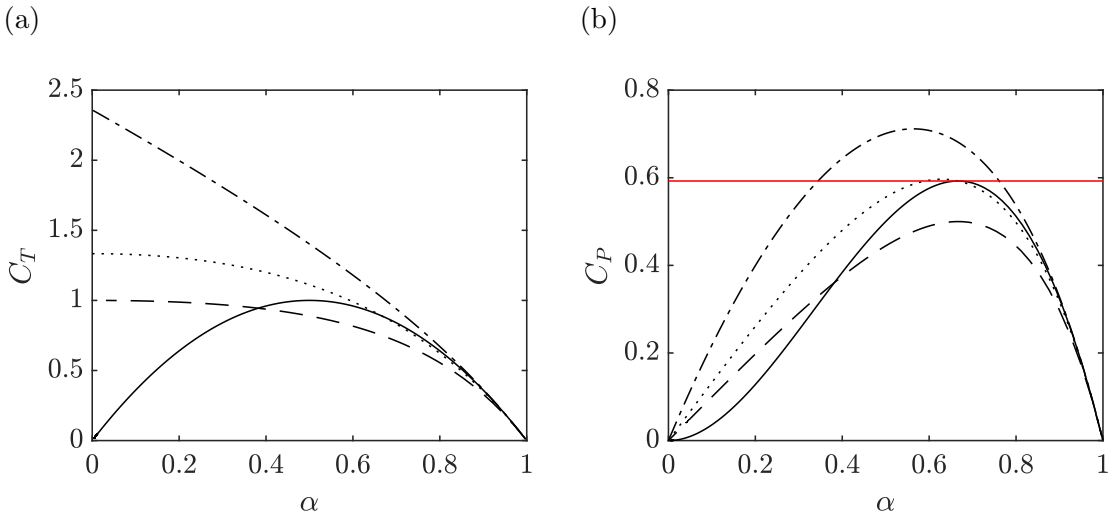

Figure 3.9: Comparisons between actuator disc and porous disc models in the literature. The solid black line is the predictions of Betz [1920] & Taylor [1944], with the solid red line indicating the Betz limit, the dashed line the predictions of Koo and James [1973], the dotted line the predictions of Steiros and Hultmark [2018], and the dash-dotted line the far-wake mixing limit prediction of the current linear momentum actuator disc theory model.

We distinguish between two alternate models; those representing the porous disc interface by a uniform distribution of sources [Taylor, 1944, Koo and James, 1973, Steiros and Hultmark, 2018], and those representing the bound vorticity of lifting lines by an actuator disc [Betz, 1920, Conway, 1998, Johnson et al., 2013], which can be exactly represented by a distribution of ring vortices in its wake. In both cases, only the axial velocity is constrained to be continuous across the disc boundary, however in general the other two components of velocity are discontinuous or absent. For a distribution of sources, where a change in streamfunction across the porous disc is required to represent the generated vorticity across the interface, this discontinuity in the radial velocity is required to conserve mass. Koo and James [1973] corrected the approximation of Taylor [1944] by manipulating the stream function for a distribution of sources to ensure mass and momentum conservation, with Steiros and

Hultmark [2018] extending on this model by including the additional base suction effect calculated implicitly with momentum theory.

For turbine blade representation however, the time average of the vorticity contained by the lifting lines is equivalent to the trailing tip-shed circulation and thus the bound surface vorticity generated at the rim of the actuator disc. For turbines which can be represented by straight lifting lines, there is hence no discontinuity in radial velocity across the actuator disc [Conway, 1998, Johnson et al., 2013]. This holds true for discs of arbitrary loading, but not for swept or curved lifting lines, which are only typically characteristic of fixed wings and propellers respectively. Detailed mathematical treatment with exact solutions of inviscid flow through a disc in the linearised limit is presented by Hough and Ordway [1964], Conway [1995], whereas Wu [1962], Conway [1998] consider exact solutions for the heavily-loaded nonlinear general case. Importantly, these methods confirm the validity of linear momentum actuator disc theory as mass- and momentum-consistent representations of the flow field behind an actuator disc in the linearised limit.

Turning our attention again to figure 3.9, the peak power coefficient predicted by Koo and James [1973] would be $C_P^* = 0.5$ (porous disc literature is typically concerned with drag estimates, however this can be readily converted to a power prediction by multiplying by the disc velocity), lower than the inviscid Betz [1920] model limit of $C_P^* = 16/27$. This is attributable to the discontinuity in radial velocity at the disc plane required to satisfy continuity for a uniform distribution of sources. The addition of the additional base suction pressure due to viscous wake mixing included by Steiros and Hultmark [2018] brings the peak predicted performance slightly above the Betz [1920] limit to $C_P^* = 0.597$. However, this similarity in peak power prediction is purely coincidental as the underlying assumptions of the models are fundamentally different. The Betz [1920] model assumes inviscid actuator disc flow with no far-wake flow velocity recovery and has been validated numerically (see section 3.6), whereas the Steiros and Hultmark [2018] model includes the effect of viscous far-wake mixing and treats the flow through the disc in a discontinuous manner. Indeed, the addition of the mixing base suction term, solved herein through the application of LMADT, raises the power prediction from that of Betz [1920] to $C_{P,\max}^* \approx 0.71$ in the viscous case where we have assumed that mixing occurs only after pressure equalisation. The power curve hence lies above the Taylor [1944]-Betz [1920] prediction for all α as mixing cannot, by conservation of momentum, result in a decrease in pressure.

If we ignore the increase in local bypass flow speed that is required to match the pressure of the entrained flow with the core wake flow for the far-wake mixing

condition (i.e. assume that $\beta_{e,i} = \beta$), both the near and far-wake mixing conditions (for gradual mixing, i.e. $\zeta_i \to 0$) predict $C_T = 2(1-\gamma)$ and $C_P = 4\gamma(1-\gamma)/(1+\gamma)$ (comparable to equations 3.26-3.27), for which $C_{P,\max} = 4(3-2\sqrt{2}) \approx 0.68$ at $\gamma = \sqrt{2}-1$. This exact result can be derived from Steiros and Hultmark [2018] by assuming no discontinuity in radial velocity and re-balancing mass and momentum, as the velocity scaling factor introduced by Koo and James [1973], and applied by Steiros and Hultmark [2018], is exact in the limit as the discontinuity approaches zero.

To summarise, for gradual mixing, where the wake pressure rise does not depend on the pressure boundary condition, the near-wake mixing lower bound presented herein reduces to the Steiros and Hultmark [2018] model when modified to assume no discontinuous drop in radial velocity across the disc plane. The far-wake mixing upper bound likewise converges to this limit with an additional simplification to the bypass flow where no wake acceleration is assumed prior to mixing.

As a further check, the blocked flow mixing models (both near and far-wake cases) approaches the Garrett and Cummins [2007] solution both when mixing base suction is assumed negligible ($\zeta_i = 0$) and also for $B \to 1$, where $Z_{\max} \to 0$.

3.5.2 Physical interpretation underlying the near and far-wake mixing interface assumptions

A complete picture of the primary features of the flow field through an actuator disc embedded in turbulent flow is illustrated in figure 3.10. A typical quasi-one dimensional simplification to the physics, assumed herein and typical of many models in the literature, is to approximate the velocity and static pressure fields by top-hat functions bounded by an inviscid streamtube upstream and a wake boundary downstream of the actuator disc. Region 1-2 is governed by inviscid fluid mechanics and the streamtube is well defined. The region between stations 3 and mixing onset station M is a transition region between the inviscid streamtube expansion dominated flow and the viscous re-energisation region. Downstream of station M is the re-energisation region, where both static pressure and velocity profiles recover to free-stream. At station 4, we see static pressure recover to free-stream conditions and at station 5 the flow velocity recovers to the upstream conditions. In general, these two equalisation stations do not occur at the same location, and LMADT assumes static pressure recovery before wake velocity recovery.

The models assume that for cases with negligible blockage, the atmospheric pressure far upstream and far downstream of the disc is the same. There is however a clear physical difference between an open and closed system, even in the limit of negligibly

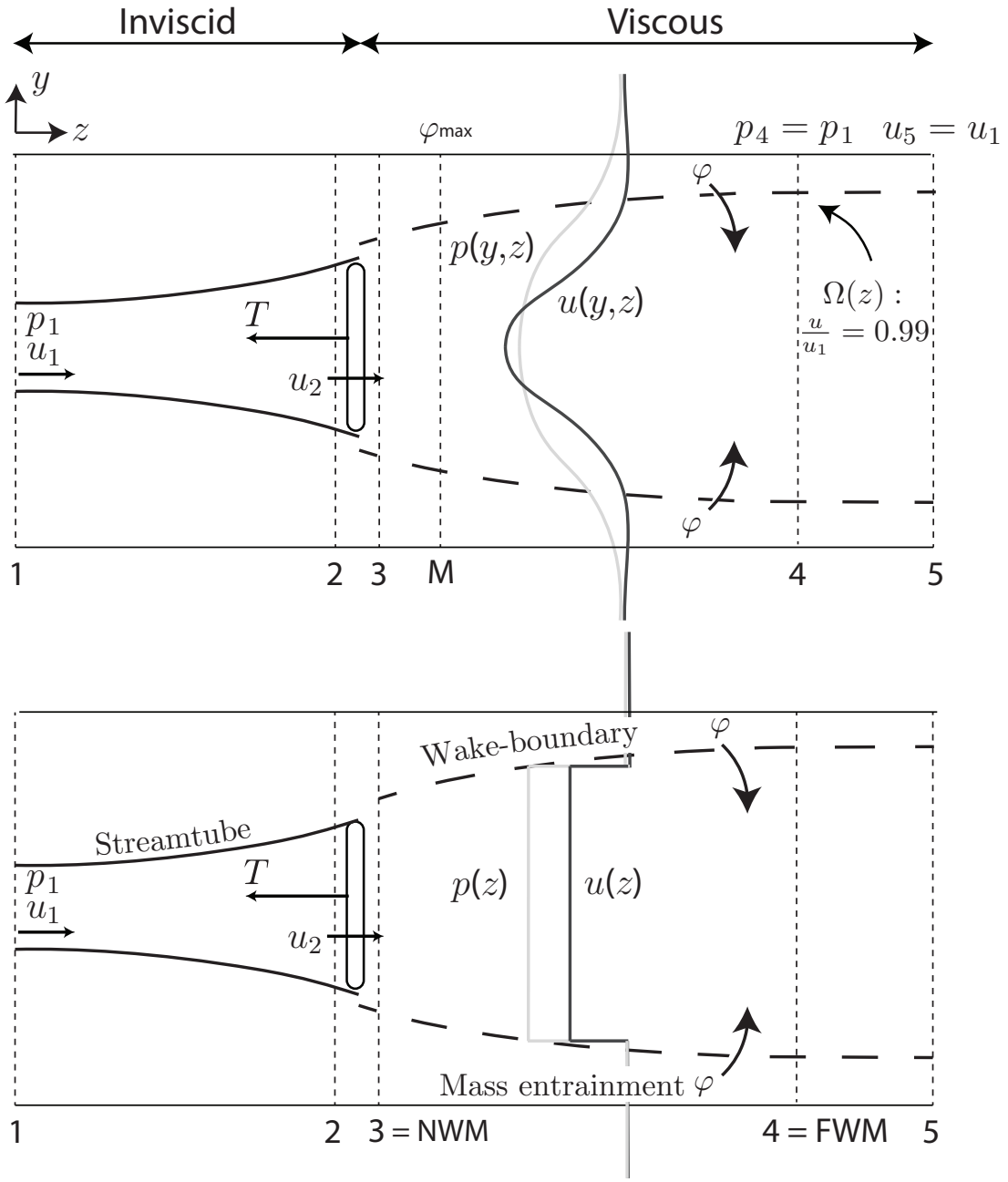

Figure 3.10: (a) Actuator disc embedded in turbulent flow schematic illustrating the major flow stages. (1) The far upstream inflow condition; (2) Just upstream of the disc; (3) Just downstream of the disc; (M) The start of the wake re-energisation region; (4) Pressure equalisation point; (5) Far downstream, velocity equalisation point. The wake boundary is taken to be an axial velocity isosurface representing 99% of the inflow velocity. (b) The analytic approximation to the problem, with velocity and pressure approximated by top-hat functions. The mixing station represents the point at which the mixing process begins; with NWM (near-wake mixing) the mixing begins just downstream of the turbine, and at FWM (far-wake mixing) the mixing begins at the pressure equalisation point, representative of the cases presented in section 3.3.

small blockage. For a closed channel system, the pressure field inside the flow passage is fully determined by the inlet and outlet conditions, and the far-wake mixing model therefore only assumes that the mixing takes place before the end of the channel. For an open flow however, and consistent with the assumptions of the Betz [1920] theory, we simultaneously consider a fixed upstream velocity and a fixed (zero) pressure difference between far upstream and far downstream. In this case, the atmosphere must impose pressure at all streamwise positions between far upstream and far downstream such that in theory, the atmosphere could equalise the bypass and core flow pressures before the start of far-wake mixing. The far-wake model therefore assumes that for an open atmospheric flow, the mixing still takes place within a streamwise distance which is shorter than the length scale for the recovery of atmospheric pressure.

The two limiting pressure conditions on the mixing boundary described in section 3.3 are representative of two limiting wake mixing scenarios. In the case of the far-wake mixing condition, the mixing is assumed to begin only after static pressure equalisation, although in reality some mixing will occur in the shear layer directly behind the disc. In the case of the near-wake mixing condition, we assume that the mixing begins shortly behind the disc, with a rapid deceleration to the minimum wake-velocity γ still assumed to be within the inviscid zone. Both of these conditions are therefore clearly approximations to the real physics and do not capture the complex coupling of the inviscid and the viscous mixing zone. Instead, we assume a system where the wake is decoupled into two zones: the first an inviscid zone, where we assume that the pressure and velocity are governed by Bernoulli; and the second where the pressure and velocity are governed by the viscous mixing physics. As a static pressure rise is an inevitable consequence of mixing, an algebraic model estimating this wake pressure rise is clearly of use, particularly for setting bounds on disc performance.

The aim of this model is therefore not to definitively predict the performance of a given actuator disc in turbulent flow but rather to algebraically demonstrate a relationship between wake-mixing and performance, discuss the fundamental underlying physics, and provide a bounded estimate on the performance uplift with a simple closed-form expression. The difference between the behaviour of the power curves with increasing ζ (mixing ratio) between the two mixing conditions speaks to the underlying non-linearity of the mixing problem. An important feature of near-wake mixing is that the upper power limit is realised for the mixing ratio $\zeta \to \infty$, implying that the performance of the disc is sensitive to the rate of mixing just downstream

of the actuator disc. Encouraging large rates of mixing prior to pressure equalisation are seen to lead to large increases in disc performance.

We have presented near and far-wake mixing bounds to the performance of an actuator disc with the additional base suction due to mixing considered. Variations in the disc performance should be observable with increasing mixing rates and in particular, for variations in the mixing boundary condition, or the radial pressure gradient at the mixing interface, for which strong sensitivity has been observed in the analytical results. Numerical validation of these physical observations, in particular the performance uplift with increased mixing and the corresponding increase in required thrust, are the subject of the following section.

3.6 Numerical Model

We now consider a low order numerical model (RANS-Actuator Disc (AD)) to isolate the turbulent mixing effect and as a comparison point to the analytic model. We consider a low blockage cuboid domain with free-slip boundaries located at $-20D \leq x \leq 20D$, $-20D \leq y \leq 20D$, $-20D \leq z \leq 40D$, where D is the disc diameter. The centre of the disc is located at $(0, 0, 0)$ and the disc is placed perpendicular to flow which is in the direction of the z-axis. Numerically, disc thickness is required to be finite and is taken to be $0.1D$, with thinner discs showing identical results. The x and y dimensions are set to be large enough such that the blockage remains small ($B \approx 0.2\%$) and the z domain large enough such that the static pressure recovers to be within 0.1% of the far upstream static pressure, with a zero pressure gradient condition at the outlet. The grid is heavily refined in the region $x^2 + y^2 < (2D)^2$, along the entire axial length, ensuring a minimum of 30 grid points in each direction across the diameter of the disc, and 20 grid points through the thickness of the disc. The disc-based Reynolds number is set to be arbitrarily large enough ($\mathrm{Re} = 1.5 \times 10^6$) for the inviscid forces and turbulent mixing in the shear layer to dominate any viscous dissipation forces. The governing equations are solved using OpenFOAM with the three-dimensional incompressible steady RANS equations (together with the continuity equation). The Reynolds stress terms are modelled using the $k - \omega_t$ SST viscosity model [Menter, 1994]. The turbulent kinetic energy at the inlet is taken to be $k = 1.5I_\infty^2$, where I_∞ is the inlet turbulence intensity, and the inlet specific rate of dissipation is assumed to be $\omega_t = 0.09^{-0.25}\sqrt{k}/L$ [Wilcox, 1993], where $L = 0.1D$ is the turbulent mixing length.

I_∞	I_{ref}
0.1%	0.1%
1%	0.85%
10%	4.6%
100%	14.12%

Table 3.1: Domain inlet turbulence intensities I_∞, and corresponding centerline turbulence intensities I_{ref} taken $2D$ upstream of the actuator disc.

The inlet turbulence intensity, which partially decays upstream of the disc, is varied through several orders of magnitude. The corrected upstream turbulence intensity level I_{ref} is then recorded at $2D$ upstream of the disc. We note that the specific details of the turbulence modelling do not impact the conclusions of this paper and that the conclusions can be reproduced as long as turbulent wake-mixing is present.

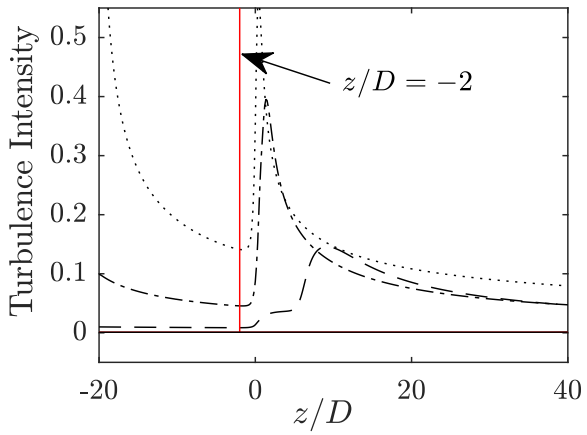

Figure 3.11: Centerline turbulence intensity for the RANS-AD model showing the decay of turbulence intensity upstream of the disc plane. The inlet turbulence intensities are 0.1%, 1%, 10% and 100% for the solid, dashed, dashed-dot and dotted lines respectively, and decay to the values given in table 3.1, at two diameters upstream of the disc (at the position of the red vertical line). The turbulence intensity profiles downstream of the disc depend on the disc operating conditions and are here shown for the disc thrust corresponding to peak power.

Table 3.1 and figure 3.11 show the relationship between inlet turbulence intensity and the turbulent intensity upstream of the disc for the four conditions considered here. The $2D$ reference point is taken to be near the minimum intensity upstream of the disc across all turbulence levels. We note again that the quantitative values of turbulence intensity do not change the conclusions of the study, even if not fully physically representative of real flow conditions (here the intensity profiles are con-

sistent in magnitude with other RANS-AD modelling [Batten et al., 2013]), and that variations in the turbulence levels simply represent variations in wake mixing rates.

The disc region acts as a momentum sink in the RANS equations, where the thrust on the disc (equivalent to the momentum sink) is given by $T = 1/8\rho u_1^2 \pi D^2 C_T$, where C_T is the disc thrust coefficient. The power removed from the mean flow is then calculated by $P = Tu_2 = 1/8\rho u_1^3 \pi D^2 C_P$, where u_2 is the disc velocity and C_P the power coefficient. For numerical implementation, the total thrust T is uniformly distributed over each cell of the actuator disc region based on the volume of each cell, and the resultant power is calculated by a sum over all disc cells $\sum_i T_i u_i$.

Due to the RANS averaging, it is important to de-rate the power and thrust coefficients by factors of $1 + 3I_{\text{ref}}^2$ and $1 + I_{\text{ref}}^2$ respectively to account for the additional energy in the averaged fluctuations (with $u_{\text{ref}}^n = \frac{1}{T}\int_T u^n(t)dt$) and assuming harmonic turbulent fluctuations) [Elliott and Cadogan, 1990, Wagner et al., 2009]. This correction is applied to all numerical simulation thrust and power curves presented in this paper.

For the four turbulence intensities considered (see table 3.1), a sweep of the global thrust coefficient is used to determine the power curves and hence locate the peak performance point. The following results concentrate principally on these peak performance points for the four cases.

3.6.1 Numerical Results

A comparison between the streamwise velocity contour maps in figure 3.12 illustrates the key differences arising from the assumptions underlying the inviscid Betz theory and an actuator disc operating in turbulent flow.

The wake velocity is seen to recover towards free stream values, with faster rates of recovery observed for larger turbulence intensities. The rate of lateral spreading of the wake, largest just downstream of the disc, likewise increases for larger turbulence intensities, and some departure from the quasi-one dimensional assumptions of the theory can be observed in the wake for the higher turbulence cases. For all of the turbulent cases, however, the minimum normalised wake velocity for peak power production remains close to the theoretical value of 1/3, (see figure 3.14).

Figure 3.13 maps out the key regions of turbulent kinetic energy (TKE) production due to turbulent flow mixing. As expected, for the lowest upstream turbulence intensity case, very low levels of TKE production are observed in the shear layer between core and bypass wake flows. For the $I_\infty = 1\%$ case, flow mixing is still observed to be primarily concentrated in the shear layer, but with significantly larger levels of

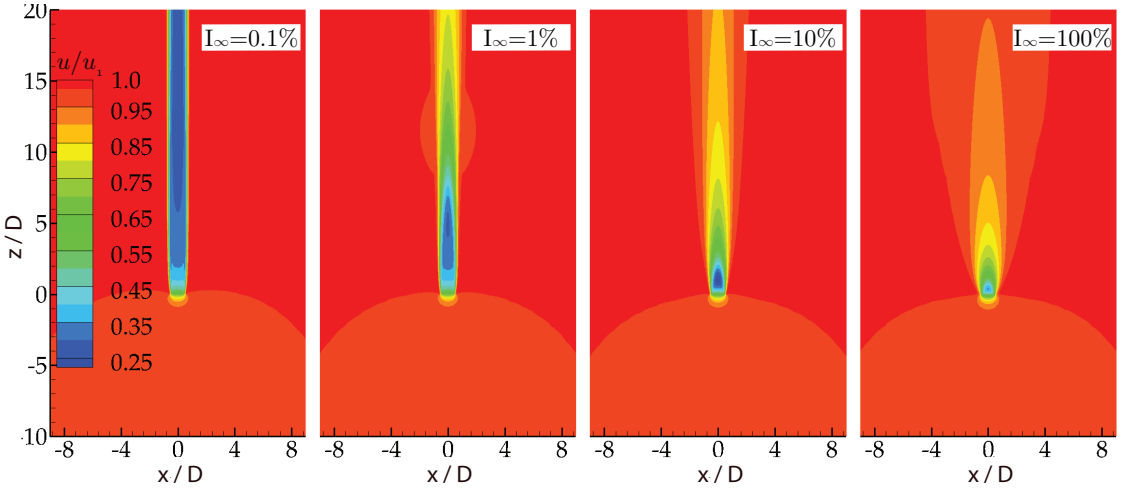

Figure 3.12: Streamwise velocity contour maps taken at the mid-disc plane at peak power for the four inlet turbulence conditions in table 3.1 illustrating the impact of flow mixing on velocity recovery in the actuator disc wake. Flow direction is from bottom to top of figure.

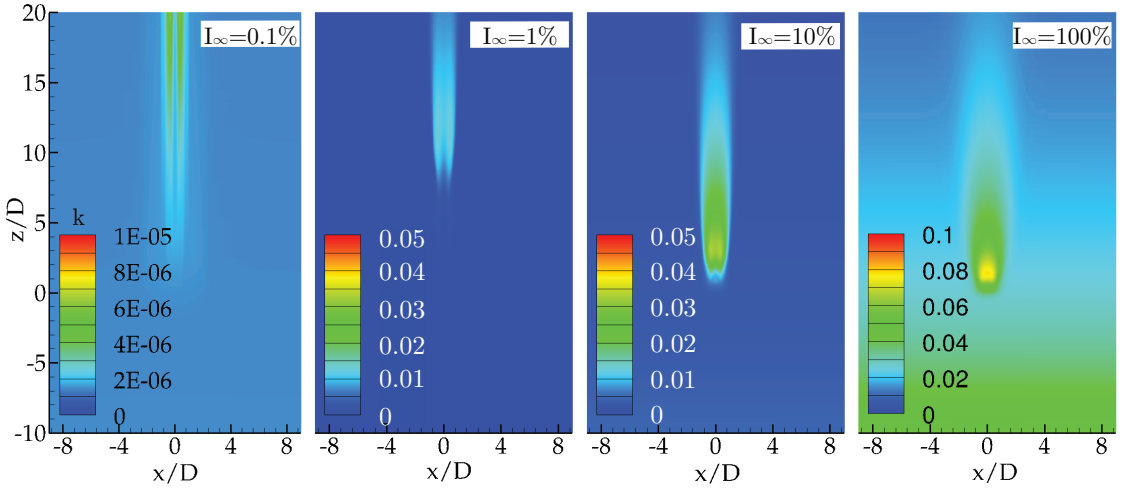

Figure 3.13: Turbulent kinetic energy contour maps taken at the mid-disc plane at peak power for the four turbulence conditions in table 3.1 illustrating the production of turbulent kinetic energy in regions of rapid flow mixing. Flow direction is from bottom to top of figure. Cases correspond to those in figure 3.12. Note the use of different contour ranges for each case.

production observed beyond around $5D$ downstream of the disc plane. For the two larger inlet turbulence cases, significant TKE production is observed in wake regions closer to the disc, with peak TKE production moving closer towards the disc plane with increasing inlet turbulence intensity.

The centerline streamwise velocity distributions shown in figure 3.14 quantify the

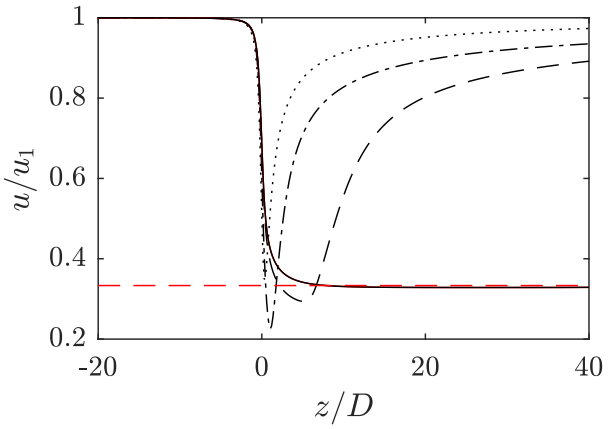

Figure 3.14: Normalised streamwise velocity along the centreline for the RANS-AD model at peak power for the four turbulence cases considered. The lowest turbulence case $I_\infty = 0.1\%$, in solid black, is representative of the inviscid Betz [1920] model, with the velocity falling to near 1/3 in the far-wake, represented by the dashed red line. For all other turbulence intensity levels ($I_\infty = 1\%$ - dashed line, $I_\infty = 10\%$ - dash-dot line, $I_\infty = 100\%$ - dotted line), the velocity recovery back towards free-stream is evident.

observations from the contour plots, and the differences between the velocity assumption underpinning the inviscid Betz theory and the actual turbulent velocity recovery are made clear. As anticipated by the inviscid theory, the very low turbulence case sees the velocity drop to 1/3 of the upstream value in the far wake, with very low rates of mixing in the shear layer responsible for minimal velocity recovery far downstream. For even relatively low turbulence levels however, a strong deviation from the Betz assumption is evident, with the $I_\infty = 1.0\%$ curve showing rapid velocity recovery that initiates from around $5D$ downstream of the disc. Consistent with the peak production of TKE moving closer to the downstream side of the disc with increasing upstream turbulence, the two highest turbulence intensity cases show velocity recovery progressively earlier, and the rate of recovery is clearly seen to increase with increasing turbulence intensity.

Of particular interest is how the observed differences in wake velocity between the various turbulence cases are related to the streamwise static pressure variation and therefore the disc performance. Figure 3.15 shows the streamwise variation in centerline static pressure at peak power, with the low turbulence case again in close agreement with the inviscid Betz theory. Noticeably, however, both the maximum upstream and minimum downstream static pressure increase with rising turbulence intensity. On the upstream (inviscid) side of the actuator disc, the increase in the maximum static pressure coefficient is attributable to larger disc loading, and con-

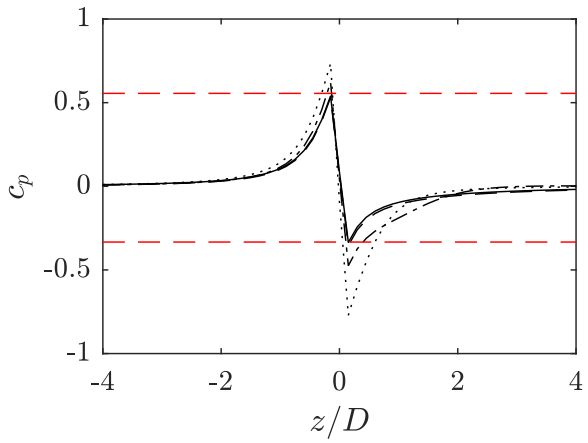

Figure 3.15: Centerline static pressure coefficient for the RANS-AD model at peak power for the four turbulence cases considered. The lowest turbulence case $I_\infty = 0.1\%$, in solid black, is representative of the expected Betz limit profile (albeit with a steeper pressure jump in the inviscid case), with the maximum and minimum pressure bounded by the two theoretical horizontal red dashed lines ($c_p^+ = 5/9$, $c_p^- = -3/9$). For all other turbulence intensity levels ($I_\infty = 1\%$ - dashed line, $I_\infty = 10\%$ - dash-dot line, $I_\infty = 100\%$ - dotted line), the pressure drop across the actuator disc at peak power is seen to increase, with the largest departures from the inviscid case observable on the downstream side of the disc.

sequently a larger deceleration and expansion of the approaching streamtube. On the downstream side of the disc however, variations in the minimum static pressure coefficient and the static pressure recovery are connected to the viscous turbulent mixing velocity recovery observed in figure 3.14. Furthermore, the relative increase by magnitude in minimum static pressure on the downstream side of the disc is larger than the change in static pressure on the upstream side of the disc, illustrating the connection between the turbulent velocity recovery (viscous mixing) and the increased static pressure rise.

For further insight into the recovery dynamics, cross-stream velocity and static pressure profiles are compared in figure 3.16 at three downstream locations to quantify differences in the limiting inviscid assumption with the turbulent cases where mass is entrained into the disc wake. Here we see deviations from the quasi one-dimensional assumption of the Betz theory with Gaussian-like profiles in the wake where the velocity and static pressure variations are not bounded by a streamtube. These profiles, and their evolution in turbulent flows, are reviewed in detail by Vermeer et al. [2003]. For the low turbulence $I_\infty = 0.1\%$ case, the normalised streamwise velocity falls to 1/3 in the far-wake as the static pressure recovers to its upstream value. For the $I_\infty = 1\%$ case, most flow mixing leading to recovery is observed beyond

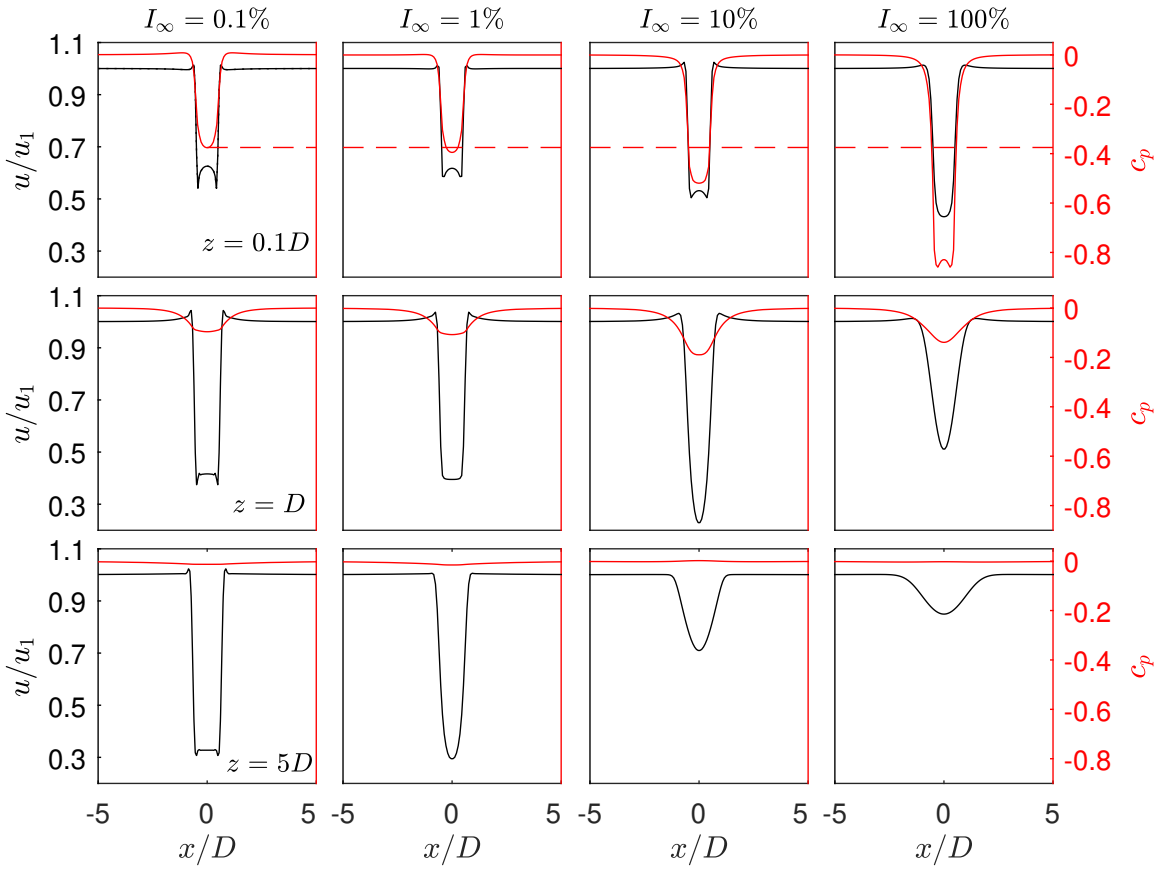

Figure 3.16: Cross-stream normalised streamwise velocity (black) and the static pressure coefficient (red) at three downstream locations in the actuator disc wake and for the four inlet turbulence conditions considered in table 3.1. The red-dashed line shows the theoretical static pressure coefficient just downstream of the disc for the inviscid Betz [1920] model.

$5D$ downstream of the disc plane, well after the static pressure has equalised. For the high turbulence intensity cases ($I_\infty = 10\%$, $I_\infty = 100\%$), the significantly lower static pressure across the wake of the disc $0.1D$ downstream is shown. Velocity recovery due to flow mixing has already commenced by approximately $1D$ downstream, before the static pressure has fully equalised between core and bypass flows. In these higher turbulence intensity cases therefore, flow entrainment at the wake boundary is further driven by a favourable radial pressure gradient in the flow that draws flow into the core wake. We also draw attention to the local bypass flow acceleration (represented by $\beta_{e,i}$ in the algebraic model), where the local flow velocity just outside of the wake boundary increases above the freestream velocity in order to approach the pressure of the core flow with which it then mixes. For lower levels of turbulence intensity the acceleration of the adjacent bypass flow persists in the far-wake of the disc.

The turbulence normalised performance curves for the actuator disc in the four variable turbulence intensity cases are shown in figure 3.17, and are readily comparable to the theoretical results in figure 3.6, with the lowest turbulence intensity case ($I_\infty = 0.1\%$) very similar to Betz [1920] limit theory. One major difference between the numerical results and the analytic model is the rapidly decaying turbulent kinetic energy upstream of the actuator disc (see figure 3.13), particularly for high turbulence intensities. This can lead to an even higher predicted power than the flow with mixing only downstream of the disc (see Nishino and Willden [2013b] for further details, where variations in the near-wake mixing rate on performance are first discussed). It is however clear that with an increase in the turbulence intensity both the peak power and associated thrust coefficients increase, consistent with what could be expected from the centerline static pressure variations shown in figure 3.15. Although the power based on the upstream kinetic flux increases, the extraction efficiency η at peak power, a measure of the ratio of power extracted by the disc to the total power removed from the flow, decreases. For the highest turbulence intensity case, we note that the actuator disc sustains the necessary high thrust at peak power without either the breakdown of the velocity deficit into a recirculating region downstream of the disc plane or time dependent shear layer instability, which can otherwise be observed through non-convergence at lower turbulence intensities for very high thrust. For lower levels of sustained thrust ($C_T \lesssim 0.8$), the curves for all turbulence intensities are approximately coincident, consistent with both the theoretical observations as well as the behaviour for turbine arrays [Dehtyriov et al., 2021].

3.6.2 Numerical wake mixing observations

We now make use of the numerical model and comparisons to the inviscid flow case to quantify the dominant mixing flow features. As is clear from the RANS results, a fundamental difference between inviscid and turbulent actuator disc flows is flow entrainment into the wake. This mass transport from bypass to core flow limits the use of a streamtube in the far wake as is typically assumed in inviscid theories, so we instead consider the wake-boundary illustrated in figure 3.18 for the case of a disc in an unbounded flow, from which to model the wake flow.

We define the wake boundary Ω to be where $u/u_1 = 0.99$ and the rates of mass

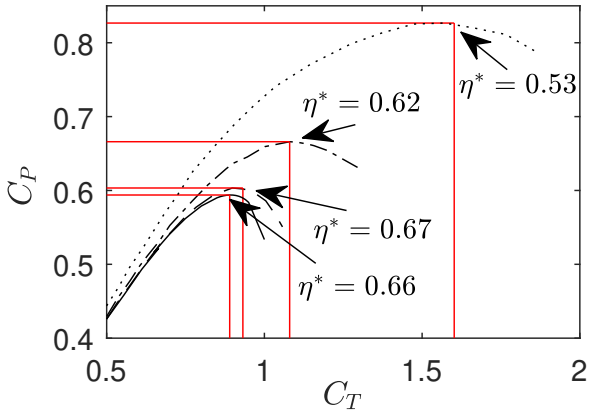

Figure 3.17: Power as a function of thrust coefficient for the four inlet turbulence cases listed in table 3.1. For increasing turbulence intensities, and consequently increasing wake-mixing, the peak power coefficient rises as the extraction (basin) efficiency at the peak power point falls. $I_\infty = 0.1\%$ - solid line; $I_\infty = 1\%$ - dashed line; $I_\infty = 10\%$ - dash-dot line; $I_\infty = 100\%$ - dotted line.

and energy entrainment into the turbine wake as

$$\varphi = \frac{4}{\pi}\int_\Omega \mathbf{u}\cdot\hat{\mathbf{n}}\, dS = \frac{4}{\pi}\int_{L_w} \delta\varphi\, dz, \tag{3.38}$$

$$\psi = \frac{8}{\pi}\int_\Omega P_0(\mathbf{u}\cdot\hat{\mathbf{n}})\, dS = \frac{4}{\pi}\int_{L_w} \delta\psi\, dz, \tag{3.39}$$

where $\hat{\mathbf{n}}$ is the inward pointing unit normal vector to the wake boundary Ω, and P_0 is the total pressure (see figure 3.18). Note that the entrainment fluxes are normalised on the flux of mass and energy of undisturbed upstream flow through an area equal to the turbine swept area.

For all cases we can assume that the streamtube is well defined upstream of the disc and that figure 3.18 can represent the physics downstream of the disc. At the disc plane there is a small region of flow between the edge of the disc, and the 99% wake boundary which surrounds the disc. This discontinuity arises from the definition of the wake boundary ($\Omega : u/u_1 = 0.99$), which is only achieved for $r(\Omega_{z=0}) > D/2$, where r is the radial distance from the center of the disc. A consideration of momentum and mass flux through the wake boundary needs to include the additional mass φ_b and energy ψ_b flux through the disc-to-wake annulus. At any given streamwise location in the wake, we assume some mass $\delta\varphi$ and energy $\delta\psi$ is entrained into the wake from the bypass. Example isosurfaces of the wake boundary are shown in figure 3.19 for the lowest and highest turbulence intensity cases simulated.

For turbulent flows, mass entrainment into the wake results in an expansion of the wake boundary by mass conservation. As is clear from the high turbulence case,

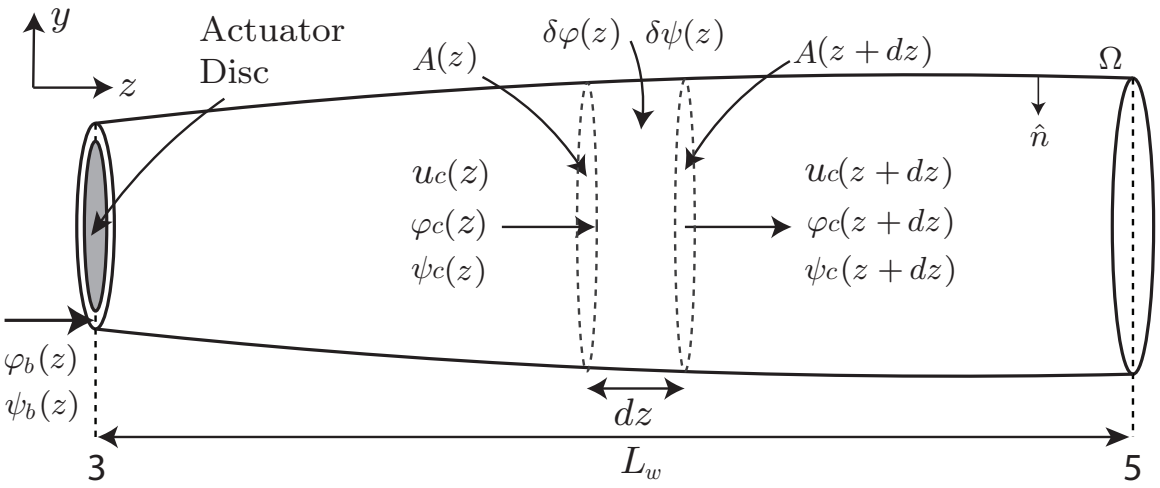

Figure 3.18: A schematic showing a wake boundary representation of the physics behind an actuator disc in turbulent flow. The actuator disc is shown as the grey shaded circle. A wake streamtube is not well defined due to mass and energy exchange between bypass and core flows. A wake boundary is here instead defined as an isosurface of axial velocity at 99% of the far-upstream velocity located between station 3 (just behind the disc) and station 5 (velocity equalisation, see figure 3.10). Mass φ and energy ψ fluxes are shown, with the wake gradually re-energised by mass and energy transport across the boundary.

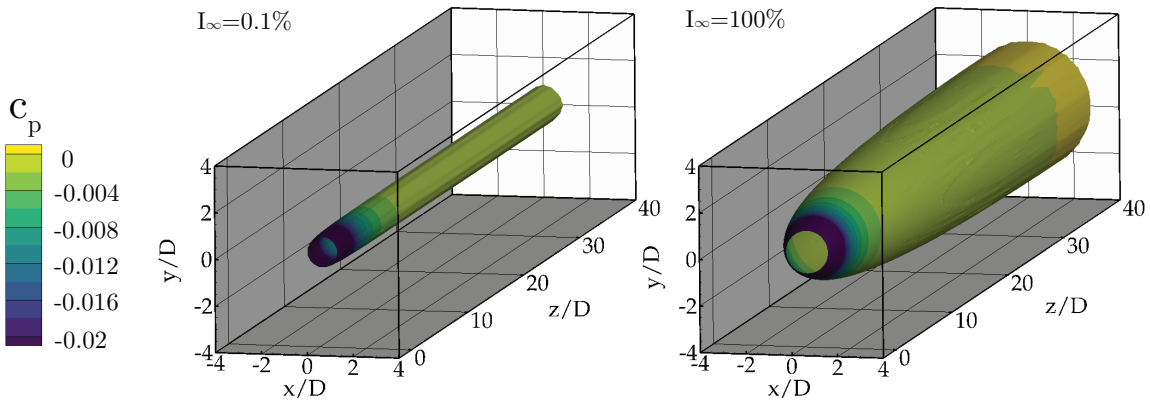

Figure 3.19: The 99% wake-boundary contoured by static pressure, defined by the isosurface $\Omega : u/u_1 = 0.99$, for the lowest and highest inlet turbulence intensity cases (see table 3.1) at peak power. Transport of mass and energy through these wake boundaries as a proxy for mixing is shown in figure 3.20.

the majority of wake boundary expansion occurs just downstream of the disc where the turbulent kinetic energy is highest, and the wake boundary gradually asymptotes in diameter far downstream as the mixing rate and therefore mass entrainment rate fall. Plots of φ and ψ for the wake at the various turbulence levels are shown in figure 3.20.

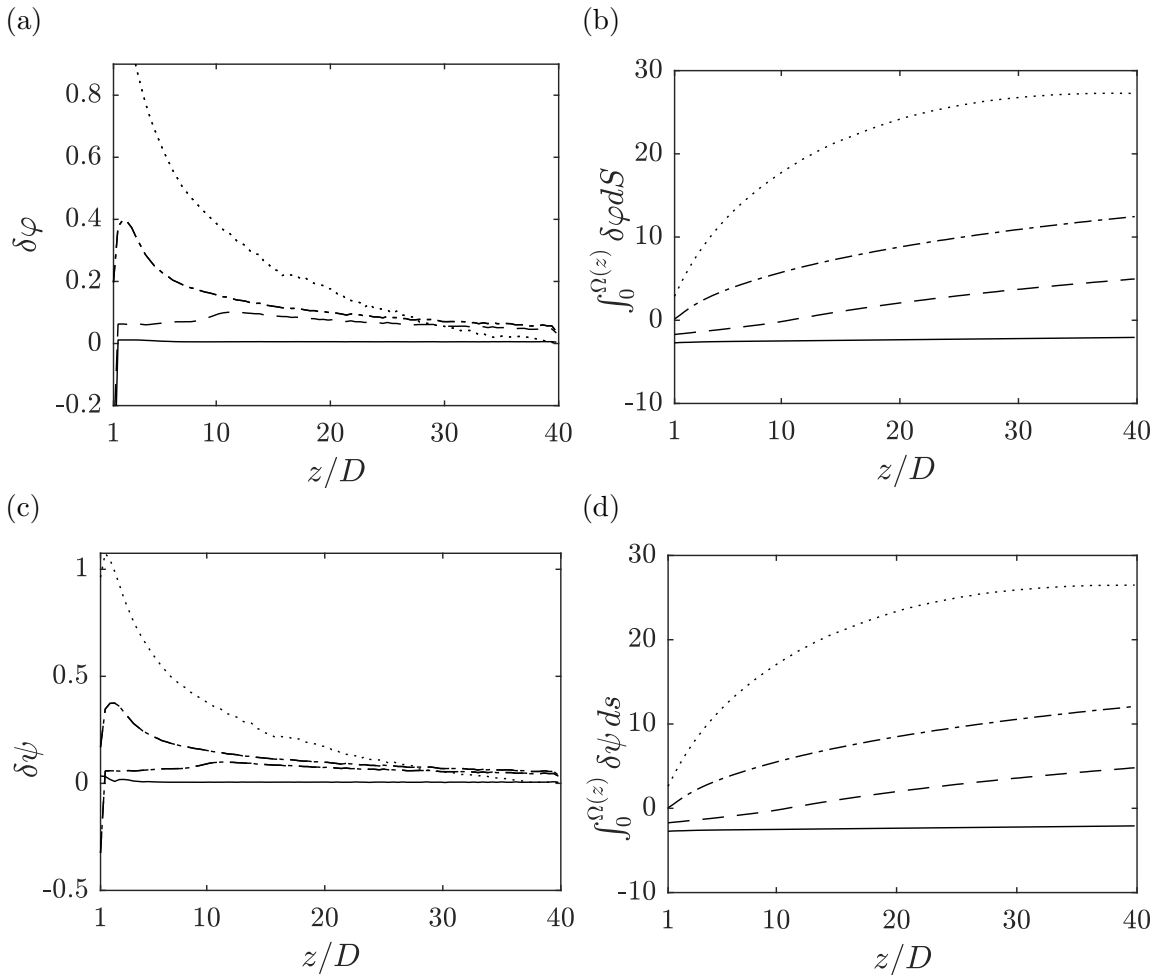

Figure 3.20: Mass (top) and energy (bottom) entrainment contributions defined by the mass and energy entering through the wake boundary illustrated in figure 3.18. Figures (a) and (c) represent the partial contributions along the length of the wake, and figures (b) and (d) represent the cumulative contributions to mass and energy entrainment. Positive entrainment contributions are a result of turbulent mixing in the wake, and any negative contributions are a result of the expanding streamtube just downstream of the disc. The solid black line corresponds to inlet turbulence intensity levels of $I_\infty = 0.1\%$, the dashed line of $I_\infty = 1\%$, the dash-dot line of $I_\infty = 10\%$, and the dotted line of $I_\infty = 100\%$, see table 3.1.

Just downstream of the disc, the wake region sees two competing influences on the mass entrainment integral φ, namely flow being diverted radially outwards by the expanding core wake streamtube, and flow mixed inwards due to large velocity and pressure gradients just downstream of the turbine. For the lowest turbulence intensity case, the streamtube expansion component dominates and the mass and energy entrainment is near negligible. For both mass and energy, the higher the upstream turbulence, the larger and further upstream the peak in inward mixing occurs. In

I_∞ (%)	I_{ref} (%)	Stations : 1	M	4	5* (90%)
0.1	0.1	-2.3	-	8.5	> 50
1	0.85	-2.2	11	7	45
10	4.6	-2.25	1.8	2.85	22
100	14.12	-2.45	1.0	2.75	8.6

Table 3.2: Approximate streamwise (z/D) locations of the various stations shown figuratively in figure 3.10. Station 1 is for $u = 0.99u_1$, station M at the maximum $\delta\varphi$, station 4 for $p = 0.01p_{\text{min}}$ and station 5* for $u = 0.9u_1$. Velocities are evaluated along the domain centreline.

all cases, the turbulent entrainment then gradually decays downstream as the radial velocity and pressure gradients decrease. Consistent with the numerical results, the integrated mass and energy entrainment increase with increasing turbulence intensity.

Table 3.2 gives indication to the approximate centreline streamwise locations of the stations for various turbulence levels at the peak power operating point. For some simulation cases the domain has been extended to determine the station location. The RANS simulations show that the upstream station 1 is broadly independent of the mixing level, with the small variations primarily dependent on the thrust/permeability coefficient of the actuator disc. As would be expected, with increasing turbulence intensity, stations M, 4 and 5* all move closer to the downstream side of the actuator disc (5* is an approximation to 5 achieved at 90% velocity recovery). The static pressure (station 4) rapidly recovers behind the actuator disc, with the peak mixing rate point moving closer to the downstream side of the actuator disc at higher turbulence levels.

The trends of the analytical mixing model show good agreement with the numerical observations. A difficulty in comparing the analytical results lies in relating the mixing condition parameter ζ_i to the mixing physics of the actuator disc. In principle, due to the separation of viscous and inviscid static pressure rise zones in the analytic model, a connection based on the underlying physics is not tractable due to the continuous non-discrete mixing that occurs in a real system. Correlations between observable quantities which affect the mixing (e.g. turbulence intensity) are likely to change under different conditions; take for example where the mixing is promoted by turbulence intensity generated by the disc as opposed to free-stream turbulence. Additionally, the one dimensional model does not account for detailed three-dimensional turbulent physics (such as the non-uniform TKE production in the wake).

As the turbulence intensity is increased, the primary mixing zone is observed to

shift from the shear layer after pressure equalisation to strong mixing just downstream of the disc (see figure 3.13), representing the variable change between the inviscid Betz [1920] model towards far and then near-wake mixing. For the high turbulence cases, the radial pressure gradient is shown to be largest in the near-wake of the disc, for which large rates of mixing are observed (see figure 3.20). For lower turbulence intensities however, the static pressure in the core first recovers and the effect of the wake on performance is significantly less pronounced. The theoretical peak power predictions are comparable to those observed in figure 3.17, with smaller increases in power where the mixing is both localised to the shear layer and predominantly occurs after pressure equalisation, and larger increases in power where the mixing occurs shortly behind the disc plane across a large radial pressure gradient. Finally, the analytic model predicts both the inverse relationship between increasing peak power and extraction efficiency (figure 3.5e,f), and the increase in disc thrust required to sustain the increased pressure drop for peak power (figure 3.5c,d).

The numerical observations make clear that in the wake region and for high turbulence intensity levels, the wake boundary expansion and viscous (turbulent) static pressure recovery mechanisms act simultaneously and are therefore coupled. In the analytical models, we assume a spatial decoupling of these two regions. Nonetheless, the trends of the numerical model align with the conclusions of the analytical model, demonstrating both the sensitivity of actuator disc performance to the wake mixing process, and the exploitability of wake-mixing to enhance the performance of an actuator disc.

3.7 Conclusions

An analytic model for the impact of turbulence induced mixing on the performance of an actuator disc has been presented and contrasted to the inviscid momentum-based disc model that assumes quasi one-dimensional inviscid flow where the velocity is not required to recover in the far-wake [Betz, 1920]. Unlike the inviscid model, where the entirety of the wake pressure recovery is related to a reduction in the wake velocity through Bernoulli's equation, we show that an additional static pressure recovery mechanism is a direct consequence of viscous mixing between core and bypass flows and therefore velocity recovery in the wake. We present an algebraic model which includes these two pressure recovery mechanisms as an extension of the inviscid Betz [1920] model, demonstrating an increase in power coefficient and a decrease in extraction (basin) efficiency when wake mixing due to turbulence is accounted for. We

show that actuator disc models [Betz, 1920, Johnson et al., 2013] are fundamentally different to porous disc models [Taylor, 1944, Steiros and Hultmark, 2018] which represent the disc as a uniform distribution of sources, and that these physical differences imply a larger upper bound of power extraction for turbines as compared to porous discs.

The presented algebraic model provides estimates of the performance variation for two limiting flow conditions: the first, where the wake flow mixing occurs in the far-wake following pressure equalisation between core and bypass flows; and the second, where strong flow mixing is observed shortly behind the actuator disc in the near-wake. To allow for algebraic closure, the model separates the wake into two regions representative of the two static pressure recovery mechanisms. The physics in the first wake region is assumed to be dominated by an inviscid streamtube expansion mechanism, where the static pressure rise is a direct consequence of flow deceleration. In the second region flow mixing is assumed to dominate, and the static pressure rise is associated with mixing and the ensuing velocity recovery mechanism. The theory is then developed to consider blocked flows for tidal turbines operating in an enclosed channel, where the conclusions are similar to those for the unblocked model, but modified broadly following a global blockage factor $(1-B)^{-2}$ [Garrett and Cummins, 2007].

We compare the results of our algebraic model to Reynolds-Averaged Navier-Stokes Actuator-Disc simulations. We find that the velocity and static pressure fields across a range of ambient turbulence levels (from 0.1% to 14%) increasingly deviate from the momentum assumptions of Betz [1920] as the inlet turbulence rises. The velocity is found to recover in the wake to upstream levels, with the rate of recovery increasing with the upstream turbulence intensity. Further, the changes in static pressure relative to ambient conditions on both sides of the disc are observed to increase, with power coefficient increases comparable to the theoretical model. In all cases, the peak power and thrust coefficients increased with increasing rates of wake mixing, whilst the extraction (basin) efficiency fell. Mass and momentum transport into the wake for the numerical model was quantified, with the transport increasing with increasing upstream turbulence.

The analytic model better represents both the underlying physics and the resultant performance variation of actuator discs in turbulent flows as compared to the classical purely inviscid model of Betz [1920]. The physical conclusions of the analytic model agree with the trends of the numerical model, with increases in peak performance corresponding to an increase in disc thrust and a decrease in extraction (basin)

efficiency. The strength of the analytic model lies in providing an upper bound to disc performance inclusive of wake-mixing. For far-wake mixing, where mixing occurs gradually after pressure equalisation, the power coefficient is shown to rise from the Betz limit of ~ 0.59 to a maximum of 0.71. If the mixing occurs abruptly just behind the disc (the near-wake mixing limit), the power coefficient is shown to further increase to a maximum of 0.81.

Finally, the model is compared to experimental data of real turbines presented by Lock et al. [1926], from which Buhl [2005] observed that the Betz [1920] model poorly predicts turbine performance at small axial velocity (or large induction) factors. We observe that the upper limit of the far-wake mixing model provides a good bound to the experimental data, and attribute the far-wake mixing bound as a generally good estimate for peak turbine performance due to the near-wake mixing suppression by the blade-tip vortices. We hence propose new algebraic relationships between the wake velocity factor γ and the optimal performance coefficients, namely $C_{P\text{max, FW}} = 3.83\gamma(1-\gamma)/(0.9+\gamma)$ as a new estimate of disc performance in realistic turbulent flow conditions with gradual far-wake mixing, and $C_{P\text{max, NW}} = \gamma(1-\gamma)(3-\gamma)^2/2$ as the maximum disc performance in an unbounded flow achieved with rapid near-wake mixing. The performance coefficients can alternatively be expressed in terms of the velocity factor at the rotor plane α.

This work clearly demonstrates the importance in the consideration of wake mixing on turbine performance through an analytic and numerical study of actuator discs in turbulent flows. Unlike the traditional assumptions for aircraft where the mixing rate is related to induced drag and is therefore to be minimised, this paper shows that an increase in the wake mixing rate can boost the local power coefficient of an individual turbine. This model therefore not only provides a new upper bound for turbine performance in turbulent flows, but provides a new lens through which to consider the design of energy extraction devices.

3.8 Acknowledgements

The authors would like to thank Dr. Takafumi Nishino for his constructive discussions.

3.9 Funding

This research was funded in part by D.D.'s EPSRC studentship (grant no. EP/S023801/1), C.R.V.'s UKRI Future Leaders Fellowship (grant no. MR/V02504X/1) and R.H.J.W.'s EPSRC Advanced Fellowship (grant no. EP/R007322/1), and by the EPSRC Supergen ORE Hub (grant no. EP/S000747/1).

3.10 Declaration of interests

The authors report no conflict of interest.

3.A Statement of authorship

The preceding chapter has been reformatted from an article *in preparation*. The inclusion of co-authors reflects the fact that the work came from active collaboration between researchers and acknowledges input into team-based research.

Publication details	
Title of paper	Turbulent wake mixing for power extraction above the Betz limit
Publication status	In preparation
Publication reference	Authors: D. Dehtyriov, C.R. Vogel and R.H.J. Willden.

Student Confirmation	
Student Name	Daniel Dehtyriov
Contribution to the paper	The theoretical development and writing was a collaborative effort between all co-authors, with the contributions and writing split $80-10-10$ between DD, CV and RHJW respectively.

Student signature

20th December 2023

Date

Supervisor Confirmation	
Supervisor name and title	Prof. Richard Willden
Supervisor comments	I confirm that Daniel has made a substantial contribution to the publication, and that the description above in the Statement of Authorship is accurate.

Supervisor signature

20th December 2023

Date

Chapter 4

A head-driven model of turbine fence performance

> "Siddhartha saw it hurrying, the river, which consisted of him and his loved ones and of all people, he had ever seen, all of these waves and waters were hurrying, suffering, towards goals, many goals, (...) a river, headed forward once again, flowed on once again."
>
> — Hermann Hesse, Siddhartha

This chapter presents an article which relaxes the time-steady assumption of the Betz model by considering the flow through a turbine fence which resists the flow rate in a tidal channel, and where the channel head dynamically governs the flow rate through the fence. The article was published in the *Journal of Fluid Mechanics* on the 31st January 2023 [Dehtyriov et al., 2023a].

A further limitation of the Betz model is the assumption that the upstream flow is steady in time and that turbine resistance has no impact on the upstream flow (constant upstream mass flux). This is particularly important for tidal channel flows, where the deployment of many turbines in a channel may have significant impacts on the channel dynamics (velocity of the tides). We hence extend on the work of Vennell [2010] and Gupta and Young [2017] to a more practical configuration by considering the coupling between channel dynamics theory and a partial fence that occupies only part of the width of the channel. We develop an analytic model which shows that the dynamics of the problem is governed by three non-dimensional groups representing the head in the channel, the channel bed friction, and the turbine characteristics, for which the number and spacing of turbines can be optimised to maximise power

per unit turbine area. This new model has great practical potential in aiding a tidal turbine developer with detailed knowledge of their site's channel and frictional characteristics, resulting in a design envelope including both environmental/peak load constraints and the maximum yield point for optimisation in a tidal channel. The model is also readily applicable to power limit estimates for resource assessment and can further be combined with real turbine characteristics to more accurately predict turbine performance.

4.1 Paper abstract

This paper presents an analytic model for the analysis of co-planar turbine fences that partially span the width of a channel in which the flow is driven by a sinusoidally oscillating driving head. The thrust presented by the turbines reduces the flow rate through the channel leading to a solution for overall power that is dependent upon turbine resistance and flow blockage as well as on channel characteristics. We introduce a return parameter, in terms of power per turbine area, to assess optimum turbine fence deployment for a given channel. We find that the optimal deployment rests on a universal curve independent of the channel characteristics, and that these characteristics, namely the integrated channel bed friction and a modified channel Froude number moves the optimum along this curve. We find that blockage considerations play a large role in the performance of a tidal farm; its achievable power, optimal return, channel flow rate reduction and device thrust, and that the scales of blockage must be considered even when designing relatively unblocked farms. The impact of the channel characteristics on the optimal arrangement, alongside environmental constraints which may limit permissible flow blockage, are quantified and discussed.

4.2 Introduction

Many advances have been made on the theoretical modelling of tidal turbine performance in confined channels. The work of Garrett and Cummins [2007] demonstrated the importance of considering the impact of blockage (flow confinement) on the upper limit of energy extraction for a homogeneously arrayed turbine fence that completely spans the width of the channel under the assumption of an undeforming free surface. This upper limit increases from the Betz limit typically assumed for unconstrained wind turbines in proportion to the square of the relative confinement. Corrections

have been applied to tidal turbines to account for the deformation of the free-surface [Whelan et al., 2009]. Nishino and Willden [2012a] extended the model by considering a long turbine fence which only partially spans the width of a channel, allowing for incomplete channel use that may be necessitated in practical turbine arrangements, for example due to bathymetric variations or shipping lanes. Here, two scales of flow confinement are considered; a local blockage (ratio of turbine frontal area to local flow passage area) dependent on tip-to-tip spacing between adjacent turbines, and a global blockage effect due to the channel geometry constraints. This model, working on the basis of scale separation between turbine and array scale flow events, located a new energy extraction limit for a closely packed tidal turbine fence in an infinitely wide channel of 79.8% of the kinetic energy flux of the undisturbed approach stream, achieved at a local blockage of ~ 0.4. The model has additionally been applied to multiple rows of tidal turbines [Draper and Nishino, 2014], where it was found that a single row of turbines outperforms a staggered arrangement, and to shallow channels with non-negligible bed friction, which was found to change both the power extraction potential and optimum fence arrangement [Creed et al., 2017]. The scale-separation effect has been demonstrated experimentally using porous discs [Cooke et al., 2015], and power uplift through the local blockage effect has been shown in large laboratory turbine experiments [McNaughton et al., 2021].

These flow confinement models however assume a fixed flow rate through the channel. Garrett and Cummins [2005] developed a channel dynamics model which accounted for the sinusoidally varying channel head as well as the response of the channel flow rate to the resistance presented by the turbines. The tidal turbine farm is modelled as a single modifiable drag (or bed-friction) coefficient in a one-dimensional channel, for which it is found that the maximum power results from a balance between increasing the drag coefficient to increase power production and the associated reduction in channel flow rate which reduces power production. A later extension by Vennell [2010] allowed for the response of the channel flow rate to the resistance presented by the turbines spanning the entire channel width by taking into account blockage effects predicted by Garrett and Cummins [2007]. The models have additionally been applied to other problems such as multiple channels [Cummins, 2013] and bays connected to oceans [Blanchfield et al., 2008].

One of the key purposes of these models is to help to determine the tidal stream resource of a tidal channel site. The models provide a well-defined upper bound on the resource, and have been widely used to assess tidal power potential [Sutherland et al., 2007, Karsten et al., 2008, O'Hara and Gallego, 2017]. However the models

either assume that the turbines occupy the full channel width or rely on numerical approximations. Vennell [2013] additionally analysed the efficiency of a tidal farm based on an actual site and found that exceeding the Betz limit needs additional careful consideration of structural load and blockage constraints. Refinements to the upper bound have been considered, with Adcock et al. [2013] locating a new upper-bound estimate for an actual site by numerically considering wake mixing losses, enabling the calculation of the power usefully available for extraction as opposed to the total power removed from the flow.

Whilst these models have significantly improved on the Betz limit for estimating tidal power efficiency, they still fall short of representing realistic turbine physics. In particular, although the Nishino and Willden [2012a] model does consider finite length fences, and is therefore appropriate for the realistically achievable low global blockages, it is restricted to a constant flow rate through the channel such that the turbine resistance has no influence on the channel dynamics. To address this issue, Gupta and Young [2017] proposed a quasi-steady theoretical model which combines the short fence extension to the two-scale theory [Nishino and Willden, 2013a] with both a free-surface deformation correction and the coupling of added drag with the upstream flow rate. Their flow rate model is based on a simplified static channel model detailed in Bryden and Couch [2007]. A numerical framework was developed in the work of Bonar et al. [2019], where the two-scale model was embedded and coupled to realistic rough and oscillatory channel flows, for which the potential power capture was found to be greater as compared to the stand-alone steady state two-scale model.

This paper presents a simplified analytic model that embeds the multi-scale partial fence model of Nishino and Willden [2012a] in the channel dynamics model of Garrett and Cummins [2005], drawing on the work of Willden et al. [2014]. The model allows for the analytic consideration of both rough bottom channels and oscillatory flow in a time-dependent framework, extending the work of Gupta and Young [2017]. The model also accounts for the increase in performance due to local and global blockage effects, extending the works of Garrett and Cummins [2005] and Vennell [2010] to a fence partially spanning the channel width. As the work of Draper and Nishino [2014] has shown, for a fixed number of turbines, a single co-planar side-by-side row of turbines outperforms multi-row array arrangements, be they streamwise aligned or staggered, the model presented in this paper is restricted to a single fence of turbines partially spanning the width of a head driven channel.

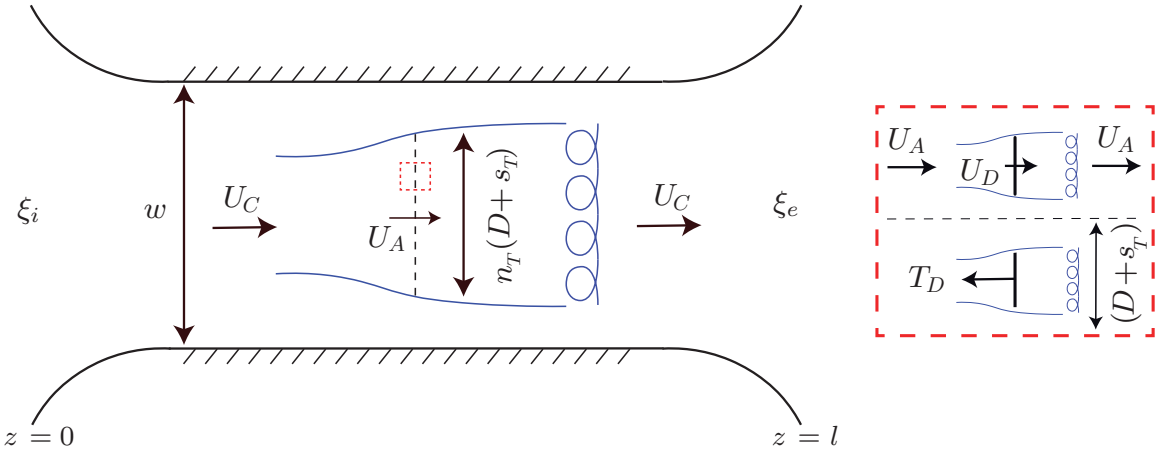

Figure 4.1: Schematic of a head-driven channel between two large basins in which a tidal turbine fence occupying part of the width of the channel is arrayed normal to the flow direction. An additional close-up view of a section of the fence shows the turbine scale flow problem. Remixing between core and bypass flows is shown for both turbine and fence scales.

4.3 Finite Fence Channel Dynamics Model

The flow problem is outlined by the sketch in figure 4.1 in which the flow is driven through the channel by a sinusoidally varying head difference between the channel ends. A turbine fence is positioned such that it partially occupies the width of the channel. The turbine fence consists of a large number, n_T, of closely spaced turbines each of diameter, D, that are arrayed with a tip-to-tip separation, s_T, in a plane normal to the channel flow direction.

The channel is simplified to be of rectangular cross-section with length l, width w and depth h. The flow is driven by the elevation difference across the channel ends, $\xi_i(t) - \xi_e(t)$, which is assumed to vary sinusoidally in time with amplitude a and frequency ω. This forcing could be extended to account for higher order interactions, for example the difference of sinusoidal tides at the ends of the channel. The resulting flow velocity through the channel is then $U_C(t) = Q(t)/A_C$, where $Q(t)$ is the flow rate, $A_C = wh$ is the cross-sectional channel area, and both U_C and Q are functions of time alone due to the geometric simplification of constant channel cross-section, and an assumption that the driving tidal wave is far longer than the channel length (as per Garrett and Cummins [2005]).

The flow through the turbine fence is modelled following the partial fence model of Nishino and Willden [2012a] in which two scales of flow are considered; device scale flow and array scale flow. At the array scale the resistance of the turbine fence causes flow diversion resulting in a lower approach velocity to the array, U_A, than the stream velocity U_C. Similarly at device scale the resistance of each individual turbine causes flow to divert around each device such that the flow velocity through each device, U_D, is less than the array approach velocity, U_A. Device scale mixing of device core and bypass flows occurs at dimensions scaling on the device diameter. This completes ahead of array scale mixing of array core and bypass flows, which occurs on dimensions scaling on the fence length. Through kinematic and dynamic coupling of the device and array scales of the finite fence problem, the Nishino and Willden [2012a] partial fence model provides a solution to the steady flow through the fence, and thus the power generated by the turbine fence, which may be conveniently parameterised by either turbine fence thrust or induction factor.

The Nishino and Willden [2012a] partial fence model is a steady flow model and hence implicitly assumes that the upstream mass flux is unaffected by the resistance within the channel, which can only be strictly true at vanishingly small global blockage. By coupling the channel dynamics problem with an assumed quasi-steady partial fence model, the impact of fence resistance on channel flow rate can be incorporated so that the more relevant problem of the performance of a partial fence placed within a head driven finite global blockage channel can be considered.

4.3.1 Channel Dynamics Model

The one-dimensional channel dynamics model of Garrett and Cummins [2005], which can be derived from the one-dimensional Euler equation, may be recast in non-dimensional form (the non-dimensional formulation was first presented in Willden et al. [2014], see appendix 4.A for a complete derivation):

$$\frac{dQ'}{dt'} - \cos t' = -\frac{1}{2}Q' \left|Q'\right| \frac{1}{\mathrm{Fr}_\omega^2}\left(B_A C_{TA} + C_f \frac{l}{h}\right) \tag{4.1}$$

in which the flow is driven through the (here presumed) rectangular cross-section channel by a sinusoidally varying head difference between the ends of the channel. $Q' = Q/Q_0$ is the non-dimensional flow rate, in which $Q_0 = (ga/\omega)(wh/l)$ is the peak volume flow rate in the undisturbed channel (assuming negligible inflow and exit kinetic energy fluxes, and the absence of bed friction). Time, t, is non-dimensionalised according to $t' = \omega t$. This non-dimensionalisation has been previously applied by

Muchala and Willden [2017] to investigate the impact of support structure drag on tidal turbine performance. In this model however, the addition of the $B_A C_{TA}$ group indicates the extension to the internal coupling of the Nishino and Willden [2012a] model.

The channel entry and exit are assumed smooth so that kinetic fluxes in and out of the channel may be neglected. The model equation (4.1) is an energy balance equation in which all terms are energy losses except for the driving head term $\cos t'$ which supplies energy to the channel. The unsteady term represents the energy required to accelerate the flow through the channel whilst the right hand side represents the energy lost to overcome opposing (resistive) forces.

The resistance to the flow has two contributions; from bed friction, included through the friction coefficient, C_f, and due to turbine array thrust, included through the array thrust coefficient, C_{TA}:

$$C_{TA} = \frac{T_A}{\frac{1}{2}\rho U_C^2 w_A h} \ , \tag{4.2}$$

in which T_A is the array thrust, $w_A = n_T(D + s_T)$ is the width of the turbine fence (array) and ρ is the fluid density. The proportion of the channel width occupied by the turbine fence is described by the array blockage ratio, B_A:

$$B_A = \frac{w_A}{w} \ . \tag{4.3}$$

The flow characteristics in the empty channel are governed by the non-dimensional groups Fr_ω and l/h, and the bed friction C_f. $\mathrm{Fr}_\omega = \omega l/\sqrt{ga}$ takes the form of a Froude number and can be shown to be proportional to the square-root of the ratio of cycle-averaged head supplied to the kinetic energy in the unresisted channel (see appendix 4.A). This channel-based Froude number describes the flow rate through the channel; for a fixed geometry channel increasing the amplitude of the tidal wave a (and thus decreasing Fr_ω) leads to an increase in flow rate through the channel as expected. The product $C_f(l/h)$ provides the overall bed resistance, and so increasing the depth of flow (and thus decreasing l/h) diminishes the importance of bed friction leading to an increase in the channel flow rate.

Specifying the product $C_f(l/h)/\mathrm{Fr}_\omega^2$ enables solution of the channel flow problem in the absence of turbines. In the case of a turbine fence installation we define the channel characteristics through specification of $C_f(l/h)$ and Fr_ω separately. The problem is then fully closed by specification of the proportion of the channel width occupied by turbines, B_A, and the array thrust coefficient, C_{TA}, which is provided

by kinematic and dynamic coupling to the partial fence model as outlined below. Although the resistive terms in the model equation (4.1) could be presented through two terms and hence two non-dimensional groups, as in Garrett and Cummins [2005], we choose here to use three; $C_f(l/h)$, Fr_ω and $B_A C_{TA}$ so as to properly separate channel characteristics from turbine characteristics.

Solution of the model equation (4.1) is achieved by first-order time marching, such that the global error grows with the time-step. Higher-order schemes can be used but are not strictly necessary given the simplicity of the model equation. Following several transient cycles, periodic solutions, of period $2\pi/\omega$, are obtained over which the time average farm thrust and power may be determined. The periodicity of the solution allows for alternative approaches to solving the model equation, particularly in the frequency domain. These could be considered for cases where rapid solutions are required, or where the phase spectrum is of direct interest. We also note that additional physical mechanisms may potentially increase the time averaged power above the model predictions such as dynamic effects following the change in tide direction [Bonar et al., 2019].

4.3.2 Partial Fence Model

Specification of the turbine fence thrust as a function of channel flow rate is sufficient to close the problem. Here we use the partial fence model of Nishino and Willden [2012a]. The turbine fence is taken to lie in a plane normal to the flow direction and the fence does not fully occupy the width of the channel as required from practical bathymetric and shipping considerations; see figure 4.1. Hence, the array approach flow is divided into an array core stream, of velocity U_A, and an array bypass stream. The array core stream may itself be divided into n_T stream tubes, with each approaching a single device. Each device stream tube may again be divided into a device core stream, with flow speed through the device of $U_D = U_A(1 - \alpha_L)$, and a device bypass stream. Downstream of the array we assume a separation of scales between device and array scale mixing. Device scale mixing, between the device core and bypass flows, scales on the device diameter D and occurs ahead of the start of array scale mixing, between the array core and bypass flows, which scales on the length of the array w_A. The model implicitly assumes that the fence is sufficiently long (large enough n_T) for this separation to be valid, and that the channel is sufficiently long, multiples of w_A, for array scale mixing to be completed within the channel. The numerical simulations of Nishino and Willden [2013a] suggest that the restriction on n_T to achieve

scale separation is not particularly onerous, with $n_T \geq 8$ achieving good agreement between theory and computation.

Each of the inner, device scale, problem and the outer, array scale, problem may be solved by application of the Garrett and Cummins [2007] model of device performance in a blocked flow passage. Their model extends the conservation of linear momentum theory conventionally applied to unbounded wind turbines in which the outer flow can expand freely, to the case of a device in a finite cross-section flow passage in which the flow can no longer expand in an unconstrained manner. Such geometric constraint results in the acceleration of the device bypass flow. It is assumed that downstream of the device, the core flow expands and the bypass flow contracts until a point of pressure equilibrium between the two streams is reached, following which the core and bypass flows remix to recover a uniform stream. Unlike the unbounded wind turbine theory this blocked theory results in a solution in which a favourable pressure gradient is developed between the far upstream and downstream conditions. As in Garrett and Cummins [2007] blocked device model, we here neglect changes in the free surface elevation and assume the flow is bounded by a rigid lid. At the channel scale, however, following Garrett and Cummins [2005], we assume a channel depth that varies in time according to the driving tidal wave. Relaxation of the rigid-lid assumption at the device and array scales only has a significant impact on the model predictions for large Froude number ($\mathrm{Fr} = U_C/\sqrt{gh}$) channels [Vogel et al., 2016] or high global blockage ratios. As Froude numbers for realistic tidal channels are comparatively low ($0.1 \leq \mathrm{Fr} \leq 0.2$ [Vogel et al., 2016]), and the results presented herein show peak performance points at modest global blockage ratios (see §4.4), the rigid-lid assumption made in the partial fence model will only introduce small errors for practical turbine array deployment scenarios.

Starting with the inner device scale problem, we use the device scale thrust coefficient, C_{TL}, to non-dimensionalise the device scale thrust, T_D, through

$$C_{TL} = \frac{T_D}{\frac{1}{2}\rho U_A^2 \pi D^2/4} \ . \tag{4.4}$$

Applying Garrett and Cummins [2007] model to the device scale problem enables this thrust coefficient to be evaluated through

$$C_{TL} = (1-\gamma_L)\left[\frac{(1+\gamma_L) - 2B_L(1-\alpha_L)}{(1-B_L(1-\alpha_L)/\gamma_L)^2}\right] \ , \tag{4.5}$$

in which γ_L is the ratio of the device scale wake velocity (at the device scale pressure equilibrium location) to the device approach velocity U_A, and B_L is the local blockage

ratio defined as

$$B_L = \frac{\pi D^2/4}{(D + s_T)h} \ , \tag{4.6}$$

in which the denominator is the cross-sectional area of the device scale flow passage. The ratio of device wake to approach velocity, γ_L, is related through mass conservation to the device induction factor, α_L, through:

$$1 - \alpha_L = \frac{1 + \gamma_L}{(1 + B_L) + \sqrt{(1 - B_L)^2 + B_L(1 - 1/\gamma_L)^2}} \ , \tag{4.7}$$

Once the local blockage has been specified, equations (4.5) and (4.7) may be solved for C_{TL} as a function of α_L alone. For each $0 < \gamma_L < 1$, equation (4.7) provides a unique solution $0 < \alpha_L < 1$, which then solves for a unique C_{TL} in equation (4.5).

Following Nishino and Willden [2012a], who first developed this two scale model, we now apply the Garrett and Cummins [2007] model to the array scale problem resulting in a similar form of equations that relate the array thrust coefficient C_{TA} to the array induction factor α_A, which itself relates the array approach flow velocity to the channel flow velocity through, $U_A = U_C(1 - \alpha_A)$. Once the array blockage, B_A, has been specified the array thrust C_{TA} is parameterised by α_A as follows:

$$C_{TA} = (1 - \gamma_A)\left[\frac{(1 + \gamma_A) - 2B_A(1 - \alpha_A)}{(1 - B_A(1 - \alpha_A)/\gamma_A)^2}\right] \ , \tag{4.8}$$

in which γ_A is the ratio of array wake velocity (at the array scale pressure recovery location) to the upstream channel velocity U_C, and relates to the array induction α_A by

$$1 - \alpha_A = \frac{1 + \gamma_A}{(1 + B_A) + \sqrt{(1 - B_A)^2 + B_A(1 - 1/\gamma_A)^2}} \ . \tag{4.9}$$

The device and array problems are coupled kinematically through the array approach velocity U_A and dynamically through specifying the array thrust to be n_T times the device thrust, i.e. $T_A = n_T T_D$, or non-dimensionally:

$$C_{TA} = (1 - \alpha_A)^2 B_L C_{TL} \ . \tag{4.10}$$

The kinematic and dynamic coupling closes the partial fence problem leading to solution for array thrust as a function of device induction factor. Each device is assumed to be a perfect energy extractor so that it delivers power $P_D = T_D U_D$. Once device thrust, and device and array velocities have been determined, the device

local power coefficient, C_{PL}, and array global power coefficient, C_{PG}, may be trivially determined from:

$$C_{PL} = \frac{P_D}{\frac{1}{2}\rho U_A^3 \pi D^2/4} \ , \tag{4.11}$$

$$C_{PG} = \frac{n_T P_D}{\frac{1}{2}\rho U_C^3 n_T \pi D^2/4} = (1-\alpha_A)^3 C_{PL} \ . \tag{4.12}$$

4.3.3 Coupled channel-partial fence dynamics model

For any given turbine layout, specified through the combination of local blockage, B_L, which represents the spacing between turbines, and global blockage, $B_G = B_L B_A$, (the ratio of total disc to channel cross-sectional areas), which represents the total number of turbines, the dynamic channel flow problem can be solved as a function of the applied fence thrust $B_A C_{TA}$. The partial fence model provides this non-dimensional group in equation 4.1 as a function of the array induction factor.

To couple the partial fence model to the channel flow model we make the assumption that the fence operates at a constant array (or indeed device) induction factor across the entire tidal cycle; that is that the turbines in the fence operate solely with local knowledge so as to reduce the speed of the approach flow through the turbines by a fixed proportion (the induction factor) (as do wind turbines operating below rated flow speeds). The partial fence model may be conveniently solved in advance of the channel flow problem to provide the fence performance parameterised across the range of array induction factors $0 \leq \alpha_A \leq 1$.

The Fr_ω and $C_f(l/h)$ groups are set based on the driving tidal wave, and channel geometry and bed friction estimates. Equation 4.1 is then integrated forward in time until the peak amplitude of the channel flow rate, $\hat{Q}/Q_0$, converges across consecutive cycles. Figure 4.2 shows an example output Q/Q_0 for the peak performance point over two tidal cycles. Across the parameter space, the solution always converges to a periodic wave-form, but not necessarily to a single frequency cosine.

The solution presents in terms of a fence performance, which we assess through the cycle-averaged channel based power coefficient C_{PC} across the range of array induction factors α_A, with each induction factor corresponding to an applied global thrust coefficient, C_{TG}, defined by:

$$C_{TG} = \frac{C_{TA}}{B_L} \ , \tag{4.13}$$

which acts to reduce the amplitude of the flow rate by a factor $\hat{Q}/Q_0$. The thrust and power coefficients normalised by the peak channel flow rate (consistent with Garrett

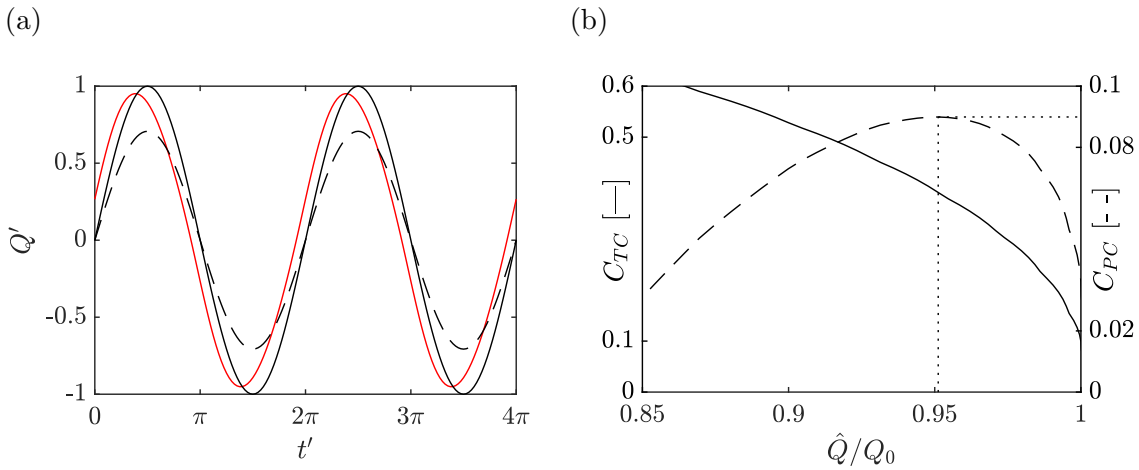

Figure 4.2: Example solutions to the channel flow rate over two tidal cycles. (a) The solid black line shows the undisturbed flow rate, the dashed line the flow rate assuming peak power production with homogeneous resistance in the Garrett and Cummins [2005] model, and the solid red line the coupled fence-channel model flow rate for a specified fence geometry. (b) For a specified arrangement of turbines, the relationship between the peak flow rate reduction and the channel thrust and power coefficients. The peak power point locates the optimal thrust and necessary flow reduction for the specified arrangement.

and Cummins [2005]) are defined by:

$$C_{TC} = \frac{n_T T_{D,\max}}{\rho g a A_C} \tag{4.14}$$

$$C_{PC} = \frac{n_T \overline{P_D}}{\rho g a Q_0} \ , \tag{4.15}$$

where the overbar denotes a time-average over a complete period of the driving tidal wave, and where $T_{D,\max}$ is the peak thrust over a tidal period.

As the channel thrust is increased the flow rate through the channel is reduced (figure 4.2b). There is a consequent variation in the channel power which at first increases until a peak performance is reached, before reducing as the channel flow rate is reduced. This paper focuses on these optimal extraction points, which are unique for each set turbine arrangement (B_L, B_G). Finally, we here define C_{TD} to be the peak single disc thrust

$$C_{TD} = \frac{T_{D,\max}}{\rho g a A_T} = \frac{C_{TC}}{B_G}, \tag{4.16}$$

as a metric to assess peak turbine loads. We assume the channel and turbine peak resistances C_{TC} and C_{TD} to be constant from cycle to cycle.

Channel	Length l (m)	Driving head amplitude a (m)	Depth h (m)	l/h	Fr_ω
Small tidal channel	5000	0.26	20	250	0.438
Pentland Firth	20000	0.9	50	400	0.946

Table 4.1: Example channel dimensions based on a hypothetical small channel and the Pentland Firth.

The partial fence formulation is the precursor step that provides one of the inputs to the channel dynamics model, and the two models may be conveniently solved sequentially. In discussion of model results, for each B_G and B_L we concentrate on the fence thrust that results in the maximum C_{PC} as being the solution of interest to the channel-fence problem. To then map the performance over a range of B_L and B_G this process may be repeated for $B_G \leq B_L \leq 1$, $0 \leq B_G \leq B_L$. In the absence of additional bed friction, the assumptions underpinning the limiting case as $B_L, B_G \to 1$ converge to the Garrett and Cummins [2005] channel model. In all cases where $C_f = 0$, the homogeneous array ($B_L, B_G \to 1$) flow rate reduction therefore approaches near $\hat{Q}/Q_0 = 2^{-1/2}$, and peak power approaches $C_{PC} = 0.24$ (see for example figures 4.3a and 4.3c, and the Garrett and Cummins [2005] homogeneous fence solution).

4.4 Finite Fence Performance in a Head Driven Channel

To contextualise the model results we first consider typical tidal channel dimensions presented in table 4.1 (taken from Vennell and Adcock [2014]), from which realistic ranges of the non-dimensional groups can be readily determined. As a reference case, we first consider a channel with a Fr_ω between that of the two example channels listed in table 4.1. We then vary Fr_ω and consider the impact of bed friction assuming a typical bed friction coefficient of $C_f = 0.002$ across channel l/h ratios spanning the typical geometric ranges observed.

4.4.1 Zero bed friction reference case

An example solution for the head driven array model is shown in figure 4.3 to demonstrate the impact of blockage on the fence performance in a channel with coupled upstream flow. This reference case is within the range of practical interest; we

take a lunar frequency of $\omega = 1.4 \times 10^{-4}$ rad s^{-1}, equivalent to the dominant lunar M_2 frequency, assume a tidal amplitude of $a = 0.5$m, a tidal turbine diameter of $D = 20$m, and a channel length of $l = 10$km, resulting in a channel Froude number of $\mathrm{Fr}_\omega = 0.635$. For now, we assume that the channel bed friction C_f is negligible, but later compare against cases with non-zero bed friction in section 4.4.3.

The channel power coefficient C_{PC}, contoured in figure 4.3a, increases with increasing global blockage. For any given global blockage (or specified flow reduction factor $\hat{Q}/Q_0$) there exists a corresponding B_L to maximise power generation, much as in the steady flow partial fence model [Nishino and Willden, 2012a]. The physics of this increase in extractable power by local and global blockage mechanisms is discussed in detail in Dehtyriov et al. [2021]. We additionally define the return parameter

$$R = \frac{C_{PC}}{B_G} \propto \frac{\text{Total power extracted}}{\text{Total frontal turbine area}} , \tag{4.17}$$

which may be usefully interpreted as income (power generated) per cost (turbine area). The maximum return, and the corresponding optimal turbine layout (B_L and B_G), can be determined from the model. Figure 4.3b shows the contours of the return parameter for the reference flow case, with the optimum indicated. For large channels where the turbine fence is expected to occupy a small proportion of the channel cross section ($B_G \to 0$), there remains an optimal spacing B_L to maximise return. Increasing B_G then increases the peak return at a new optimal B_L, with the largest return ratio in this case realised for $B_G \approx 0.18, B_L \approx 0.49$. Further increases in B_G then allow higher levels of achievable channel power C_{PC} at the cost of a lower return, i.e. there are diminishing benefits from adding more turbines.

Furthermore, there may exist maximum permissible flow rate reductions, as shown by the contours in figure 4.3c, due to environmental constraints for which a typical limit is $\hat{Q}/Q_0 = 0.95$ [The Carbon Trust, 2011]. For the reference case, the maximum return falls just within this assumed environmental constraint, however careful consideration of the environmental impact is necessary for layout design where the optimal return requires larger attenuation of flow rate. For a quantified understanding, figure 4.3d plots the maximum return and channel power coefficients, together with the channel thrust coefficient at which these occur, along contours of the maximum allowable flow reduction. As the constraint is tightened, channel power and thrust monotonically fall (tending to zero as $\hat{Q}/Q_0 \to 1$), but the optimal return is here realised for $\hat{Q}/Q_0 = 0.95$, and movement away from this optimum decreases the return. Therefore, all else being equal, tightening of the constraint, i.e. reducing flow rate impact, requires the turbine layout to be changed with reductions in both global

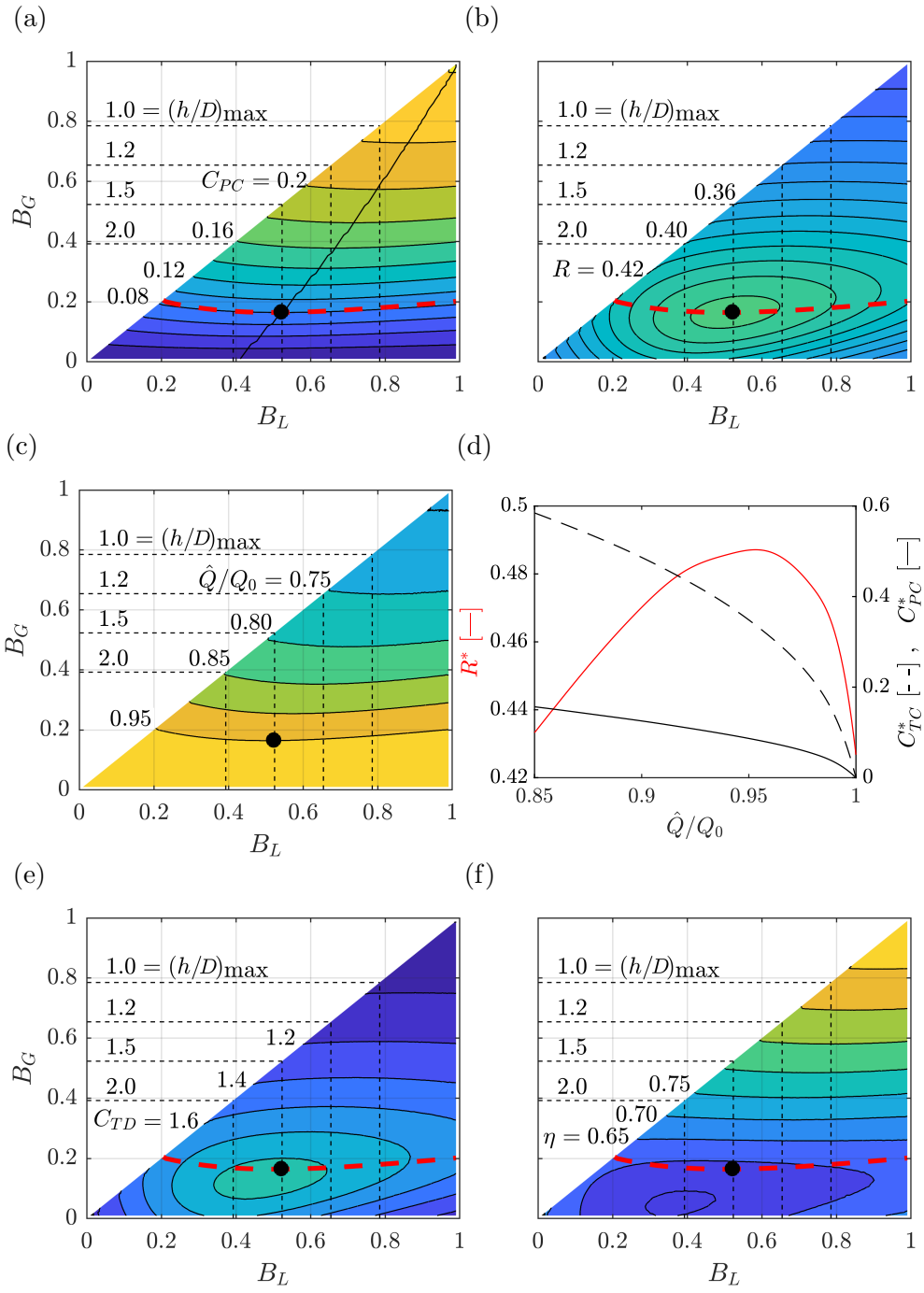

Figure 4.3: Contours of fence performance for $\mathrm{Fr}_\omega = 0.635$, $C_f = 0$, l/h undefined. Figures correspond to the array thrust setting that achieves maximum fence performance C_{PC} at the indicated combination of blockage ratios. The black circle represents the maximum return point and the red dashed line the locus of the channel environmental constraint $\hat{Q}/Q_0 = 0.95$. Dashed lines provide geometric limits on blockages for ratios of channel depth h to turbine diameter D. (a) Channel power coefficient with the solid black line indicating the locus of maximum C_{PC} with global blockage; (b) return parameter; (c) normalised peak flow rate; (d) peak return, peak power coefficient and corresponding channel thrust across contours of normalised peak flow rate; (e) disc thrust coefficient; (f) basin efficiency.

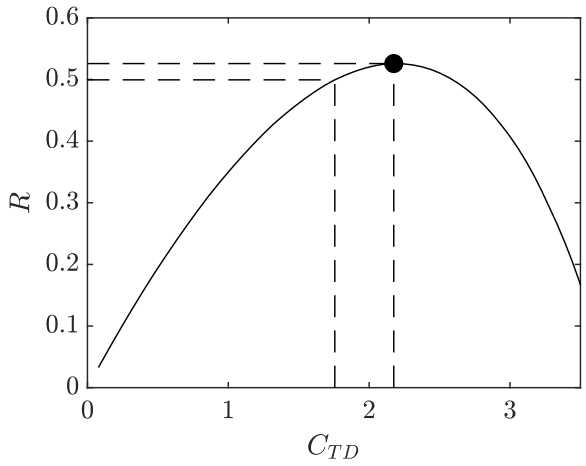

Figure 4.4: The impact of varying the peak disc thrust coefficient, C_{TD}, on the return parameter at the optimal design (B_L, B_G) point for the reference flow case shown in figure 4.3. The impact on return of a 20% de-rating of the thrust is also shown.

blockage (fewer turbines) and local blockage (more spaced out) in order to maximise return and power.

At this optimal return point, the local blockage is relatively high, and the optimal induction factor to maximise the channel power coefficient increases when compared to unblocked and blocked flow models at the same global blockage [Garrett and Cummins, 2007]. Similar to the two-scale and blocked flow models, this leads to a larger peak operating disc thrust coefficient shown in figure 4.3e which needs to be further accounted for in the design of the turbine structure. The root-mean-squared thrust can be estimated by dividing the peak thrust by $\sqrt{8/3}$, but, depending on the global blockage, it is likely that power capping control strategies will still be required by real turbines to limit the maximum thrust whilst operating at the optimal flow reduction factor as suggested by Vogel et al. [2019]. For instance, figure 4.4 shows how a controlled reduction in the thrust at the optimal design point for maximising return would impact the return. An example 20% de-rating from the peak thrust point would only decrease the return by 5%. Furthermore, such thrust capping may also only be necessary at near peak flow speeds.

Additionally, an increase in extractable power due to non-zero local blockage results in a decrease in the basin efficiency η, the ratio of power extracted by the turbines to the total power removed from the flow (figure 4.3f) (with the latter necessarily exceeding the former due to the energy lost in wake remixing processes). A minimum allowable basin efficiency could be considered as an additional constraint for optimisation of the return. It is here useful to note that a Betz-optimum unblocked wind

turbine operates with a basin efficiency of 2/3, and so for the model parameters set in this reference case, the efficiency of extraction (basin efficiency) does not fall far below the unblocked optimum ($\eta = 0.59$ for maximum return).

Finally, we note that the maximum local blockage is constrained by the depth of the channel. In this case, the optimal return is realised for $(h/D)_{\max} \approx 1.5$. For the assumed turbine diameter of $D = 20$m, the channel depth is therefore bounded by $h \leq 30$m to achieve this optimal blockage ratio in a fence configuration. For deeper channels, alternative non single row fence arrangements of turbines are hence necessary to optimise return.

Of further interest is how variations in the channel parameters affect the optimal turbine configuration. In sections 4.4.2-4.4.3 we hence consider variations in the non-dimensional groups governing the channel characteristics, namely the channel Froude number $\mathrm{Fr}_\omega = \omega l/\sqrt{ag}$, and the channel friction parameter $C_f(l/h)$.

4.4.2 Effect of variation in channel Froude number

The channel based Froude number can be physically interpreted as proportional to the square-root of the ratio of cycle-averaged driving head to kinetic head (see appendix 4.A). Therefore for a fixed driving head, the kinetic head decreases with increasing Froude number, and we might therefore expect a lower return. Figures 4.5-4.6 illustrate the impact of the channel Froude number on both the fence performance and the environmental impact respectively. Here, we consider two simple changes to the reference channel flow case. For figures in the left columns, we assume that the tidal range has risen to $a = 0.8$m such that $\mathrm{Fr}_\omega = 0.5018$ (for the same channel dimensions and tidal frequency), and in the right columns we assume that the tidal range has fallen to $a = 0.2$m such that $\mathrm{Fr}_\omega = 1.004$.

For a fixed global blockage or relative flow rate, there remains an optimal local blockage to maximise the channel power coefficient. However, increase in channel Froude number for fixed B_G causes the channel power coefficient to decrease (figures 4.5a-4.5b). For example, in this case for $B_G = 0.2$, C_{PC} falls $\sim 64\%$ through the increase in Fr_ω considered. Interestingly, for either fixed B_G or $\hat{Q}/Q_0$, the optimal spacing B_L for maximising C_{PC} between the two cases does not change. For a fixed number of turbines or fixed environmental constraints therefore, the channel dynamics only impact the resultant power output and not the optimal configuration.

By contrast, both the magnitude and location of the maximum return vary significantly with variation in Fr_ω (figures 4.5c-4.5d). The magnitude of the optimal return

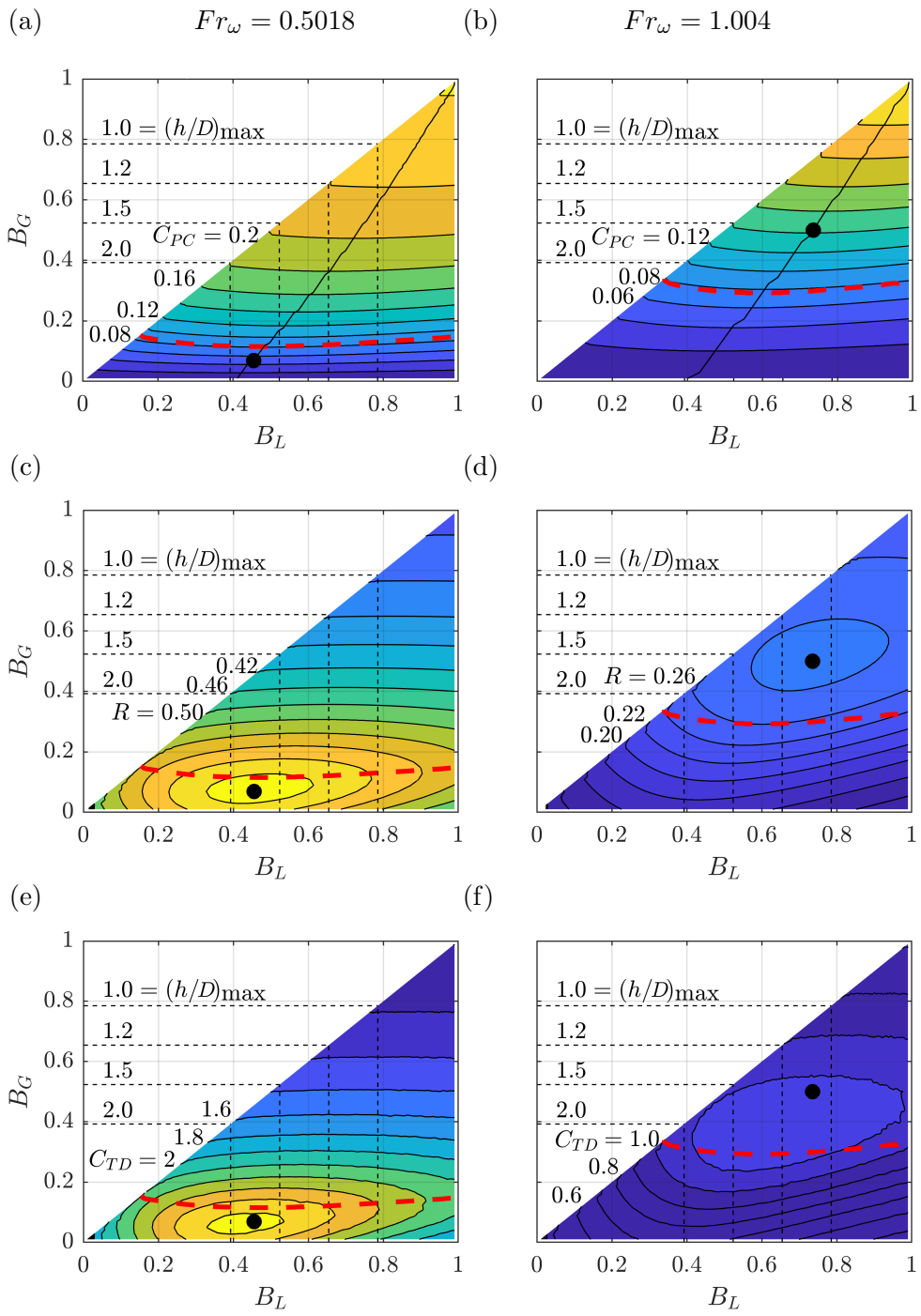

Figure 4.5: Contours of fence performance comparing $\mathrm{Fr}_\omega = 0.5018$ in the left column and $\mathrm{Fr}_\omega = 1.004$ in the right column, both for $C_f = 0$ and l/h undefined. Figures correspond to array thrust setting that achieves maximum fence performance C_{PC} at indicated combination of blockage ratios. The black circle represents the maximum return point and the red dashed line a locus of the channel environmental constraint $\hat{Q}/Q_0 = 0.95$. Dashed lines provide geometric limits on blockages for ratios of channel depth h to turbine diameter D. (a)-(b) Channel power coefficient with the solid black line indicating the locus of maximum C_{PC} with global blockage; (c)-(d) the return parameter; (e)-(f) the disc thrust coefficient.

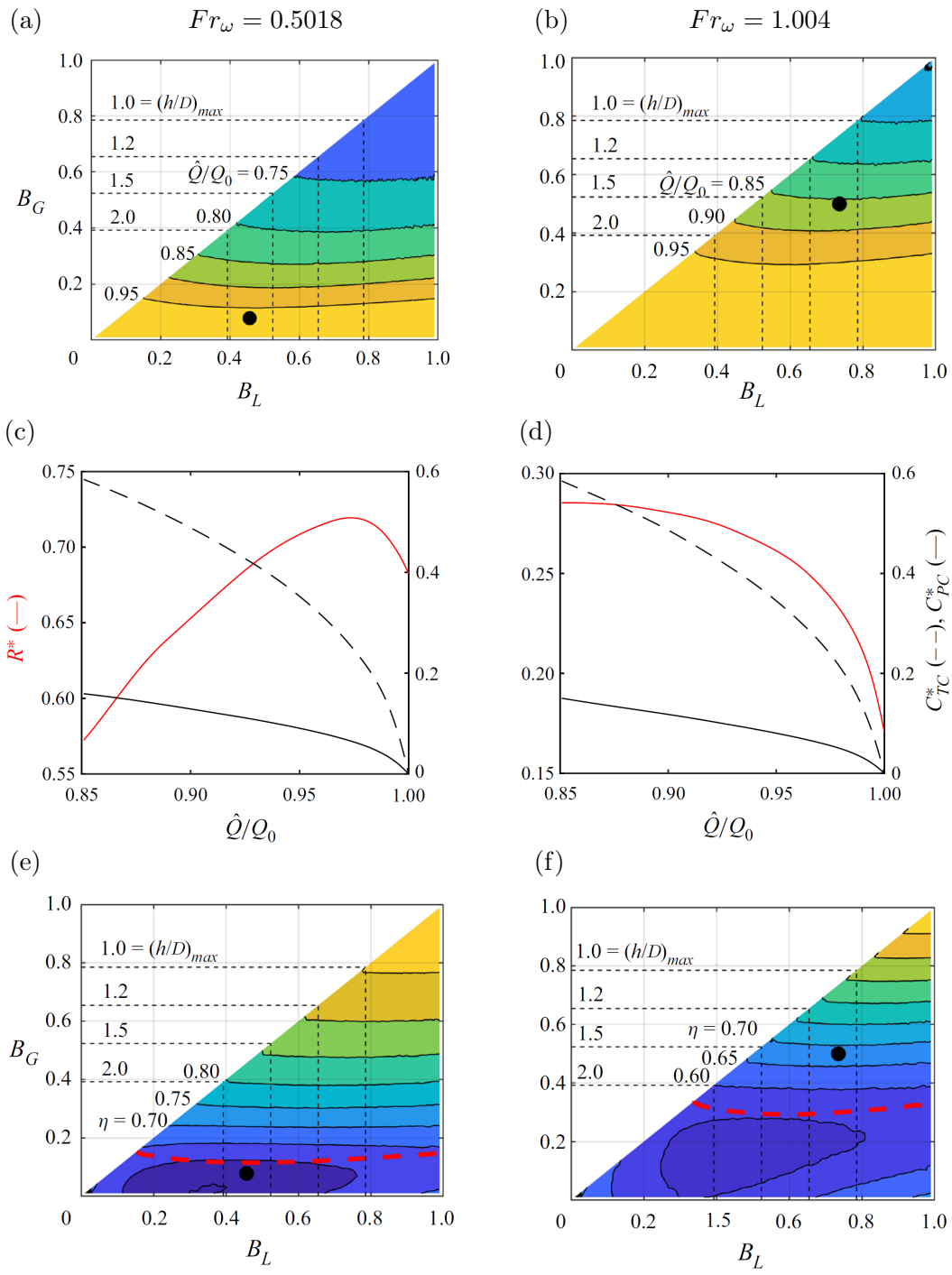

Figure 4.6: Contours related to channel environmental constraints for $\mathrm{Fr}_\omega = 0.5018$ (left column) $\mathrm{Fr}_\omega = 1.004$ (right column), with $C_f = 0$ and l/h undefined. Figures correspond to the array thrust setting that achieves maximum fence performance C_{PC} at the indicated combination of blockage ratios. The black circle represents the maximum return point and the red dashed line the locus of the channel environmental constraint $\hat{Q}/Q_0 = 0.95$. The dashed lines provide geometric limits on ratios of channel depth h to turbine diameter D. (a)-(b) normalised flow rate; (c)-(d) peak return, peak channel power coefficient and corresponding channel thrust coefficient across contours of normalised flow rate; (e)-(f) basin efficiency.

increases with decreasing channel Froude number, and is realised at both lower local blockage and global blockage. This is particularly important when considering constraints on the flow reduction, with high Fr_ω channels necessitating a larger move away from the optimum under the same constraint (here plotted for $\hat{Q}/Q_0 = 0.95$). Similar to the reference flow case, as well as the two-scale and blocked flow models, an increase in the return can be broadly correlated to an increase in the disc thrust coefficient (figures 4.5e-4.5f), with peak C_{TD} of the low Fr_ω case more than three times larger than the high Fr_ω case. Turbines will therefore need to be carefully designed for the specific channel dynamics and both channel and turbine fence configuration selection is critical for optimal return at a given site.

Figure 4.6 details the environmental impact of turbines operating in channels of varying Fr_ω. The decreases in C_{PC} with increasing Fr_ω observed in figure 4.5 correspond to smaller environmental impacts, and so the gradients with respect to the global blockage ratio of both the relative flow rate (figures 4.6a-4.6b) and basin efficiency (figures 4.6e- 4.6f) are likewise smaller. For high Fr_ω channels, the larger B_G and B_L necessary to maximise return and increase channel power C_{PC} are therefore more attainable due to reduced environmental impact. However, for a given flow rate constraint, the maximum return moves further outside of the constraint envelope as Fr_ω increases. This is quantified in figures 4.6c-4.6d, where for the large Fr_ω case, the maximum return continues to rise with further relaxation of the constraints to $\hat{Q}/Q_0 = 0.85$, whilst for the low Fr_ω case, peak return is achieved at minimal environmental impact ($\hat{Q}/Q_0 \approx 0.98$). Note that although the lower Fr_ω case achieves its maximum return at reduced environmental impact, the power delivered, C_{PC}, is itself lower than in the higher Fr_ω case.

A final consideration for optimising channels with high Fr_ω is that as the optimal blockage ratio increases, the maximum allowable channel depth for a single row turbine fence configuration falls. For turbines operating in high Froude number channels with large depths, interlaced co-planar multi-row arrangements of turbines are a more likely design consideration for optimal energy extraction.

4.4.3 Effect of channel bed friction

We now turn our attention to the effect of $C_f(l/h)$ on both the environmental constraints and array performance. To allow for a clear comparison, the bed friction coefficient is assumed to be $C_f = 0.002$, and we present the results for the reference case channel Froude number $\mathrm{Fr}_\omega = 0.635$. As $C_f(l/h)$ appears combined as a non-dimensional group in equation 4.1, any change in l/h for a fixed bed friction and fixed

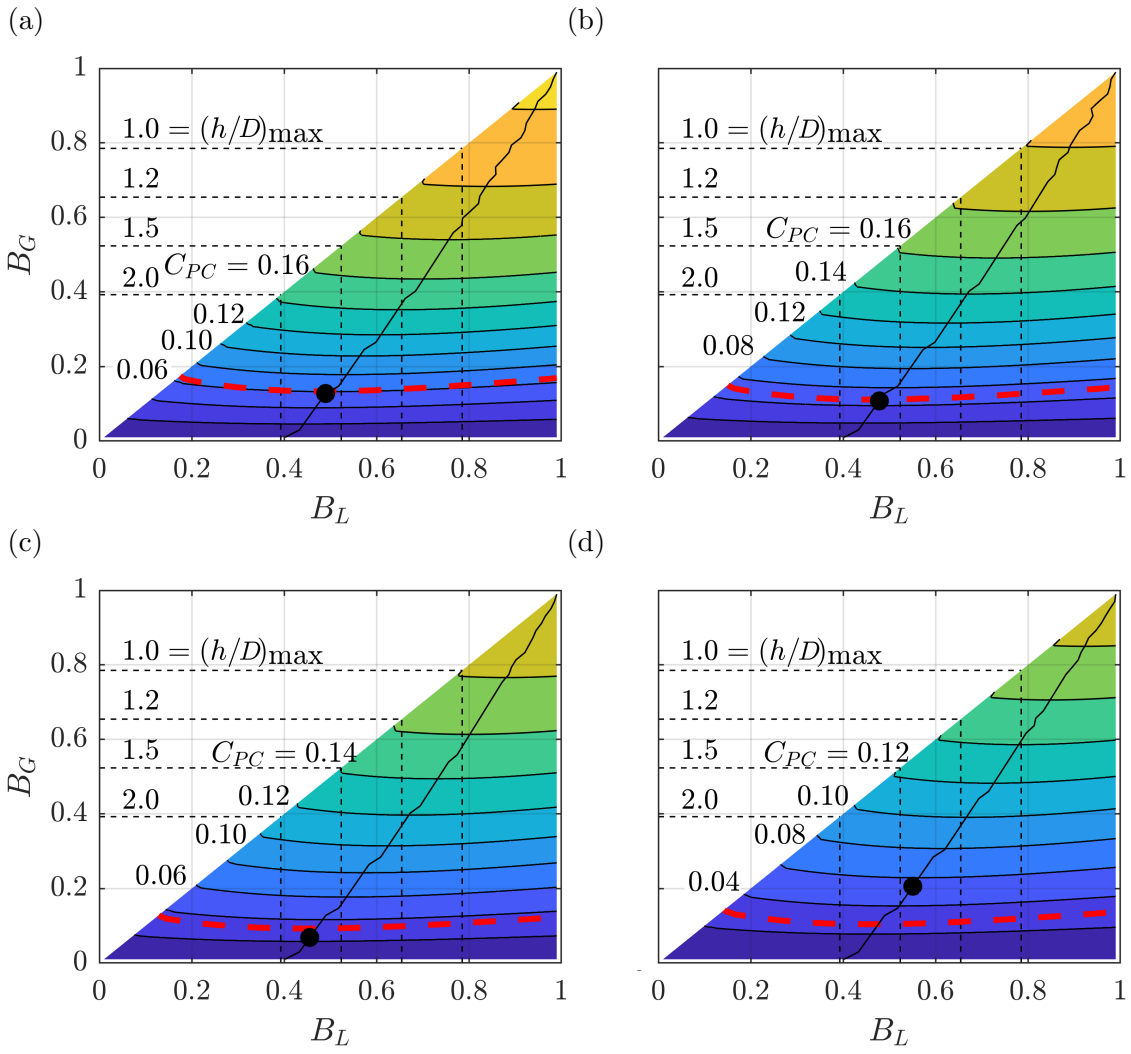

Figure 4.7: Contours of the channel power coefficient C_{PC} for $\mathrm{Fr}_\omega = 0.635$ and $C_f = 0.002$ comparing differences in the impact of bed friction by varying l/h. All figures correspond to the array thrust setting that achieves maximum fence performance C_{PC} at the indicated combination of blockage ratios. The black circle represents the maximum return point and the red dashed line the locus of the channel environmental constraint $\hat{Q}/Q_0 = 0.95$. The dashed lines provide geometric limits on blockages for ratios of channel depth h to turbine diameter D. (a) $l/h = 50$; (b) $l/h = 100$; (c) $l/h = 250$; (d) $l/h = 500$.

channel Froude number is equivalent to holding l/h constant and varying C_f by the same amount. It is also useful to interpret increasing l/h with Fr_ω and C_f fixed as a reduction in channel depth, which should increase the significance of bed friction in the dynamical balance equation. Bed friction and turbine resistance compete with each other to resist the flow, and hence for a fixed global blockage (and non-zero bed friction), increases in l/h increase the bed resistance leading to reductions in the performance of the tidal fence.

Figure 4.7 illustrates this decrease in channel power with increasing $C_f(l/h)$. For instance, for $B_G = 0.2$, C_{PC} falls by close to 50% with an increase in l/h from 50 to 500. As with changes in Fr_ω, the C_{PC} locus does not vary with changes in $C_f(l/h)$, suggesting that this locus is universal. A curve fit shows that

$$B_L = \frac{9B_G + 4}{3B_G + 10} \tag{4.18}$$

is a good approximation to estimating the turbine spacing required to maximise power depending on the achievable level of global blockage. We also note that in all cases, the maximum return lies on this locus, but may occasionally lie outside of the acceptable environmental constraint envelope. As $B_G \to 0$, the optimum local spacing $B_L \to 0.4$ which recovers the local blockage for maximum power found in the partial fence model without channel flow interaction [Nishino and Willden, 2012a].

The return is shown in figure 4.8, where we observe that compared to variations in Fr_ω, the blockage ratios required to achieve peak return do not vary nearly as strongly. Although the optimal return decreases monotonically with increasing l/h, the location of the optimal return does not, due to nonlinearity of the governing equation, first occurring at decreasing B_G up to $l/h = 250$ before at increasing B_G for $l/h = 500$. The magnitude of the optimal return is significantly impacted by frictional losses. Additionally, as the integrated bed friction increases, the gradient of the return decreases, and near maximum returns can be realised across a large range of B_L and B_G. Approximately optimal returns can be achieved across a broad range of blockages whose bed friction is significant. By contrast, the low Fr_ω zero bed friction channel (see figure 4.5c), has a steep return gradient, and careful consideration of blockage is necessary to optimise return.

The nominal flow rate Q_0, which for $C_f(l/h) > 0$ is defined to be the channel flow rate without turbines but with bed friction, naturally decreases significantly with increasing bed friction, however the normalised flow rate $\hat{Q}/Q_0$ shown in figure 4.9 is not significantly impacted. This stands in contrast to variations in Fr_ω, and implies that an increase in the bed friction does not significantly change the environmental constraints on permissible blockage ratios. For high bed friction channels, design for large blockage ratios to maximise C_{PC} will be highly constrained by flow rate considerations, principally due to the flow rate reduction caused by the bed friction itself. These observations are consistent with Vennell [2013], Vennell et al. [2015] who observed diminishing returns for additional turbines in channels with high relative bed friction.

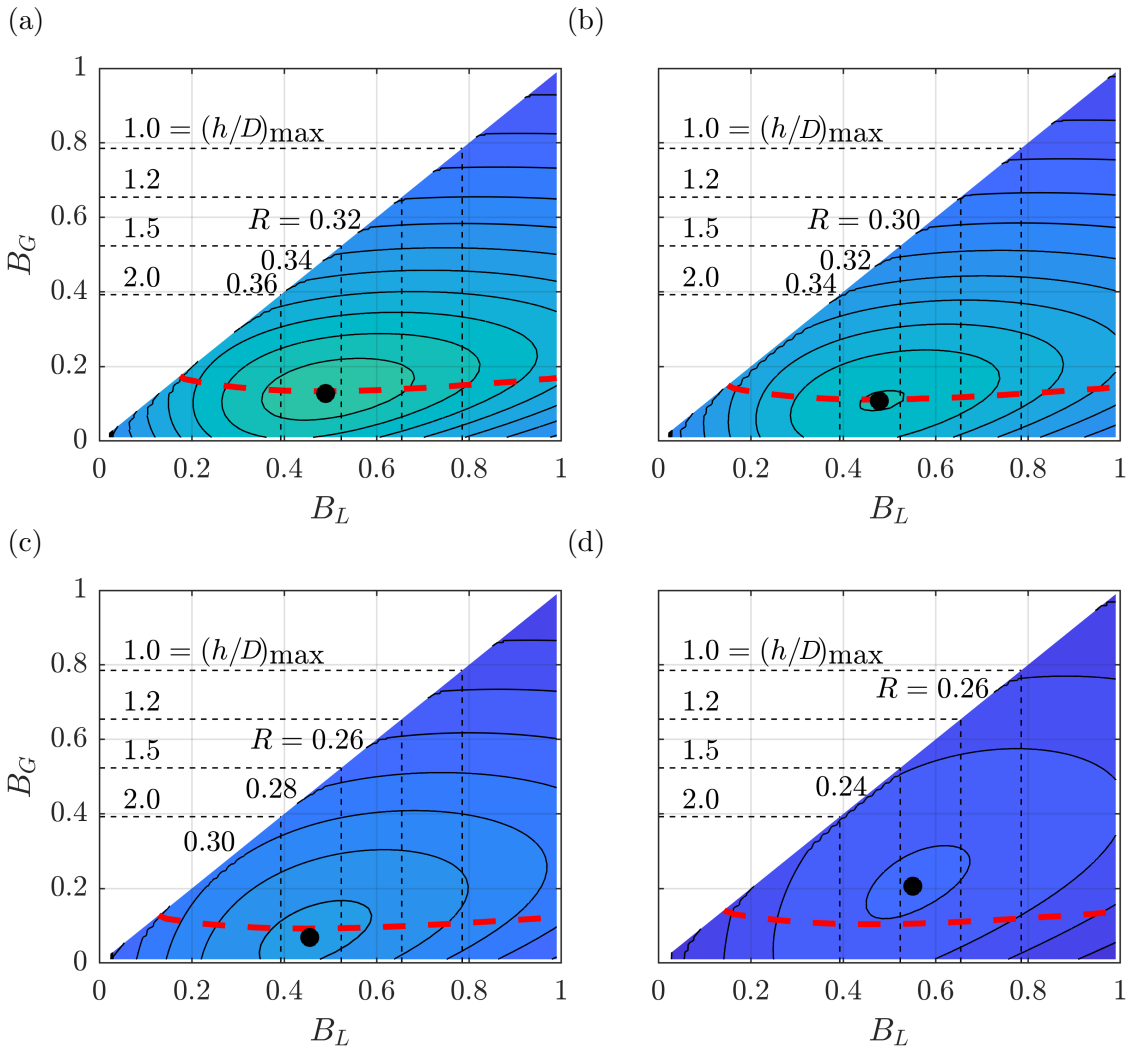

Figure 4.8: Contours of the return parameter R for $\mathrm{Fr}_\omega = 0.635$ and $C_f = 0.002$ comparing differences in the impact of bed friction by varying l/h. All figures correspond to the array thrust setting that achieves maximum fence performance C_{PC} at the indicated combination of blockage ratios. The black circle represents the maximum return point and the red dashed line the locus of the channel environmental constraint $\hat{Q}/Q_0 = 0.95$. The dashed lines provide geometric limits on blockages for ratios of channel depth h to turbine diameter D. (a) $l/h = 50$; (b) $l/h = 100$; (c) $l/h = 250$; (d) $l/h = 500$.

4.4.4 Designing for maximum return

Horizontal slices through the return contours at the global blockages for maximum return and for globally unblocked channels are shown in figure 4.10. For a given set of non-dimensional channel groups, there is always a local blockage B_L which maximises return, and homogenous spacing that does not exploit the local blockage effect decreases the return in all cases. As the channel Froude number decreases,

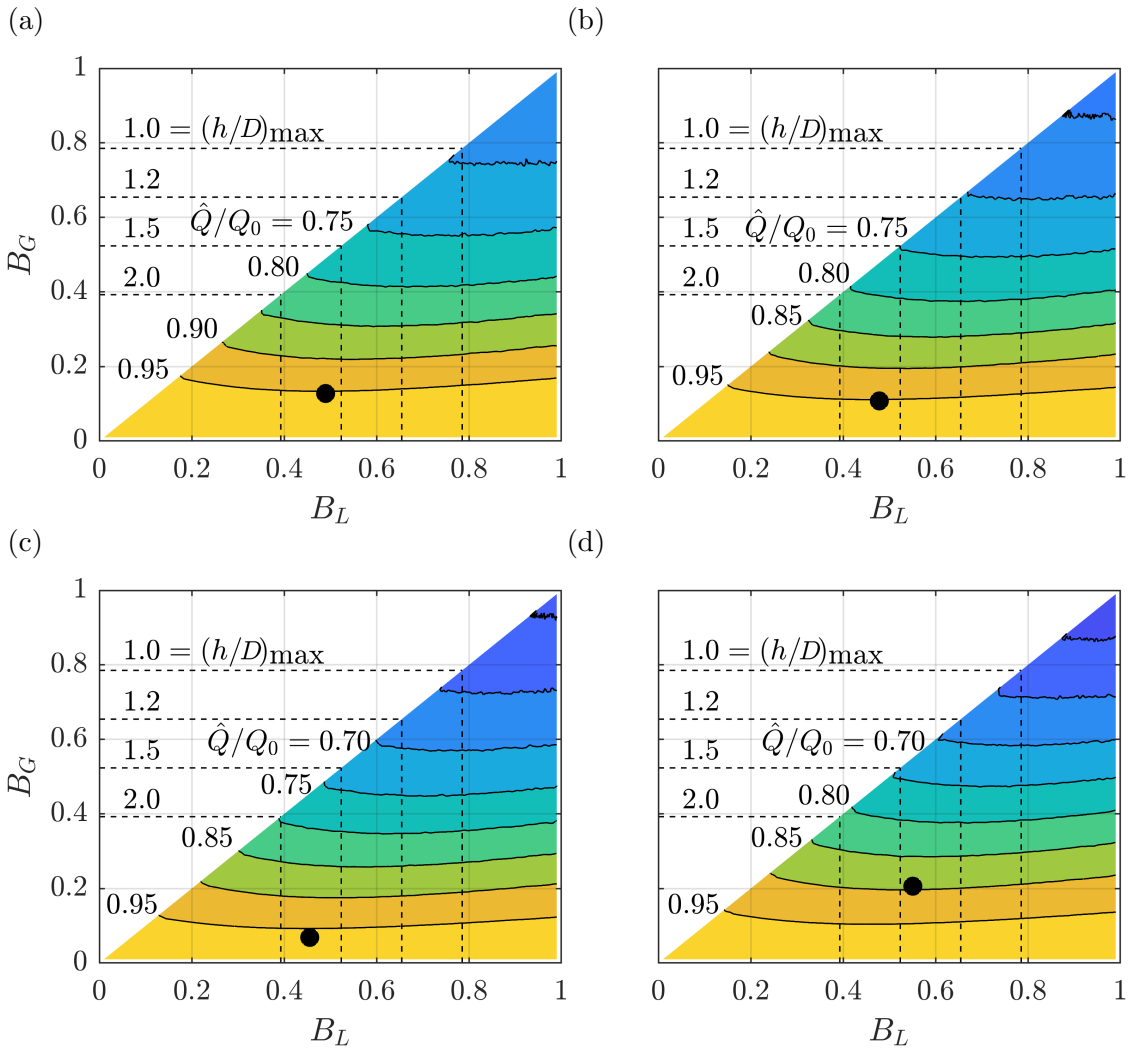

Figure 4.9: Contours of the normalised flow rate $\hat{Q}/Q_0$ for $\mathrm{Fr}_\omega = 0.635$ and $C_f = 0.002$ comparing differences in the impact of bed friction by varying l/h. All figures correspond to the array thrust setting that achieves maximum fence performance C_{PC} at the indicated combination of blockage ratios. The black circle represents the maximum return point. The dashed lines provide geometric limits on blockages for ratios of channel depth h to turbine diameter D. (a) $l/h = 50$; (b) $l/h = 100$; (c) $l/h = 250$; (d) $l/h = 500$.

the optimal global blockage for maximum return falls (figure 4.10a) and the local blockage effect becomes the primary mechanism for increases in the return. For globally unblocked channels, the local blockage for peak return is identical to the maximum power found in the partial fence model without channel flow interaction [Nishino and Willden, 2012a], and is lower than optimally blocked channels at the same channel Froude number. The maximum return must however be de-rated for increases in the channel bed friction (figure 4.10b), and for particularly high bed-

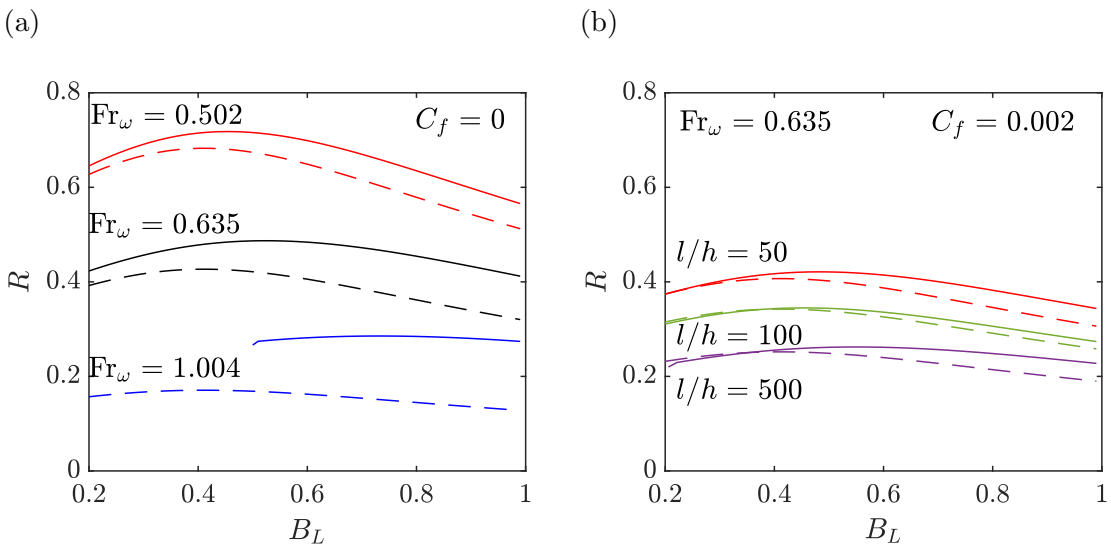

Figure 4.10: Slices (at constant B_G) across contour maps of the return at the required global blockage ratio for maximum return (solid lines) and for globally unblocked channels (dashed lines) for which each curve shows a distinct peak with local blockage. (a) shows how variations in the channel Froude number impact the arrangement for maximising return. The optimal global blockage ratios for peak return are $B_G = 0.07$ for $\mathrm{Fr}_\omega = 0.502$, $B_G = 0.17$ for $\mathrm{Fr}_\omega = 0.635$ and $B_G = 0.50$ for $\mathrm{Fr}_\omega = 1.004$. (b) shows how variations in the bed friction impact the optimal return arrangement, here for $\mathrm{Fr}_\omega = 0.635$ and $C_f = 0.002$. The optimal global blockage ratios for peak return are $B_G = 0.11$ for $l/h = 50$, $B_G = 0.07$ for $l/h = 100$ and $B_G = 0.21$ for $l/h = 500$.

friction channels, a relatively low maximum return is realised at high global blockage, making such channels difficult to optimise and exploit.

The interplay between these two non-dimensional groups and the maximum return is illustrated in figure 4.11, where the convergence of the zero global blockage and global blockage for peak return for low Fr_ω is illustrated. The universality of the optimal C_{PC} locus, and the fact that the maximum return must always lie on this curve, implies that figure 4.11b and equation 4.18 can be used to specify the number (B_G) and spacing (B_L) of turbines to optimise return for low bed friction channels at a given Fr_ω. The required local and global blockages are illustrated in figure 4.11b as a function of Fr_ω. This figure gives a simple look up for B_G^* and B_L^* as a function of Fr_ω for $C_f(l/h) = 0$, which should be very useful for an engineer.

For channels with non-negligible bed-friction (in this case for $l/D \geq 50$ with $C_f = 0.002$), the optimal return can be approximated by linearly de-rating the return from the zero friction case (figure 4.11c). The dependency of the return on the optimal blockage is however non-monotonic (figure 4.11d) and the turbine layout can be fine tuned for optimal return by altering B_G. However, recall that the gradients of return

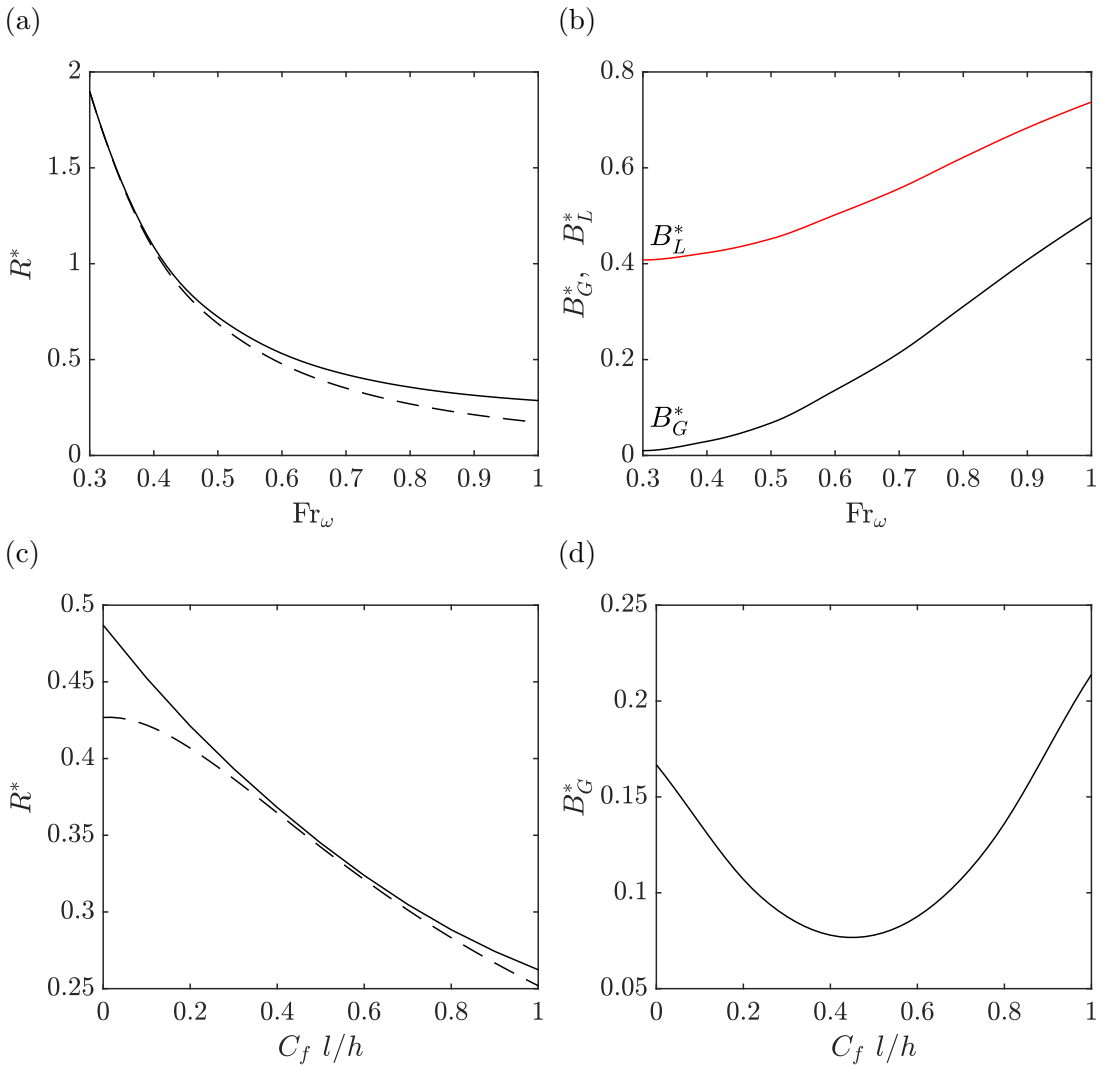

Figure 4.11: Impact of channel-scale non-dimensional groups, the channel Froude number Fr_ω and the channel bed friction $C_f(l/h)$, on the maximum return point. In all plots the solid line represents solutions for non-zero global blockage, whilst where appropriate the dashed line represents zero global blockage. For the case of zero bed friction $C_f = 0$, l/h undefined, (a) shows the optimal return for non-zero global blockage (solid-line) with the corresponding optimal global blockage (black) and local blockage (red) presented in (b). Here presented for the $\mathrm{Fr}_\omega = 0.635$, $C_f = 0.002$ case, (c) shows the optimal return across varying l/h ratios for non-zero global blockage (solid-line) with the corresponding optimal global blockage presented in (d).

with blockage are small for non-zero friction cases, and so the optimal return for globally unblocked and blocked channels lie close together for a wide range of $C_f(l/h)$ and hence although an optimum global blockage exists, the return remains rather insensitive to it.

We summarise by including a simple dimensional design example for a new tidal

array. Suppose we wish to install turbines with diameter $D = 20$m in a tidal channel that is $l = 8$km long, $h = 30$m deep, and $w = 4$km wide, with a driving head amplitude of $a = 0.5$m. For an initial estimate, assume an idealised channel with no bed friction. First, find the channel based Froude number $\mathrm{Fr}_\omega = \omega l/\sqrt{ga} \approx 0.5$, where we have assumed that the tidal forcing frequency $\omega = 1.4 \times 10^{-4}$rad s^{-1} is equal to the dominant lunar M_2 frequency. Reading from figure 4.11b, the optimal blockage ratios are then $B_G^* \approx 0.08$ and $B_L^* \approx 0.46$. The number of turbines for optimal deployment is then $n_T = whB_G/(\pi D^2/4) \approx 30$. The local blockage $B_L = (\pi D^2/4)/(h(D + s_T))$ can then be used to calculate the required tip-to-tip spacing s_T between each turbine such that $s_T = \pi D^2/(4hB_L) - D \approx 2.8$m. For this example channel therefore, a fence of 30 turbines of diameter $D = 20$m spaced $s_T = 2.8$m apart for a total fence width of $w_A \sim n_T(D + s_T) = 684$m, representing approximately 17% the entire width of the channel, is the optimal configuration. The expected return can be read off figure 4.11a at $R^* \approx 0.7$, for a channel power coefficient of $C_{PC} = R^* B_G^* = 0.056$. To estimate the power output, first find the peak undisturbed flow rate $Q_0 = (ga/\omega)(wh/l) \approx 526,000$ m^{3}s^{-1}. The optimal time-averaged turbine array power output for the channel is then $n_T\overline{P_D} = \rho g a Q_0 C_{PC} \approx 144$MW, with each individual turbine generating $\overline{P_D} = 144/30 = 4.8$MW. For detailed solutions which take flow rate and thrust constraints into account, as well as layout optimisation for sites with non-negligible bed friction, a solution of the governing equation as outlined in section 4.3 is recommended.

4.5 Conclusions

A theoretical model has been proposed to quantify the efficiency of an array of turbines that partially span the width of a tidal channel in which the flow is driven by a sinusoidally oscillating head. The framework for this analysis is the two-scale finite fence approach [Nishino and Willden, 2012a] embedded within and coupled to the one-dimensional channel dynamics model of Garrett and Cummins [2005]. The model hence accounts for both the beneficial constructive interference between turbines in fences that partially span the channel width as well as the coupling between turbine resistance and flow rate, and is an extension of previous models by considering both rough bottom channels and time-dependent oscillatory flow. The model makes no additional assumptions beyond those used in the two models from which it is derived, and the solutions to the non-dimensional equation governing the model are presented. We do note however the importance of scale separation assumptions for the combined analytic model. We assume that the device-scale mixing takes place much faster

relative to the array-scale mixing, but that the flow rate through the channel is constant along the length of the channel at any given point in time, and hence that the driving tidal wave is longer than the channel length, which must be considerably larger than the array mixing length scale.

Three non-dimensional groups are shown to fully characterise the flow problem: the channel Froude number group $\mathrm{Fr}_\omega = \omega l/\sqrt{ga}$, representing the relative (for a given channel length) oscillatory tidal elevation difference between the two ends of the channel (and is proportional to the square root of the cycle averaged potential to kinetic head in the channel); the channel bed friction group $C_f(l/h)$; and the turbine characteristics group $B_A C_{TA}$. This paper explores the impact of these three groups on both the channel scale flow dynamics and turbine performance characteristics. We introduce the return parameter R, the maximum yield per turbine area, proportional to a ratio of the total power extracted to the total frontal area of the turbines, as an optimisation metric for the arrangement of turbines in a channel. For a given set of channel parameters, which specify the channel Froude number and bed friction non-dimensional groups, there is an optimal number (B_G) and arrangement (B_L) of turbines to maximise return. By then further considering environmental constraints on the limiting values of acceptable reductions in relative flow rate, basin efficiency and thrust coefficient, we quantify the optimisation envelope for tidal turbine layouts.

We find that blockage plays a major role in the performance of a tidal farm operating in a head driven flow, with flow reduction in the channel, return parameter, and turbine performance strongly influenced by the different scales of blockage. For even relatively unblocked tidal farms, and especially for optimally arranged tidal farms, modelling the channel flow dynamics and resistance is crucial for farm yield estimation. To gain the full benefit of blockage, turbines and their layouts must therefore be carefully designed for their intended blockage environment.

In general, the channel Froude number Fr_ω heavily constrains the maximum possible return and both channel power and the optimal return decreases as Fr_ω is increased. Increasing Fr_ω, proportional to the square root of cycle averaged potential to kinetic head, requires high blockage arrangements to extract at optimal power. Increases in the channel bed friction act to decrease the achievable channel power coefficient and to decrease the peak return. Further, increasing bed friction renders sensitivity of flow rate reduction and return optima on local and global blockage ratios less significant. In all cases, the optimal channel power coefficient lies along a universal curve approximated by $B_L = (9B_G + 4)/(3B_G + 10)$, with the maximum return

moving along this curve as the channel Froude number and channel bed friction are varied.

Both environmental and engineering constraints heavily restrict the operational envelope of the tidal fence. In general, with increases in Froude number, the channel environmental constraint becomes more restrictive and the device thrust constraint less restrictive. For thrust coefficients that are larger than achievable by conventional rotors, power capping control strategies are critically important, particularly at peak flow speeds.

This model has great practical potential in aiding tidal turbine developers with detailed knowledge of the channel and frictional characteristics of a candidate site, resulting in a design envelope including both environmental/peak load constraints and the maximum yield point for optimisation in a head driven tidal channel. The model is also readily applicable to power limit estimates for resource assessment and can further be combined with real turbine characteristics to more accurately predict turbine, as opposed to optimal disc, performance.

4.6 Acknowledgements

This research was funded in part by DD's EPSRC studentship, grant number EP/S023801/1; CRV's UKRI Future Leaders Fellowship, grant number MR/V02504X/1; RHJW's EPSRC Advanced Fellowship, grant number EP/R007322/1, and by the EPSRC Supergen ORE Hub, grant number EP/S000747/1. For the purpose of Open Access, the authors have applied a CC BY public copyright licence to any Author Accepted Manuscript (AAM) version arising from this submission.

4.7 Declaration of Interests

The authors report no conflict of interest.

4.A Non-dimensionalised channel dynamics governing equation

We start with the Garrett and Cummins [2005] model equation which comes directly from the streamwise integration of the one-dimensional Euler equation

$$c\frac{dQ}{dt} - ag\cos\omega t = -\int_0^l F dz \ , \tag{4.19}$$

in which we have assumed smooth inflow and outflow so that the kinetic energy fluxes may be neglected. We assume that the channel cross-section is constant such that the channel geometric factor $c = \int_0^l A^{-1} dz = l/A_C$.

F is the total resistive force per unit mass and may be arbitrarily distributed along the channel length. The force of the turbines is given by

$$F_T = \frac{1}{2}\rho U_C^2 A_C C_{TC} = \frac{1}{2}\rho U_C^2 A_C C_{TA} B_A \ , \tag{4.20}$$

and the bed shear stress by

$$\tau_b = \frac{1}{2}\rho U_C^2 C_f \ , \tag{4.21}$$

which integrated over the bed surface gives the resistive force due to bed friction

$$F_b = \tau_b A_b = \tau_b A_C \frac{l}{h} = \frac{1}{2}\rho U_C^2 A_C \frac{l}{h} C_f \ . \tag{4.22}$$

The total force per unit mass F (where $\rho A_C l$ is the mass of fluid in the channel) is therefore

$$F = \frac{1}{\rho A_C l}\left(\frac{1}{2}\rho U_C^2 A_C C_{TA} B_A + \frac{1}{2}\rho U_C^2 A_C \frac{l}{h} C_f\right) \ , \tag{4.23}$$

and substituting this into equation (4.19)

$$\frac{dQ}{dt} = \frac{ag}{c}\cos\omega t - \frac{1}{\rho A_C c}\left(\frac{1}{2}\rho U_C^2 A_C C_{TA} B_A + \frac{1}{2}\rho U_C^2 A_C \frac{l}{h} C_f\right) \ , \tag{4.24}$$

results in the channel equation including arbitrary resitance from turbines and bed shear.

By non-dimensionalising with $t' = t\omega$, $Q' = Q/Q_0$, where $Q_0 = ga/(\omega)(wh/l) = ga/\omega c$ this simplifies to

$$\frac{dQ'}{dt'} = \cos(t') - \frac{U_C^2}{2ga}\left(C_{TA} B_A + C_f \frac{l}{h}\right) \ , \tag{4.25}$$

and as by definition $Q = U_C A_C$ so $U_C = Q/A_C = Q'(ga/\omega c A_C)$ we can write

$$\frac{dQ'}{dt'} = \cos(t') - Q'^2 \frac{ga}{2\omega^2 l^2}\left(C_{TA} B_A + C_f \frac{l}{h}\right) \ . \tag{4.26}$$

Defining a non-dimensional channel Froude-number as $\mathrm{Fr}_\omega = \omega l/\sqrt{ga}$, this can be re-written as the non-dimensional model equation

$$\frac{dQ'}{dt'} = \cos(t') - \frac{1}{2}Q'^2 \frac{1}{\mathrm{Fr}_\omega^2}\left(C_{TA} B_A + C_f \frac{l}{h}\right) \ , \tag{4.27}$$

which is the form of the non-dimensional equation first presented in Willden et al. [2014] and is solved for in this paper.

Equation (4.19) carries units of energy per unit mass, and so the cycle-averaged energy supplied to the channel by the driving head is given by

$$\overline{E}_\zeta = \frac{1}{T_P}\int_0^{T_P} |ag\cos\omega t|\,\rho A_C l\,dt = \frac{2\rho l^2\omega}{\pi}Q_0\ , \tag{4.28}$$

where $T_P = 2\pi/\omega$ is the cycle period. Similarly, in the absence of flow resistance so that $Q = Q_0\sin\omega t = A_C U_C$, the cycle-averaged channel kinetic energy is given by

$$\overline{E}_k = \frac{1}{T_P}\int_0^{T_P} \frac{1}{2}\,\rho A_C l\,U_C^2\,dt = \frac{\rho l}{4A_C}Q_0^2\ , \tag{4.29}$$

and so the channel based Froude number

$$\mathrm{Fr}_\omega = \sqrt{\frac{\pi}{8}}\left(\frac{\overline{E}_\zeta}{\overline{E}_k}\right)^{1/2}, \tag{4.30}$$

may be usefully interpreted as being proportional to the square-root of the ratio of the cycle-averaged driving head to kinetic head in the channel.

4.B Statement of authorship

The preceding chapter has been reformatted from an article published in the *Journal of Fluid Mechanics*. The inclusion of co-authors reflects the fact that the work came from active collaboration between researchers and acknowledges input into team-based research.

Publication details	
Title of paper	A head-driven model of turbine fence performance
Publication status	Published
Publication reference	D. Dehtyriov, C.R. Vogel and R.H.J. Willden. A head-driven model of tur bine fence performance. *Journal of Fluid Mechanics*, 956:A14, 2023. doi: 10.1017/jfm.2023.14

Student Confirmation	
Student Name	Daniel Dehtyriov
Contribution to the paper	The writing of section 1 was split $40-40-20$ between DD, RHJW and CV respectively. The model development in section 2 and in the appendix was primarily developed by RHJW with writing contributions from DD for a $10-90$ split between DD and RHJW. The contribution to numerical results and writing in section 3 and conclusions in section 4 was split $45-35-20$ between DD, RHJW and CV respectively.

Student signature

20th December 2023

Date

Supervisor Confirmation	
Supervisor name and title	Prof. Richard Willden
Supervisor comments	I confirm that Daniel has made a substantial contribution to the publication, and that the description above in the Statement of Authorship is accurate.

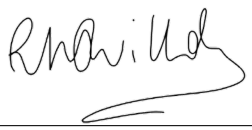

Supervisor signature

20th December 2023

Date

Chapter 5

A two-scale blockage correction for an array of tidal turbines

> "And you give me the choice between a description that is sure but that teaches me nothing and hypotheses that claim to teach me but that are not sure. (...) Hence the intelligence, too, tells me in its way that this world is absurd."
>
> — Albert Camus, The Myth of Sisyphus

This chapter presents an article which derives a theoretical blockage correction of test results from turbine arrays. The article was published in the 15^{th} *European Wave and Tidal Energy Conference* on the 2^{nd} September 2023 [Dehtyriov et al., 2023b].

Having developed the theoretical models, we now turn our attention to supporting experimental validation of blockage effects. A primary difficulty encountered in experimental testing is that the flow conditions in a wind/water tunnel are not the same as those in an unbounded flow; primarily because the tunnel test cross-section is finite in size. These blockage effects modify the performance of the array, such that corrections to experimental curves are necessary to translate laboratory-scale results to full-scale conditions. Corrections have however only been developed for single turbines with the difficulty for turbine arrays being the non-linear interaction between the effects of turbine spacing and channel walls. This work therefore presents an analytical blockage correction for arrays of turbines based on two-scale momentum theory, separating out the tunnel global blockage to isolate and quantify the local blockage effect.

5.1 Paper abstract

This work presents an analytical blockage correction for co-planar arrays of tidal turbines based on two-scale momentum theory. The study aims to address the issue of correcting blockage effects for arrays where constructive interference between turbines can significantly improve performance. The proposed analytical model is validated by correcting Reynolds-Averaged Navier-Stokes computations of turbine arrays across a range of realistic tip-to-tip spacings (local blockage) and channel widths (global blockage) to free-flow conditions, thereby demonstrating its validity and broad applicability. By comparing the proposed two-scale correction with a single turbine correction, the necessity of the model is highlighted. Additionally, an iterative method to apply the correction is presented. This novel correction method allows for the decoupling of local and global blockage effects, enabling the isolation and quantification of the local blockage effect observed in laboratory-scale experiments. The blockage correction will further allow for comparisons of performance between arrays , and allow for an improved understanding of how tidal turbine arrays perform *in-situ*.

5.2 Introduction

Although the Lanchester-Betz [Lanchester, 1915, Betz, 1920] limit provides an upper bound to the power extraction of an idealised turbine in an unconstrained flow, blockage can be used to constrain the flow to raise this theoretical limit. This has been particularly relevant in tidal channels [Garrett and Cummins, 2007], where both the sea-bed and the free surface of the sea constrain the expansion of the stream-tube which encloses the turbine area. It was shown that for even modest increases in the global blockage ratio B_G, the ratio of swept turbine area to channel cross-section area, the power coefficient can significantly exceed the Lanchester-Betz limit. Constraining the flow, therefore, provides a mechanism by which the power extraction efficiency of turbines can be significantly enhanced. Extensions of this model have included the influence of free-surface deformation (non-zero Froude numbers) [Vogel et al., 2016] and the development of an updated blade element momentum theory method for tidal turbines [Vogel et al., 2018].

The ratio of swept rotor area to channel cross section, represented by the global blockage ratio, is however typically very small for commercial-scale tidal energy extraction [Coles and Walsh, 2019], and turbines often cannot be placed to cover the entire channel width due to practical constraints such as bathymetry variations or

shipping lane requirements. The flow around the turbines may however be constrained by placing turbines adjacent to one another to form a turbine fence partially spanning the width of the tidal channel. By reducing the inter-turbine spacing within a fence of turbines, it has been demonstrated that the turbines operate at increased efficiencies for even for small global blockage ratios [Nishino and Willden, 2012a]. This phenomenon is referred to as the constructive interference effect.

Fences consisting of multiple turbines placed side-by-side can therefore make use of this constructive interference, or local blockage effect, to raise the energy extraction efficiency of the fence above that of the Lanchester-Betz limit, even for the case where the fence makes up a negligible proportion of the channel width. The flow problem may thus be described in terms of two scales: a local scale consisting the flow around an individual turbine and its wake, and a global scale consisting of all turbines and the flux through the tidal channel. For this two-scale problem of a long array of turbines partially spanning the width of a much wider channel (vanishing global blockage) the efficiency of energy extraction, normalised by the undisturbed kinetic energy flux, rises from the Lanchester-Betz limit of 0.593 to the partial fence limit of 0.798 [Nishino and Willden, 2012a]. Experiments on pairs of side-by-side turbines at large laboratory scale [McNaughton et al., 2021] have confirmed the important aspects of the underlying partial fence theory and that some of the performance benefits offered by constructive interference effects can be achieved in practice.

Experimental validation of constructive interference performance benefits in laboratory facilities are however prone to global blockage effects not seen in full-scale open channel flows due to the close proximity of flow boundaries to the body. These global blockage effects modify the thrust and power performance of the turbines, such that corrections to experimental curves are necessary to either translate laboratory-scale experimental results to full-scale conditions, or to calculate the expected loads and power on tidal turbines deployed in blocked-flow conditions [Zilic de Arcos et al., 2020, Ross and Polagye, 2020]. The difficulty with applying blockage corrections to turbine arrays is the non-linear interaction between local and global blockage. These two effects cannot be simply decoupled as for various turbine tip-to-tip spacings (affecting local blockage), changes in the global blockage have a different impact on turbine performance.

A number of blockage corrections have been developed for single turbines operating in blocked flow conditions. These corrections are all based on Glauert's method [Glauert, 1935], and typically seek to describe an equivalent free-stream velocity

which, in the absence of global blockage, would result in the same thrust and velocity through the turbine as in the blocked case. Thrust and power curves are then scaled non-linearly with the ratio of the experimental tank velocity and the equivalent free-stream velocity. For channel flow, the most widely used correction is a method developed by Barnsley and Wellicome [1992], and introduced to the marine energy community by Bahaj et al. [2007]. Various other single-turbine corrections have been proposed [Mikkelsen and Sørensen, 2002, Werle, 2010, Houlsby et al., 2008, Maskell, 1963]; see Zilic de Arcos et al. [2020] for detailed numerical and Ross and Polagye [2020] for detailed experimental comparisons of these blockage corrections. These single-scale blockage corrections can however only account for global blockage, and simplifications for turbine arrays must currently be made based on the assumption that global and local blockage effects can be linearly decoupled [McNaughton et al., 2021].

This work therefore presents an analytical blockage correction for co-planar arrays of tidal turbines based on two-scale momentum theory developed for partial turbine fences [Nishino and Willden, 2012a]. The correction allows for a decoupling of the global blockage and constructive interference effects, such that the local blockage effect can be isolated and quantified. This correction is compared to the Barnsley and Wellicome [1992] correction for a single turbine to demonstrate the necessity of the two-scale blockage correction. Finally, Reynolds-Averaged-Navier-Stokes (RANS) computations of turbine arrays across various local and global blockage ratios are corrected using the analytical model, demonstrating its validity.

5.3 Theoretical model

5.3.1 Two-scale partial fence model

We start with the two-scale partial turbine fence theoretical model presented by Nishino and Willden [2012a]. A rectangular channel with uniform depth h and width w, contains a large number n_T of turbine rotors with a diameter of D which are spaced with equal spacing s_T in a spanwise fence configuration as shown in Fig. 5.1. The flow through the channel is assumed to be incompressible and inviscid, and the flow far upstream of the array U_C is assumed uniform and fixed. The analysis of the flow problem assumes a separation of scales between the flow around each device and around the entire array, such that all device-scale flow events, including the local wake-mixing, take place much faster than the streamtube expansion of the flow around the entire array. This allows the flow system to be solved as a combination

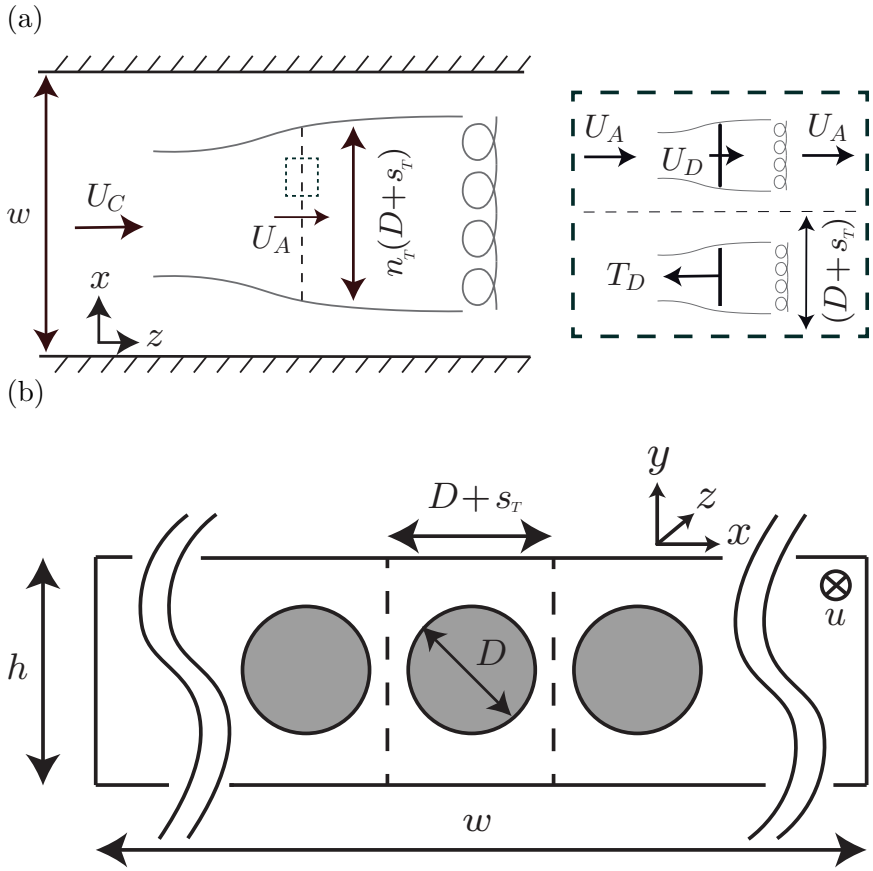

Figure 5.1: A schematic of a tidal channel with a co-planar fence of turbines. (a) Top-down view of the tidal channel, showing the global array and local device scales. (b) Channel cross-section at the fence plane. For a given channel depth h and turbine diameter d, the spacing s between each turbine defines the local blockage, and for a fixed number n of turbines, the width of the channel w, defines the global blockage. At the global array scale, the channel flow velocity U_C is reduced by the presence of the array to U_A at the fence, and recovers to U_C far downstream of the fence after wake-mixing. At the local device scale, the array velocity U_A is reduced to U_D at the discs before again recovering to U_A after local-scale wake mixing. The channel is typically significantly wider than the turbine fence.

of two coupled quasi-inviscid problems of different scales, namely the array scale and device (local) scale, see Fig. 5.1.

Blockage ratios for these two scales are defined. The first is an array scale blockage, which represents the array constrained by the sea-bed and sea-surface. This array scale blockage, or the ratio of representative array area to channel cross sectional area is

$$B_A = \frac{hn_T(D+s_T)}{hw} = \frac{1+s_T/D}{w/(n_T D)}. \tag{5.1}$$

We define the streamwise velocity at the fence U_A, and assume it to be uniform across

the array. The second geometric ratio is the local (device) scale blockage, where the turbines are constrained by adjacent devices. This local scale blockage, or ratio of single turbine area to local passage cross-sectional area is

$$B_L = \frac{\pi D^2/4}{h(D+s_T)} = \frac{\pi}{4(h/D)(1+s_T/D)}. \tag{5.2}$$

The streamwise velocity through the turbines is denoted U_D, and is likewise assumed to be uniform across the device area. The global blockage $B_G = B_L B_A$ is then the ratio of total device area to channel cross-sectional area.

These blockage ratios define the geometry of the flow problem. The turbine operating condition is defined in terms of the thrust coefficients at each scale. The local thrust coefficient defines the disc thrust in terms of the local inlet velocity

$$C_{TL} = \frac{T_D}{\frac{1}{2}\rho U_A^2 A_T}, \tag{5.3}$$

where T_D is the turbine thrust and A_T the turbine area. The array thrust ($n_T T_D$) is normalised by the array area and channel inlet velocity for the array thrust coefficient

$$C_{TA} = \frac{U_A^2}{U_C^2} B_L C_{TL} = (1-\alpha_A)^2 B_L C_{TL}, \tag{5.4}$$

where $(1-\alpha_A)$ is the array scale velocity induction factor. Finally, the global thrust coefficient is the total thrust (equal to the array thrust), normalised by the channel inlet velocity and total device area ($n_T A_T$)

$$C_{TG} = (1-\alpha_A)^2 C_{TL}. \tag{5.5}$$

Alongside the array scale velocity induction factor, we additionally define the local scale induction factor $\alpha_L = 1 - U_D/U_A$ and global induction factor $\alpha_G = 1 - U_D/U_C$, where $(1-\alpha_G) = (1-\alpha_L)(1-\alpha_A)$.

For a given geometry (blockage ratio) and turbine operating condition (thrust coefficient), we are interested in the power extraction $T_D U_D$, which similar to the thrust coefficients can be parameterised by the local $C_{PL} = C_{TL}(1-\alpha_L)$, array $C_{PA} = C_{PL} B_L (1-\alpha_A)^3$ and global $C_{PG} = C_{PL}(1-\alpha_A)^3$ power coefficients.

Conservation of mass, momentum and energy can then be solved for both local and array scales to obtain thrust coefficients in terms of velocity induction factors (see [Nishino and Willden, 2012a] for details)

$$C_{TL} = (1-\gamma_L)\frac{(1+\gamma_L) - 2B_L(1-\alpha_L)}{(1-B_L(1-\alpha_L)/\gamma_L)^2}, \tag{5.6}$$

$$C_{TA} = (1-\gamma_A)\frac{(1+\gamma_A) - 2B_A(1-\alpha_A)}{(1-B_A(1-\alpha_A)/\gamma_A)^2}, \tag{5.7}$$

where γ is the wake velocity induction factor and is related to the disc velocity induction factors by

$$1 - \alpha_L = \frac{1 + \gamma_L}{(1 + B_L) + \sqrt{(1 - B_L)^2 + B_L(1 - 1/\gamma_L)^2}}, \tag{5.8}$$

$$1 - \alpha_A = \frac{1 + \gamma_A}{(1 + B_A) + \sqrt{(1 - B_A)^2 + B_A(1 - 1/\gamma_A)^2}}. \tag{5.9}$$

The two scales are then coupled by (5.4) & (5.7), as the array thrust from both expressions must be equal.

5.3.2 Two scale blockage correction model

Blockage correction methods seek to find a relationship between the upstream velocity in a blocked flow and the equivalent upstream velocity in free-flow for which the turbine would be operating at the same conditions, i.e. the same mass flux and turbine thrust through the rotor plane. We use a prime ' to denote the free-flow unblocked case, where we are therefore looking for the equivalent channel free-stream velocity U'_C to generate the same thrust and disc velocity through the turbines as in the original blocked case.

Setting the disc velocity and thrust to be equivalent between unblocked and blocked flow cases

$$U_D = U_C(1 - \alpha_G) = U'_D = U'_C(1 - \alpha'_G), \tag{5.10}$$

$$T_D = \frac{1}{2}\rho U_A^2 A_T C_{TL} = T'_D = \frac{1}{2}\rho U_A^2 A_T U_A'^2 C'_{TL}. \tag{5.11}$$

Noting that $U_A = U_C(1 - \alpha_A)$ and that $(1 - \alpha_G) = (1 - \alpha_A)(1 - \alpha_L)$ the condition on the thrust reduces to

$$\frac{C_{TL}}{(1 - \alpha_L)^2} = \frac{C'_{TL}}{(1 - \alpha'_L)^2} \tag{5.12}$$

$$f(\gamma_L) = f(\gamma'_L), \tag{5.13}$$

where if we assume that f is an injective function (see equations 5.6 & 5.8), which must be true for the physical equations to have unique solutions, $\gamma_L = \gamma'_L$. It then follows that $\alpha_L = \alpha'_L$ and that $C_{TL} = C'_{TL}$. This result can be intuited from the fact that the function f excludes the array scale blockage B_A, which is the variable that changes between the unblocked and blocked flow equations (B_L remains the same). These identities can additionally be readily verified numerically.

Now consider the unblocked free-flow case, for which $B'_A = B'_G = 0$. Equations for the array scale variables (5.9), (5.4) and (5.7) reduce to

$$(1 - \alpha'_A) = \frac{1 + \gamma'_A}{2} \tag{5.14}$$

$$C'_{TA} = (1 - \alpha'_A)^2 B_L C'_{TL} \tag{5.15}$$

$$C'_{TA} = (1 - \gamma'_A)(1 + \gamma'_A). \tag{5.16}$$

By writing γ'_A in terms of α'_A (5.14), setting $C_{TL} = C'_{TL}$ (5.12) and equating (5.15) & (5.16), these expressions allow for a relationship between the free-flow array scale axial induction factor and the blocked flow conditions

$$4\alpha'_A(1 - \alpha'_A) = (1 - \alpha'_A)^2 B_L C_{TL} \tag{5.17}$$

$$(1 - \alpha'_A) = \frac{4}{4 + B_L C_{TL}} \tag{5.18}$$

Finally, we seek a relationship between the blocked and free-flow upstream channel flow velocities which, by assuming the disc velocity is the same between the two cases as in (5.10), can be shown to be related to the array scale induction factors by

$$\frac{U_C}{U'_C} = \frac{(1 - \alpha'_G)}{(1 - \alpha_G)}, \tag{5.19}$$

$$\frac{U_C}{U'_C} = \frac{(1 - \alpha'_L)(1 - \alpha'_A)}{(1 - \alpha_L)(1 - \alpha_A)}, \tag{5.20}$$

$$\frac{U_C}{U'_C} = \frac{(1 - \alpha'_A)}{(1 - \alpha_A)}. \tag{5.21}$$

Combining (5.18) and (5.21), the correction factor reduces to

$$\frac{U_C}{U'_C} = \frac{4}{4(1 - \alpha_A) + B_L C_{TL}(1 - \alpha_A)} \tag{5.22}$$

or alternatively

$$\frac{U_C}{U'_C} = \frac{(1 - \alpha_A)}{(1 - \alpha_A)^2 + B_L C_{TL}(1 - \alpha_A)^2/4}, \tag{5.23}$$

$$\frac{U_C}{U'_C} = \frac{4(1 - \alpha_A)}{4(1 - \alpha_A)^2 + C_{TA}}. \tag{5.24}$$

This form of the correction factor is comparable to the Barnsley and Wellicome [1992] correction, except extended from a single disc to a turbine fence partially spanning a channel by applying two-scale momentum theory. Note that the array thrust coefficient C_{TA} is a function of the local blockage ratio B_L, coupling the two scales in (5.24).

Equation (5.24) can now be used to correct for the tip-speed ratio (TSR), thrust and power coefficients:

$$\mathrm{TSR}' = \mathrm{TSR}\left(\frac{U_C}{U_C'}\right), \tag{5.25}$$

$$C_T' = C_T\left(\frac{U_C}{U_C'}\right)^2, \tag{5.26}$$

$$C_P' = C_P\left(\frac{U_C}{U_C'}\right)^3. \tag{5.27}$$

For a given recorded tip-speed ratio, thrust and power coefficient in a blocked flow (for example in a laboratory scale towing tank experiment), (5.24) can be used to find U_C/U_C' and (5.25)-(5.27) can then used to correct to the device operating in free-flow conditions. We note that the same formulation can be applied to consider corrections to a non-zero global blockage ratio, say for instance to estimate the performance of an array in a large tidal channel which has been tested in a towing tank, i.e., where $B_A > 0$.

5.3.3 Numerical solutions to the two-scale blockage correction

We now outline a numerical scheme which can be followed to implement the proposed blockage correction. The inputs are the array scale blockage B_A and the local blockage B_L, which can be found from (5.1)-(5.2) and depend on the channel geometry and turbine layout. Assuming turbine power P_D, thrust T_D and the free-stream velocity U_C are measured, both C_{TG} and C_{PG} are known.

By the array thrust coupling outlined in section 5.3.1

$$C_{TG} = \left(\frac{1-\gamma_A}{B_L}\right)\left(\frac{(1+\gamma_A) - 2B_A(1-\alpha_A)}{(1-B_A(1-\alpha_A)/\gamma_A)^2}\right), \tag{5.28}$$

where we have used (5.5) and where α_A is given by (5.9). This can be solved iteratively by a root-finding algorithm for γ_A, which can then be substituted back into (5.9) for $(1-\alpha_A)$. The local thrust coefficient is then $C_{TL} = C_{TG}/(1-\alpha_A)^2$, from which (5.6) can again be used with a root-finding method to find both γ_L and $(1-\alpha_L)$. Finally, (5.4) can be used to find C_{TA}. This process is illustrated diagrammatically in Figure 5.2 for reference.

These solutions can be substituted into (5.24) for the velocity correction factor, and (5.25)-(5.27) for the blockage correction factors. This procedure can then be looped over a number of inputs for the blockage corrected curves, for instance a range of turbine spacing or range of turbine thrust.

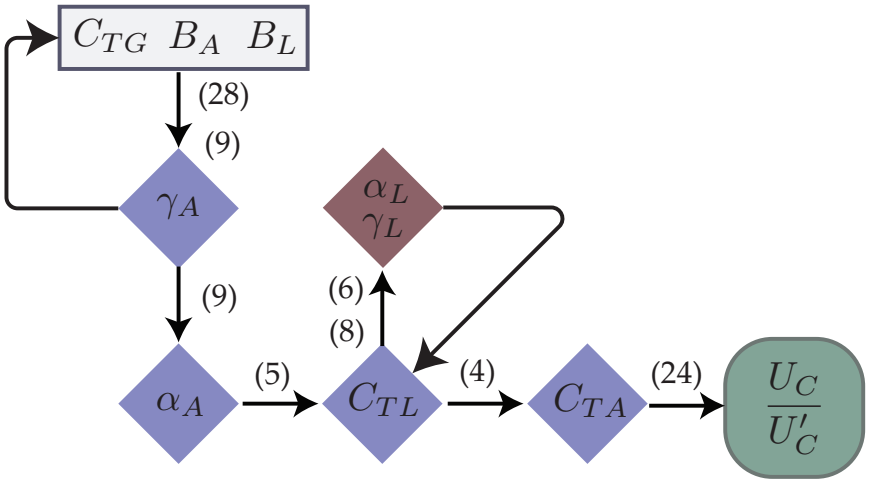

Figure 5.2: Flowchart outlining the process to solve for the blockage correction, with the relevant equations which need to be solved shown. Loops imply that the respective equations need to be solved iteratively.

5.4 Numerical method

We validate the proposed blockage correction on 3-D Reynolds-Averaged-Navier-Stokes simulations of turbine fences in channels of varying widths and realistic turbine tip-to-tip spacings.

5.4.1 Numerical setup

Fig. 5.1 shows an example of the cross-section of the simulated channel. The Cartesian coordinates (x, y, z) represent the spanwise, vertical and streamwise directions. The domain boundaries are located at $0 \leq x \leq (w/(nd))/2$, $0 \leq y \leq (h/d)/2$, $-50d \leq z \leq 50d$, with the streamwise boundaries set far enough from $z = 0$ such that the boundary location does not influence the results. Uniform streamwise flow is assumed at the inlet, and zero streamwise flow gradients at the outlet. We simulate a quarter of the entire domain by setting a symmetry condition at the $x = 0$ and $y = 0$ boundaries, with the remaining boundaries set to a free-slip condition.

We consider a fence of $n_T = 8$ discs of diameter D, located at the centre of the channel at $z = 0$. We fix the depth of the channel $h/D = 2$, and vary the local and global blockage through the disc spacing s/D and channel width $w/(n_T D)$ respectively.

An O-grid mesh with a minimum of 30 grid points across the diameter of each disc is used to model each disc in $x - y$ plane of the channel, with additional mesh refinement at the disc boundary. The discs thickness is taken to be $0.02D$, with axial

Table 5.1: Summary of the numerical simulation conditions

Number of discs n_T	8
Disc thickness	$0.02D$
Disc resistance	$K(U_D^2/2)$
Turbulence model	$k-\epsilon$ Launder and Spalding [1974]
I_∞	0.1%
k/U_C^2	$1.5I_\infty^2$
C_μ	0.09
$C_{\epsilon,1}$	1.36
L/D	0.1
$\nu/(U_C D)$	10^{-6}

grid refinement to ensure a minimum of 10 grid points across the disc thickness. The disc thickness and grid density are selected such that further decreases/refinement do not influence the results by over 0.5%.

The RANS equations are then solved with second order accuracy in OpenFOAM with the Reynolds stress terms modelled using the $k-\epsilon$ viscosity model [Launder and Spalding, 1974]. We assume an inlet turbulence intensity of $I_\infty = 0.1\%$, with the non-dimensionalised inlet turbulent kinetic energy then $k/U_C^2 = 1.5I_\infty^2$ and inlet kinetic energy dissipation rate $\epsilon L/U_C^3 = C_\mu^{0.75}(3/2I_\infty)^{1.5}$, where we take $C_\mu = 0.09$ and the reference length scale as $L/D = 0.1$. Changes to the inlet turbulence conditions do not affect the results as long as the inlet turbulence intensity remains relatively small. Finally, the non-dimensionalised kinematic viscosity is set to $\nu/(U_C D) = 1/\mathrm{Re} = 10^{-6}$, which needs to be arbitrarily small enough such that the inertial forces dominate the viscous forces.

As demonstrated by Nishino and Willden [2013a], the performance of the disc fence is limited by the mixing rate, which can be controlled by variations in the turbulence model coefficient $C_{\epsilon,1}$. Following [Nishino and Willden, 2013a], we set $C_{\epsilon,1} = 1.36$ to promote stronger mixing relative to the typical choice of $C_{\epsilon,1}$, which itself does not represent anything physical in terms of wake mixing of actuator discs. Similar results would however be observed under different choices (including the regular choice) of $C_{\epsilon,1}$ [Nishino and Willden, 2013a].

Disc resistance is modelled by a change in the momentum flux equal to $S_U = K(U_D^2/2)$, where U_D is the local streamwise velocity, and is added to the momentum equation by distribution over the cell volumes at the location of the discs. The disc

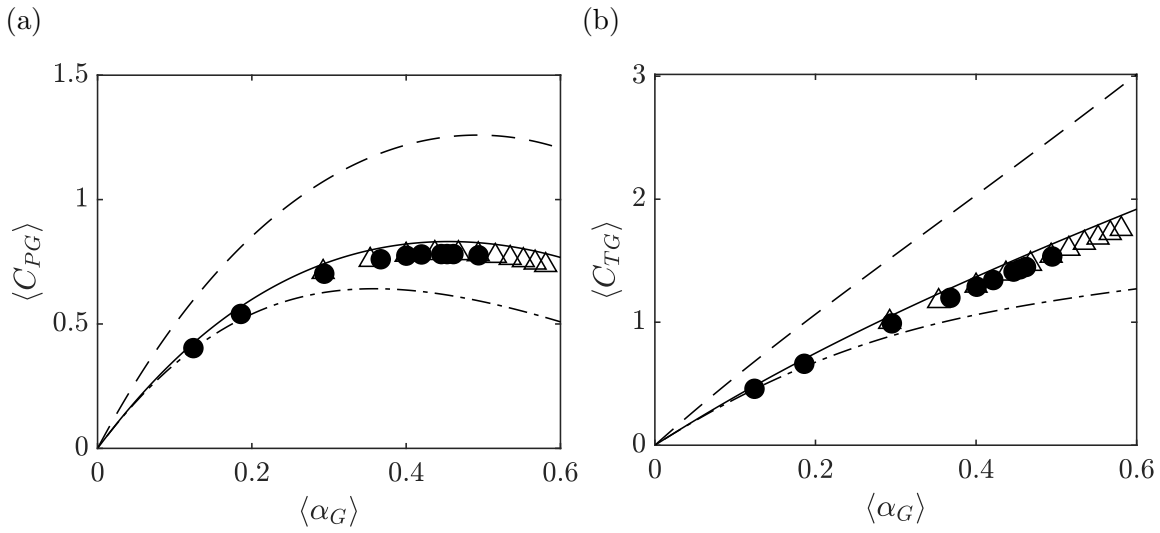

Figure 5.3: A validation study comparing numerically simulated fence averaged performance coefficients plotted against the fence averaged axial induction factor against both theoretical and published numerical results. (a) Fence averaged power coefficient. (b) Fence averaged thrust coefficient. Triangles show the results for the $s_T/D = 0.25$, $w/(n_T D) = 10$, $n_T = 8$ case, with the circles showing results for the same case in [Nishino and Willden, 2013a]. The dashed and dash-dot curves represent the Garrett & Cummins [Garrett and Cummins, 2007] single-scale model assuming that the blockage is global or local respectively. The solid curve represents the two-scale turbine fence model [Nishino and Willden, 2012a]. Our simulation results closely match both theory and literature.

momentum loss factor K is assumed to be uniform across the surface of all discs. We neglect rotational effects, which we assume are decoupled from the blockage effect, and can therefore be considered separately. The global axial induction factor can then be defined as $\langle \alpha_G \rangle = 1 - \langle U_D \rangle / U_C$, and the resultant disc averaged global thrust and power coefficients can then be determined by $\langle C_{TG} \rangle = K \langle U_D^2 \rangle / U_C^2$ and $\langle C_{PG} \rangle = K \langle U_D^3 \rangle / U_C^3$, where the angle brackets represent volume averaging over all discs in the fence. The numerical simulation conditions are summarised in table 5.1, and simulations are performed over a range of K such that the peak power point is always located.

5.4.2 Numerical validation

We validate our formulation against the $n_T = 8$, $s_T/D = 0.25$, $w/(n_T D) = 10$ simulations presented by Nishino and Willden [2013a], shown in Fig. 5.3. Three analytical curves are shown, representing the Garrett and Cummins [2007] model assuming local or global blockage for B as the lower and upper bounds respectively,

Table 5.2: The range of tip-to-tip disc spacing considered for numerical simulations to validate the theoretical blockage correction. For all simulations the channel depth $h/D = 2$ and number of discs $n_T = 8$.

s_T/D	B_L
0.1	0.357
0.25	0.314
0.5	0.262
1.0	0.196

Table 5.3: The range of channel widths considered for numerical simulations to validate the theoretical blockage correction. For all simulations the channel depth $h/D = 2$ and number of discs $n_T = 8$.

$w/(n_T D)$	B_G
2	0.196
4	0.098
10	0.039
40	0.010

and the Nishino and Willden [2012a] two-scale model which uses both. Across all local and global blockage ratios, the fence performance curves rest between the upper and lower bounds of the Garrett and Cummins [2007] model, with the Nishino and Willden [2012a] model an excellent fit for the actual performance. The numerical formulation presented herein clearly matches the theoretical curve and previous numerical simulation results, giving further confidence in both the grid quality and finite volume formulation for the momentum sink.

5.4.3 Numerical results

We present results for the channel and turbine configurations in Table. 5.2 and Table. 5.3, representing 16 simulations of varying turbine and channel configurations.

Two example simulation results representing the lowest ($s_T/D = 1$, $w/(n_T D) = 40$) and highest ($s_T/D = 0.1$, $w/(n_T D) = 2$) blockage cases are shown in Fig. 5.4, with streamwise velocity contours at peak power, taken at an axial channel-cross section at the plane of the turbines for both configurations. The entire channel width is not shown, but is patently significantly smaller for the channel with larger global

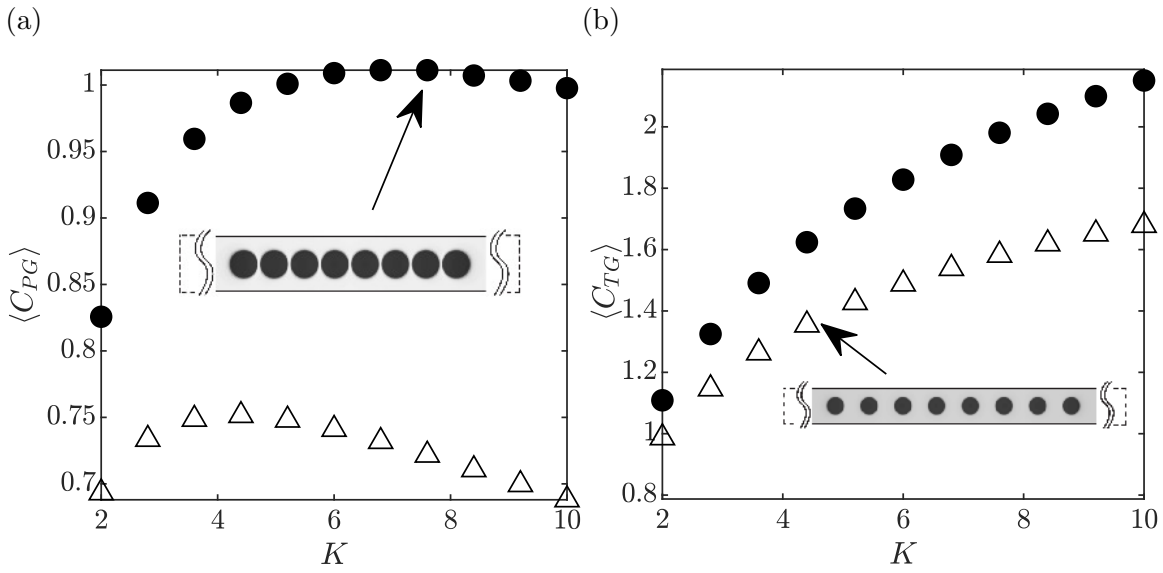

Figure 5.4: Example solutions to the numerical model, here shown for the two cases representing the largest (with circles, $s_T/D = 0.1$, $w/(n_T D) = 2$) and smallest (with triangles, $s_T/D = 1$, $w/(n_T D) = 40$) combination of local and global blockage. (a) Fence averaged power coefficient. (b) Fence averaged thrust coefficient. Fence averaged performance coefficients are plotted against the momentum loss factor K, which is assumed uniform across the array and is an input to the numerical model. For all simulations we assume a fixed disc number $n_T = 8$ discs and fixed channel depth $h/D = 2$. The two insets show a shaded representation of each array, taken at an axial channel-cross section at the plane of the turbines for the two configurations. Note that the entire width of the channels are not shown.

blockage. For all channels, the averaged thrust coefficient monotonically increases with the momentum loss factor K, and the averaged power coefficient sees a distinct maximum for $2 \leq K \leq 8$, where we note that $K = 2$ is the optimal momentum loss factor for a single disc in an unbounded flow. An increase in the global blockage always increases the peak power coefficient for a given number of discs and turbine spacing. Note that the power coefficient can, as in Fig. 5.4, exceed $C_{PG} = 1$, as additional energy can be extracted from the pressure drop along the channel length. For a given global blockage, however, there exists an optimal turbine spacing, or local blockage, to maximise the power coefficient. As the peak power coefficient increases for a given configuration, the required thrust to realise this peak power also increases.

Fig. 5.5 first demonstrates the need for a two-scale blockage correction by an example correction of the $s_T/D = 0.25$, $w/(n_T D) = 10$ case by comparing the widely used Barnsley and Wellicome [1992] single-turbine correction to the proposed two-scale correction. Unlike the thrust and power curves in Fig. 5.3 for which the two-

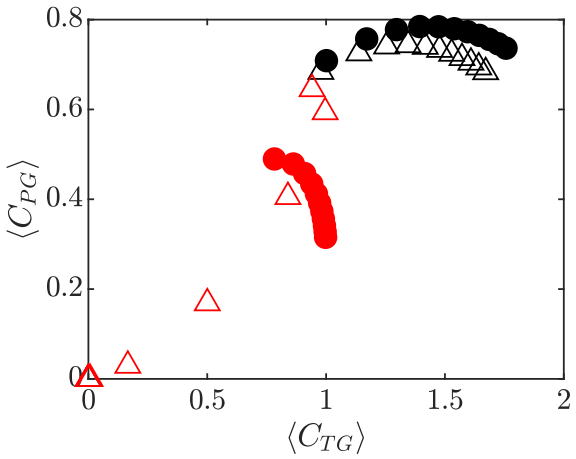

Figure 5.5: A comparison of the presented blockage correction model against a widely used single-scale blockage correction model presented by Barnsley and Wellicome [1992], here shown for an example case of $s_T/D = 0.25$, $w/(n_T D) = 10$. The solid black circles show the numerical results, with the triangles the corrected curve applying our model. The red triangles and circles show the corrected curves applying the single-scale model assuming that the blockage ratio is local and global respectively, demonstrating the necessity for a two-scale correction.

scale model is bounded by the single-scale model assuming $B = B_G$ and $B = B_L$ for upper and lower bounds respectively, the single-scale blockage correction gives inconsistent results for the turbine fence, due to the large differences in operating conditions between a turbine fence and single tidal turbine.

5.4.4 Two-scale blockage corrected simulations

We now consider correcting the blocked flow simulations by applying the proposed theoretical blockage correction to the thrust and power curves for the various channel configurations. Fig. 5.6 presents the results of all numerical simulations of the channel and turbine configurations presented in Table. 5.2 and Table. 5.3, alongside the free-flow blockage corrected curves found by applying the theoretical formulation presented herein. Each subfigure represents a fixed turbine configuration, represented by a fixed tip-to-tip turbine spacing or local blockage. The range of tip-to-tip distances represent realistic turbine fence spacings. The channel width is then varied by over an order of magnitude, representing the range from laboratory scale flow testing to a near unblocked, or a near infinitely wide, channel.

The proposed blockage correction applied to the numerically simulated cases always corrects the performance curves to values slightly below the simulated lowest

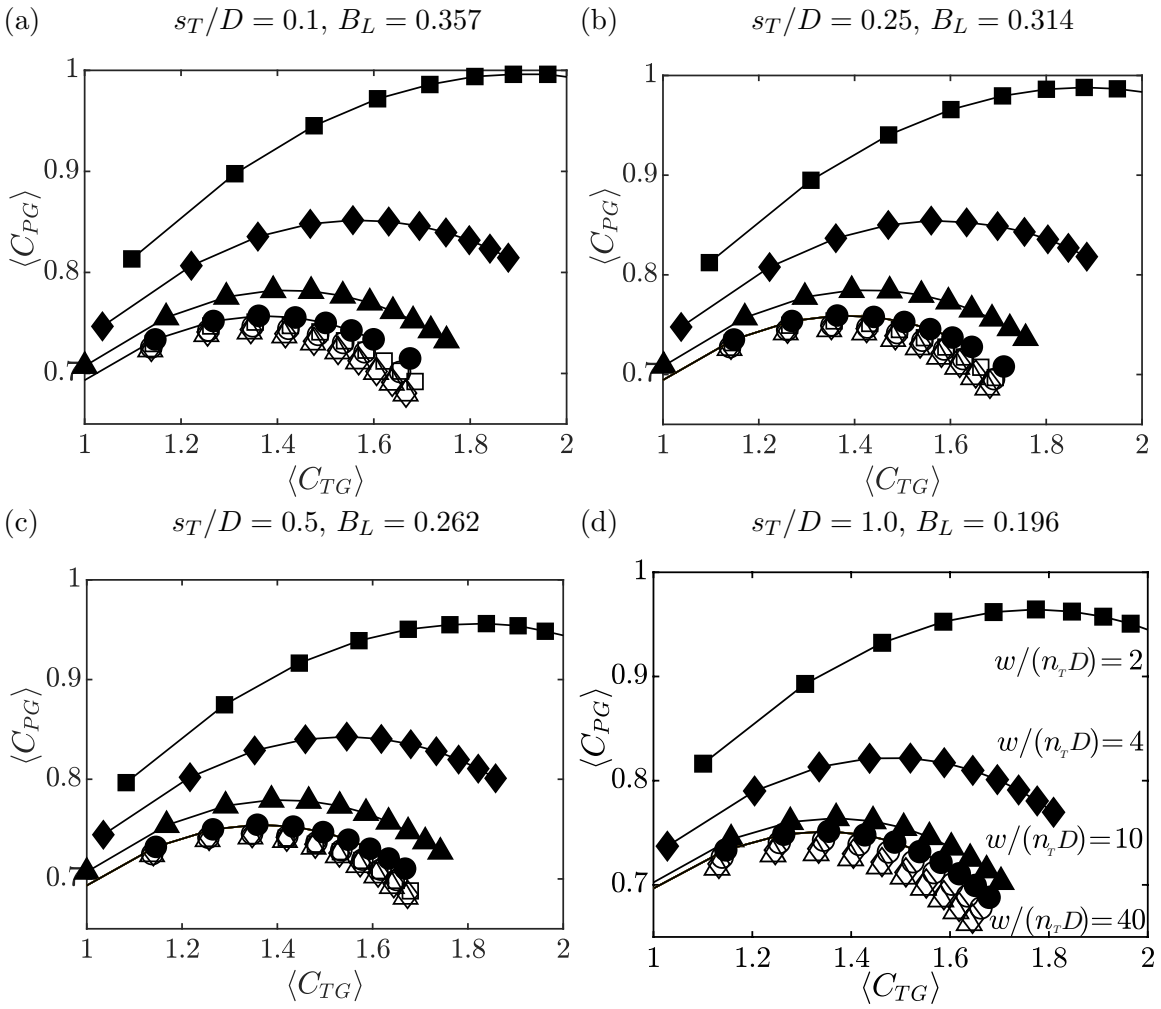

Figure 5.6: Two-scale blockage corrections to the numerical results for the range of local and global blockage ratios presented in Table. 5.2 & Table. 5.3. Solid symbols represent simulation results, connected with a line between points for convenience. Hollow symbols represent two-scale blockage corrected results. The channel widths of $w/(n_T D) = 2$, $w/(n_T D) = 4$, $w/(n_T D) = 10$, $w/(n_T D) = 40$ are represented by squares, diamonds, triangles and circles respectively. For a set tip-to-tip turbine spacing, the corrected curves closely follow one another just below the nearly unblocked simulation case, demonstrating the validity of the proposed correction.

blockage case ($B_G = 0.01$), confirming the validity of the theoretical model. Additionally, with the blockage correction applied to all cases (including the $B_G = 0.01$ cases), the correction predicts consistent free-flow performance (for each given turbine spacing) with small error margins for the fixed turbine arrangements.

In general, slightly larger errors in the correction predictions occur for large thrust coefficients, well above the peak power point, and for the smallest turbine spacing (i.e. largest local blockage $B_L = 0.196$). These increased errors stem from the limitations

of the proposed model. The two-scale theory from which the blockage correction is derived assumes that the device-scale wake mixing takes place much faster than the array-scale flow expansion i.e. that the two-scales are completely separated. This is however only valid when the number of turbines in the fence is sufficiently large. Nishino and Willden [2013a] developed a model to account for short fences and found that the solutions asymptote to the two-scale theory as the number of turbines in the fence increases. When accounting for finite number of turbine fences, deviation from the two-scale theory depends on the operating conditions, channel and turbine layouts, as well as the numerical mixing assumptions. Correcting the various configurations, particularly at larger disc loadings where the finite fence effect is expected to be of larger significance, is therefore expected to lead to the slightly increased errors observed. Secondly, the validity of the proposed blockage correction is limited in the case of $B_L \approx B_G$, or where $B_A \approx 1$. For example in the limit for $B_A = 1$, it can be shown from the theory in section 5.3.2 that the model is only valid for $B_L C_{TG} \leq 1/3$, and therefore breaks down at larger B_L and C_{TG}. This impacts the largest turbine spacing combined with smallest channel width cases for which the correction can no longer be applied. These cases are however typically outside of the area of interest as widely spaced turbines are unlikely to be placed in a co-planar fence configuration in a very narrow channel. In these cases however, existing single-scale blockage corrections are recommended instead.

Nonetheless, the proposed two-scale blockage correction clearly corrects the performance of blocked turbine arrays to free-flow conditions with excellent accuracy across a wide range of disc spacing (local blockage), channel width (global blockage), and operating conditions.

5.5 Conclusions

This study proposes a new two-scale blockage correction method for an array of turbines operating in a channel. It extends a two-scale theoretical model [Nishino and Willden, 2012a] for the performance of a row of co-planar turbines partially spanning the width of a tidal channel by developing a relationship between free-flow (unblocked) and blocked flow conditions.

The model is validated by RANS-AD simulations with an array of $n_T = 8$ turbines across a range of realistic turbine tip-to-tip spacings (local blockage) and channel width (global blockage). The proposed correction shows excellent agreement with the numerical results across a wide range of realistic local and global blockage ratios.

A limitation of the proposed correction is that it relies on the assumption of complete separation between local and array scales, which is only true for a large number of discs in the fence. The correction can therefore be extended on by following the same formulation but with short-fence theory [Nishino and Willden, 2013a] instead to account for low turbine number fence configurations. An additional extension to the two-scale correction can be to consider the effects of free-surface deformation [Vogel et al., 2016], here assumed negligible.

A particularly useful aspect of the theoretical model is to allow for experimental quantification of the local blockage effect for turbine fences which partially span the width of a tidal channel. While constructive interference effects which exploit the local blockage ratio may be present in both full-scale deployments and reproduced in experiments, the constraints imposed by the dimensions of experimental facilities will likely introduce array, and therefore global, blockage effects as well that would not otherwise be observed at full scale. For instance, doubling the fence length doubles the global blockage, but increases in fence thrust and power cannot be attributed solely to the change in global blockage due to non-linear coupling between local and global blockage effects. This correction allows for a decoupling of these two effects, such that the local blockage effect can be isolated and quantified. The blockage corrected results can then for example be combined with models of fence performance in channels with an oscillatory tidal current [Dehtyriov et al., 2023a] for a complete understanding of *in-situ* performance.

Acknowledgement

This research was funded in part by D.D.'s EPSRC studentship (grant no. EP/S023801/1), C.R.V.'s UKRI Future Leaders Fellowship (grant no. MR/V02504X/1) and R.H.J.W.'s EPSRC Advanced Fellowship (grant no. EP/R007322/1), and by the EPSRC Supergen ORE Hub (grant no. EP/S000747/1).

5.A Statement of authorship

The preceding chapter has been reformatted from a conference article published in the *15th European Wave and Tidal Energy Conference* (EWTEC 2023). The inclusion of co-authors reflects the fact that the work came from active collaboration between researchers and acknowledges input into team-based research.

Publication details	
Title of paper	A two-scale blockage correction for an array of tidal turbines
Publication status	Published
Publication reference	D. Dehtyriov, C. Vogel, and R. Willden, "A Two-scale blockage correction for an array of tidal turbines", *Proc. EWTEC*, vol. 15, Sep. 2023. doi: 10.36688/ewtec-2023-366

Student Confirmation	
Student Name	Daniel Dehtyriov
Contribution to the paper	The theoretical development and writing was a collaborative effort between all co-authors, with the contributions and writing split 80−10−10 between DD, CV and RHJW respectively.

Student signature

20th December 2023

Date

Supervisor Confirmation	
Supervisor name and title	Prof. Richard Willden
Supervisor comments	I confirm that Daniel has made a substantial contribution to the publication, and that the description above in the Statement of Authorship is accurate.

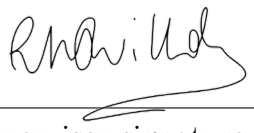

Supervisor signature

20th December 2023

Date

Chapter 6

Conclusions

> "I say let the world go to hell, but I should always have my tea."
>
> — Fyodor Dostoevsky, Notes from Underground

This thesis has theoretically investigated the dynamics of energy extraction from fluid flows, extending on the models set by the Lanchester-Betz-Joukowsky theory. The idealised flow conditions underpinning this classical theory are viewed as constraints in an optimisation framework and the present work extends beyond these limits for more realistic flow conditions by relaxing the constraints associated with the unbounded, inviscid, and steady flow assumptions. For turbines or turbine arrays with velocity recovery in their wakes, it is identified that additional static pressure recovery associated with wake mixing is a key mechanism by which peak power extraction efficiency may increase above that of the idealised conditions of the Betz model.

The pressure recovery mechanism is first identified for velocity recovery in the wake of turbine arrays in chapter 2. By reformulating the blockage-constrained problem as a constrained optimisation problem and generalising to an arbitrary number of scales, it is demonstrated that the asymptotic limit to power extraction efficiency for any energy extracting device in an unbounded fluid is bounded by unity, a 27/16 increase on the Betz limit. Importantly, chapter 2 demonstrates that is not the minimisation of mixing losses by which power extraction increases with the number of scales. Conversely, wake mixing provides an additional source of static pressure rise in the device wake that enables additional reduction in static pressure on the downstream side of the extractor, and consequently an increase in the static pressure drop across the device, leading to increased power extraction.

The distinction between overall energy extraction efficiency (basin efficiency) and device power extraction efficiency (power coefficient) is highlighted, and it is observed that as the latter increases, the former necessarily decreases. For a single disc operating at the Betz limit in a globally unblocked flow, 1/3 of the energy is lost in wake remixing. By contrast, it is shown that at most 1/2 of the total energy removed from the flow can be usefully extracted when the multi-scale device power coefficient is maximised, with the remaining half instead lost to wake remixing.

For devices placed in a finite width channel, the device thrust is additionally balanced by a far-field streamwise pressure gradient, again enabling a reduction in the static pressure on the downstream side of the extractor, and providing an additional source of increased power extraction. The two mechanisms that decrease the pressure on the downstream side of the extractor are shown to be nonlinearly additive so that multi-scale devices placed in channels can achieve even higher levels of power extraction.

Building on this understanding, chapter 3 considers a relaxation in the inviscid assumption of the Betz theory, where mixing is allowed to occur between the bypass and wake flow as would be expected in a real flow system. In contrast to the inviscid model, where the entirety of the wake pressure recovery is associated with a decrease in wake velocity, this chapter demonstrates that an additional recovery mechanism associated with static pressure results directly from the mixing between the core and bypass flows, leading to complete velocity recovery to upstream conditions in the turbine wake. The presented models do not make assumptions about how the mixing process occurs, only that the control volume boundaries across each mixing event are shear-stress free. While the models do not therefore require turbulence, it is the mechanism by which the flow would be mixed in a real turbulent turbine wake.

Comparable to the physics for multi-scale arrays, the addition of this static pressure recovery mechanism enables a lower pressure to be maintained immediately downstream of the disc, and a larger pressure drop to therefore be achieved across the device. Estimates of the performance variation for two limiting flow conditions are derived: the first, where the wake flow mixing occurs in the far-wake following pressure equalisation between core and bypass flows; and the second, where strong flow mixing is observed shortly behind the actuator disc in the near-wake and in advance of pressure equalisation between core and bypass flows. The algebraic relationships between the wake velocity factor, γ, and optimal performance coefficients are shown to be $C_{P\text{max, FW}} = 3.83\gamma(1-\gamma)/(0.9+\gamma)$ as a new estimate of disc performance in realistic turbulent flow conditions with gradual far-wake mixing, and

$C_{P\text{max, NW}} = \gamma(1-\gamma)(3-\gamma)^2/2$ as the maximum disc performance in an unbounded flow achieved with rapid near-wake mixing, which yield the new performance limits of 0.71 and 0.81 respectively.

This highlights the importance of accounting for wake mixing in assessing turbine performance, challenging the conventional assumptions prevalent in aircraft design, where minimising the mixing rate is typically associated with reduction in induced drag. Contrary to these norms, the results indicate that enhancing the wake mixing rate can in fact amplify the local power coefficient of individual turbines. The physical insights derived from the analytical model are confirmed by patterns observed in numerical simulations and with previous experimental measurements for the thrust of operating turbines across all axial induction factors. It may therefore be concluded that the analytical model provides a more accurate representation of both the fundamental physics and resultant variations in the performance of actuator discs in turbulent flows compared to the classical inviscid model proposed by Betz. Increasing the mixing rate to enhance device performance aligns synergistically with efforts to re-energise the wake by enhancing the wake mixing rate for increased mean power extraction across turbine farms. Physical controls which attempt to accelerate the rate of wake mixing through, for example, tip-vortex breakdown, will therefore need to carefully account for the impact on turbine performance. Active and passive control mechanisms may additionally be useful to exploit this effect in practice.

The model not only establishes a new upper limit for turbine performance in flows with wake mixing present but also provides a fresh perspective for optimising the design of energy extraction devices by recognising the positive impact of increased wake mixing rates. This leads to further questions regarding the implicit constraints and limitations of the Betz model, and how these might impact performance and design. For wind and tidal turbines with turbulent and sheared upstream flows, farm wakes re-energised by the atmospheric boundary layer, bathymetric variation, free-surface deformation, compressiblity effects and so on, there remain further challenges regarding variations and extensions to the constraints and how these can be exploited for optimal power generation. Theoretical extensions to the Betz model can additionally be readily linked to blade element momentum theory to inform the design of higher efficiency blades.

Another significant limitation to the classical model is the assumption of steady flow. In chapter 4, the leading order effect has been considered, namely sinusoidal time-unsteady forcing of the flow in a channel, where the mass flux through a turbine fence is no longer fixed but is dynamic, governed by the channel head and can be

modified by the action of the turbines. The turbine fence model comprises a co-planar closely spaced series of turbines that partially span a much wider channel. The analysis highlights the diminishing returns in adding turbines to a channel due to the deleterious impact on the flow rate through the channel. Three dimensionless parameters are shown to comprehensively define the flow problem for forced sinusoidal oscillation in a tidal channel: firstly, the channel Froude number $\mathrm{Fr}_\omega = \omega l/\sqrt{ga}$, representing the relative oscillatory tidal elevation difference between the channel ends, which is shown to be directly proportional to the square root of the cycle-averaged potential to kinetic head in the channel. Secondly, the channel bed friction represented by $C_f(l/h)$. Lastly, the turbine characteristics $B_A C_{TA}$, representing the turbine spacing and thrust. The return parameter R is introduced as the yield per turbine area, proportional to the ratio of total power extracted to total frontal area of turbines, as an optimisation metric for the arrangement of turbines in a channel.

Blockage again plays a major role in the performance of a tidal farm, with the return parameter and flow reduction strongly influenced by the different scales of blockage. For even relatively unblocked tidal farms, and especially for optimally arranged farms, modelling the channel flow dynamics and resistance is crucial for farm yield estimation. It is shown that for a given channel there exists an optimal number and spacing between turbines, and that the optimal arrangement of turbines always lies along a universal curve $B_L = (9B_G + 4)/(3B_G + 10)$, with B_L and B_G the local and global blockages respectively. The channel Froude number heavily constrains the maximum possible return, and increases in bed friction diffuse the sensitivity of return to turbine arrangement.

The operational range of the tidal fence is shown to be significantly limited by both environmental and engineering constraints. As the Froude number increases, the environmental constraint of limiting impact on flow rate becomes more stringent, whereas the device thrust constraint becomes less restrictive. Effective control strategies for power capping are crucial, especially at peak flow speeds, and generally when dealing with thrust coefficients beyond what conventional rotors can achieve.

This model can be applied to estimate limits of energy extraction for resource assessment with environmental flow constraints included, and can be extended and applied to large wind farms where the farm resistance interacts with the atmospheric boundary layer to reduce the mean mass flux through the farm.

Integration of actual turbine characteristics into the models, by including three-dimensional blade effects, rotational effects and thrust limits, must be considered to further bridge this scientific work to engineering application. For the work presented

herein, the unsteady head-driven channel model can be seamlessly integrated with actual turbine characteristics, enhancing the accuracy of predictions as opposed to relying solely on optimal disc performance. In other cases, where the theoretical work has been supported by Reynolds-Averaged-Navier-Stokes simulations of actuator discs, the studies can be extended to large-eddy simulation of actuator lines or three-dimensional blades to further connect the work to real turbines. Further investigation into relaxation of the steady flow assumption (a non-zero $\frac{d\mathbf{u}}{dt}$ term) of the Betz model, beyond the leading order effect for channel flow, is clearly of practical interest for turbines subject to gusts, waves or oscillatory tidal flows.

Finally, experimental validation plays a key role in determining the practical limits to exploiting power coefficient increases for turbine fences. Chapter 2 has however shown that the two physical mechanisms which modify the disc performance are nonlinearly additive; namely the far-field static pressure gradient associated with the presence of the channel geometric constraints, and the static pressure rise associated with bypass flow mixing in the wake. In chapter 5, this nonlinearity is shown to invalidate the theoretical assumptions of single-scale corrections which necessitates the development of a two-scale correction. The two-scale blockage correction model presented in chapter 5 decouples the two mechanisms, removing the global blockage effect due to tunnel constraints, but preserving the intended local blockage effect. The proposed correction shows excellent agreement with Reynolds Averaged Navier-Stokes computations of 8 disc fences. However, the results are expected to show dependency on the finite length of the fence, real turbine geometries, and variations in the wake mixing rate. Detailed experimental campaigns which seek to isolate the global and local physical phenomena considered herein will therefore likely be needed to extend the model to account for the nonlinear interaction between these effects.

This work challenges the limitations of the Betz model by extending the model to constrained, viscous, and time-dependent flows. Through the development of theoretical models, this thesis reveals novel flow physics and operational insights that will support enhancement of efficiency through extending conventional understanding of isolated single turbines to more complex and integrated multi-turbine operation. Further extensions to this work could delve into proposing and testing practical flow control methods based on the identified physical mechanisms, high-order numerical simulation for validation and design, and a deeper exploration of the model assumptions to continue navigating flow physics beyond the Betz limit.

Appendix A

Publications

Journal articles

- **D. Dehtyriov**, A.M. Schnabl, C.R. Vogel, S. Draper, T.A.A. Adcock, and R.H.J. Willden. Fractal-like actuator disc theory for optimal energy extraction. *Journal of Fluid Mechanics*, 927:A40, 2021.
- **D. Dehtyriov**, C.R. Vogel, and R.H.J. Willden. A head-driven model of turbine fence performance. *Journal of Fluid Mechanics*, 956:A14, 2023.
- **D. Dehtyriov**, C.R. Vogel, and R.H.J. Willden. Turbulent wake mixing for power extraction above the Betz limit. *In preparation.*

Conference papers

- **D. Dehtyriov**, C.R. Vogel, and R.H.J. Willden. A two-scale blockage correction for an array of tidal turbines. *Proceedings of the European Wave and Tidal Energy Conference*, 15 Sep. 2023.
- **D. Dehtyriov**. Flow physics beyond the Betz limit. *Osborne Reynolds Competition, University of Manchester*, 7 Jul. 2023. Runner-up prize winner.
- K. Wen, **D. Dehtyriov**, B. Byrne. Impact of wind turbine aerodynamics on offshore foundation design. *Wind Europe, Bilbao*, 21 Mar. 2024.

Appendix B

Glossary

(x, y, z) Spanwise, depth/height and streamwise coordinate respectively.

A_C Cross-sectional channel area.

A_R Representative channel area.

A_T Turbine swept/disc area.

A_b Channel bed area.

A_j Core flow area at station j.

A_{D_s} Representative device area at each fractal scale s.

A_{M_i} Mixing area for mixing stage i.

A_{e_i} Exit core flow area for mixing stage i.

B Blockage ratio.

B_A Array scale blockage ratio.

B_D Device blockage ratio.

B_G Global blockage ratio.

B_L Local blockage ratio.

C_P Power coefficient.

C'_P Blockage corrected power coefficient.

C^*_P Optimal power coefficient at fixed mixing ratio.

C_T Thrust coefficient.

C'_T Blockage corrected thrust coefficient.

C^*_T Thrust coefficient for optimal power at fixed mixing ratio.

C_μ Turbulence model coefficient.

C_f Channel bed friction coefficient.

$C_{P,\mathbf{Betz}}$ Betz Limit.

$C_{P,max}$ Power coefficient at optimal mixing ratio.

C_{PA} Array scale power coefficient.

C_{PC} Cycle-averaged channel power coefficient.

C_{PG} Global power coefficient.

C_{PL} Local power coefficient.

$C_{T,max}$ Thrust coefficient at optimal mixing ratio for maximum power.

C_{TA} Array scale thrust coefficient.

C_{TC} Channel flow rate normalised thrust coefficient.

C_{TD} Peak single disc thrust coefficient.

C_{TG} Global thrust coefficient.

C_{TL} Local thrust coefficient.

$C_{\epsilon 1}$ Turbulence model coefficient.

D Turbine/disc diameter.

F Total resistive force per unit mass.

F_T Turbine array resistive force.

F_b Bed friction resistive force.

Fr Froude number.

Fr_ω Modified channel Froude number.

H Tidal channel head.

I_∞ Upstream inlet turbulence intensity.

$I_{\mathbf{ref}}$ Reference upstream turbulence intensity.

K Disc momentum loss factor.

L Turbulent mixing length scale.

L_T Turbine farm length.

P Power.

P_0 Total pressure.

P_D Delivered device power.

P_G Useful power generated.

Q Channel volume flow rate.

Q_0 Peak undisturbed channel volume flow rate.

R Return parameter.

Re Reynolds number.

S_U Disc momentum flux.

T Thrust.

T_D Channel disc thrust.

T_G Global array thrust.

T_P Tidal period.

$T_{D,\mathbf{max}}$ Peak thrust over tidal period.

T_{b_s} Equivalent bypass thrust at each scale.

U_A Array scale channel flow approach velocity.

U_C Channel flow velocity.

U'_C Equivalent zero blockage channel velocity.

U_D Local disc streamwise flow velocity.

Z_i Cumulative mixing area ratio for mixing stage i.

$Z_{\mathbf{max}}$ Maximum permissible cumulative mixing area ratio.

Δ Change in quantity.

Ω Wake boundary.

α Disc velocity induction factor.

α_A Array scale axial velocity factor.

α_G Global velocity induction factor.

α_L Local scale axial disc velocity factor.

$\bar{E}_\zeta$ Cycle-averaged energy in driving channel head.

$\bar{E}_k$ Cycle-averaged channel kinetic energy.

β Bypass flow velocity factor.

β_{e_i} Bypass flow mixing flow acceleration ratio for mixing stage i.

$\delta\psi$ Incremental wake energy entrainment.

$\delta\varphi$ Incremental wake mass entrainment.

δp_i Static pressure change across each mixing stage i.

$\dot{E}$ Energy flux.

$\dot{m}$ Mass flux.

$\dot{m}_t$ Mass flux through the disc core flow.

$\dot{m}_{b_s}$ Mass flux through the bypass flow at each scale.

ϵ Rate of turbulent kinetic energy dissipation.

η Basin efficiency.

γ Wake velocity induction factor.

γ_A Array scale axial wake velocity factor.

γ_G Global velocity tuning factor.

γ_L Local scale axial wake velocity factor.

$\hat{Q}$ Peak volume flow rate amplitude.

λ Lagrangian multiplier.

$\hat{\mathbf{n}}$ Normal vector.

$\mathcal{L}$ Lagrangian.

ν Kinematic viscosity.

ω Tidal frequency.

ω_t Specific rate of turbulent kinetic energy dissipation.

ψ Wake energy flux entrainment.

ρ Fluid density.

τ_b Bed friction shear stress.

φ Wake mass flux entrainment.

ξ Tidal elevation.

ξ_e Elevation at channel exit.

ξ_i Elevation at channel inlet.

ζ_i Mixing area ratio for mixing stage i.

a Driving head amplitude.

c Channel geometric parameter.

c_p Static pressure coefficient.

c_{pd} Static pressure coefficient just downstream of the turbine.

c_{pu} Static pressure coefficient just upstream of the turbine.

d_s Number of discs at each scale.

g Gravitational acceleration.

h Channel depth.

k Turbulent kinetic energy.

l Channel length.

n Number of fractal scales.

n_R Number of rows.

n_T Number of turbines.

p Static Pressure.

p_∞ Undisturbed static pressure.

p_i Static pressure at station i.

p_{4m} Mixing bypass static pressure.

p_b Bypass bulk flow static pressure.

p_c Core wake flow static pressure.

q Dynamic head.

r Radial coordinate.

s Fractal scale index.

s_T Tip-to-tip spacing between turbines.

t Time.

u_s^b Bypass velocity at a given fractal scale.

u_s^w Wake velocity at a given fractal scale.

u_∞ Undisturbed upstream velocity.

u_i Flow velocity at station i.

u_s Flow-through velocity at a given fractal scale s.

u_{e_i} Exit flow velocity for mixing stage i.

w Channel width.

w_a Turbine fence width.

Appendix C

Acronyms

AD Actuator disc.

CV Control volume.

FW Far wake.

NW Near wake.

RANS Reynolds averaged Navier Stokes.

SST Shear stress transport.

TKE Turbulent kinetic energy.

TSR Tip-speed ratio.

Bibliography

T. A. A. Adcock, S. Draper, G. T. Houlsby, A. G. L. Borthwick, and S. Serhadlıoğlu. The available power from tidal stream turbines in the Pentland Firth. *Proceedings of the Royal Society A: Mathematical, Physical and Engineering Sciences*, 469(2157): 20130072, 2013.

T. A. A. Adcock, S. Draper, R. H. J. Willden, and C. R. Vogel. The fluid mechanics of tidal stream energy conversion. *Annual Review of Fluid Mechanics*, 53(1):287–310, 2021.

I. Afgan, J. McNaughton, S. Rolfo, D. D. Apsley, T. Stallard, and P. Stansby. Turbulent flow and loading on a tidal stream turbine by LES and RANS. *International Journal of Heat and Fluid Flow*, 43:96–108, 2013.

M. H. B. Ahmadi. Influence of upstream turbulence on the wake characteristics of a tidal stream turbine. *Renewable Energy*, 132:989–997, 2019.

A. S. Bahaj, A. F. Molland, J. R. Chaplin, and W. M. J. Batten. Power and thrust measurements of marine current turbines under various hydrodynamic flow conditions in a cavitation tunnel and a towing tank. *Renewable Energy*, 32(3):407–426, 2007.

M. J. Barnsley and J. F. Wellicome. Wind tunnel investigation of stall aerodynamics for a 1.0 m horizontal axis rotor. *Journal of Wind Engineering and Industrial Aerodynamics*, 39:11–21, 1992.

W. M. J. Batten, M. E. Harrison, and A. S. Bahaj. Accuracy of the actuator disc-RANS approach for predicting the performance and wake of tidal turbines. *Philosophical Transactions of the Royal Society A: Mathematical, Physical and Engineering Sciences*, 371(1985), 2013.

H. Berry and Y. Yao. Double multiple streamtube model and numerical analysis of vertical axis wind turbine. *Energy and Power Engineering*, 3:262–270, 2011.

A. Betz. Das Maximum der theoretisch möglichen Ausnützung des Windes durch Windmotoren. *Zeitschrift für das gesamte Turbinenwesen*, 26:307–309, 1920.

J. Blanchfield, C. Garrett, P. Wild, and A. Rowe. The extractable power from a channel linking a bay to the open ocean. *Proceedings of the Institution of Mechanical Engineers, Part A: Journal of Power and Energy*, 222(3):289–297, 2008.

J. Bleeg, M. Purcell, R. Ruisi, and E. Traiger. Wind farm blockage and the consequences of neglecting its impact on energy production. *Energies*, 11(6), 2018.

P. A. J. Bonar, L. Chen, A. M. Schnabl, V. Venugopal, A. G. L. Borthwick, and T. A. A. Adcock. On the arrangement of tidal turbines in rough and oscillatory channel flow. *Journal of Fluid Mechanics*, 865:790–810, 2019.

I. G. Bryden and S. J. Couch. How much energy can be extracted from moving water with a free surface: A question of importance in the field of tidal current energy? *Renewable Energy*, 32(11):1961–1966, 2007.

M. L. Buhl. New emperical relationship between thrust coefficient and induction factor for the turbulent windmill state. Technical Report NREL/TP-500-36834, NREL, 2005.

T. L. Burton, N. Jenkins, E. Bossanyi, D. Sharpe, and M. Graham. *Wind Energy Handbook*. John Wiley & Sons Ltd, United Kingdom, May 2021. ISBN 978-1-119-45109-9.

R. H. Byrd, M. E. Hribar, and J. Nocedal. An interior point algorithm for large-scale nonlinear programming. *SIAM Journal on Optimization*, 9(4):877–900, 1999.

D. Coles and T. Walsh. Mechanisms for reducing the cost of tidal stream energy. In *Proc. 13th European Wave and Tidal Energy Conference, Naples, Italy*, 2019.

J. T. Conway. Analytical solutions for the actuator disk with variable radial distribution of load. *Journal of Fluid Mechanics*, 297:327–355, 1995.

J. T. Conway. Exact actuator disk solutions for non-uniform heavy loading and slipstream contraction. *Journal of Fluid Mechanics*, 365:235–267, 1998.

S. C Cooke, R. H. J. Willden, B. Byrne, T. Stallard, and A. Olczak. Experimental investigation of tidal turbine partial array theory using porous discs. In *Proc. 11th European Wave and Tidal Energy Conference, Nantes, France*, 2015.

S. C. Cooke, R. H. J. Willden, and B. W. Byrne. The potential of cross-stream aligned sub-arrays to increase tidal turbine efficiency. *Renewable Energy*, 97:284–292, 2016.

M. J. Creed, S. Draper, T. Nishino, and A. G. L. Borthwick. Flow through a very porous obstacle in a shallow channel. *Proceedings of the Royal Society A: Mathematical, Physical and Engineering Sciences*, 473(2200):20160672, 2017.

E. Cumberbatch. Two-dimensional flow past a mesh. *The Quarterly Journal of Mechanics and Applied Mathematics*, 35:335–344, 1981.

P. F. Cummins. The extractable power from a split tidal channel: An equivalent circuit analysis. *Renewable Energy*, 50:395–401, 2013.

J. O. Dabiri. Theoretical framework to surpass the Betz limit using unsteady fluid mechanics. *Physical Review Fluids*, 5(2), 2020.

D. Dehtyriov, A. M. Schnabl, C. R. Vogel, S. Draper, T. A. A. Adcock, and R. H. J. Willden. Fractal-like actuator disc theory for optimal energy extraction. *Journal of Fluid Mechanics*, 927:A40, 2021.

D. Dehtyriov, C. R. Vogel, and R. H. J. Willden. A head-driven model of turbine fence performance. *Journal of Fluid Mechanics*, 956:A14, 2023a.

D. Dehtyriov, C. R. Vogel, and R. H. J. Willden. A two-scale blockage correction for an array of tidal turbines. In *Proc. 15th European Wave and Tidal Energy Conference, Bilbao, Spain*, 2023b.

S. Draper and T. Nishino. Centred and staggered arrangements of tidal turbines. *Journal of Fluid Mechanics*, 739:72–93, 2014.

S. Draper, T. Nishino, T. A. A. Adcock, and P. H. Taylor. Performance of an ideal turbine in an inviscid shear flow. *Journal of Fluid Mechanics*, 796:86–112, 2016.

D. L. Elliott and J. B. Cadogan. Effects of wind shear and turbulence on wind turbine power curves. *Wind Energy*, 1:10–14, 1990.

R. E. Froude. On the part played in propulsion by differences in fluid pressure. *Transactions: Royal Institution of Naval Architects*, 30:390, 1889.

E. Gaertner, J. Rinker, L. Sethuraman, F. Zahle, B. Anderson, G. E. Barter, N. J. Abbas, F. Meng, P. Bortolotti, W. Skrzypinski, G. N. Scott, R. Feil, H. Bredmose, K. Dykes, M. Shields, C. Allen, and A. Viselli. IEA wind TCP task 37: Definition of the IEA 15-megawatt offshore reference wind turbine. Technical Report NREL/TP-5000-75698, National Renewable Energy Lab. (NREL), 3 2020.

C. Garrett and P. Cummins. The power potential of tidal currents in channels. *Proceedings of the Royal Society A: Mathematical, Physical and Engineering Sciences*, 461(2060):2563–2572, Aug 2005.

C. Garrett and P. Cummins. The efficiency of a turbine in a tidal channel. *Journal of Fluid Mechanics*, 588:243–251, 2007.

H. Glauert. *The Elements of Aerofoil and Airscrew Theory.* Cambridge Science Classics. Cambridge University Press, 1926.

H. Glauert. *Airplane Propellers*, pages 169–360. Springer Berlin Heidelberg, Berlin, Heidelberg, 1935. ISBN 978-3-642-91487-4.

H. Glauert. *The Elements of Aerofoil and Airscrew Theory.* Cambridge University Press, 2nd edition, 1947.

M. Grabbe, E. Lalander, S. Lundin, and M. Leijon. A review of the tidal current energy resource in Norway. *Renewable and Sustainable Energy Reviews*, 13:1898–1909, 2009.

M. D. Greenberg and S. R. Powers. Nonlinear actuator disk theory and flow field calculations including nonuniform loading. Technical Report NASA-CR-1672, NASA, 1970.

V. Gupta and A. M. Young. A one-dimensional model for tidal array design based on three-scale dynamics. *Journal of Fluid Mechanics*, 825:651–676, 2017.

G. R. Hough and D. E. Ordway. The generalized actuator disk. Technical report, Therm Advanced Research Inc Ithaca NY, 1964.

G. T. T. Houlsby, S. Draper, and M. L. G. Oldfield. Application of Linear Momentum Actuator Disc Theory to Open Channel Flow. Technical Report July 2015, University of Oxford, 2008.

W. Hunter, T. Nishino, and R. H. J. Willden. Investigation of tidal turbine array tuning using 3D Reynolds-Averaged Navier–Stokes Simulations. *International Journal of Marine Energy*, 10:39 – 51, 2015.

P. B. Johnson, A. Wojcik, K. R. Drake, and I. Eames. Impulsively started planar actuator surfaces in high-Reynolds-number steady flow. *Journal of Fluid Mechanics*, 733:302–324, 2013.

N. E. Joukowsky. Windmill of the NEJ type. In *Transactions of the Central Institute for Aero-Hydrodynamics of Moscow*, 1920.

M. C.R. Juniper and T. Nishino. Single and multi-row turbine performance in bounded shear flow. *Journal of Fluid Mechanics*, 957:A10, 2023.

R. H. Karsten, J. M. McMillan, M. J. Lickley, and R. D. Haynes. Assessment of tidal current energy in the Minas Passage, Bay of Fundy. *Proceedings of the Institution of Mechanical Engineers, Part A: Journal of Power and Energy*, 222(5):493–507, 2008.

N. Kolekar, A. Vinod, and A. Banerjee. On blockage effects for a tidal turbine in free surface proximity. *Energies*, 12(17), 2019. ISSN 1996-1073.

J. K. Koo and D. F. James. Fluid flow around and through a screen. *Journal of Fluid Mechanics*, 60(3):513–538, 1973.

F. W. Lanchester. A Contribution to the Theory of Propulsion and the Screw Propeller. *Journal of the American Society for Naval Engineers*, 27(2):509–510, 1915.

B. E. Launder and D. B. Spalding. The numerical computation of turbulent flows. *Computer Methods in Applied Mechanics and Engineering*, 3(2):269–289, 1974.

L. E. M. Lignarolo, D. Ragni, C. Krishnaswami, Q. Chen, C. J. Simão Ferreira, and G. J. W. van Bussel. Experimental analysis of the wake of a horizontal-axis wind-turbine model. *Renewable Energy*, 70:31–46, 2014.

C. N. H. Lock, H. Batehmen, and H. C. H. Townsend. An extension of the vortex theory of airscrews with applications to airscrews of small pitch, including experimental results. Technical Report 1014, Aeronautical Research Committee Reports and Memoranda, London: Her Majesty's Stationery Office, 1926.

R. Martin-Short, J. Hill, S. C. Kramer, A. Avdis, P. A. Allison, and M. D. Piggott. Tidal resource extraction in the Pentland Firth, UK: Potential impacts on flow regime and sediment transport in the Inner Sound of Stroma. *Renewable Energy*, 76:596–607, 2015.

E. C. Maskell. A theory of blockage effects on bluff bodies and stalled wings in a closed wind tunnel. Technical report, HMSO, London, 1963.

J. McNaughton, B. Cao, A. Nambiar, C. R Vogel, and Richard H J Willden. Constructive interference effects for tidal turbine arrays. *Journal of Fluid Mechanics*, 2021.

J. McNaughton, S. Ettema, F. Zilic de Arcos, C. R. Vogel, and R. H. J. Willden. An experimental investigation of the influence of inter-turbine spacing on the loads and performance of a co-planar tidal turbine fence. *Journal of Fluids and Structures*, 118:103844, 2023. ISSN 0889-9746.

F. R. Menter. Two-equation eddy-viscosity turbulence models for engineering applications. *AIAA Journal*, 32(8):1598–1605, 1994.

R. F. Mikkelsen and J. N. Sørensen. Modelling of wind tunnel blockage. In *Global Windpower Conference and Exhibition*, 2002.

S. Muchala and R. H. J. Willden. Impact of tidal turbine support structures on realizable turbine farm power. *Renewable Energy*, 114:588–599, 2017.

T. Nishino and R. H. J. Willden. The efficiency of an array of tidal turbines partially blocking a wide channel. *Journal of Fluid Mechanics*, 708:596–606, 2012a.

T. Nishino and R. H. J. Willden. Effects of 3-D channel blockage and turbulent wake mixing on the limit of power extraction by tidal turbines. *International Journal of Heat and Fluid Flow*, 37:123–135, 2012b.

T. Nishino and R. H. J. Willden. Two-scale dynamics of flow past a partial cross-stream array of tidal turbines. *Journal of Fluid Mechanics*, 730:220–244, 2013a.

T. Nishino and R. H. J Willden. The Efficiency Of Tidal Fences: A Brief Review and Further Discussion On The Effect Of Wake Mixing. In *32nd International Conference on Ocean, Offshore and Arctic Engineering*, pages 1–10, Nantes, France, 2013b. ASME.

D. R. Noble, S. Draycott, A. Nambiar, B. G. Sellar, J. Steynor, and A. Kiprakis. Experimental assessment of flow, performance, and loads for tidal turbines in a closely-spaced array. *Energies*, 13(8):1977, 2020.

A. Olczak, T. Stallard, T. Feng, and P. K. Stansby. Comparison of a RANS blade element model for tidal turbine arrays with laboratory scale measurements of wake velocity and rotor thrust. *Journal of Fluids and Structures*, 64:87–106, 2016.

F. G. O'Neill. Source models of flow through and around screens and gauzes. *Ocean Engineering*, 33:1884–1895, 2006.

M. R. O'Hara and A. Gallego. A modelling study of the tidal stream resource of the Pentland Firth, Scotland. *Renewable Energy*, 102:326–340, 2017.

W. J. Rankine. On the mechanical principles of the action of propellers. *Transactions: Royal Institution of Naval Architects*, 6:13, 1865.

A. Roshko. On the wake and drag of bluff bodies. *Journal of Aerospace Sciences*, 22: 124–132, 1955.

H. Ross and B. Polagye. An experimental assessment of analytical blockage corrections for turbines. *Renewable Energy*, 152:1328–1341, 2020.

J. Schluntz and R. H. J. Willden. The effect of blockage on tidal turbine rotor design and performance. *Renewable Energy*, 81:432–441, 2015.

A. Segalini and J. Å. Dahlberg. Blockage effects in wind farms. *Wind Energy*, 23(2): 120–128, 2020.

C. R. Shapiro, G. M. Starke, and D. F. Gayme. Turbulence and control of wind farms. *Annual Review of Control, Robotics, and Autonomous Systems*, 5(1):579–602, 2022.

J. N. Sørensen. Aerodynamic aspects of wind energy conversion. *Annual Review of Fluid Mechanics*, 43(1):427–448, 2011.

T. Stallard, R. Collings, T. Feng, and J. I. Whelan. Interactions between tidal turbine wakes: experimental study of a group of three-bladed rotors. *Philosophical Transactions of the Royal Society A*, 371:20120159, 2013.

K. Steiros and M. Hultmark. Drag on flat plates of arbitrary porosity. *Journal of Fluid Mechanics*, 853:R3, 2018.

K. Steiros, N. Bempedelis, and M. M. Cicolin. An analytical blockage correction model for high-solidity turbines. *Journal of Fluid Mechanics*, 948:A57, 2022.

R. J. A. M. Stevens and C. Meneveau. Flow structure and turbulence in wind farms. *Annual Reviews of Fluid Mechanics*, 49(1):311–339, 2017.

G. Sutherland, M. Foreman, and C. Garrett. Tidal current energy assessment for Johnstone Strait, Vancouver Island. *Proceedings of the Institution of Mechanical Engineers, Part A: Journal of Power and Energy*, 221(2):147–157, 2007.

G. I. Taylor. Air resistance of a flat plate of very porous material. *Reports and Memoranda of the Aeronautical Research Council, no. 2236*, 1944.

The Carbon Trust. Carbon Trust foreword to UK tidal current resource and economics study. Technical report, Black & Veatch Ltd., 2011.

Z. Ugray, L. Lasdon, J. Plummer, F. Glover, J. Kelly, and R. Marti. Scatter search and local NLP solvers: A multistart framework for global optimization. *INFORMS Journal on Computing*, 19(3):328–340, 2007.

R. Vennell. Tuning turbines in a tidal channel. *Journal of Fluid Mechanics*, 663: 253–267, 2010.

R. Vennell. Tuning tidal turbines in-concert to maximise farm efficiency. *Journal of Fluid Mechanics*, 671:587–604, 2011.

R. Vennell. Exceeding the Betz limit with tidal turbines. *Renewable Energy*, 55: 277–285, 2013.

R. Vennell and T. A. A. Adcock. Energy storage inherent in large tidal turbine farms. *Proceedings of the Royal Society A: Mathematical, Physical and Engineering Sciences*, 470(2166):20130580, 2014.

R. Vennell, S. W. Funke, S. Draper, C. Stevens, and T. Divett. Designing large arrays of tidal turbines: A synthesis and review, 2015. ISSN 13640321.

L. J. Vermeer, J. N. Sørensen, and A. Crespo. Wind turbine wake aerodynamics. *Progress in Aerospace Sciences*, 39(6-7):467–510, 2003.

C. R. Vogel, G. T. Houlsby, and R. H. J. Willden. Effect of free surface deformation on the extractable power of a finite width turbine array. *Renewable Energy*, 88: 317–324, 2016.

C. R. Vogel, R. H. J. Willden, and G. T. Houlsby. Blade element momentum theory for a tidal turbine. *Ocean Engineering*, 169:215–226, 2018.

C. R. Vogel, R. H. J. Willden, and G. T. Houlsby. Tidal stream turbine power capping in a head-driven tidal channel. *Renewable Energy*, 136:491–499, 2019.

R. Wagner, I. Antoniou, S. M. Pedersen, M. S. Courtney, and H. E. Jørgensen. The influence of the wind speed profile on wind turbine performance measurements. *Wind Energy*, 12(4):348–362, 2009.

R. A. Walters, M. R. Tarbotton, and C. E. Hiles. Estimation of tidal power potential. *Renewable Energy*, 51:255–262, 2013.

M. J. Werle. Wind turbine wall-blockage performance corrections. *Journal of Propulsion and Power*, 26(6):1317–1321, 2010.

J. I. Whelan, J. M. R. Graham, and J. Peiró. A free-surface and blockage correction for tidal turbines. *Journal of Fluid Mechanics*, 624:281–291, 2009.

D. C. Wilcox. Comparison of two-equation turbulence models for boundary layers with pressure gradient. *AIAA Journal*, 31(8):1414–1421, 1993.

R. H. J. Willden, T. Nishino, and J. Schluntz. Tidal stream energy: designing for blockage. In *Proc. 3rd Oxford Tidal Energy Workshop, Oxford, UK*, 2014.

K. L. Wu and F. Porté-Agel. Flow adjustment inside and around large finite-size wind farms. *Energies*, 10(12), 2017. ISSN 1996-1073.

T. Y Wu. Flow through a heavily loaded actuator disc. *Schiffstechnik*, 9(47):134–138, 1962.

F. Zilic de Arcos, G. Tampier, and C. R. Vogel. Numerical analysis of blockage correction methods for tidal turbines. *Journal of Ocean Engineering and Marine Energy*, 6(2):183–197, 2020.